Enhancing the performance of concentrating photovoltaics through multi-layered microchannel heat sink and phase change materials

Submitted by Idris Hamood Salim Al Siyabi, to the University of Exeter
as a thesis for the degree of
Doctor of Philosophy in Renewable Energy
In November 2018.

I certify that all material in this thesis which is not my own work has been identified and that no material has previously been submitted and approved for the award of a degree by this or any other University.

(Signature)……

Abstract

Concentrating Photovoltaic technology is considered now as a promising option for solar electricity generation along with the conventional flat plate PV technology especially in high direct normal irradiance areas. However, the concentrating photovoltaic industry sector still struggles to gain market share and to achieve adequate economic returns due to challenges such as the high temperature of the solar cell which causes a reduction its efficiency.

The work presented in this thesis is targeted to influence the overall performance of a high concentrated photovoltaic system by integrating both the multi-layered microchannel heat sink technique and a phase change material storage system. The proposed integrated system is composed of a multi-layered microchannel heat sink attached to a single solar cell high concentrated photovoltaic module for thermal regulation purposes. This is expected to reduce the solar cell temperature hence increasing the electrical output power. The high concentrated photovoltaic and multi-layered microchannel heat sink system is then connected to a phase change material thermal storage system to store efficiently the thermal energy discharged by the high concentrated photovoltaic and multi-layered microchannel heat sink system.

The first part of the thesis discusses the influence of the multi-layered microchannel heat sink on the high concentrated photovoltaic module using both the numerical and experimental approaches. The multi-layered microchannel heat sink has been integrated for the first time with the single cell receiver and tested successfully. A numerical analysis of the high concentrated photovoltaic and multi-layered microchannel heat sink system shows the potential of the heat sink to reduce the solar cell maximum temperature and its uniformity.

The thermal behaviour of the multi-layered microchannel heat sink under non-uniform heat source was experimentally investigated. The results show that in extreme heating load of 30W/cm² and in heat transfer fluid flow rate of 30ml/min, increasing the number of layers from 1-layer to 4-layers reduced the heat source temperature from 88.55°C to 73.57°C, respectively. In addition, the single layer multi-layered microchannel heat sink suffers of the most heat source temperature non-uniform compared to the heat sinks with higher number of layers. Also, the

results show that increasing the number of layers from 1-layer to 4-layers reduced the pressure drop from 16.6mm H_2O to 3.34 mm H_2O.

The indoor characterization of the high concentrated photovoltaic and multi-layered microchannel heat sink system investigated the effect of the number of layers, the homogeniser materials, and the heat transfer fluid flow rate and inlet temperature on the electrical and thermal performance of the system. The results show that the maximum power of the high concentrated photovoltaic module with glass homogeniser is 3.46W compared to 2.49W when using the crystal resin homogeniser for the 2-layers multi-layered microchannel heat sink and 30ml/min under 1000W/m² irradiance intensity. Increasing the number of layers from 1-layer to 3-layers on the high concentrated photovoltaic and multi-layered microchannel heat sink system increased the maximum electrical power by 10% and decreased the solar cell temperature 3.15°C for the heat transfer fluid flow rate of 30ml/min. This gives an increase in the maximum electrical power of 98.4mW/°C.

The outdoor characterisation of the high concentrated photovoltaic and multi-layered microchannel heat sink system performance was evaluated at the University of Exeter, Penryn Campus, UK. The achieved maximum output electrical power of the system was 4.59W, filling factor of 75.1%, short circuit current of 1.96A and extracted heat of 12.84W which represents of 74.9% of the maximum solar irradiance of 881W/m². In addition, the maximum solar cell temperature reached to 60.25°C.

Secondly, the experimental studies were carried out in order to investigate the performance of the phase change material storage system using paraffin wax as the PCM materials. The thermal storage system performance was evaluated in various conditions. The results show that inclination of the phase change material storage influences the melting behaviour of the phase change material where the phase change material storage of 45º inclination position melts faster than the phase change material storages in the 0º and 90º inclination positions. The phase change material melting time is reduced in the PCM storage of 45º inclination position by 13% compared to the 0º inclination position.

The last part of the thesis discusses the integration of the phase change material storage with the high concentrated photovoltaic and multi-layered microchannel

heat sink system. A 3D numerical model was developed to predict the behaviour of the integrated high concentrated photovoltaic and multi-layered microchannel heat sink system with the phase change material storage system using variable source conditions. The results show a higher heat absorption rate on phase change material storage that uses a lower melting temperature phase change material compared to the higher phase change material melting temperature. The multi-stages storage with different phase change materials melting temperature showed a lower heat absorption compared to the phase change material arrangement with the lower melting temperature. Also, the rate of the absorbed heat fluctuation is less affected by the phase change material arrangement with higher melting temperature.

Acknowledgments

Firstly, I would like to express my sincere gratitude to my supervisors Dr. Senthilarasu Sundaram and Prof. Tapas Mallick for the continuous support of my Ph.D study, for their patience, motivation, and immense knowledge. Their guidance helped me throughout my research and writing. My sincere thanks go to James Yule, Dr. Katie Shanks and Dr. Sourav Khanna for their discussions and ideas supports my research and for giving me their precious time helped to complete the experimental side.

I would like to thank my fellow at the solar group for the stimulating discussions and suggestions, and my friends for the times in and out of university. My PhD experience would not have been the same without any of them.

I am very grateful to Ministry of Higher Education at the Sultanate of Oman, for providing the scholarship funding my PhD at the University of Exeter. I am very obliged to Petroleum Development Company (PDO) LLC for their generous offer of giving a paid leave.

Lastly, but not the least, I would like to thank my family; my parents, my wife and my children for their joining and completing this journey in a country away from the whole family.

List of Contents

List of Tables

List of figures

Nomenclature

Symbol	Definition	Unit
A_{cell}	Cell's active area	cm²
A_{fins}	Area of the finned surface	cm²
C_p	Specific heat capacity	J/K
D	Diameter	mm
F	Friction factor	
f_{app}	Apparent friction factor	
g	Gravitational acceleration	m/s²
Gr	Grashof number	
Hc	Channel height	µm
h	Heat transfer coefficient	W/m²K
I	Current	A
I_{sc}	Short circuit current	A
J	Current density	A/m²
k_B	Boltzmann constant	
K	Thermal conductivity	W/mK
L	Latent heat of fusion	J/kg
Nu	Nusselt number	
P	Power	W
Pr	Prandtl number	
Q	Heat power rate	W
q_{conv}	Convection heat transfer rate	W
q_{rad}	Radiaition heat transfer rate	W
q_{eff}	Fluid effective heat	W
R	Thermal resistance	K/W
Re^*	Laminar equivalent diameter	
R_{cont}	Constriction resistance	K/W
R_{cond}	Conduction rsistance	K/W
R_{spread}	Spread resistance	K/W
R_{bulk}	Bulk resistance	K/W
$T_{ch,out}$	Microchannel outlet temperature	K/W
$T_{f,out}$	Outlet HTF temperature	°C

tb1	Thickness	
Tamb	Ambient temperature	°C
Tsurf	Surface temperature	°C
T_m	Melting temperature	°C
V	Voltage	V
V_{avg}	Average velocity	m/s
Wc	Channel width	µm
Wf	Fins width	µm

Greek symbols

η	Efficiency	%
β	Temperature coefficient	
λ	Wavelength	
σ	Stefan-Boltzmann constant	
Ω	Ohm	
β	Thermal expansion coefficient	
ΔP	pressure drop	Pa
ΔT	Temperature difference	°C
ρ	Density	Kg/m3
µ	Viscosity	

Subscripts

opt	Optical
in	Input
Out	Output
min	Minimum
max	Maximum
c	Cell

Abbreviations

AHCM	Apparent Heat Capacity Method
CFD	Computation Fluid Dynamics
CPV	Concentrated Photovoltaic
CR	Concentration Ratio
CPVT	Concentrated Photovoltaic Thermal
EBM	Enthalpy-Based Method
ERH	Electrical Resistance Heater
EQE	External Quantum Efficiency
FF	Fill Factor
Ge	Germanium
HCPV	High Concentration Photovoltaic
HTF	Heat Transfer Fluid
IRENA	International Renewable Energy Agency
LCPV	Low Concentration Photovoltaic
LHTES	Latent Heat Thermal Energy Storage
MCPV	Medium Concentration Photovoltaic
MLM	Multi-Layered Microchannel
PCM	Phase Change Material
PV	Photovoltaic
SBM	Source-Based Method
SSADT	Stress Accelerated Degradation Test
STC	Standard Test Conditions
TBM	Temperature-Based Method
TES	Thermal Energy Storage

List of Publications

International Journals

1. Al Siyabi, S. Khanna, T. Mallick, S. Sundaram, Multiple Phase Change Material (PCM) Configuration for PCM-Based Heat Sinks—An Experimental Study, Energies. 11 (2018) 1629. doi:10.3390/en11071629.
2. I. Al Siyabi, S. Khanna, S. Sundaram, Experimental and Numerical Thermal Analysis of Multi-Layered Microchannel Heat Sink for Concentrating Photovoltaic Application, (2019). doi:10.3390/en12010122.
3. I. Al Siyabi, S. Khanna, T. Mallick, S. Sundaram, An Experimental and Numerical Study on the Effect of Inclination angle of Phase Change Materials Thermal Energy Storage System, Energy storage, Elsevier, Resubmitted.
4. I. Al Siyabi, Katie Shanks, Sourav Khanna, Tapas K. Mallick, and Senthilarasu Sundaram. "Evaluation of Concentrating Photovoltaic Performance under Different Homogeniser Materials." Materials Letters (2019). doi.org/10.1016.
5. I. Al Siyabi, K. Shanks, S. Khanna, T. Mallick, S. Sundaram; Indoor and outdoor performance analysis of high concentration photovoltaic with multi-layered heat sink, Applied energy, Elsevier, Under preparation.

Peer-reviewed Conference Publications

1. Al Siyabi, S. Khanna, T. Mallick, S. Sundaram, Electricity enhancement and thermal energy production from concentrated photovoltaic integrated with a 3-layered stacked micro-channel heat sink, AIP Conference Proceedings 2012 (1) (2018) 080001. doi:10.1063/1.5053529.
2. Al Siyabi, K. Shanks, T. Mallick, S. Sundaram, Thermal analysis of a multi-layer microchannel heat sink for cooling concentrator photovoltaic (CPV) cells, AIP Conference Proceedings 1881 (1) (2017) 070001. doi:10.1063/1.5001434.

3. Al Siyabi, S. Sharma, T.K. Mallick, S. Sundaram, Thermal regulation of building-integrated concentrating photovoltaic system using phase change material, AIP Conference Proceedings 1766 (1) (2016) 090001. doi:10.1063/1.4962107.

Chapter 1 : Introduction

Solar energy is one of the most abundant renewable energy sources on the planet. The amount of solar energy received by the earth in six hours is greater than the world's total annual energy consumption. However, the high cost and low efficiency of the energy conversion systems are the most important issues in terms of harnessing energy from the sun. Concentrating solar photovoltaic is one of the promising solutions to reduce the cost of the electrical generation by replacing the expensive solar cells with inexpensive concentrator materials. For certain applications, such as electrical- thermal integration, high concentrating photovoltaic systems can be an efficient way to generate higher electrical power while concentrating high solar irradiance, using the generated heat for domestic heating. This chapter provides an introduction to the thesis topic, the motivation for carrying out the research, its objectives, methodology and finally its contribution in this field.

1.1 Introduction

The energy demand in the world is raising continuously because of global population increase, fast urbanisation and industrialisation. The fossil fuels are the major energy source about 92% of the total world energy until now [1]. The higher proposition of the energy consumption is for the domestic heating especially in Europe where the winter temperature might fall below 0°C. In 2012, 45% of the total energy produced in the UK was used for heating purposes. The source of generating this amount of heat is mainly by using fossil fuels (80%) [2].

Due to all the above facts, using renewable energy sources such as wind and solar have become more essential. Solar energy is considered as an important renewable energy source globally. It is considered one of the promising solutions of the future energy as the earth is exposed to a huge amount of solar radiation every moment. The solar energy can be collected by photovoltaic for electricity generation or by solar collectors to collect the thermal energy. The direct radiation availability and its intensity variation during the day and seasons causes a real challenge to the solar technology where this cause a mismatch between the supply and demand.

Thermal energy storage (TES) is another topic important topic in the solar energy technology. For example, thermal energy storage technology can be used to store the thermal energy that is collected by solar collector in order to be used later. The other application of TES is to be used to store the heat generated by the photovoltaic especially the medium and high concentrated photovoltaic (CPV) and hence to increase the overall system efficiency. Researches show that integrating the two technologies: CPV and TES will lead to a good overall system efficiency when compared to the stand alone CPV system.

1.2 Motivation

1.2.1 Concentrating photovoltaic (CPV)

Photovoltaic energy contributed to around 10% of the total world renewable energy in 2017 according to the International Renewable Energy Agency (IRENA) [3]. The Solar PV technology is considered one of the fastest growing renewable energy sources [4]. Between 2016 and 2017, the total energy generated by PV technology has increased by 32%. This amount of increase reflects the maturity and the reliability of the PV technology.

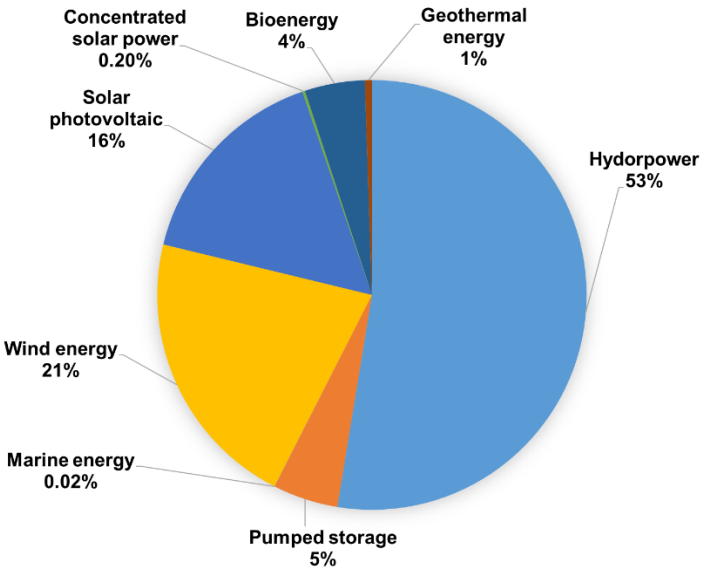

Figure 1. World 2017 Renewable energy sources contribution.

The continuity of the growth of the PV market depends on the achievement of higher performance, reliability and low cost. Like all other renewable energy sources, all PV manufacturers have to continue conducting the research and on reducing the manufacturing expenses in order to bring the cost per watt of their

systems to a competitive level for market acceptance. Each price reduction in PV system cost opens up large market segments with a great potential [5].

The main approach to reduce the total system cost is to reduce the material and/or manufacturing expenditure for the PV system elements. In any photovoltaic system, the solar cell is the most expensive element. Generally, it costs 50% or more in typical systems. Therefore, the solar cell is the key factor to reduce the cost of any photovoltaic system [5]. Hence, a lot of researches focus on the solar cell efficiency improvement as it is considered as a main area in this technology.

PV technologies have proven their maturity for large-scale applications, but their efficiency is relatively low [6]. Scientist has found that photovoltaic cell temperature effects the cells efficiency [7]. A reduction of the solar cell efficiency of about 0.13% per Kelvin has been reported in GaInP/GaAs/Ge cells at 500x concentration [8,9]. Therefore, the thermal energy management of solar cells play an important role on their efficiency and the design of an efficient heat dissipation system becomes an important subject and a necessary requirement to achieve the high performance.

1.2.2 Thermal Energy Storage

Thermal energy storage (TES) technology is used to store the thermal energy for days, weeks or even for seasons. TES system becomes a necessary component in the renewable energy due to its importance to increase the overall system efficiency. In solar thermal system, TES system is needed to overcome the mismatch between the supply and the demand especially at night and at cloudy times. In addition, thermal energy storage is a solution to recover the waste heat form different systems where the waste heat availability can be utilized at different periods or in other applications that use the thermal energy [10].

Thermal energy can be stored using two basic forms such as sensible heat and latent heat storage. In the sensible heat storage, the heat causes the temperature of the storage material to raise proportionally whereas the latent heat storage technique uses the phase change to absorb heat instead to temperature increase.

Latent Heat Thermal Energy Storage (LHTES) technology has attracted considerable attention worldwide since it provides a high-energy storage density and has the capacity to store the heat at the phase transition temperature [11]. For example in the case of water, it requires 80 times as much energy to melt 1 kg of ice as to raise the temperature of 1 kg of water by 1^{o}C which means that a much smaller weight and volume of material is needed to store a huge amount of energy [12]. Phase Change Materials (PCM) melts and solidifies at a narrow melting temperature range. In addition, a small amount of material is required for a latent heat storage system, thereby the heat losses from the system maintains in a reasonable level during the charging and discharging of heat [13]. Phase change materials have been recently used to regulate the thermal in the photovoltaic system and remove the excessive heat away of the PV system in order to increase its performance.

1.3 Research objectives

The overall aim of this research is to propose an efficient integrated CPV-TES system. As shown in Figure 2, the efficiency of the CPV-TES integrated system is to be improved by increasing the generated electrical power by the CPV system, storing the extracted heat from CPV system using an efficient thermal storage system. Therefore, two techniques have been proposed to analyse their influence on the CPV; the multi-layered microchannel (MLM) heat sink and the PCM storage technique.

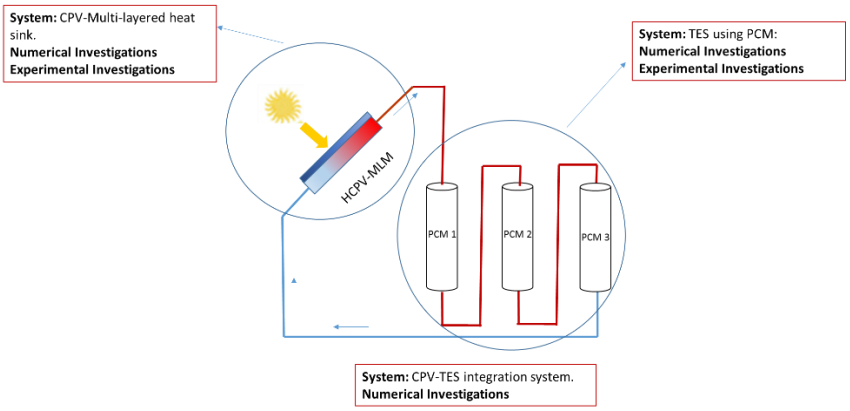

Figure 2. Schematic of the proposed CPV-TES system.

To achieve the main aim, numerical and experimental investigations are to be conducted to analyse the fluid flow and heat transfer of the proposed the system

concepts under different configurations and operating conditions. In order to achieve this aim, the following main objectives are defined:

1. To carry out a comprehensive literature review related to the CPV receivers, CPV thermal challenges and their opportunities and the different thermal regulation techniques. The literature review also includes the thermal storage systems design and configurations and the methods of heat transfer enhancement techniques.
2. To apply the multi-layered microchannel (MLM) heat sink technique in the HCPV applications by developing CFD models of the HCPV-MLM system to study the effect of different parameters.
3. To experimentally investigate the performance of the MLM heat sink with the HCPV in different analysis approaches. Also, the experiments aim to test the HCPV-MLM module in the real outdoor conditions of the UK.
4. To develop a CFD model of PCM storage and validate it using the obtained information and investigate wider range of geometries and configurations of thermal storage systems with PCMs.
5. To experimentally investigate the performance of thermal storage system using the phase change material (PCM) at different working conditions and inclination positions. Also, the experiments aim to investigate on the multi-storage technique as thermal conductivity enhancement technique of the PCM.
6. To numerically study the integration of the HCPV-MLM with the multi-stages PCM storage using the obtained outdoor experiments results.

This research will focus on the following areas:

System configuration development and optimization: Any newly designed system, to have any chance of succeeding, must be both economical and efficient. This includes its configuration and geometry optimization.

Mathematical modelling: A comprehensive model study using the momentum equations, energy balance equations for the HCPV-MLM to understand the internal behaviour of the system. COMSOL multi-physics package is to be used

for the numerical modelling. Both systems; the HCPV-MLM and the PCM system is to be modelled and studied the effects of the working parameters.

Heat transfer enhancement: A quick heat transfer process for removing heat from the CPV is vital for the entire system performance. Also, the heat must be transferred at a high transfer rate to/from the PCM. One of the main barriers is the need of improvement of the low thermal conductivity of the PCM to achieve a quick thermal absorption and dissipation response and provide a longer thermal control period for integrated system.

Materials selection: A key area affecting the system performance is the selection of the heat sink materials. In addition, the selection of the PCM temperature range and their suitability for the application to ensure the effective storing and releasing the heat to other media, such as for water or air heating.

Experimental measurements, performance evaluation and demonstration: The HCPV-MLM and PCM storage system prototypes with the optimized system configurations is to be tested experimentally. Experimental tests would be conducted to study the electrical and thermal behaviour. Additionally, the performance of the system to be examined in relation to outdoor climatic conditions.

1.4 Research methodology

Although experiments are necessary at some point in the design process to test and verify the performance of the system, the computational modelling is an efficient and cost-effective way to perform much of the preliminary design work. For this research the computational models and experimental works are two basic components to achieve the objectives. The thesis discusses two systems such as the HCPV-MLM and the PCM storage. Therefore, the study has been divided into three parts such as the HCPV-MLM, the PCM storage and the integration of both systems.

The investigation of the HCPV-MLM system is conducted using both the numerical and experimental approaches as per the chart shown in Figure 3. At the beginning, the MLM heat sink concept has been chosen due to its attractive criteria of its ability to reduce the heat source temperature with less pressure drop compared to the conventional microchannel heat sink. The investigation is to be

started by conducting a numerical study on the HCPV-MLM to examine the heat sink performance under the heat load generated by the HCPV system. This will include a geometrical study of the channel size. After that, an experimental setup of the MLM heat sink is to be constructed and to be tested under a non-uniform heat source of a maximum power rate of 30W/cm². Then the MLM heat sink is to be attached to the constructed HCPV. The full system is then tested experimentally inside the lab under the solar simulator. The importance of this test is to compare the effect of different parameters such as the homogeniser material type, number of layers and HTF flow rate under a constant solar irradiance. Finally, the HCPV-MLM module to be tested in the outdoor conditions at the university location in the UK for several days to investigate its real performance. In the outdoor experiments, only a specific number of layer heat sink and HTF flow rates are selected.

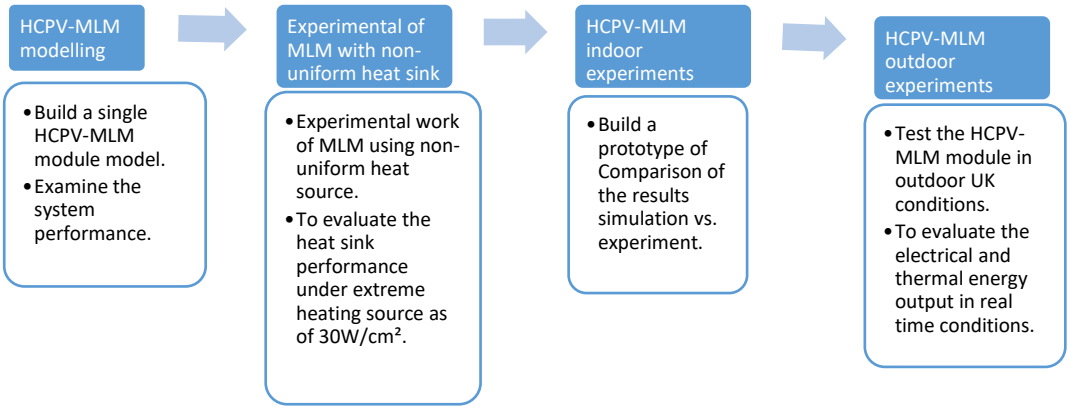

Figure 3. Flowchart of the HCPV-MLM investigations.

The second part of the study is the PCM storage system investigations and conducted as per the chart shown in Figure 4. At the beginning, a cylindrical PCM storage system is modelled using COMSOL. The model is then validated using an experimental result published in the literature. The validated model is then to be used to conduct a geometrical parametric study. Based on the study outcomes, the PCM storage to be constructed for the experimental investigation. The setup is to investigate the different operation working conditions such as the HTF flow rate and inlet temperature and under different inclination positions. Then, a three PCM storage containers are connected in a series arrangement to investigate the multi-stages PCM storage technique. Various parameters are to

be studied in this arrangement such as PCM material arrangements and the working conditions.

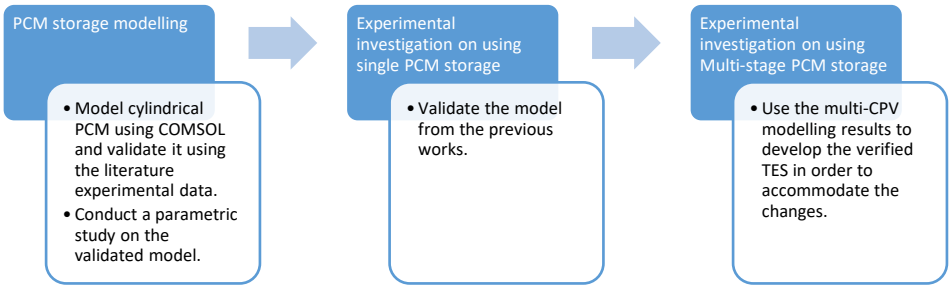

Figure 4. Flowchart of the PCM storage investigations.

The last part of the research is to study the performance of the integration of both systems as per the chart shown in Figure 5. The importance of this part is that the expected thermal energy generated by the HCPV-MLM varies throughout the day and throughout the year. Due to the experimental outdoor testing complication in terms of the requirements of special instruments, it is decided that the integration is to be done using the numerical approach. Therefore, the HTF outlet temperature from the HCPV-MLM system is to be considered to charge the multi-stage PCM storage. Different PCM arrangements are to be considered.

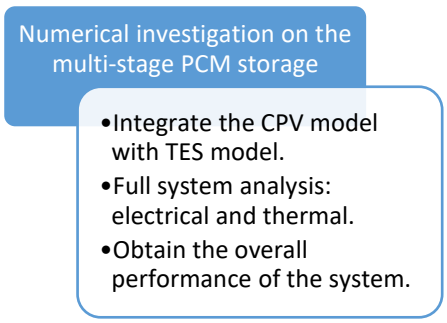

Figure 5. Flowchart of the integrated HCPV-MLM with PCM investigations.

1.4.1 Numerical investigations

CFD modelling has been used to simulate numerically the heat and mass transfer processes taking place as per the methodology explained in the previous section. The study has involved modelling the HCPV-MLM using the three-dimensional CFD models and the PCM storage is to be modelled using the 2D axisymmetric approximation for saving the time and effort. The modelling and simulation have been conducted using COMOL multi-physics and validated using the experimental data.

1.4.2 Experimental investigations

As stated above, different experimental work has been conducted throughout the research parts. Therefore, two main experimental setups are to be used; the HCPV-MLM and the PCM storage system. The HCPV-MLM setup is to test the MLM heat sink under non-uniform heat source, to investigate of the MLM heat sink in the HCPV applications in the indoor and the outdoor conditions. The PCM experimental setup is to investigate the heat transfer in different working conditions and the investigations will include the multi-stage PCM storage technique as a thermal conductivity enhancement technique.

1.5 Contribution to the field

In this work, several techniques and parameters have been investigated which are greatly contribute to the HCPV and the PCM storage fields and their applications in the real world. As stated above, the main aim of this work is to rise the overall efficiency of the HCPV system. This can be achieved by rising the solar cell efficiency, reducing its working temperature and utilizing the discharged thermal energy in useful applications.

Despite its various advantages over the conventional techniques, it has been found that the MLM heat sink has not been yet investigated in the application of the thermal regulation of the HCPV. Therefore, this work is considered as the first work conducted on applying the MLM heat sink in the HCPV using the numerical and experimental approaches. The numerical study offers a strong platform to the researchers in the future into the two systems of HCPV and the MLM heat sink in which several conclusions can be obtained especially in terms of high or ultra-high ratios. The indoor and outdoor experimental work of the HCPV-MLM provides further evidence for the ability of the MLM heat sink technique to extract the heat generated by the solar cell under the studied high concentration ratio. Also, this work can be considered as a contribution to the research of applying the HCPV-MLM system specifically in the south-west region in the UK.

The second part of the research is the PCM thermal storage system. Several investigations in this study can be considered as contributions in the field of the PCM storage. The investigation of the effect of the inclination of the cylindrical PCM storage can be a strong contribution to the field due to the low number of conducted studies. The investigation of this study is to be conducted using both

the experimental and numerical approaches. Multi-storage PCM storage technique has been found as another field for investigation due to the lack of the number of studies. Therefore, this multi-stage PCM storage investigations are to be conducted experimentally and numerically using different PCM arrangements and working conditions. The integration of the HCVP-MLM with the multi-storage PCM storage is a further contribution that the researchers could be referred to due to the speciality of the heat profile obtained from the HCPV-MLM system to the multi-storage PCM system.

1.6 Thesis structure

Chapter 1, Introduction: This chapter highlights the scope of the research, aims and research objectives and methodology. It also highlights the contribution to the field and the thesis structure.

Chapter 2, Background and literature review: This chapter presents the results of the comprehensive review of the most significant studies which are relevant to the current research topics; CPV receiver, CPV cooling techniques and PCM thermal storage. The review focuses on the techniques applied to regulate the solar cell temperature such as fins, heat pipe, PCMs, microchannel and jet impingement. A more detailed comprehensive review is given for the MLM technique as it a key topic of the main topics in this research. The review also focuses on the PCM thermal storage techniques which include the thermal storage arrangements, heat transfer in PCMs, classification of the PCM and the thermal conductivity enhancement techniques. The last part of the chapter describes the published results and discussions on the CPV-TES integration to increase the overall system efficiency.

Chapter 3, Materials and methods: In this chapter the components and instruments used in the experimental part are presented describing their specifications and working limits. The software packages used in the modelling work are also presented. In the other section of the chapter, the analysis of various ranges of PCMs is presented in order to use these data for the numerical analysis in the later chapters. In the last section, error and uncertainty is analysed for the necessary sections of the research.

Chapter 4, Thermal management of HCPV receivers using a multi-layered microchannel heat sink: design, fabrication and experimental

characterization: In this chapter the extensive study of applying the MLM heat sink in the HCPV is presented. This includes the heat transfer correlations and the numerical analysis. Following this, the experimental work is presented which includes the microchannel fabrication, MLM test section, HCPV module and the experimental setup for both the indoor and outdoor tests. The last section of the chapter presents the results obtained from the experiments and their discussions.

Chapter 5, PCM thermal storage: design, fabrication and experimental characterization: This chapter presents both the numerical and experimental investigations of the PCM storage. A parametric study is conducted numerically using the validated model to be used for the design stage for the experimental setup. After that, the description of the experimental setup arrangement for the single and multi-stages experiments is presented. Then, the results are presented for the single PCM storage experiment for the effect of the HTF flow rate, inlet temperature and its orientation. Finally, the results for the multi-storage technique are presented.

Chapter 6, HCPV-MLM and PCM storage integration: This chapter discusses the integration study of the HCPV-MLM and the PCM storage using the numerical approach. The thermal energy generated from the outdoor experiments by the HCPV-MLM is considered during the simulation of the multi-stage PCM storage. Different types of PCM arrangement are considered. The model is used to analyse the heat transfer in the storage under a dynamic charging process.

Chapter 7, Conclusion and future recommendations: This chapter highlights the major findings and presents the main conclusion from the conducted study for each system of HCPV-MLM, PCM thermal storage and the integration between the systems. Finally, the chapter presents the author’s views and recommendations for future investigations.

Chapter 2 : Background and literature review

This chapter presents a literature review of CPV thermal regulation techniques as well as the thermal energy storage (TES) using phase change materials (PCMs). At the beginning, the chapter discusses the importance of the thermal regulation of CPV on the performance of the solar cell and then the outcomes of previous studies on different cooling techniques; passive and active. Finally, it discusses the previous studies on the PCM storage and the techniques to enhance its thermal conductivity.

2.1 CPV receivers

Photovoltaic technology is divided in two categories based on the solar concentration: non-concentrated and concentrated. The non-concentrated PV is the conventional type PV which is used widely. The concentrating photovoltaic (CPV) technology uses lenses or mirrors to concentrate the solar irradiance on to the solar cells. Zahedi [14] has listed the advantages and disadvantages of concentrating PV. The advantages of the CPV system is increasing the light received on the solar cell surface [15] and very suitable for sunny regions [16]. It replaces the expensive cell materials with low-cost materials such as glass, mirror and plastic. In addition, the CPV offers a compact size, requires less space and reduces the land utilization compared to the conventional flat PV [17,18].

The concentration is achieved using two different of optic techniques: reflection and transmission [19]. The schematic of both techniques is shown in figure 6. The reflection optic consists of primary and secondary mirror to reflect the solar rays into the optical rod and then to the solar cell. The transmittance optic uses Fresnel lens to concentrate the sun rays to the optical rod and then to the solar cell.

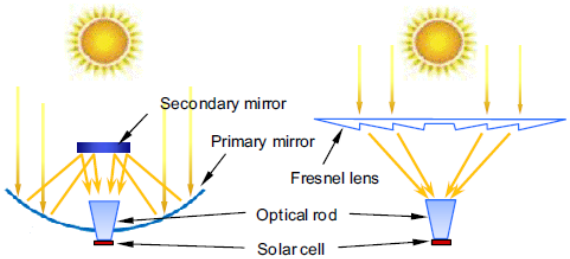

Figure 6. Typical structure of CPV optic types, adopted from [19].

The CPV system is classified according to the amount of solar concentration ratio (CR) and one concentration ratio is represented by 1x [20]. For, low concentration photovoltaic (LCPV), concentration ratio is less than 3x and uses low cost, less efficient silicon solar cell and not require active tracking mechanisms and simple thermal regulation solution. For medium concentration photovoltaic (MCPV), concentration ratio is between 3x and 100x and often require an attention for heat sinks and solar tracking systems. For high concentration photovoltaic (HCPV), concentration ratio is more than 100×. Proper optical and thermal management systems are basic requirements to maximize the HCPV system efficiency [16]. Also, the HCPV requires an accurate sun tracking system which is considered as a disadvantage of the CPV according to some studies. An efficient thermal solution is very important due to the high rate of the generated heat [14].

Because of HCPV systems mirrors and lenses are used to concentrate the direct sunlight hundreds of times, using high efficiency PV cells is very essential. Nowadays, a CPV module is composed of two different kinds of solar cells: high efficiency silicon and multi-junction photovoltaic cells [6]. At present, the maximum concentrator cell and module efficiencies at 25°C for 3 and 4 multi-junction are 44.4% and 46% respectively [9]. The effect of the concentration ratio to the cell efficiency for two types of solar cells is presented by Pérez-Higueras et al. [6] as shown in Figure 7. A significant increase of the MJ solar cell efficiency is noticed as the concentration ratio increases from 1x to 100x by 10%. On the other hand, a slight increase in the silicon solar cell efficiency is noticed when the concentration ratio increases from 1x to 100x.

The solar cell under concentration suffers from a series of losses based on concentrator geometry errors, optical materials losses, reflection losses and tracking losses [21]. These losses cause non-uniform illumination across the solar cell and increase the generated heat. Researches show that the solar cell temperature could reach 1400°C under 500x concentration ratio when it is installed properly [2]. The increase of solar cell temperature more than the manufacturer specified temperature will result in a decrease of its efficiency. The studies show that the temperature effect on the solar cell efficiency depends on its type for instance the output power declines of an order of -0.65%/ºC, -0.4%/ºC and -0.248%/ºC for crystalline PV cells, thin-film cell and triple-junction solar cells

respectively [22]. In addition, it can cause long-term degradation if it exceeds the temperature maximum limit [3]. The non-uniform solar cell temperature can decrease its electrical efficiency [4]. Therefore, solar cell temperature regulation should be considered in any CPV system design by removing the generated heat efficiently [5]. It has been found that CPV single solar cells can be cooled using passive techniques of less than 1.7K/W heat sink thermal resistance but in extreme outdoor conditions lower thermal resistance is needed (1.4 K/W) [6].

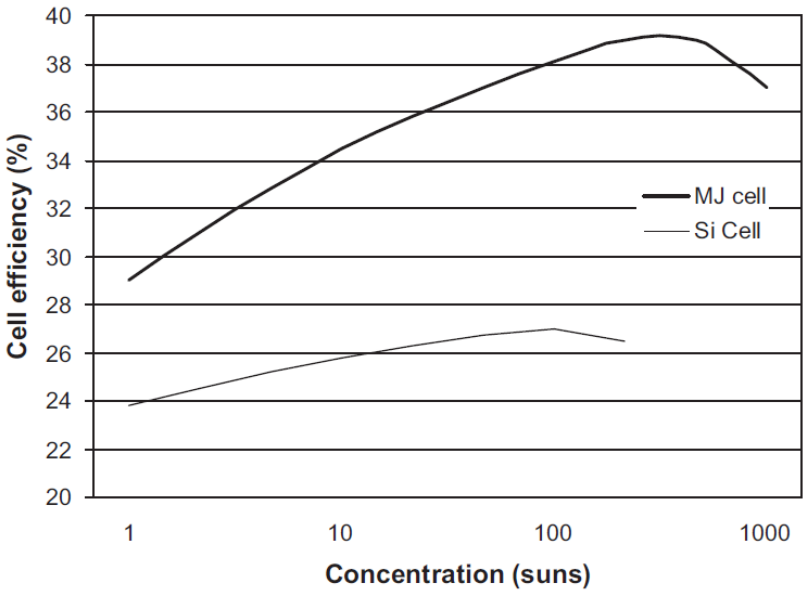

Figure 7. Cell efficinecy versus concentration ratios, adopted from [6].

2.2 CPV thermal challenges

As stated earlier, CPV thermal regulation is one of the prevailing challenges on the CPV because of its direct effect on reducing the solar cell efficiency. The efficiency of the solar cell decreases as its temperature increases due to its effect on the open circuit voltage and the short circuit current. The current-voltage parameter temperature coefficients (dJ_{sc}/dT) is considered as valuable parameter in establishing the solar cell performance versus temperature [23]. Radziemska and Klugmann [24] have investigated the effect of the thermal parameters on the current-voltage characteristics in silicon solar cell. Due to the illumination, the solar cell temperature increased from 22°C to 70°C. The study showed a small increase of the short circuit current and a significant reduction of the open circuit voltage and electric power from the photovoltaic cells due to the temperature increase. Whereas their experimental investigations on several silicon cells, showed that the product of the short circuit current and the open circuit voltage degrades by 0.8%/K and the output power by 0.65%/K. The same authors [25]

have investigated the effect of temperature on the power drop in crystalline silicon solar cells where the fill factor was decreased by a rate of -0.2%/K. Feteha and Eldallal [26] has reported that the I-V characteristics and spectral response of the multi-junction solar cell under different temperature values and light intensities. They found that the open-circuit voltage decreases with the temperature increase at rate of 5.5mV/°C. Pérez-Higueras et al. [6] have reported the dependency equation of the solar cell efficiency on the cell temperature (T_c) as:

$$\eta_{\text{cell}} = \eta_{\text{ref}} - \beta(T_c - T_{ref}) \qquad 2.1$$

Where η_{ref} is the cell efficiency at the reference temperature (T_{ref}) and β is the temperature coefficient of the efficiency.

Luque et al.[27] have highlighted the effect of non-uniform illumination in a CPV cell on the electrical performance by measuring the thermal resistance of the electric insulator by supplying a current to the module and measuring the temperature drop between both faces of the module. However, the study reduced the consequences of the illumination inhomogeneity as the strong internal drop switch off the poor parts of the solar cell and leaving the outstanding part of the solar cell. The efficiency reduction was much less of have been expected. There are reports highlighting the effect of illumination intensity and non-uniform illumination of the solar cells [28–36].

The outdoor conditions such as the temperature and wind speed have an impact on the thermal behaviour of the solar cell and thus on its performance. Almonacid et al. [37] have investigated about the relation between the cell temperature of a HCPV module and atmospheric parameters by developing a model for estimating the cell temperature from one year measurements. This model can be used to estimate the cell temperature of a HCPV module with a root mean square error of 7.4%. However, Fernández et al. [38] have compared the different methods on calculation of the cell temperature based on artificial neural networks (ANN) and found that methods based on direct measurements of an HCPV module provide better results than methods based on atmospheric parameters.

2.3 CPV thermal opportunities

Despite its disadvantage on the solar cell efficiency, the heat generated by the solar cell could offer opportunity on increasing the overall system efficiency by

combining the electrical and thermal technologies. This technology is called the PV/T for the photovoltaic thermal system or the CPVT for the concentrated photovoltaic thermal system. The extracted heat could be in the form of hot air, hot water, two phase refrigerant or a heat to be used to generate electricity form the thermoelectric devices [39]. A lot of research works have been carried out to study the performance of various PV and thermal configurations

The concentrated photovoltaic thermal system (CPVT) is a combination of photovoltaic and the solar thermal technology. This technology has appeared since late 1970s and early 1980s [40–43]. Since then, the CPV/T systems have been designed, build and tested both theoretically and experimentally [44]. The studies showed a very good potential of the system in the market energy sector. The total system efficiency can reach 65% where the outlet fluid temperature can reach up to 196^{o}C [45].

This approach has yield to use the produced thermal energy produced into other applications like domestic cooling. Borgren and Karlsson [46] have investigated the CPV with active cooling by designing and evaluating of low concentrating water cooled photovoltaic system with fixed parabolic reflector. It was found that the annual electricity produced by this design is about two times higher than in conventional setup. Stefan Krauter [47] has proposed another way of active cooling by passing a thin film of water in the front of the PV module. The overall cell temperature decreased by 22^{o}C as shown in Figure 8. In addition, the electrical energy production increased by 10.3 %. Also, it is clearly shown from the figure that the efficiency of both systems is same when the temperature of the cell is less than 24^{o}C. In a recent study, Bahaidarah et al. [48] have investigated the performance of a PV module cooled using water cooling. The module temperature decreased by 20% leading to increase the PV efficiency by 9%.

In order to eliminate the circulating pump for the active cooling system and therefore increasing the overall system efficiency, Earle Wilson [49] has proposed a novel design by utilizing the gravity to feed cooling water flow at the back of the PV module. The temperature was reduced from 62^{o}C to 32^{o}C which increased the system efficiency.

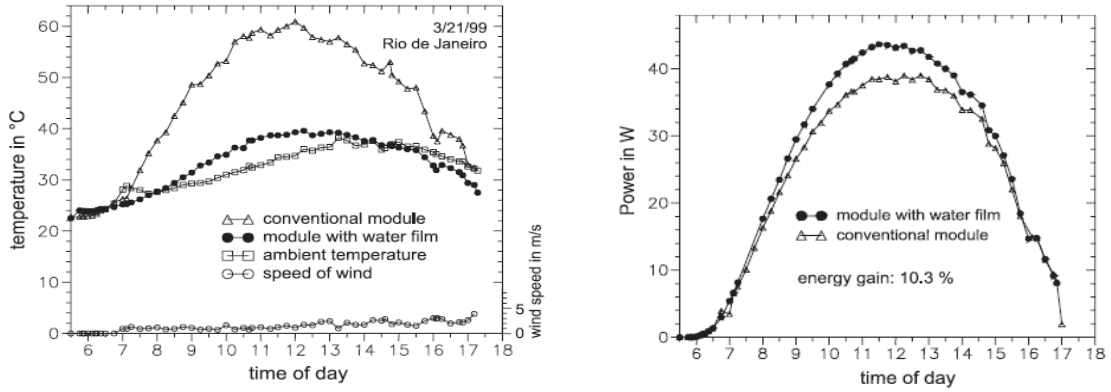

(a) (b)

Figure 8. Comparision between different PV modules (a) cell temperature and (b) power output, adopted from [47].

Zimmermann et al. [50] have investigated a hybrid system of CPV and thermal receiver. Water was circulated in heat sink attached to HCPV system. It was found that the overall system efficiency improved from 15% to 60% and the hot water led to 55% rise in the efficiency of the receiver. Li et al. [51] have studied the performance of solar cell arrays with water circulation thermal system using concentration ratios of 4.23x and 8.46x for crystalline silicon single cell or array, respectively. Zondag et al. [52] have numerically and experimentally investigated the combined photovoltaic-thermal system for a domestic hot water system. The results showed a reduction on the temperature and an increase of the thermal efficiency of the uncovered collector of 52%. Kandilli [44] has presented a novel CPV/T system using numerical and experimental approach by combining the CPV with vacuum tube. The results show an overall efficiency of 7.3% and the energy production cost was 6.37$/W.

Forced air circulation is one way of CPV thermal regulation. Fans are used to blow air in a specific channel in order to reduce the cell temperature. This type of approach has been studied by Tonui et al. [53]. The efficiency of PV has been improved from 16% for natural convection to 25% for forced convection. Janjai and Tung [54] have investigated the performance of solar collectors in the application of drying herb using the hot air. The average daily efficiency of the system was 35%. Amori and Al-Najjar [55] have analysed the PV/T system based on air solar collector. The proposed system was to use air to reduce the solar cells by circulating air through a duct at the back of the panel. They found that

the efficiency was higher in the winter than in the summer where the thermal efficiency reached to 22.8% and its electrical efficiency was 9%. This is due to the drop of the average cell temperature in winter compared to summer of 32°C and 80°C, respectively.

The CPV systems have used effectively in the air conditioning and refrigeration. Mittelman et al. [56] have investigated the CPV/T system so that the thermal energy can drive process such as absorption cooling cycle. The authors showed that the temperature extracted from the CPV system is enough to be used for several thermal applications (the outlet temperatures vary in the range between 65 and 120°C). Al-Alili et al. [57] have investigated a novel thermal application of the CPV system in the air conditioning. They found that the average cooling coefficient of performance for the solar absorption cycle of 0.68. Zhao et al. [58] have investigated theoretically the performance of PVT for heat pump operation under typical Nottingham (UK) climatic conditions. It was found that the system would achieve 55% of thermal efficiency and 19% of the electrical efficiency.

Thermoelectric is a device that generates electricity using heat effect. Many studies investigated about attaching the thermoelectric to a CPV system [59–63]. Ju et al. [62] have investigated numerically the CPV-thermoelectric hybrid system. They found that the hybrid system has a good electrical performance for a CPV system with solar concentration ratio ranged between 550x and 770x. Li et al. [62] have conducted a study for the integrated system of PV and thermoelectric found that 30% improvement could be achieved on this system. A feasibility study on PV-thermoelectric hybrid has been conducted by van Sark [62]. The study found that employing thermoelectric may lead to an efficiency enhancement of up to 23% for the integrated PV-TE modules.

The CPV system is usually thermally regulated using two approaches such as passive and active. The passive approach usually uses the natural convection phenomena and requires no mechanical equipment to circulate the air. It could be very simple such as using a simple flat plate or more complicated air-cooled micro-channel fins [1] and using the phase change materials [3]. The active cooling approach uses mechanical equipment such as fans and pumps to circulate the coolant fluid.

2.4 CPV passive cooling techniques

As stated earlier that the CPV passive cooling method does not require any mechanical or electrical means and it depends on the three basic heat transfer mechanisms: convection, conduction and irradiance. Passive cooling is very effective technique and able to efficiently handle the heat generated in the solar cell under concentrated irradiance. Royne et al. [64] stated that passive cooling is a feasible solution for the following cases: single cell geometries for concentration values of at least 1000x and linear concentrators less than 20x concentration ratio. Passive cooling uses a lot of techniques and methods in order to regulate the cell temperature to the desired range. These methods could be very simple such as using simple flat heat sinks to more complicated ones such as the fins, heat pipes or using the phase change materials. Here are some of passive cooling techniques for CPV found in the literature:

2.3.1 Heat spreading

Heat spreading is considered as the simplest method to dissipate heat from CPV systems. In order to illustrate the effect of a very simple heat sink at the backside of the solar cell, Araki et al. [65] have developed high concentration photovoltaic single solar cell module with its simple passive cooling structure. The module consisted of a base plate and cell assembly. Epoxy film has been used in order to reduce the contract thermal resistance and high electrical insulation. The outdoor experiment showed that using simple cooling arrangement rises the cell temperature only 18^{o}C over the ambient temperature.

Hong et al. [66] have performed a degradation analysis of concentrator solar receivers using triple junction solar cells under high concentration ratio . The cooling device for the experimental work was a simple aluminium plate and with a printed bonded ceramic substrate as shown in Figure 9 . The concentration ratio for the experiment was 476x using a Fresnel lens system. This analysis was conducted using step stress accelerated degradation test (SSADT) applied to the solar cell. The setting temperatures of heat treatments were 90°C, 110°C, 130°C and 150^{o}C. It was concluded that there will be a slight cell degradation after cell heat treatment temperature which decrease its efficiency and filing factor. This work showed clearly that high concentration receiver can sustain the high temperature using a simple heat sink.

Cooper et al. [67] have reported the design and performance of a novel high concentration photovoltaic (HCPV) collector of 600 concentration ratio. In order to utilize the high concentration ratio, high efficiency triple-junction cells have been used. The concentration has been performed using 2-axis tracker, parabolic trough concentrator as primary and a novel secondary concentrator. The receiver consisted of 53 multi-junction solar cells with active area 1 cm^2. In this system, thermal energy was passively transferred to the ambient and the system achieved 25% efficiency.

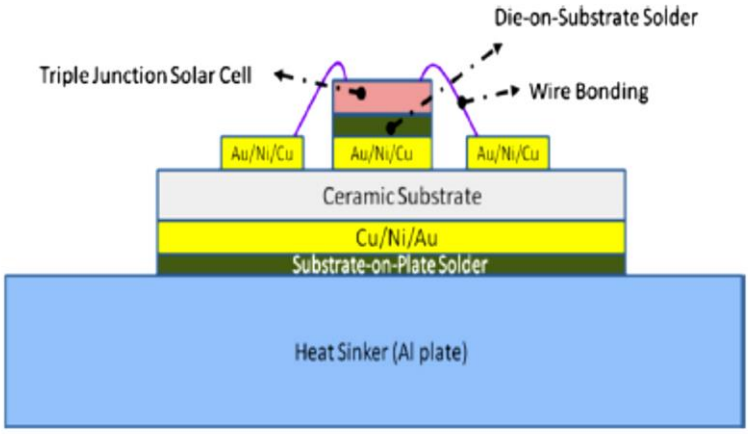

Figure 9. CPV receiver as suggested by Hong et al. [66].

Min et al. [68] have investigated experimentally the effect of metal plates as heat sinks for cooling the CPV system for a 400x base on energy conservation principles. The solar cells were triple-junction of 3x3 mm^2 and the area of the heat sink was 700 times larger than the solar cell area and the solar cell temperature was about 37°C. This study shows the importance of the heat spreading phenomena in reducing the solar cell temperature and the heat sink area needs to increase as the unction of the concentration ratio for a constant solar cell temperature.

2.3.2 Cooling fins

Cooling fins is another passive cooling technique for CPV thermal regulation. In this technique, fins are attached at the back of the module to enhance the natural convection effect. Natarajan et al. [69] have numerically investigated the solar cell temperature with and without the cooling fins for 10x. The investigated fins size is of 20mm width and 60mm height. The maximum solar cell temperature reached was 68.2°C without with fins and it reached to 55.1°C and 49.2°C for 2

and 6 fins, respectively. Despite its high efficiency, cooling through the fins introduces high weight to the system which can be an issue in the tracked system.

In order to study the temperature-dependent model for CPV, Sheng et al. [70] have used their model to assess the temperature dependency using the optical and multi-junction solar cell elements under high concentration. The module was of concentration ratio of 576x and consists of Fresnel lenses and parabolic dishes as primary optical element, secondary optical element. The CPV was attached to a finned heat sink. The solar cell temperature was able to be maintain in less than 380K.

Micheli et al. [20,71–78] have conducted an extensive studies on using the micro-finned heat sink in CPV application. The studies used both the numerical and experimental approach on studying the geometry, orientation and thermal performance of natural convective micro-finned heat sinks. In addition, the performance of pin micro-fins and plate micro-fins was compared.

2.3.3 Heat pipe

The concept of the heat pipe was founded by R.S.Gaugler in 1942. A schematic diagram of the heat pipe is shown in Figure 10. Heat pipe is a simple device transfer the heat from heat source to other medium like fins. It is considered as passive cooling technique for the CPV cooling. The heat pipes use heat transfer phenomena to transfer the heat and do not require any power input [79]. It removes the generated heat by the solar cells and reject it to the ambient using the natural convection phenomena. The working fluid inside the heat pipe near to the heat source absorbs the heat and evaporates to gas. The evaporated fluid moves naturally to the fins where it condenses to liquid and goes back to its initial position.

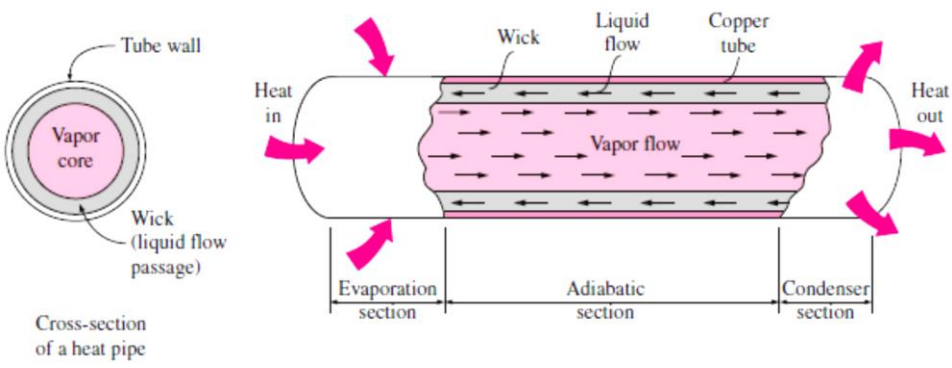

Figure 10. Typical heat pipe working principle, adopted from [79].

Heat pipes technique has been explored by Anderson et al. [80] on a high solar concentration for a single cell. The heat pipe was made from copper and water was used as the working fluid due to its high heat capacity. In order to increase the heat removal rate, aluminium fins were attached to the heat pipe. The prototype was tested under 400x in two orientations corresponding to the morning and afternoon irradiance difference. The results showed that the temperature difference between solar cell and the ambient was significantly reduced without and with the heat pipe by 210^{o}C to 40^{o}C, respectively. In addition, the orientation had a slight effect on the temperature difference.

Cheknane et al. [81] have used heat pipe technique to reduce the solar cell temperature and hence enhancing the performance of the solar cell where the silicon solar cell with a concentration ratio of 500x was used. The heat pipe was made from copper and two types of working fluids were used for comparison: water and acetone. The selections of working fluid depend on the working temperature. It was found that fill factor decreases as the optical concentration increases and for a slight change was noticed for both working fluids. Akbarzadeh and T. Wadowski [82] have investigated using heat pip cooling system for CPV. The system was designed for a 20x. This cooling system was able to reduce the cell's surface temperature to 46°C and increase the electrical efficiency of about 10%.

2.3.4 Phase change materials (PCM)

A phase change material (PCM) is a substance with a high latent heat. PCM melts and solidifies at a certain temperature range, is capable of storing and releasing large amounts of energy. PCM has many applications such as latent heat storage materials and thermal regulation of electronics, photovoltaic.

Thermal regulation of CPV using phase change material (PCM) is considered as a promising cooling technique due to the attractive features of PCM such as high storage density, ability to withstand a large number of cycles and isothermal nature at relatively constant melting temperature [83–86]. It was first proposed for avionics thermal control in 1977 [87] and since then a lots of studies have investigated the PCM based heat sink [88–96]. The main drawback of the PCM is its low conductivity. Due to the low conductivity, it needs various enhancement

techniques such as using extended surfaces of different configurations [97–100], employing multiple PCMs [101] and PCM encapsulation [102].

Many factors affect the performance of PCM based heat sink for CPV applications such as the container orientation [103–106], quantity of PCM [107,108], heating rate and PCM melting temperature. Kandasamy et al. [109,110] have reported numerical and experimental investigation of cooling of electronics using PCM. The studies conducted a comparison of heat sinks with and without PCM and examined the effect of heating power level of a horizontal uniform heat source ranging from 2 to 6W. It was showed that a PCM heat sink has a major effect in improving the cooling performance compared to a non-PCM heat sink. Also, it was found that a lower heating power level causes a longer PCM melting time and a lower system maximum temperature. Fok et al. [111] have concluded that using a PCM in a heat sink has two advantages compared to a non-PCM heat sink such as (i) the PCM heat sink maintains the solar cells at a lower temperature compared to a non-PCM heat sink and (ii) the rate of temperature rise of PCM's heat sink is lower compared to a non-PCM heat sink during the absorption of latent heat.

The selection of the PCM in terms of melting temperature is a key factor in designing an efficient PCM heat sink. Fan et al. [112] have investigated the importance of selection of the PCM melting temperature in a horizontal heat sink arrangement with a heating source ranged between 60W to 120W. The used PCMs were eircosane and hexadecanol. The study showed that longer thermal regulation period is achieved when using a higher melting temperature of PCM. However, the lower PCM melting temperature performs better in terms of reducing the maximum temperature in a short period. Mahmoud et al. [113] have studied the PCM based heat sink for a heating rate ranging from 3W to 5W for six types of paraffin wax for a horizontal heat sink. The results showed that the maximum operating temperature was reduced by 10^{o}C when the PCM melting temperature reduced from 42 ^{o}C to 29 ^{o}C. Huang et al. [114] have studied the effect of PCM melting temperature in thermal regulation of PV for a constant insolation of 750W/m^2. The results indicated that using PCM of melting temperature of 25^{o}C is better in reducing the temperature by 15^{o}C by the end of operating period (150min). Wang et al. [115] have conducted a parametric study of the PCM heat sink, examining the effect of temperature difference between the

heat source and the melting point of the PCMs on the heat sink performance. The results showed that the greater the temperature difference between the heat source and the PCM's melting temperature, the higher the melting speed.

Also, the amount of PCM used in the heat sink plays an important role in the heat sink size, weight and cost. This is because more PCM means larger, heavier and more expensive heat sink. Arshad et al. [116] have studied experimentally the effect of the PCM fraction in a horizontal PCM heat sink arrangement. The results showed that the fully filled heat sink with PCM performs better than heat sink filled with only by a melting fraction of 0.33 and 0.66. Saha et al. [117] have also examined experimentally and numerically the effect of PCM fraction for similar type of PCM heat sink with heating rate ranging between 4W and 8W. The study found that the heat sink performance was better when using a PCM fraction of 88% compared to full PCM heat sink.

Using two PCMs in the heat sink is considered as a thermal conductivity enhancement technique as highlighted earlier and very few works investigated this approach for electronics heat sink applications. Emam and Ahmed [118] have studied numerically the effect of using three PCMs series cavities heat sink in CPV applications of 20 concentration ratio system. The selected PCMs melting temperature range is between 22.5ºC to 29.8ºC. The results showed that medium-low-high PCM melting temperature arrangement is the best in terms of reducing the solar cell maximum temperature (average temperature of 106ºC) for an operating time of 120 minutes. In a similar study of using multiple PCMs heat sink in application of thermal regulation of solar cell, Huang [101] has explored numerically two types of arrangements of two PCMs of triangular cells and semi-circular cells under actual operating conditions. The PCM melting temperature is ranging between 27ºC to 60ºC. The author concluded that higher-lower PCM melting temperature order achieves the highest temperature drop during the daily operation [119].

2.5 CPV active cooling techniques

The active cooling approach usually uses a mechanical equipment such as pump or fan to remove the generated heat in the PV system. The heat removal using this approach is very efficient in reducing the solar cell temperature which can lead to improve the efficiency of the PV module. However, the operation and

maintenance costs of the system are sometimes much greater than the improved efficiency. The utilization of the removed heat for a domestic heating application might lead to a feasible advantages of the system [85]. Active cooling is more feasible to use in linear concentrator for a concentration ratio above 20x concentration, single cell for concentration more than 1000x concentration [64]. Here, some active cooling techniques are as listed below:

2.5.1 Microchannel

Microchannel heat sinks using fluid such as water are considered as the most common and promised in CPV cooling techniques [120]. An extensive study conducted by Philips [121] on the microchannel heat sinks applications. He demonstrated that microchannel heat sinks have a low thermal resistance as 0.072°C/(W/cm^2) which allows to dissipate heat loads of 1000W/cm^2. The proposed microchannel heat sinks can be fabricated using acid etching method.

Aldossary et al. [122] have examined the active cooling on 1cm^2 solar cell under high concentration ratio (500x) using a rectangular cooling channel with 10mm height. The solar cell maximum surface temperature was maintained at 60°C for 0.01 m/s water velocity with heat transfer coefficient of 1645 W/ (m^{2}K). Reddy et al. [123] have carried out a numerical analysis of a microchannel heat sink for a 1.5 kW$_e$ HCPV receiver. It was found that only 0.2% of the produced power by the CPV module is needed for pumping water. Tuckerman and Pease [124] have investigated a high-performance microchannel heat sink to dissipate heat of density of 790W/cm^2. The proposed heated area was approximately of 1cmx1cm and the channel width of 50μm. The maximum substrate temperature was found of 71°C above the input water temperature.

Wang and Ding [125] have proposed a novel microchannel heat sink for a uniform constant heat flux of 10.4W/cm^2. The proposed heat sink was using transverse channels and a larger heat transfer area was created to develop a high local heat transfer efficiency for the microchannel heat sink. The maximum heat source temperature was maintained under 85°C which is less than the allowable temperature for electronics. In another study, Knight et al. [126] have optimized the microchannel heat sinks for both laminar and turbulent flow using the governing equations for fluid dynamics and heat transfer. The new designed heat sink has an improvement ranged from 10 to 35%. Mittelman et al. [127] have

studied numerically and experimentally the effect of orientation of microchannel heat sinks on convection. The study concluded that higher heat transfer coefficient is found for larger fin spacing and fin height has less effect.

2.5.2 Jet impingement

Jet impingement heat sinks are considered relatively new technique and attract the attention due to its high heat transfer rates. Jet impinges of the fluid on a surface, it creates very thin hydrodynamics and thermal boundary layers resulting increase in pressure and hence an extreme high heat transfer coefficients [128]. Barrau et al. [129–131] have designed a hybrid jet impingement/microchannel cooling system for a densely packed CPV module. Low thermal resistance (up to $6.2x10^{-5}$ K/W) and a uniform temperature across the receiver were achieved.

2.5.3 Liquid immersion

Liquid immersion is another technique for CPV thermal regulation and many studies have been performed to investigate its performance on cooling the CPV [132–135]. This technique uses a dielectric liquid to remove the heat from the CPV system. Wang et al. [136] have investigated the performance of silicon solar cell immersed into liquid for the enhanced heat removing. The used liquids were ethanol, non-polar silicon oil and tap water and the performance was compared with air. They found that the open circuit voltage was improved by 1.0% when using tap water. However, the short circuit current was improved by 1.47% when using the silicon oil. Han et al. [137] have investigated experimentally and numerically the electrical and thermal performance of silicon solar cells immersed in dielectric liquids. The liquids used in this study were De-ionized water, isopropyl alcohol, ethyl acetate, and dimethyl silicon oil. The study confirmed that silicon oil performed the best optical effect by 7.3% whereas the best electrical effect was achieved when using isopropyl alcohol by 8.0%. De-ionized water achieved the lowest average temperature compared to other liquids. Liu et al. [138] have studied the heat dissipation using the liquid immersion technique under irradiance conditions of 50 and 70Kw/m² using silicon oil. In this study, the solar cell temperature was maintained to 30°C corresponding to heat transfer coefficient to 1000 W/ (m². °C).

Zhu et al. [139] have presented their experimental study on cooling HCPV system using water immersion of a concentration ratio of 250x. The experimental results

showed that the maximum temperature was 49°C and the temperature uniformity of less than 4°C within with the DNI above 900W/m². The overall heat transfer coefficient was about 6000 W/m².K.

2.5.4 Multi-layered microchannel (MLM) technique

A stacked micro channel heat sink technique is considered more efficient in terms of pumping power and heat removal capability among many other cooling techniques [140]. Vafai and Zhus [141] are the first who proposed the concept of multi-layered microchannel heat sink (MLM) in electronic cooling applications. They have studied numerically the performance of two layers for a counter flow and a uniform heat source and found interestingly that the pressure drop and temperature rise on the base surface have been reduced compared to the conventional one layered heat sink. In the later years, a lot of studies has been published investigating the multi-layered microchannel techniques of different channel shapes, materials, flow and fluids. The optimum number of layers has been investigated by Wei and Joshi [142] where the number of layers was varied between 1 and 6. The analysis showed a significant effect of the thermal resistance and pumping power by the number of layers and the optimum number of layers was found to be 3-layers. In addition, studies have proposed different materials of layers such as silicon [143–145], copper [146,147], aluminium [148], steel and diamond [140]. Also, the studies have investigated different fluid flow pattern of parallel flow [149–151], counter flow [152–155] and both flows comparison [156–158]. Different coolants have been tested for the MLM heat sink applications such as water [159], air [160,161] , nanofluids [162,163], deionized water and ethylene glycol [164]. The MLM heat sink investigations have also studied the shape of channel effect of different shapes such as rectangle [165–167] , square [168,169], triangle [148] and wavy [170]. Table 1 summarizes the MLM heat sink studies and their important findings.

Table 1. Comparative study of different MLM heat sink [171].

Ref.	type of study	Number of layers	Type of coolant	Flow directions	Type of heat source	Heat sink materials	Shape of channel	Channel size	Objectives	Important Findings
[152]	Modelling	1 & 2	Water	Counter flow	uniform ($1.3x10^7$ W/m^2)		Rectangular	(h=100xW=100) µm	• Optimisation of heat sinks design in the laminar and turbulent flow conditions.	• For a single layer counter flow: Heat sink performance (heat transfer and hydrodynamic) in laminar flow can be similar of that in turbulent flow. • For a double layer counter flow: Heat sink performance in laminar flow is better than that of the turbulent.
[142]	Modelling	1-6	Water	Parallel flow	Uniform		Rectangular	-	• Optimum fins width, channel width and aspect ratio of two-layered micro-channel heat sink. • The optimum number of layers for lower thermal resistance and pumping power.	• Thermal resistance is inversely proportional to the pumping power. • Thermal resistance depends on the channel length. The shorter length, the small thermal resistance. • In this study the optimum number of layers is 3.
[153]	Modelling	2	water	Counter flow	Uniform		Rectangular	-	• To determine the lowest thermal resistance by varying the height sink dimensions such as height and width of	Double layer counter flow micro-channel heat sink has less thermal resistance compared to parallel and counter flow single layer micro-channel heat sink.

									channels, height and width of fins.	
[168]	Analytical, numerical experimental	1-4	water	Parallel flow	Uniform	Silicon carbide (SiC)	Square	1150-500µm	•A closed-form analytical, numerical and experimental analysis.	•For same flow rate, the pressure drop decreases as the number of layers increased.
[140]	Numerical simulation	1-5	water	Parallel flow	Uniform	Steel, Silicon, copper and diamond	Square	71µm	•A comparison of multi-layers heat sinks with single-layer using numerical simulation and thermal resistance network analysis.	•For materials with low thermal conductivity, the thermal resistance increases with increase of layers. •The materials thermal conductivity is not important for low coolant flow rate.
[159]	Numerical simulation	2	water	Parallel flow	Uniform	-	Square	-	•To determine the effect of the fluid flow on the overall heat transfer performance.	•The performance of the heat sink is dependent on the flow characteristics in the channels.
[160]	Numerical simulation	2	Air and water	Counter flow	Uniform	-	Rectangular	(h=100xW=30) µm	•To investigate the effect of presence of passive microstructure in the channel	•The increase of the height of passive microstructure compared to microchannel height leads to lower thermal resistance.
[169]	Modelling and experimental	1-5	water	Parallel flow	Uniform	Copper	Square	(h=508xW=508) µm	•The comparison of performance of single and multiple layers of minichannel heat sink.	•The increase of the minichannel layers leads to reduce the thermal resistance and pumping power.

[166]	Modelling and experiment	3	water	-	Uniform	Silicon	Rectangular	(h=400xW=50) µm	• To determine the effect of silicon/micro/nanopillars on multilayer water-cooled heat sink.	• The overall thermal resistance and heat dissipation rate of the heat sink are reduced with silicon pillars Compared tod to one without.
[156]	Modelling	1-2	water	Parallel and counter flow	Uniform	Silicon	Rectangular	(h=100xW=30) µm	• To investigate the effect of fluid flow on the heat sink performance.	• Two-layered heat sink perform better in terms of the overall thermal resistance and temperature uniformity in the chip. • At low Re number, thermal resistance is lower in parallel flow. • Counter flow arrangement gives more temperature uniformity in the chip.
[161]	Modelling and experiment	1-2	air	Parallel flow	Uniform	Silicon	Rectangular	(100x400) µm	• Investigation of non-uniform allocation of micro-channel for more temperature uniformity and less pumping power.	• The study was able to achieve 50% less pumping power with sufficient cooling.
[150]	Modelling	2	water	Parallel flow	Uniform	Silicon	Rectangular	-	• Analysis of the effect of individual geometric parameters in the performance of the heat sink and to find out its optimum parameters.	• Optimal thermal resistance decreases with pumping power. • As the coolant pumping power increases, the optimal channel number, lower and upper aspect ratio increase and the optimal width ratio decreases.

[162]	Numerical modelling	2	Nanofluid (Al2O3–water)	counter flow	Uniform	Silicon	Rectangular	-	• Analysis of enhancement double-layered heat sink by using a nanofluid and geometric parameters variation.	• Significant thermal performance improvement of heat sink when using the nanofluid compared to water. • The heat sink effectiveness declines significantly under high pumping power.
[172]	Numerical modelling	2	deionized water	Parallel flow	Uniform	-	Rectangular	(h=1000xW=196) µm	• Parameters optimization under high heat source of 556W/cm2	• The optimization achieved the satisfy requirement if chip of 98ºC temperature.
[164]	Numerical modelling	2	Glycerol Ethylene glycol Distilled water	counter flow	Uniform	Steel Silicon Aluminium Copper	Rectangular	-	• The effect of substrate materials, coolants and geometric parameters on the performance of heat sink.	• Heat sink heat transfer performance is enhanced by: • Coolant with high thermal conductivity and low dynamic viscosity • Substrate with higher thermal conductivity
[170]	Numerical	1 & 2	Water		uniform(100W/cm²)		Rectangular and wavy	(h=100xW=400) µm	• Investigation of the effect of wavy on the heat sink performance	• Double Wavy channel heat sink performed cooling performance and lower pressure drop than the single wavy channel heat sink.
[146]	Experiment	1-2	water	counter flow	-	copper	Rectangular	(h=650xW=210) µm	• Comparison of fluid flow in single and double-layered heat sink. • Liquid-liquid counter-flow heat transfer.	• Double-layered heat sink suffers less than half of pressure drop compared to single heat sink.

[149]	Modelling	2	water	counter flow	Uniform	copper	Rectangular	-	• Optimization of mini-channel parameters for optimal temperature uniformity and pump work.	
[158]	Modelling	2	water	Parallel and counter flow	Uniform	Silicon	Rectangular	(h=400xW=100) µm	• The thermal and flow behaviour of double-layered heat sink is investigated under different flow rates.	• Parallel flow is better when the flow rate is at low value and counter flow is better in high flow rate.
[157]	Modelling	2	water	Parallel and counter flow	Uniform	Silicon	Rectangular	-	• Study the behaviour of two-layered heat sink under various channel aspect ratios.	• Parallel flow is better in heat transfer performance than counter flow except in high Reynolds number and high channel aspect ratio. • Small middle rib leads to lower thermal resistance.
[154]	Modelling	2	water	counter flow	Uniform	Silicon	Rectangular	-	• Optimization of geometry and flow rate for double-layered heat sink.	• Increasing the pumping power requires more channel, small bottom channel and thinner vertical rib.
[163]	Modelling	2	water Nanofluid (Al2O3–water)	counter flow	Uniform	copper	Rectangular	-	• Two advanced micro-channel heat sinks (double-layer and double sided) are compared	• Sandwich structure with counter flow shows a significant reduction in thermal resistance compare with single-layer, double-layer.
[155]	Modelling	2	water	counter flow	Uniform	Silicon	Rectangular	-	• The effects of channel number, aspect ratio and velocity on performance.	

Most of the studies were conducted for the MLM heat sink have considered a uniform heat source and very few has considered the non-uniform heat source. Wei et al. [173] have compared the behaviour of MLM heat sink under uniform and partial heat source numerically and experimentally. The experiments have used several heaters to simulate the partial heating scenario. The results showed that heat sink for partial heating had a higher total thermal resistance than the full heating due to local heat source. Also, the partial heating effect increased as flow rate increased. The authors have pointed out the importance of the location of the heat source to minimize the localized heating effect. In addition, the flow directions (counter flow and parallel flow) have been explored. The results showed that double layers heat sink experience similar thermal resistance for both flow patterns of 0.09°C/(W/cm²). However, the heat sink temperature in the counter flow pattern had better temperature uniformity than the parallel flow of 40% less. Recently, Ansari and Kim [174] have explored numerically the performance of double-layered heat sink under non-uniform heating conditions with random hotspot for microprocessor cooling applications. However, the study showed the effect of the flow pattern without any comparison with single a layer heat sink.

Applying an MLM heat sink in a CPV cooling application requires special attention due to the rapid temperature increase in the CPV module and the importance of solar cell temperature uniformity. The only two studies found in applying this cooling technique in the CPV applications are published as the results from this research [175,176]. Al Siyabi et al. [175] have conducted numerically a thermal analysis of using MLM heat sink in a single solar cell receiver. The results showed a significant temperature reduction of the solar cell when the number of layers increased from single layer to 4 layers by 15ºC. In addition, the pressure drop was decreased by more than 50% when using 4 layers heat sink and reduced the temperature non-uniformity of the solar cell.

2.6 PCM thermal energy storage system

Thermal storage system (TES) is a very important topic in solar energy applications. The need for the TES system in solar systems is due to the mismatch between the energy supply and demand or to recover the waste heat generated from photovoltaic systems. Thermal energy system is classified base

on the temperature ranges into three categories low, medium and high. Low temperature thermal energy stores the heat that is less than 100°C and this type of heat can be used in distillation, district water heating and space heating. The medium thermal energy system temperature range between 100°C to 300°C. This type of thermal energy can be used in heating, ventilation and air conditioning.

The thermal energy can be stored in two forms sensible, latent-thermal and thermal-chemical heat storage as shown in Figure 11 . The chemical form is performed by storing the absorbed thermal energy in breaking and reforming molecular bonds in a reversible chemical reaction. The sensible thermal form is performed by using the absorbed thermal energy to rise the temperature of the material as shown in Figure 12. This is a basic and the simplest way of storing the thermal energy. Water is the best sensible thermal storage medium due to its inexpensive cost and having a high thermal capacity.

The other form of storing the thermal energy is in the latent form and stored through the change of the phase of the material from solid to liquid or from liquid to solid. A huge amount of heat is stored by the materials during the phase change. It has been proven in many studies that storing heat into the latent form such as phase change materials (PCMs) in TES applications are an effective good due to their high latent heat storing in a relatively small volume over a relatively low temperature range.

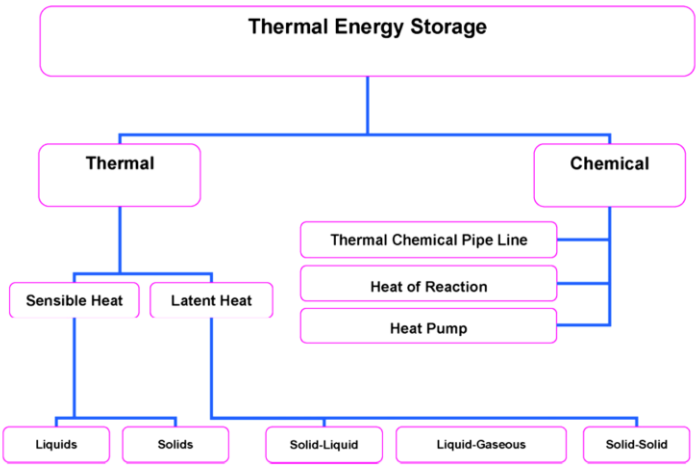

Figure 11. Types of thermal energy storage forms [177].

The development of a latent heat storage system falls into two main areas: material investigation and heat exchanger development. The material investigation study includes the characterization of the material and their thermo-

physical property such as melting temperature and heat of fusion. The heat exchanger development includes the heat exchanger concept, geometry and parametric operation investigations [178]. This research will mainly focus on the heat exchanger development and with a little attention to the chemical composition of the material.

The PCM storage concepts are very important area in designing thermal storage systems and it mainly depends on the application and the type of materials used. There are two concepts to store the thermal energy active and passive system (Figure 13). The passive system uses conduction heat transfer method for solid to solid and used by attaching the PCM at the back of the photovoltaic surface to enhance their electrical performance using the thermal regulation.

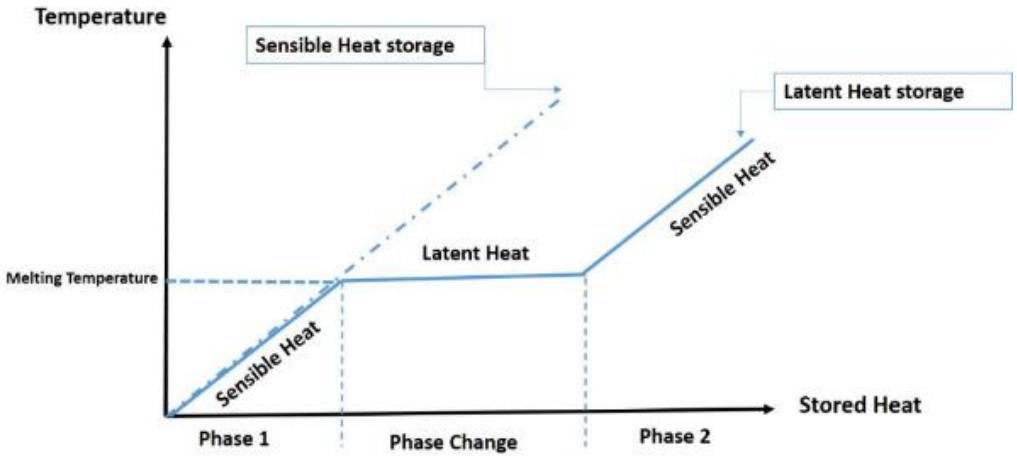

Figure 12. Temperature versus the stored heat for sensible and latent heat.

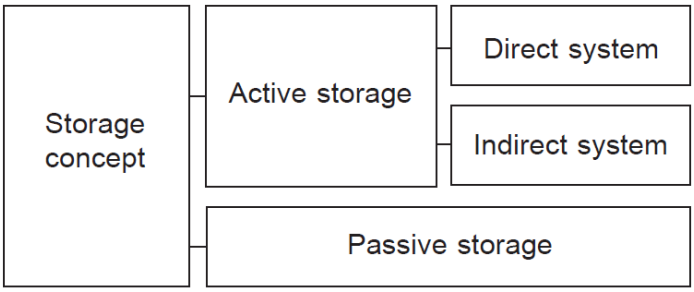

Figure 13. Classification of storage concepts.

An active storage system uses the forced convection heat transfer into storage material. It can be direct system, where the heat transfer fluid serves as storage medium or indirect systems, where a second medium is used for storing the heat. Basically, these configurations are divided into three types of storage (Figure 14):

- Storage with heat transfer on the storage surface: it is used mainly on temperature control applications, where the temperature of a heat source is required to maintain under the operational limit. This method is used for low heat application due to the PCM low thermal conductivity. The amount of used of PCM is determined by the amount of heat absorbed during phase change (latent heat of fusion) and the time required to maintain the low temperature.

- Storage with heat transfer on internal heat transfer surfaces: its application is to recover the waste energy, where the heat/cold effect delivered from the source to the storage so that it can be used later upon the demand. The main objective of these systems is usually to mismatch between the supply and demand. Usually the heat exchanger is packed with the storage medium (latent or sensible material) and heat transfer fluid is used to transfer the heat. Moreover, the use of extended surfaces (fins) is still possible to further enhance the thermal conductivity of the PCM.

- Storage with heat transfer by exchanging the heat storage medium: In this type, the heat storage and heat transfer medium become one fluid that is liquid and consists of a component that stores heat. The main characteristics of these systems are increasing the storage density compared to the pure heat transfer fluid but less than the previous other two types pointed out, high power is transported per volume of heat transfer fluid and improved heat transfer.

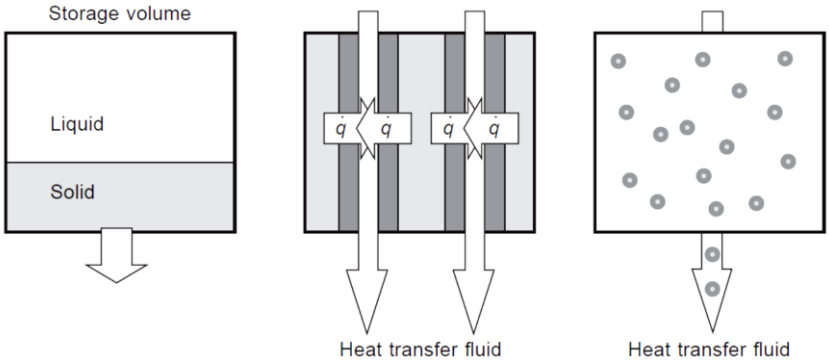

Figure 14.Types of heat transfer storage designs.

2.6.1 Thermal storage heat exchanger arrangement

Once the phase change materials is selected to suit the desired application, the next important design stage is the geometry of the container and its operating

parameters [179]. In order to ensure a very high thermal performance of the PCM system, the size and shape of the container must be designed to accommodate the heat produced by the heat source as well as to achieve the PCM melting point. This factor ensures high long-term thermal performance. Typically, two types of geometry are used as PCM container: cylindrical and rectangular as shown in Figure 15.

Because of the low thermal conductivity of PCM, the increase of heat transfer surface between the heat transfer fluid and PCM is very essential to enhance the thermal conductivity. The shell and tube arrangement actually offers the best heat transfer area between HTF and PCM and more than 70% of latent heat thermal energy storage (LHTES) units are shell and tube arrangement [180].

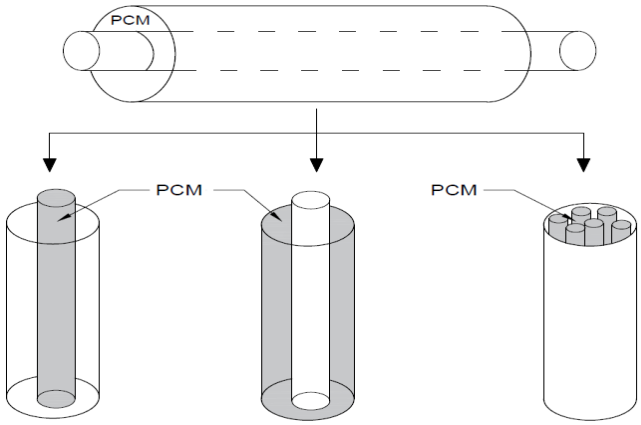

Figure 15. Different PCM storage configurations [44].

Esen et al. [181] have studied the melting time of the pipe mode and cylinder mode. They found that shorter time was needed for the PCM in the pipe mode compared to the cylinder mode. This is because of the thicker PCM mass is at the cylinder mode.

Agyenim et al.[182] have studied experimentally two TES configurations consisting of a single heat transfer tube and four heat transfer tubes. They used in their analysis the isothermal counter plots and temperature time curves. Both systems were packed with medium melting temperature of the phase change (117.7°C). It was found that multi-tube system improves the heat transfer rate during charging and it can generate a suitable temperature to run absorption cooling system.

The direction of fluid flow in the thermal energy during the charge and discharge is another factor to enhance the heat transfer. There are two modes of fluid flow:

parallel or counter-current flow as shown in Figure 16. If the fluid flow during charging and discharging mode is in the same direction and it is called parallel flow type. If the fluid flow direction during charging and discharging is opposite to each other then it is called counter-current heat transfer flow. Gong and Mujumdar [183] have studied the two modes using numerical analysis. The study investigated the effects of the fluid flow rate, inlet temperature and the duration of the charge and discharge period. The results showed that parallel flow was more desirable than the counter-current flow in the amount of the energy rate during the charge and discharge mode due to the higher temperature difference at the fluid inlet in parallel flow compared to counter-current flow.

Apart from the above pointed out parameters, others operating and geometry parameters must be considered when designing a full thermal storage system and this includes: the PCM shell radius, heat transfer fluid mass flow rate and heat transfer fluid inlet temperature.

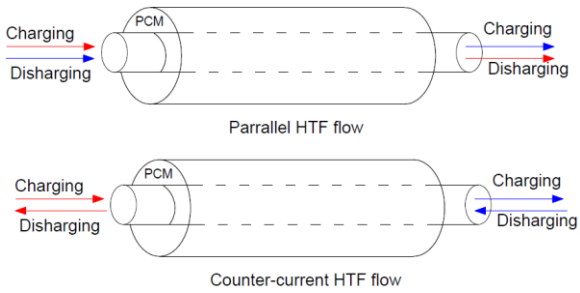

Figure 16. Parallel and counter-current HTF flow diagrams [184].

Apart from the above-mentioned parameters, others operating and geometry parameters must be considered when designing a full thermal storage system and this includes: the PCM shell radius, heat transfer fluid mass flow rate and heat transfer fluid inlet temperature.

2.6.2 Heat transfer in PCMs

The PCM heat transfer analysis is considered to be a complex problem[185–187]. This is due to the solid-liquid moving boundary during the PCM melting process [180]. During the heat charging process, the heat transfer within the solid PCM uses conduction mode only and once the PCM starts melting the heat is transferred mainly by natural convection between the liquid and the solid PCM. The influence of natural convection on the phase change process has been realized since 1970s [188,189]. However, the natural convection can be neglected during the solidification stage and only the heat is transferred by

conduction [102]. Both the PCM storage geometry and its inclination position have a major influence on the natural convection during the melting process and hence the overall heat transfer performance. The two most common PCM storage shapes used in the TES applications are the rectangular and the cylindrical types. Several investigations have been performed to study the role of storage inclination position on the PCM heat transfer in rectangular heat exchangers [104,105,190–193]. Those studies show clearly that the applied heat direction to a rectangular heat exchanger effects the PCM melting rate and profile. The heat source located at the bottom of the heat exchanger leads to a faster PCM melting in the horizontal orientation compared to vertical orientation [193]. On the other hand, if the heat is applied at the top of the storage, the PCM in the vertical orientation heat exchanger melts faster than horizontal orientation [105]. On the cylindrical PCM storage, the PCM melting process is completely different than the rectangular storage and this leads to the necessity for specific studies on the melting of PCM in this type of storage. Many studies have investigated the effect of convection on the melting process of PCM thermal storage systems. The existing studies have explored the natural convection on different fin types and sizes, heat transfer fluid (HTF) inlet temperature and flow rate effects and the orientation of the TES system in a vertical and horizontal arrangement.

Longeon et al. [194] have studied experimentally and numerically the natural convection and heat transfer rate within a vertical annular PCM storage system. The investigation included the effect of the top and bottom charging mode on PCM melting profile. The study found that the top charging mode causes the PCM to melt from top and gradually moves downward. The authors conclude this is due to the natural convection effects of the liquid-solid PCM interface. In the bottom charging mode, the PCM melts first along the tube and then the melted PCM moves towards the top of the cylinder as a result of natural convection due to the density difference between the two phases as explained previously by Ettouney et al. [195]. The work concluded that top charging is recommended due to the more temperature gradient in the axial direction than the bottom charging.

In a later study, Kibria et al. [196,197] have investigated numerically and experimentally the heat transfer between the PCM and HTF with different dimensions and operation conditions for a simple shell and tube system. The parametric study shows that HTF inlet temperature has a great influence on the

PCM melting rate whereas its mass flow rate has a minor effect on the PCM melting rate. In terms of the system dimensions, the bigger the tube radius leads to a lower melting time and an increase in the HTF temperature difference. These numerical findings match with the experimental findings in Kaygusuz and Sari's work [198].

Murray and Groulx [199,200] have extensively studied experimentally and numerically the energy characteristics of a vertical PCM storage in a simultaneous heat charging/discharging using different HTF inlet temperatures and flow rates. The test section consists of two tubes inside a PCM shell. Each tube is attached with four longitudinal copper fins as an enhancement method for the PCM thermal conductivity. The studies found that the direct heat transfer between the supply and demand occurs only when the PCM completely melted and no direct heat transfer between them during the solid phase. The studies concluded that the temperature variation along the HTF tube is as the result of the natural convection and not as the result of temperature variation of the PCM along the storage.

Esapour et al. [201] have investigated numerically the effects of the increase on the number of HTF inner tubes in a vertical PCM storage during the charging process under different operation conditions. The considered number of tubes are single, two, three and four tubes. The HTF flows in the outer shell of the storage and in the inner tubes which are located in the inner shell, where the PCM is also placed. The study found that increasing the number of inner tubes leads to an increase of the natural convection within the PCM and hence increasing the PCM melting rate. The study confirms the fact found by Kibria et al. that the HTF inlet temperature has more effect in increasing the melting rate and the natural convection heat transfer mechanism than the increase in the HTF mass flow rate.

In an extended study, Caron-Soupart et al. [202] have experimentally explored the impact on the heat transfer rate and natural convection inside cylindrical PCM using two types of fin: longitudinal steel and helical copper fins in a vertical PCM storage arrangement. The study shows that a higher melting rate is experienced when using longitudinal fins compared to the helical fins arrangements. This is due to the natural convection zones that are created between the longitudinal fins during the melting process as explained by the authors. They also concluded that

the fins orientation is a key factor in increasing the melting rate and not the type of the PCM.

Agyenim et al. [182] have experimentally investigated the heat transfer enhancement of the PCM using a multi-tube heat transfer array using a horizontal PCM storage. The study recorded that the multi-tube system improves the heat transfer rate compared to a single tube. The authors attributed this increase in the melting rate due to the natural buoyancy effect, natural convection and the formation of multiple convective cells at the multitude array.

Liu et al. [179,203] have investigated experimentally the heat transfer inside a horizontal PCM storage. The study also explored the effect of fins orientation in the system performance. The study confirmed the importance of the HTF inlet temperature in the PCM melting and heat transfer rate compare to the HTF flow rate. In terms of the fins orientation, the study concluded that straight fins have a small influence on the melting time compared to angled fins at low HTF inlet temperature (50ºC). For discharging process, the study reported no change on the heat transfer rate for both fins orientations. Similar investigation has been conducted by Tao and He [204] but using the numerical approach where the importance of natural convection on a horizontal cylindrical heat exchanger was confirmed.

Tay et al. [205–209] have reported an extensive work of designing, testing and analysing the performance of a novel multi-tube heat exchanger using numerical and experimental approaches. The authors highlighted that the natural convection plays an important role on melting the PCM and ignoring the effect of natural convection in the CFD model causes different melting profile compared to the experimental results. However, a greater number of HTF tubes reduces the distance between the tubes and the natural convection was found insignificant.

Very few studies have investigated the influence of the inclination angle on the melting and solidification process of PCM in a shell and tube PCM storage [210–212]. Seddegh et al. [211] have investigated numerically the thermal behaviour of shell and tube storage system in two orientations; vertical and horizontal by evaluating the PCM liquid fraction and the PCM average temperature. The study showed that the PCM in the horizontal orientation melted faster in the upper part of the storage compared to the lower part and a good heat rate performance was

experienced during the initial stage of melting. However, a slow melting of PCM was observed after the complete melting of the upper PCM due to the slower melting of PCM in the lower part. Also, the melting rate of PCM in the vertical position is more stable during the charging period compared to the horizontal position. In addition, the study showed a great impact of HTF inlet temperature in the charging process for both positions whereas the HTF flow rate has a slight effect during the charging period. Similarly Koush et al. [212] have studied experimentally and numerical the effect inclination angle on the PCM storage performance and more orientation angles were have been considered. The results of this study confirm the finding of [211] about the melting rate and working conditions effects. However, none of the studies have shown the solid-liquid interface along the axial direction or studied the internal flow of the liquid PCM in the different inclination angles.

2.6.3 Phase change materials classifications

There are wide variety of phase change materials available that melt and solidify at a wide range of temperatures which can be utilized in many applications. In this section, a brief is to be given about the classification of the PCMs. In 1983, Abhat [178] classified phase change materials into three main groups: organic, inorganic and eutectics. Organic phase change material is divided as paraffin and non-paraffin organics [10]. These materials cover the melting temperature ranged between 0^{o}C and 200^{o}C. The density of organic PCM is less than 1000 kg/m^{3}. Organic compounds present several advantages such as non-corrosive, possess chemical and thermal stability, ability of consistent melting, self-nucleating properties and compatibility with conventional materials of construction. The disadvantages of the organic are its low phase change enthalpy, low thermal conductivity, flammable and expensive.

Inorganic compounds include salt hydrates, salts, metals and alloys. Inorganic PCMs are better for medium to high temperature heat storages applications (>100^{o}C) because of their higher melting point compared to the organic PCMs. The main advantages of inorganic compounds are a high volumetric latent heat storage capacity, often twice the capacity of organic compounds and high thermal conductivity. Whereas the main disadvantage of the inorganic PCM is the

problem with most of the salt hydrates are super cooling, phase segregation, corrosion and lack of thermal stability.

For thermal storage, there are certain materials properties (thermal, physical, kinetic and chemical properties) that are desired in order of the system to perform efficiently [213]. Table 2 lists the desired properties of the PCM.

The main two evaluation techniques for the measurement of the thermos-physical properties of the PCMs are the Differential Thermal Analysis (DTA) and Differential Scanning Calorimetry (DSC) and this will be highlighted in section 3.3.

Table 2. The desired PCM properties.

Property type	Desired Property
Thermal	- Suitable phase transition temperature. - High latent heat of transition. - High thermal conductivity in both liquid and solid phases.
Physical	- Favourable phase equilibrium. - High density. - Small volume of change or low-density variation with temperature. - Low vapour pressure.
kinetic	- Non-super-cooling. - Sufficient crystallization rate.
Chemical	- Long-term chemical stability. - Compatibility with materials of construction. - Non-toxic. - Non-flammable.

2.6.4 Thermal conductivity enhancement techniques

As pointed out earlier that the most challenge of using the PCM in the thermal storage applications is its low thermal conductivity compared to the sensible heat materials. Several studies have been conducted to enhance the thermal conductivity during the charging and discharging. Many techniques have been proposed to overcome the thermal conductivity issue such as fins tube, micro-encapsulation of the PCM and using multiple PCMs.

2.6.4.1 Fins

Increasing the area between the PCM and the heat source is considered as one of the enhancement techniques of the thermal conductivity of the PCM. Different

fins arrangements have been studied of longitudinal or radial fins, circular fins and multi-tubes. Lacroix [214] has numerically studied the heat transfer behaviour of latent heat thermal energy with a finned tube. The author found that the finned tube is suitable for moderate mass flow rates and small inlet temperatures. Ogoh and Groulx [215] have studied numerically the effect of the thermal fluid velocity on cylindrical PCM storage in the presence of cooper fins. The number of fins were varied from no fins to 18 fins configurations. It was clearly showed that more fins caused a higher energy stored rate and less melting time. Lorente et al. [216] have investigated numerically the effect of using a vertical spiral positioned coaxially in the PCM storage and with variable inner radius. The authors concluded that the global performance of the storage system could be increased by selecting the geometric features such as spiral pitch, diameter and number of concentric spirals. In another study, Mon and Gross [217] have studied numerically fins spacing in the annular finned tube heat exchanger. It was found that the heat transfer coefficient increases as with the find spacing to height ratio until 0.32 and then it has no effect on this.

Kim [218] has optimized fins thicknesses in the direction normal to the fluid flow. The results showed that the thermal resistance of the concave fins thermal storage was reduced by 12% in the case of employing with straight fins regardless of the pumping power and the tube length. Castell et al. [219] have investigated experimentally the effect of a coil in the PCM tank for cooling applications using two different configuration of different tube packing factor. The results showed that higher packing factor more than 90% has no effect on the performance on the storage. Khalifa et al. [220] have studied numerically and experimentally the solidification of axially finned heat pipes for high temperature thermal storage system. The results show that the finned heat pipes have improved the thermal energy storage by 86% compared to the bare heat pipes.

Zhao and Tan [221] have numerically investigated the shell and tube thermal storage for air-conditioning application. The study showed that the HTF flow rate and fins height provide higher heat charging rate and shorter total charging time. The effectiveness of the proposed storage system is higher than 0.5. In another study, the enhancement of the PCM storage system in triplex tube with fins has been investigated numerically by Mat et al. [222]. The results showed no effect

on the melting rate of the internal and external fins. However, using both type of fins reduced the melting time by 43.3% compared to no fins system.

2.6.4.2 Micro encapsulated

Encapsulation of PCM inside an enclosed metallic object is another enhancement technique to increase its low thermal conductivity. Zhao et al. [223] have studied numerically the heat transfer in encapsulated PCM using two dimensional heat transfer model. The considered PCM was the $NaNO_3$ encapsulated in a cylindrical shaped capsule made from stainless steel. The results showed that the heat transfer process was influenced by the capsules materials. The size of capsules and type of heat transfer fluids have a great impact on the heat transfer rate and melting time. In a similar study, Bellan et al. [224] have studied numerically the charging and discharging of a cylindrical thermal storage with encapsulated PCM. The authors showed that the melting time is shorter than the solidification time due to the higher heat transfer coefficient during the melting process. Also, the natural convection effect increased as increasing the capsule size. The ratio of the tank length to the diameter has a significant effect on the complete melting and solidification time.

Nithyanandam and Pitchumani [225] have illustrated a method for designing and optimization of an encapsulated PCM for the thermal energy storage system. Kalaiselvam et al. [226] have conducted an experimental investigation of melting and solidification of PCMs inside cylindrical encapsulation. The results showed that the complete solidification time is effected significantly by the radius of capsules between 0.05 to 0.06m. Bédécarrats et al. [227,228] have conducted an experimental and numerical study on the PCM storage using spherical capsules to study the influence of various operating diameter on the charging and discharging modes. The HTF inlet temperature and its flow rate have an impact on the storage rate. The authors introduced the super cooling effect of which is charging mode that follow the incomplete of discharging mode and this produced a higher temperature with a relatively shorter duration [229].

2.6.4.3 Multiple PCMs

Employing multiple PCMs of different melting temperature in thermal energy storage systems is considered as an effective method for PCM enhancement [230].The multiple PCMs means that more than one PCM type is packed in the

thermal storage system. The PCMs are arranged in a descending order of their melting temperature. Therefore the HTF decreases its temperature i.e. heat transfer rate as it flows through the first PCM, it enters the second PCMs storage of less PCM melting temperature and this causes an increase on the overall system performance [231].

The multiple PCM storage system was first introduced in 1995 by Gong and Mujumdar [232] in a horizontal cylindrical storage using 5 PCMs arranged in descending melting temperature order. The results showed that using multiple PCM can enhance greatly the charge and discharge rate of thermal energy as compared to a single PCM. Also, the multiple PCM system can significantly reduce the fluctuation of the HTF outlet temperature. In another study by the same authors [233], their novel storage unit of multiple PCMs was tested under cyclic heat transfer rate. The results show a lower HTF outlet temperature during the charging process and a higher HTF outlet temperature during the discharging mode for the 5 PCMs arrangement compared to the single PCM arrangement.

Michels and Pitz-Paal [234] have showed experimentally the use of a cascade of multiple PCM to ensure the optimal utilization of the storage materials. The experiments were conducted using vertical shell and tube heat exchangers. The results showed that the cascaded arrangement offers a uniform heat transfer fluid outlet temperature during the discharging than a non-cascaded storage system. Seeniraj and Narasimhan [235] have combined the two enhancement techniques of using fins and multiple PCMs. Their results confirmed the better performance of multiple PCM compared to the single PCM and the uniformity of the exit HTF temperature with the multiple PCM. Fang and Chen [236] have studied numerically the effect of different multiple PCMs arrangements on the performance of the PCM storage. The study found that there is an optimum proportion between the PCMs for the maximum thermal charging and an appropriate selection of the PCMs plays an important role for the performance improvement.

2.7 CPV-TES system

From the literature review, it was found that the integration of the concentrated photovoltaic with the thermal energy storage has not received much attention. However, there are a lot of studies where the thermal energy storage using PCM,

concentrating photovoltaic cooling and photovoltaic thermal have been conducted separately. The integration of the thermal energy storage with solar heat pump or solar collector can be a good approximation of the CPV/TES. The similarity areas are the load profile, amount of energy to be stored and type of analysis. The use of exergy analysis is an important in developing a good understanding of the thermodynamic behaviour of thermal energy storage systems because it clearly takes into account the loss of availability and temperature of heat in storage applications, and hence it reflects the thermodynamic and economic value of the storage operation [237]. The analysis of the system, which is solely dependent on the first law of thermodynamics, is inadequate as a measure of the energy storage because it does not consider the effect of time duration through which heat is supplied and the temperature of the surroundings. The energy analysis might produce a workable design, but not necessarily one with the highest possible thermodynamic efficiency [238]. In contrast any analysis consideration leads to the optimal design operation of thermal systems.

Yumrutas and Kaska [239] have investigated the thermal performance of a solar heat pump system integrated with an energy storage system. The heat was generated by solar collector and it was stored in a cylindrical tank and water was used as the HTF. The heat was used in space heating application. In this system the variation of solar irradiance, solar collector performance and overall system performance were calculated and evaluated. Kumaresan et al. [240] have studied the integrated solar parabolic trough collector with sensible thermal energy storage. The performance has been measured using different parameters of overall heat loss coefficients. It was evaluated from the experimental temperature variation of the HTF in the storage tank with respect to time. The useful heat gain is the energy gained by the heat transfer fluid when it passed the solar collector. Solar collector efficiency is the ratio of the instantaneous useful heat gained by the HTF, and the instantaneous incident solar irradiance. Energy collected/energy stored in the thermal storage. Charging efficiency/overall system efficiency is the ratio of the energy stored in TES/ energy collected by the solar collector. Huang et al.[241] have evaluated PV/thermal systems using water as working fluid and then compared it to a conventional solar water heater. They showed that the PV/T system reached a daily efficiency of 0.38 which is about

76% higher than the conventional system. Also, the study proved the economic feasibility of the PV/T system. Ozgenera, and Hepbasli [242] have investigated experimentally the performance of integrating the solar thermal with storage system for greenhouse applications. The proposed system achieved heating coefficient of performance of 2.64 and an energetic efficiency of 67.7%.

A PV/T system has been evaluated numerically by Tiwari and Sodha [243]. The proposed system integrated the PV system with water storage tank. The results showed a significant increase of the thermal efficiency from 24% to 58% of using the thermal storage. Fraisse et al. [244] have studied the performance of water hybrid PV/T for solar floor heat applications. Due to the cooling of PV, the electrical efficiency was increased by 6% compared to no cooling PV. The study concluded that, hybrid solar is promising but required to maintain a strong partnership between the PV and thermal field.

Kerzmann and Schaefer [245] have simulated a LCPV system with active cooling and storage system for economic and environmental perspective point of view. The proposed system can supply of 6.2kWp as well as displace 10.35 tons of CO2. Bakirci and Yuksel [246] have studied the integration of solar collector with thermal storage in cold climate(-10.8°C to 14.6°C). The study showed that the system of solar collector- thermal storage could be used for residential heat in cold climate where the average collector efficiency varied between 0.4 and 0.6 and the maximum average storage temperature was between 28°C to 40°C. Similar study were conducted of solar collector and thermal storage for domestic heating [247] where the storage tank temperature varied between 9°C and 35°C. Naghavi et al. [248] have investigated the thermal performance of a compact heat pipe with latent heat storage. The results showed a thermal efficiency of a range between 38% and 42% in sunny days and of 34%-36% in cloudy-rainy days [249].

2.8 Conclusions

This chapter has presented an extensive review of significant relevant topics of this PhD research. The detailed review includes the CPV thermal regulations and thermal energy storage using PCM techniques. In the last section, the integration of the solar system with the PCM storage has been presented.

From the review, it can be seen that the CPV receivers offer promising opportunity in the future to generate electricity compared to the conventional PV

technology. This is due to the dramatic reduction in the semi conductive materials in the CPV where the more expensive and efficient multi-junction cells (46%) are generally employed to replace the lower-efficiency silicon solar cells for high concentrations. Then, the CPV thermal challenges have been presented by highlighting the increase of the solar cell temperature in reducing the open circuit voltage and short circuit current electrical performance. The non-uniform illumination on the solar cell has been presented as another factor for the need for a highly efficient thermal regulation technique.

The review shows that the generated heat by the CPV system offers great opportunities for utilizing the heat in a useful heating applications. A considerable number of studies have been devoted to utilizing this heat in the useful application leading to an increase the overall system performance.

The review has discussed the different types of CPV thermal regulation techniques specifically the passive and active cooling techniques that have been investigated by researchers in the few decades. The passive cooling techniques are likely to increase the reliability of CPV systems and, at the same time, reduce the operation costs. However, the active cooling technique is considered as more efficient and is the currently thermal regulation solution for high or even the ultra-high CPV in the future.

The MLM heat sink technique is considered as an efficient technique in terms of reducing the heat source maximum temperature and the pressure drop compared to the conventional microchannel heat sink. The literature review shows that the MLM heat sink has not yet been investigated in detail for the non-uniform heat source applications and in the CPV application. Therefore, investigating this type of technique will be considered as an important contribution to the CPV thermal regulation.

The second topic discussed in this chapter was the PCM thermal storage. The review has presented a considerable number of studies in the thermal storage heat exchanger, concept of heat transfer in PCMs, types of PCMs and the techniques to enhance the PCMs thermal conductivity. In summary, the literature shows a lack of research on the thermal analysis of the cylindrical PCM storage in some areas such as the storage orientation effect and the multiple PCM technique especially on the experimental side. Therefore, those two topics (the

orientation and the multiple PCM) will be further investigated in this research by conducting an extensive thermal analysis using both the numerical and the experimental approaches.

The last part of the literature review investigated the integration of the CPV-PCM storage system. However, the literature survey shows a lack of studies on the integration of the CPV-PCM storage system and the only studies were on the solar collectors and thermal storage. Therefore, this study will be considered as an important contribution to the CPV-PCM thermal storage research.

As stated above this research will be divided into three parts. The first part is the CPV thermal regulation where the MLM heat sink technique has been selected. The second part is the PCM storage where the thermal analysis will be conducted on studying several criteria such as the orientation and multiple PCM. In the last part, the integration between the CPV and PCM thermal storage will be studied in several scenarios. The numerical and experimental approaches will be used by the researcher in all the investigations. In the next chapter the experimental components, instruments and materials analysis will be presented.

Chapter 3 : Materials and methods

3.1 Materials components and instruments

3.1.1 The solar cell

Triple-junction cells developed by the German company AZUR SPACE Solar Power were employed in this work [250]. They are multi-junction solar cell (GaIn/GaAs/Ge) with an active area of 10mm^2 and a thickness of 190um. These solar cells were rated to a peak efficiency of 42.1% and at maximum power point (MPP) of 10.59W under standard conditions at 250x concentration. They were chosen because of their high performance and its availability at the solar lab facilities. The cell has a wavelength range of 300– 1700 nm and a peak efficiency of 42.2% depending on 500x concentration ratio and at temperature of 25°C as shown in Figure 17.

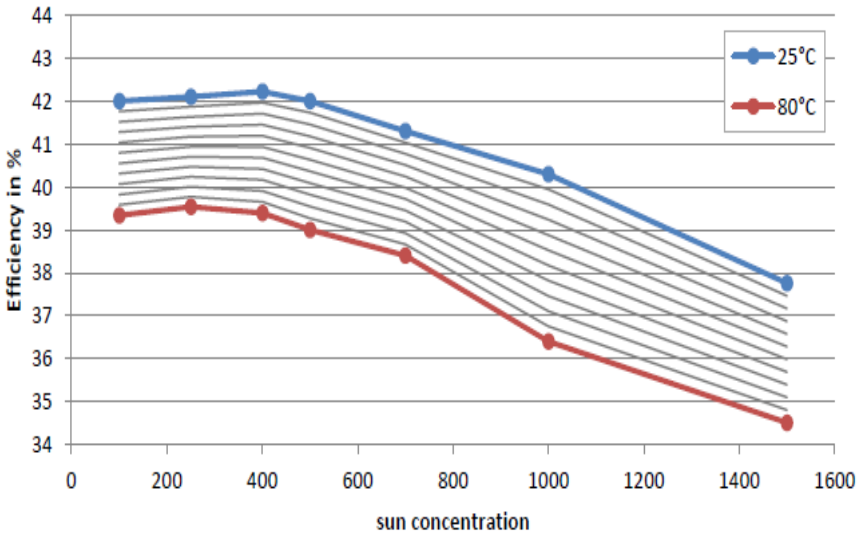

Figure 17. Electrical efficiency versus concentration ratios for 3C42 solar cell [250].

3.1.2 CPV assemblies

The commercial solar assembly used in this work was the 3C42, supplied by AZUR SPACE. The solar cell is attached on a substrate of 0.25mm thick made from copper/Al_2O_3 ceramic/copper and a lower copper plate thickness of 0.25mm. A ceramic layer is used to separate the top and bottom copper layer for dielectric insulation. These cells are connected with 2x10A Schottky diodes. A photograph of the receiver is shown in Figure 18.

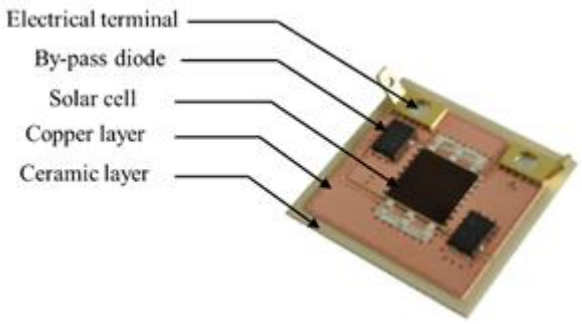

Figure 18.Photograph of Azurspace 3C42 CPV assembly [250].

3.1.3 Thick film resistor

Electrical resistance heater (ERH) (Figure 19) manufactured by Bourns® as shown in Figure 19 is used to simulate the heat load generated by the CPV in some parts of the research. The resistor is made of thick film material with an aluminium plate at the back. The ERH power rating is 30W and its size is 10mmx10mm and is operated by DC power supply.

Figure 19. Photograph of electrical resistance heater (ERH).

3.1.4 Sylgard 184

Sylgard® 184 is a transparent encapsulant solution produced by Dow Corning. It is a Polydimethylsiloxane elastomer suited as refractive material used for the homogeniser for the CPV applications for the protection of electrical and electronic components. It has a high optical transmittance and its wide operating temperature range (-45°C to 200°C). A summary of the physical and thermal properties is shown in Table 3.

Table 3. Sylgard's physical properties by Dow corning.

Viscosity (Mixed)	Thermal Conductivity	Coefficient of Thermal Expansion	Volume Resistivity	Operating Temperature
3.5 Pa.sec	0.2 W/m. K	$3.1 \cdot 10^{-4} K^{-1}$	$2x10^{14}$ Ω· cm	-45 to 200°C

The optical transmittance of the sylgard was measured using the spectrometer by Shanks et al. [251] for different thicknesses as shown in Figure 20. It is noticed

that transmittance decreases from 92% to 75% at 800nm wavelength as the thickness increases from 1mm to 95mm, respectively.

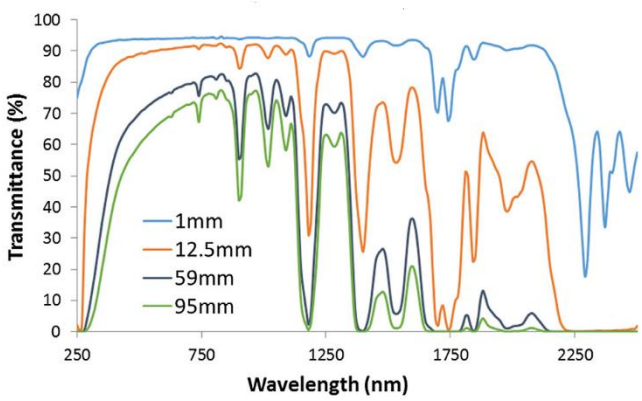

Figure 20. Transmittance spectra for varous sylgard thicknesses [251].

Sylgard 184 is provided as two parts liquid components. The base and the curing agent must be mixed in a mass ratio of 10:1. After mixing, they were manually stirred. Then, the solution was placed in a vacuum chamber until bubbles were no longer visible. Sylgard was then dispensed directly on the surface and to allow spreading it as uniformly as possible. Depending on the curing temperature, Sylgard could then be cured at room temperature for 48 hours, at 100°C for 45 minutes or at 150°C for 10 minutes.

3.1.5 Crystal clear resin

Crystal Clear™ 200 EU is water white clear produced by Smooth-On Inc. Crystal Clear™ resins cures at room temperature with negligible shrinkage. Its applications include encapsulation, making prototype models, lenses, sculpture reproductions, decorative cast pieces. A summary of the physical and thermal properties is shown in Table 4.

Table 4. Crystal clear resin physical properties by Smooth-On.

Viscosity (Mixed)	Heat Deflection Temperature	Shrinkage
600 cps	50ºC	0.001 in/in

Crystal Clear™ 200 EU is provided as two parts liquid components. The base and the curing agent must be mixed in a 100:90 ratio by weight. After mixing, they were manually stirred. Then, the solution was placed in a vacuum chamber until bubbles were no longer visible. Then, the mixer was then dispensed directly onto the mould. The curing time of this resin is 16 hours at 23°C.

3.1.6 Paraffin wax

The PCMs used in this research are organic types manufactured by Rubitherm Technologies GmbH. They are solid-liquid PCM and they come in different melting temperature. The melting temperature range is narrow in these types of PCM due to purity and specific components. A details study of the PCM thermal properties will be carried out in section 3.3.

3.1.7 Spectrometer

The materials optical properties such as transmittance, reflectance and absorbance were measured through a Perkin Elmer Lambda 1050 in the range between 175nm and 3300nm, with a resolution that could be set down to 0.5nm. The samples were placed in a sample holder: transmittance and absorbance were measured with reference to air, whereas the reflectivity with reference to a calibrated reflective white surface. This instrument was used in this research for transmittance measurements of the homogeniser and the glass. Is was used also to measure the reflectance of the primary and the secondary reflector.

3.1.8 Solar simulator

A WACOM WXS-300S-50 AM1.5G solar simulator was used for the indoor characterization of the CPV receivers in this research. The simulator irradiance range is 70 and 120mW/cm^2 with effective irradiance area of 210mmx210mm. This is generated using a 5000W Xenon short arc lamp, which yielded a high non- uniformity and a temporal instability within 2%. This device achieved a Class AAA spectral match (Figure 21).

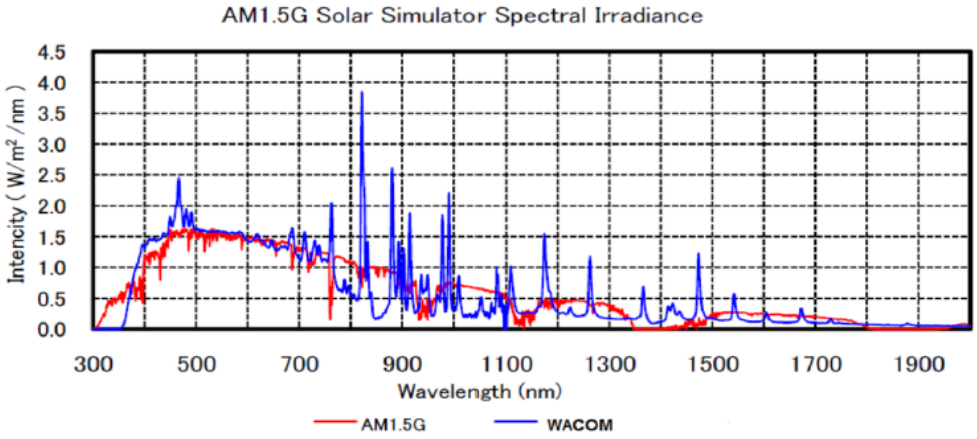

Figure 21. Solar spectrial irradiance of WACOM simulator and AM1.5G [252].

A calibrated silicon cell was used to calibrate the solar simulator before each test to ensure the irradiance to the desired level. The current flowing through the silicon cell was the used parameter to calibrate the instrument. The standard solar cell current is 127mA for 1000 W/m^2 irradiance. A temperature controller kept the cell temperature at 20°C.

The tests were conducted at different constant irradiance. This is adjusted using the XE level intensity. This is given by the manufacturer graphs. The simulator was used after some time after being switched on to reach a steady energy flux.

3.1.9 I-V tracer

An EKO MP-160 I-V tracer was used for the indoor and outdoor characterization of the CPV. This instrument operated in the voltage range between 0.5V and 300V and current range between 0.005A and 10A and the maximum power of 300W. A four-wire configuration was used to extract the electrical outputs from the cell. The instrument gives several parameters such as the open circuit voltage, the short circuit current, the maximum power, the filling factor and the I-V curve.

3.1.10 Solar tracker

A SOLYS 2 automatic sun tracker was used to track the sun for the outdoor characterization of the CPV module. The CPV was fixed in the tracker using a steel structure. In order to track the sun accurately, all levels should be adjusted according to the manufacturer recommendations. The solar tracker has been designed for small and medium sized of loads (<20kg). Also, similar tracker was used to collect the outdoor solar irradiance both the direct and the diffused. The manufacturer specified of two tracking errors of positioning and levelling and estimated of less than 2° for both.

3.1.11 Vacuum oven

The EQ-DZF-6210 oven was used for air bubbles removal from casted homogeniser and from the sylgard material. Also, the machine works an oven for high temperature curing at maximum temperature of 270ºC with three heaters and three temperature controllers.

3.1.12 DSC

NETZSCH, 214 Polyma Differential Scanning Calorimetry (DSC) instrument was used for the analysis of the melting temperature, heat capacity, and phase transition for PCM properties. The instrument works in temperature range from -170^{o}C to 600^{o}C with heating rates between 0.001K/min and 500K/min. The instrument uses a very low thermal mass samples to perform the test. Proteus software was used to analyse the data to obtain the heat capacity.

3.1.13 Thermocouples

Thermocouples were used as the main instruments for measuring temperatures for system characterization and evaluation for the MLM heat sink and PCM storage system. The temperature was measured and reordered at several locations within the MLM heat sink and the CPV module. Also, the temperature was used for measuring the PCM temperature at different locations during the charging processes to determine the temperature distribution within the system.

K-type thermocouples were chosen in this study as they have appropriate temperature range. Various thermocouples sizes and types were used according to the location as shown in Figure 22. In most of the measurements, the thermocouples of tip size of 0.25mm were used. A fine thermocouple of tip size of 0.076mm was used to solar cell temperature in order to reduce any solar irradiance due to the thermocouple shading. In addition, the pro type K thermocouples were used to measure the HTF inlet and outlet temperatures (1mm) and the middle channel temperature of the heat sink (0.5mm). The thermocouples were calibrated according to the temperature of water melting ice (0°C) and boiling at atmospheric pressure (100°C).

(a) (b)

Figure 22.Photographs of K-type thermocouples (a) wire thermocouple and (b) prop type.

The signals from the thermocouples were logged with a Keithley 2700 system. It has different methods for temperature measurements, internal, external and simulated. These modules are designed for high-accuracy thermocouple measurements. This system can run up to two modules at a time to create up to an 80-channel system (shown in Figure 23). A Graphical program was used for monitoring the readings and saving them in a text format.

(a) (b)

Figure 23. Photographs of (a) Keithley 2700 and (b) channel module.

3.1.14 Water flowmeter

NFX variable area flowmeter was used to measure water flow rates in both the PCM storage and the MLM heat sink experiments. The flowmeter measuring scale is between 30-380 cm3/min. The flowmeter consists of glass tube, end blocks of nicked plated brass with ended stainless steel block. The experiment setup was connected to the flowmeter using $^{1}/_{4}^{"}$ BSP fittings. The flowmeter is fitted with a fine control valve to control the fluid flow rate. The flowmeter was calibrated by the manufacture of an accuracy of 2.5%.

3.1.15 Water differential pressure instrument

A differential Digitron 2080P Pressure instrument from Rototherm group (shown in Figure 24) was used to measure the pressure drop across the MLM heat sink test section. The instrument gives a variety of display readings options of psi, mbar, inH_2O, mmH_2O, mmHg, inHg and Pa. The working range of the instrument is ranged from 0 to 25 mbar. This instrument is designed to work in a temperature range of +20°C to +50°C of a measuring accuracy of 0.10%. The pressure transducer channel was calibrated by the manufacturer and a calibration certificate.

Figure 24. Photograph of Digitron digital pressure instrument.

3.1.16 Water circulation bath

A MultiTemp III bath was used to supply the heat transfer fluid at constant temperature and flow rate to the test rig. A summary of the technical details of the temperature-controlled circulating bath is presented in Table 5. Distilled water was used as the HTF of the experiments.

Table 5. Technical specifications of the circulating Bath

Technical Data	value
Working temperature range	-10 to 90°C
Temperature accuracy control	±0.1°C
Heater capacity	800W
Cooling capacity	265W
Pump capacity, pressure, max	0.32 bar
Pump capacity flow rate	12 l/min
Bath volume	3 Litres

3.2 Methods

3.2.1 CAD tools

The simulations, illustrations and design files were drawn using AutoCAD and Solidworks. AutoCAD was used for the 2D model representation a 2D Computer Assisted Design software tool developed by Autodesk Inc. Solidworks was used to draw the 3D models due to its simplified interface to users. The length and the angles of the components could be reproduced with high accuracy at any scale. In addition, COMSOL Multiphysics offers the live-link tool with Solidworks to simplify the geometry parametric studies.

3.2.2 COMSOL multi-physics

COMSOL Multi-physics is a computational fluid dynamics software that can be used to analysed different applications. Versions 5.1 have been used to study the

MLM heat sink and PCM storage systems. The “Heat Transfer” physics was employed for modelling the heat transfer within the system and this includes heat transfer in solid, fluids and phase change materials. Also, the fluid flow physics was included to model the HTF flow and phase change materials during the melting and solidification.

The simulations were conducted in 2-D axisymmetric environment and in time dependent mode for the PCM storage whereas a three-dimensional environment and in stationary modes were conducted for the MLM heat sink analysis. The modelled geometries were reproduced in the graphic window for the PCM storage studies. Because of the system complications, the MLM system was drawn using the solidworks software and import tools in COMSOL were used to import the geometry. The SI units were used in COMSOL such as millimetres and degrees for length and angular units, respectively. Then the materials of the domains are defined using the built-in materials library or the properties could be defined manually. For each domain, the boundary and the initial conditions were set according to assumptions and working conditions. Then, the mesh was defined where the geometry was automatically discretized into small elements. The size of elements was decided after conducting an independent study to examine its effect of certain interest parameters. Once the model was developed, COMSOL automatically generates the solver sequence and computes the solution. In additions, COMSOL offers several functions such as parametric and materials sweep for examining the effect of geometry and materials effect, respectively.

COMSOL offers several types of results outputs such as graphs and domains isotherms which can be plotted in the software graphic windows. In addition, the results can be exported in table format to other software’s such as excel for personalization point of view.

3.3 Thermal analysis for paraffin wax

Paraffin wax is selected as the PCM throughout this research and its properties will be extensively studied in this section. Rubitherm RT series is supplied by Rubitherm GmbH, Berlin, Germany and it is classified as an organic material. RT’s series are a promising choice with a high latent heat of fusion, low super-cooling, non-corrosive, non-toxic and cheap in cost[253]. The PCMs used are RT27, RT28HC, RT31, RT35, RT42 and RT47. The last two digits on the PCM

name indicates the PCM melting temperature. This various PCMs melting range are required for the investigation on effect of the melting temperature on the efficiency of the thermal storage system i.e. melting temperature range between 27°C and 46°C. The thermal properties of the used PCMs as per the manufacturer data sheet are shown in Table 6. Most of the thermos-physical properties such as the density, specific heat and thermal conductivity are the same for all the listed PCMs.

Table 6. Thermal properties of used PCMs
((Rubitherm® Technologies GmbH, Germany, http://www.rubitherm.de)

PCMs	PCM 1	PCM 2	PCM 3	PCM 4	PCM 5	PCM 6
Product code	RT27	RT28HC	RT31	RT35	RT42	RT47
Melting temperature (°C)	27	28	31	33	41	46
Solid density (kg/m³)	870	880	880	860	880	880
liquid density (kg/m³)	760	770	760	770	760	770
Latent heat (kJ/kg)	179	250	168	160	165	165
Specific heat (kJ/kg °C)	1.8	2	2.1	2	2	2
Thermal conductivity (W/m K)	0.2	0.2	0.2	0.2	0.2	0.2
Volume expansion (%)	12.5	12.5	12.5	12.5	12.5	12

The melting point, latent heat of fusion and specific heat might vary from the same manufacturer as they are made bulky and in different conditions and a dependent investigation on the thermal properties are required. As explained in chapter 2, the DSC technique provided a quick, accurate and detailed measurement results, and very small quantities of the sample, hence this technique is used to investigate the thermos-physical properties.

In this study, NETZSCH, 204 Differential Scanning Calorimetry (DSC) has been used for the analysis of the PCM properties such as latent heat of fusion (L), melting temperature (T_m), melting range (ΔT), heat capacities at solid and liquid phase (C_{ps}, C_{pl}). The instrument has been calibrated by the manufacturer and these settings has been used during the tests. The PCM samples have been prepared according to the manufacturer procedures. 10mg weighting samples were prepared for each type of PCMs. The samples have been manually weighed using a scale of readability of 0.001mg. Standard aluminium crucibles provided by the manufacturer have been filled with the PCMs sample. The selected

crucibles are of less than 0.01mg so that the error in the aluminium weight is minimized [254]. The lids were perforated to avoid the building of vapour pressure during the test. The crucible and the lid were then cold welded using a manual sealing press.

Two samples were tested for each type of PCM in order to ensure accuracy and repeatability in the results as the sample was arbitrarily selected from the bulk. In order to run the measurements on the samples, the following procedure was adopted:

(i) Baseline run: two empty crucibles of the same mass are placed in the instrument, out of which one was the reference crucible.

(ii) Calibration run: the reference empty crucible with the Sapphire disc are placed for testing. The sapphire is a standard material of known specific heat and mass. The smallest Sapphire disc (Ø = 0.00025 m) supplied with the instrument with the mass of 12.707±0.005 mg was selected for the standard run.

(iii) Sample run: in which the reference empty crucible and another crucible with PCM sample is tested. The PCM analysis cycle has been started at 0°C and kept it at this temperature for 5 minutes to allow temperature uniformity in the sample. Then, the temperature is raised to 75°C. Different heating rate has been used of 2K/min, 5K/min and 10K/min to figure out its effect. After that, the sample is kept at this temperature for 5 minutes. Finally, the sample has been cooled to 0°C at the same rate.

The DSC analysis of the PCMs are used to obtain the melting temperature, melting temperature range, specific heat capacity at solid and liquid phases and latent heat. The obtained thermos-physical properties for the different PCMs are summarized in Table 7. It is noted that, all the properties are affected by the heating rate where the melting temperature varies slightly with the heating rate as in RT27 and RT31. The difference between the supplied properties in the manufacturer data sheet and the obtained results can be refereed partly on the selection of the heating rate.

The specify heat variation with temperature for different heating rate for the different PCMs are presented in Figure 25 to Figure 30. It is noticed that the

distribution of the heat capacity of the PCMs depend on the heating rate. So, the faster the PCM is heated up, the more the curve is flattened and shifted. The specific heat measurements for RT27, RT28HC, RT35, RT42 and RT47 are shown in the figures from 25 to 30.

Table 7. Melting temperature of PCMs

PCMs	Heating rate (K/min)	Melting temperature (°C)	Temperature melting range	Specific heat at solid (J/g.K)	Latent heat(J/g)	Specific heat at liquid (J/g.K)
RT27	2	26.5	23-27.9	2.845	126.7	1.958
	5	27.3	13.4-29.9	2.134	127	1.504
	10	28.7	13.4-34.6	2.840	127.7	1.981
RT28HC	2	29.8	21.3-32.5	1.942	227.4	2.295
	5	31.9	21.3-35.9	1.977	224.6	2.373
	10	34.7	23.2-42.6	1.949	222.8	2.522
RT31	2	28.5	30.9-12	3.186	119.6	2.083
	5	29.9	8-33.5	3.542	119.7	2.320
	10	30.6	8-36.6	3.327	121.5	2.204
RT35	2	35.7	22.6-51.6	3.862	146.5	2.472
	5	38.1	22.8-45.7	2.388	120	1.883
	10	42.7	27.1-55.1	3.311	111.2	2.201
RT42	2	42.4	32-45.2	3.695	152.9	2.644
	5	43.8	32-49.2	3.475	153.2	2.618
	10	46.1	33.2-55.7	3.578	153.4	2.632
RT47	2	47.0	52.3-35	3.981	153.3	2.820
	5	49.7	36-56.8	2.322	130	1.817
	10	53.4	37.5-66.5	3.377	115.9	2.395

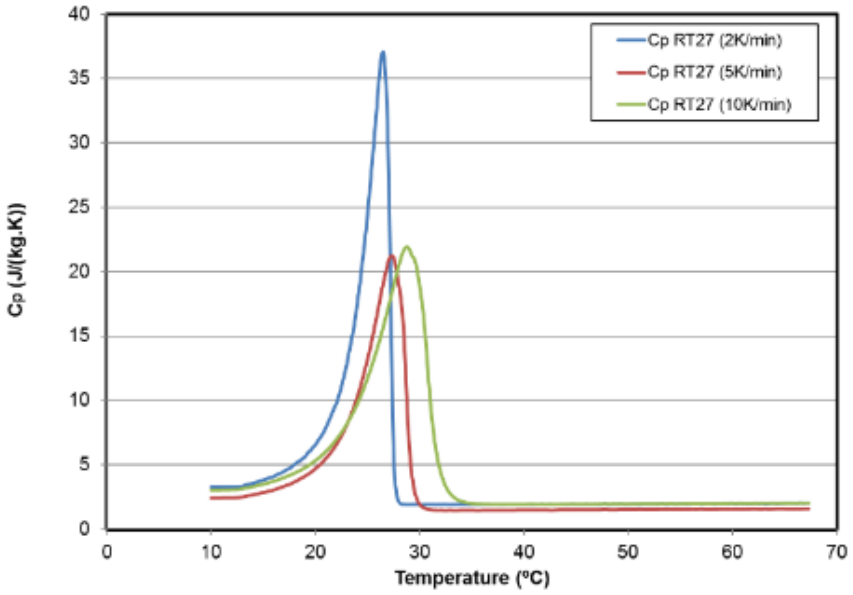

Figure 25. Specific heat measurement versus temperature for RT27 at different heating rates.

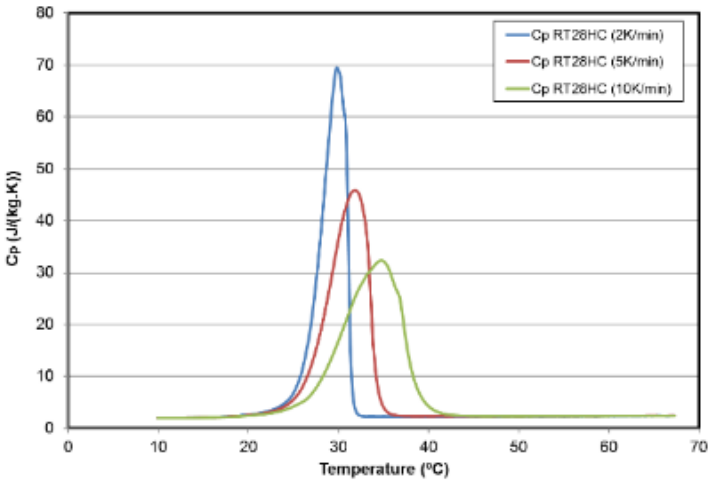

Figure 26. Specific heat measurement versus temperature for RT28HC at different heating rates.

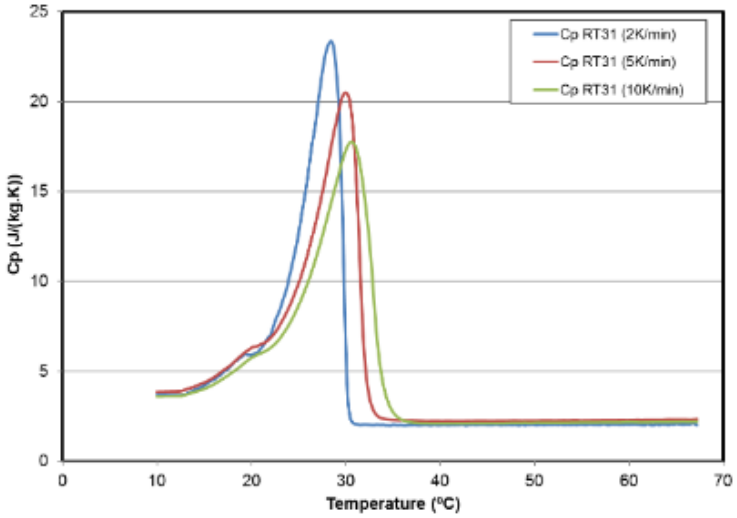

Figure 27. Specific heat measurement versus temperature for RT31 at different heating rates.

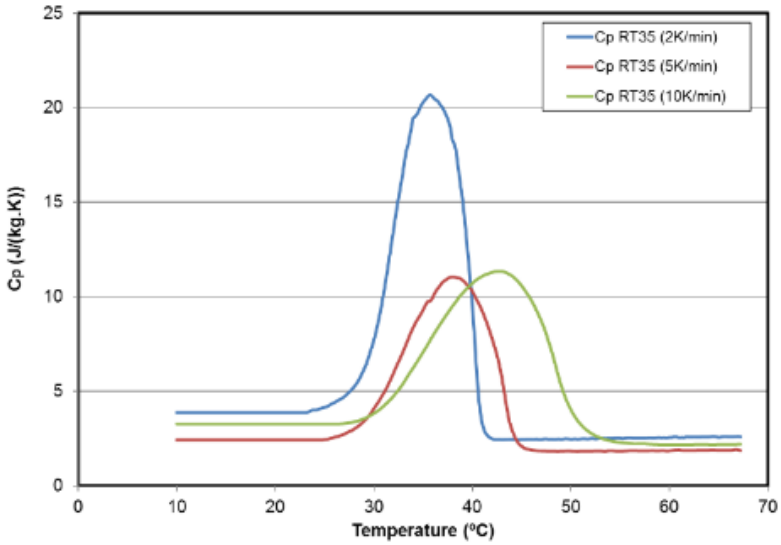

Figure 28. Specific heat measurement versus temperature for RT35 at different heating rates.

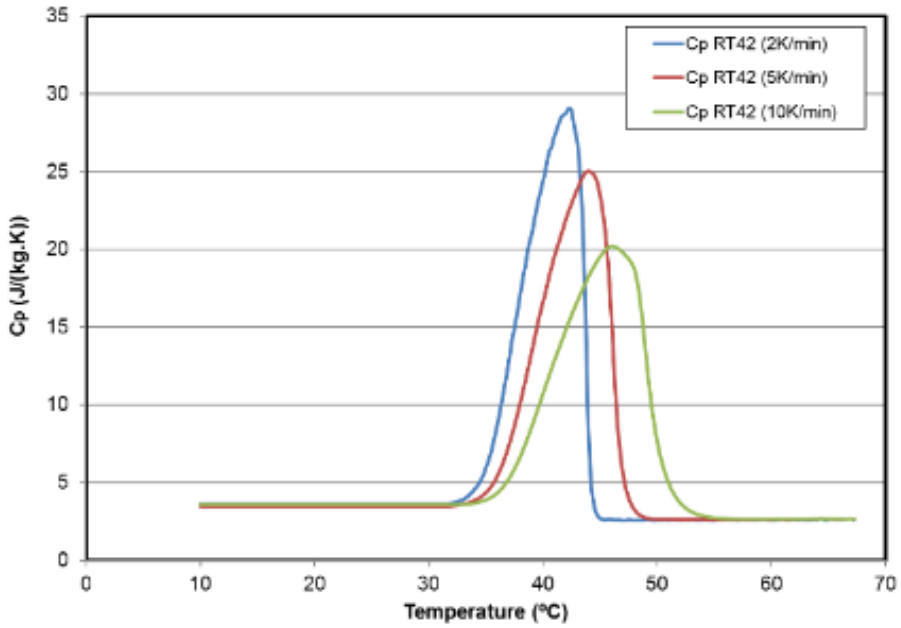

Figure 29. Specific heat measurement versus temperature for RT42 at different heating rates.

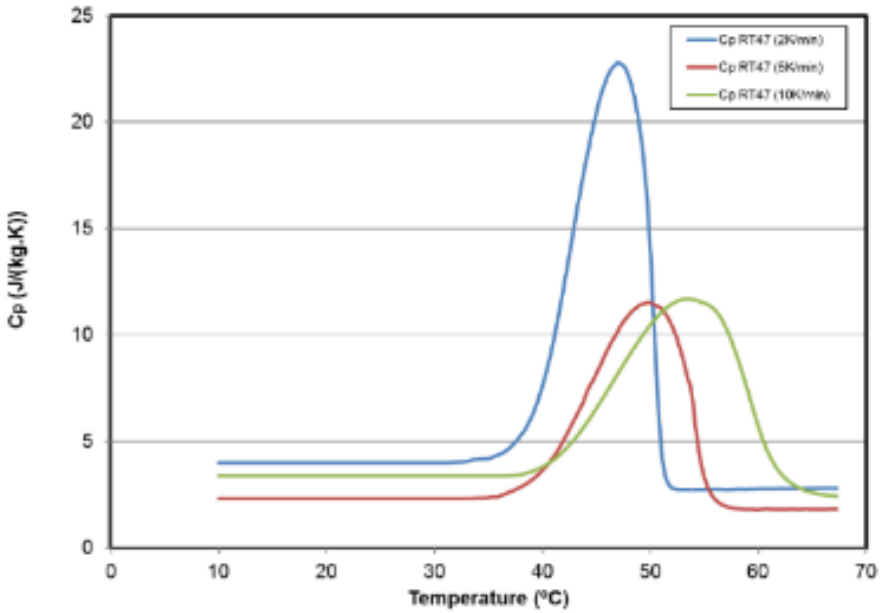

Figure 30. Specific heat measurement versus temperature for RT47 at different heating rates.

3.4 Error and uncertainty analysis

The measurements taken into this research on the experimental work for the HCPV-MLM heat sinks and the PCM storage were temperature, fluid volume flow rate, pressure, solar irradiance, voltage and current. Temperature is one of the important measuring parameters in this research. All the used thermocouples were of wired K-type. As pointed out in section 3.1.13, the different structure of thermocouples used were the wired or prop type according to the location. The

thermocouple prop types were used to measure the temperature of fluid flowing inside the tubes, the inlet and outlet temperature at the test section. This type of thermocouples was brand new and have been purchased ready to use from a well-recognized manufacturer/supply. Therefore, the tip of the thermocouple is the place of taking measurements and this is ensured to be in full contact with the fluid. Because for the large number of thermocouples required for the research experiments, a roll of thermocouple was purchased and cut according to the desired length. The tips of the thermocouples were made on our own using thermocouple welder using the L60 thermocouple welder.

Three important factors affect the measurements accuracy during making the tips of thermocouples; the tip length, perfect connection and free of any oxide particles. Therefore, the tips were made as shortest as possible. Visual inspection using an eye magnifier has been used to check the tips perfection and if free from any oxide particles. A voltmeter has been used to check the connection of the thermocouples. The thermocouples and the data acquisition system were calibrated using two points of temperatures; boiling water and liquid-ice water mixture against a precision mercury thermometer to an uncertainty of ±0.1°C.

The calibrated props type thermocouples for the inline fluid flow temperature measurements in the HTF inlet & outlet temperature in the heat sink and the PCM storage system, middle micro-channel temperature) allowed to be fixed in its locations permanently at the time of the all experiments. Combining these effects gives an uncertainty of ±0.2°C.

The uncertainty of measuring the PCM inside the storage is expected to be very low due to the full immersion of the thermocouples inside of the PCM and the permanent location of the thermocouples using a rod supported at the in the HTF tube. The uncertainty of measuring the temperatures across the CPV surface was reduced by reducing the exposed tips surface to the ambient and by increasing the contact between the round tip of the thermocouples and the flat surface. This is done by using a thermal compound paste between the surface and the tips.

The solar cell temperature measurement was another important parameter in this research. The thermocouple of measuring the solar cell was encapsulated by Sylgard 184. The sylgard is characterized of a very low thermal conductivity of

0.2 W/m. K (Table 3). This acts as an insulator to the thermocouple and the solar cell temperature measurements had a low uncertainty.

The power dissipation by the ERH is determined from the product of the voltage and current measured at the electrical terminals. The measured voltage and current ranged between 8 and 21.5 volts and current of ranged between 570 and 1450mA, respectively. Uncertainties for direct voltage measurement are negligible due to the low voltage drop between the measured terminals. In this experiment, voltage input for the heaters were measured across the ERH and the current meter with 0.1 Ω shunt resistance. For the current settings we have, this will cause 0.1 volts loss in the actual ERH. For a 21.5 volts case, this results in ±0.46% uncertainty in voltage measurement. As per the product manual, the current measurement has uncertainty of ±0.1 % uncertainty. These uncertainties cause a ±0.56% in power input measurement.

The heat lost to the environment in the HCVP-MLM experiment was controlled by reducing the heat lost using thermal insulation at the case and fixing the room temperature during the experiments. The amount of lost heat was measured by the difference between the input power and the heat collected by the HTF. It was found that the measured heat delivered by the HTF agreed within 5% of the input power to the ERH heat transferred to water.

As for flow rate measurement, the glass flowmeter has been calibrated by the manufacturer of accuracy of 2.5% (section 3.1.15). The HTF flow affected by the fluid properties, so the flow rates adjusted using water column and stop watch. Table 8 shows the measurements variation errors between the two methods in which is less than 5% in all cases. In addition, the mass flow rate is recorded for finding the density of water.

Table 8. HTF volume and mass flow rates.

Volume flow rate using flowmeter ml/min	Volume flow rate using water column ml/min	Variation %	Mass flow rate g/min
30	29	3	29.99
40	39	2.5	40.00
50	48	4	46.31
60	58	3.33	56.90

For each microchannel plate, the channel dimensions were measured at 20 locations across the using microscope. The calibration uncertainty due to the microscope is estimated to be ±0.5μm and the data scattering is around ±3%.

3.5 Conclusions

Identifying the instruments and characteristics of the materials outputs is crucial for the design and testing stage and later on the operation stage. In the light of this different materials, instruments and software used in this research for both the numerical and experimental part have been presented in this chapter.

For the experimental part of the HCPV-MLM heat sink experiments, the solar cells and the CPV assemblies were purchased from Azurspace. The used solar cell size is 1cm² of a peak efficiency of 42.2% at 500x concentration. A solar simulator was used for the indoor characterization of the solar cell assembly.

The properties of the two types of materials used to manufacture the homogeniser (crystal resin and glass) has been reported. The spectrometer is an important instrument and will be used later to measure the transmissivity and the reflectivity of the different optical parts of the CPV, such as the reflectors and homogeniser.

In section 3.3, the chapter reports the methodology followed for the characterization of the PCM used in this research using the DSC machine. Various ranges of PCM had been investigated to identify their thermos-physical properties such as the melting temperature, specific heat capacities and latent heat of fusion for both phases. These properties are very important in understanding the behaviour of the PCM and in the modelling section later in Chapter 5. In addition, this chapter reports the error and uncertainties of the different instruments in measuring the parameters of temperature, HTF flow rates, the current and the voltage.

The next chapter of this thesis reports the thermal management of the CPV receivers under high concentration. This includes the numerical study for the design purpose, fabrication, indoor and outdoor experimental characterization.

Chapter 4 : Thermal management of HCPV receivers using a multi-layered microchannel heat sink: design, fabrication and experimental characterization

This chapter presents a detailed electrical and thermal analysis of a high concentration photovoltaic (HCPV) system attached to a multi-layered microchannel (MLM) heat sink. Both numerical and experimental approaches have been used in this analysis. This is the first experimental work conducted for the thermal regulation of a HCPV system using the MLM heat sink technique.

4.1 Introduction

The analysis of the HCPV-MLM system is carried out by understanding the thermal behaviour of each component individually. This is by presenting the analytical correlations of the HCPV and MLM systems where the heat flow is represented using the thermal resistance network technique. The HCPV-MLM system is then explored using the numerical analysis to identify the electrical and thermal effects of using MLM on the HCPV module. The numerical analysis is also important for the optimization of design parameters, especially to minimize the maximum temperature and its gradient in the solar cell surface [255]. Then, the behaviour of the MLM heat sink is explored experimentally under the operation of non-uniform heat source. This analysis explores some parameters which normally not offered in the HCPV analysis such as the surface temperature uniformity under a high-power rate. Following this, the performance of the MLM heat sink is examined using a HCPV single solar cell module under the solar simulator for the indoor test at different operation conditions such as HTF flow rates and number of layers. Finally, a real time outdoor experiments is conducted for the system to measure its performance.

4.2 Heat transfer analytical correlations

The purpose of this section is to present the correlations that describe the heat transfer and fluid flow in the HCPV receiver and the MLM heat sink, from the solar cell to the ultimate MLM heat sink.

4.2.1 HCPV

The CPV receiver, illustrated in Figure 31, consists of a solar cell located under a conductive layer made of copper. A ceramic layer placed under the copper layer is used as electrical insulation. Finally, the full arrangement is placed in a second copper layer for thermal conduction purposes. The assembly also consists of two by-pass diodes and two electrical terminals.

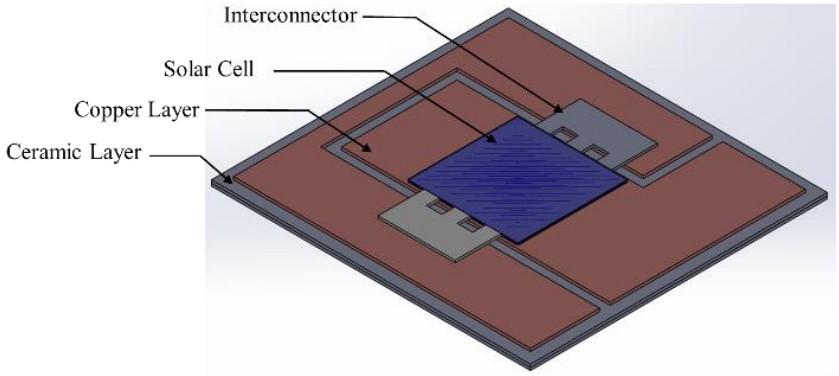

Figure 31. Schematic of typical 3C42 Azurspace CPV receiver.

The solar cell receives the direct irradiance from the sun and converts partially to electricity and the rest into heat. Therefore, the solar cell's electrical efficiency is the ratio between the electrical output power (P_{out}) to the input power (P_{in}), which is defined as

$$\eta_{\mathrm{cell}} = \frac{\mathrm{P_{out}}}{\mathrm{P_{in}}} \tag{4.1}$$

Where $\mathrm{P_{in}}$ can be represented for concentration system as below:

$$\mathrm{P_{in}} = \mathrm{CR.A.G.}\eta_{\mathrm{opt}} \tag{4.2}$$

Where CR is the concentration ratio, G is the direct normal irradiance (DNI) and η_{opt} is the optical efficiency. The electrical output power is the product of the voltage by current. The total current density of the solar cell is the minimum among the three sub-cells. The current density distribution for each sub-cell is a function of temperature and given by [256]:

$$\mathrm{J_{SC,i}(T)} = \int_{\lambda_{\mathrm{i,min}}}^{\lambda_{\mathrm{i,max}}} \frac{\mathrm{q.\lambda.EQE_i(\lambda,T_c).CR.G(\lambda).\eta_{opt}(\lambda)}}{\mathrm{h.c}}.\mathrm{d\lambda}, \tag{4.3}$$

Where, λ is the wavelength of the incident photons, $\lambda_{\mathrm{i,min}}$ and $\lambda_{\mathrm{i,max}}$ correspond to the minimum and maximum wavelength for each sub-cell, respectively. $\mathrm{EQE_i}$ is the External Quantum Efficiency, h is Planck's constant and c is the speed of light in the vacuum.

The total voltage of the solar cell is the sum of the voltage in each sub-cell and can be found by [257]:

$$V = \frac{k_B.T_c}{q}\left[\sum_{i=1}^{3} n_i \ \ln\left(\frac{J_{SC,i}(T_c)-J}{J_{o,i}(T_c)}+1\right)\right] - J.A.R_s \qquad 4.4$$

Where k_B is Boltzmann constant, T_c is solar cell's temperature, A is the solar cell's area and R_s is the series resistance.

The heat (q_{heat}) produced by the solar cell is obtained by:

$$q_{heat} = P_{in}.(1-\eta_{cell}) \qquad 4.5$$

The change in the surface area of the solar cell and the substrate develops a heat flow restriction which is known as constriction effect. The constriction resistance is caused by the area change between the heat source and the substrate. Figure 32 (a) shows the "constriction effect" where the heat flow diverges in the region next to the heat sink (substrate) when the heat source surface area is smaller than the substrate. However, the heat flow converges in the region next to the heat source (substrate) in the case of the heat source surface area is larger than the substrate area as shown in Figure 32 (b). In addition, some heat is conducted laterally from the heat source [121].

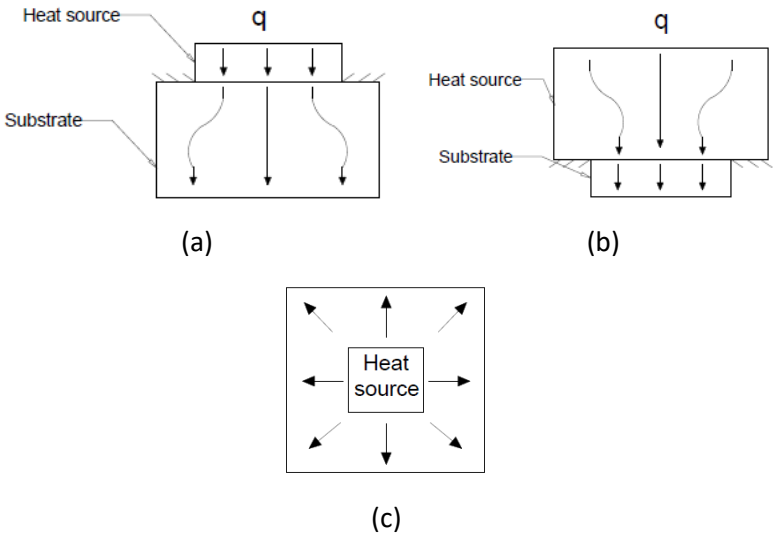

Figure 32. The constriction effect between a heat source and a substrate.

The thermal resistance network for the CPV receiver is illustrated in Figure 33. Spreading and constriction resistances are incorporated into the network and the heat flow is assumed to be from the top to the bottom and the heat transferred to the ambient using the natural convection effect is neglected in this analysis.

However, in later stages in the numerical analysis, the effect of the natural convection is considered. In this figure, Rsub1 is the equivalent thermal resistance for the resisters from R1 to R6 and it is represented by:

$$\frac{1}{\text{Rsub1}} = \frac{1}{\text{R1}} + \frac{1}{\text{R2+R3+R4+R5}} + \frac{1}{\text{R6}} \quad 4.6$$

Rsub2 is the equivalent thermal resistance for R7 and R8 and expressed as:

$$\frac{1}{\text{Rsub2}} = \frac{1}{\text{R7}} + \frac{1}{\text{R8}} \quad 4.7$$

And the total thermal resistance (Rtot) is given by:

$$\text{Rtot} = \text{Rsub1} + \text{Rsub2} + \text{R9} + \text{R10} \quad 4.8$$

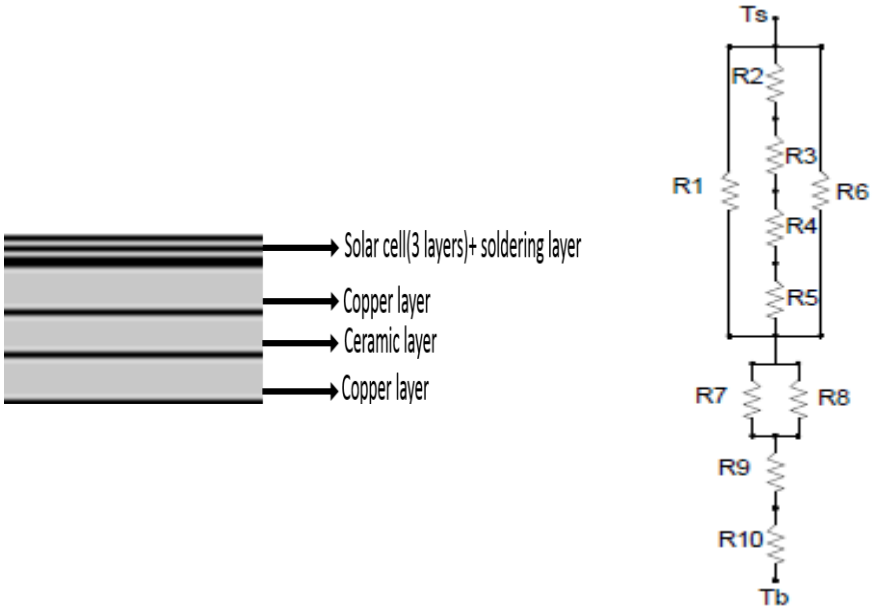

(a) (b)

Figure 33. Schematic of the CPV receivor (a) cross section and (b) thermal resistance network.

The changes of the surface area in the system occur at the bottom of the solar cell immediately where the soldering layer spreads the heat to the first copper layer and the other surface change is between the interconnectors and the first copper layers. Therefore, the total resistance in those two areas are the sum of the conduction resistance and the spreading resistance for the expanded area and the thermal resistance of each component is as the following:

$$\text{R1} = \text{R}_{\text{cond}} + \text{R}_{\text{spread}} \quad 4.9$$

$$\text{R2} = \text{R3} = \text{R4} = \text{R}_{\text{cond}} \quad 4.10$$

$$\text{R5} = \text{R6} = \text{R7} = \text{R}_{\text{cond}} + \text{R}_{\text{spread}} \quad 4.11$$

$$R9 = R_{cond} \quad 4.12$$

4.2.2 MLM heat sink

A schematic of the MLM heat sink is shown in Figure 34 showing the dimension representation. Spreading and constriction resistances have been derived by Phillips [121] and incorporated in this model. Also, The thermal resistance network of the MLM heat sink under a uniform heat source is presented by Wei and Joshi [142].

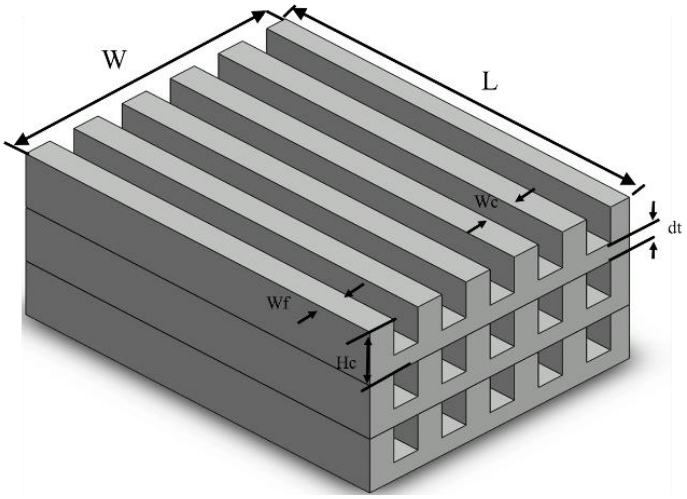

Figure 34. Three-dimensional MLM heat sink: spacing (W_c), fins height (H_c), thickness (W_f), length (L), base width (W), base thickness (t_b).

Despite the number of layers of the MLM heat sink, four different types of thermal resistances exist in the MLM heat sink system; conduction, fins convection, constriction, spread and bulk due to the temperature increase in the fluid and they are defined as in the following equations:

$$R_{cond} = \frac{t}{K\,W\,L} \quad 4.13$$

$$R_{cont} = \frac{\ln\left[1 \Big/ \sin\left(\frac{\pi}{2}\frac{1}{1+W_c/W_f}\right)\right]}{K\,W\,L} \quad 4.14$$

$$R_{spread} = \frac{\ln\left[1 \Big/ \sin\left(\frac{\pi}{2}\frac{1}{1+W_c/W_f}\right)\right]}{K\,W\,L} \quad 4.15$$

$$R_{conv,fin} = \frac{1}{h.n.L.W_c + 2.h.\eta_f.n.L.H_c} \quad 4.16$$

$$R_{conv,c} = \frac{1}{h.n.L.W_c} \quad 4.17$$

$$R_{bulk} = \frac{1}{\rho.C_p.v_m.n.H_c.W_c} \quad 4.18$$

The thermal resistance network is illustrated in Figure 35. The R_1 resistance considers the heat transfer due to materials conduction and constriction. Then, part of the heat is transferred by the fluid and this is considered by R_{12} i.e. forced convection. The other part of the heat is transferred to the next layer using R_2 which considers the conduction heat transfer. A similar process occurs on the other layers where:

$$R_1 = R_{cond} + R_{cont}$$

$$R_2 = R_{cond}$$

$$R_3 = R_{cond} + R_{cont} + R_{spread}$$

$$R_4 = R_{cond}$$

$$R_5 = R_{cond} + R_{cont} + R_{spread}$$

$$R_6 = R_{conv,ch}$$

$$R_7 = R_{conv,fin}$$

$$R_8 = R_{conv,ch}$$

$$R_9 = R_{conv,fin}$$

$$R_{10} = R_{conv,ch}$$

$$R_{11} = R_{bulk}$$

$$R_{12} = R_{bulk}$$

$$R_{13} = R_{bulk}$$

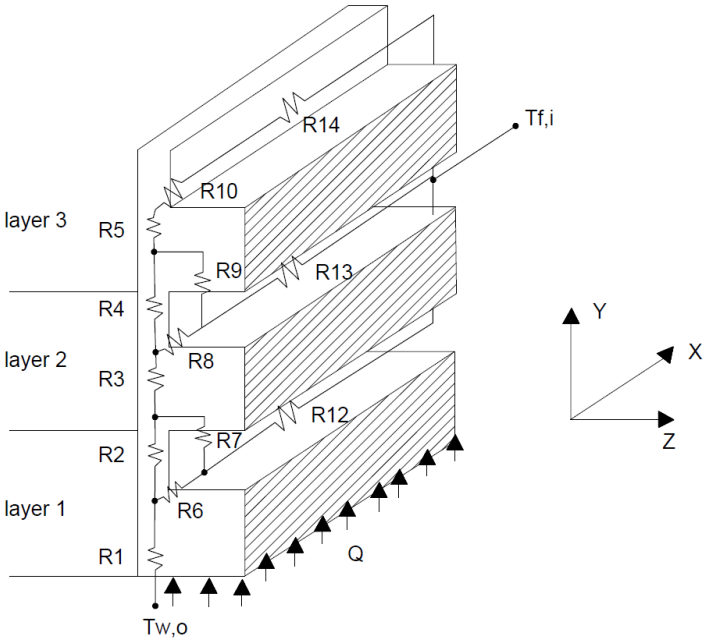

Figure 35. Thermal resistance network for 3-layers MLM heat sink.

For a uniform heat source on a microchannel heat sink with fully developed laminar flow, the microchannel outlet temperature ($T_{ch,out}$) is a function of the outlet HTF temperature ($T_{f,out}$) and is defined follows:

$$T_{ch,out} = T_{f,out} + \frac{q''_{eff}(W_c+f)}{h.(W_c+2.\eta.H_c)} \quad 4.19$$

Where, q_{eff} is the fluid effective heat and expressed by:

$$q''_{eff} = \frac{P_w}{N.A_w} \quad 4.20$$

Where, P_w is the heat produced by the solar cell, N is the number of the channels and A_w is the channel area: $A_w = (2H_{ch} + W_{ch})L$. The HTF outlet temperature is obtained by:

$$P_{f,out} = \frac{P_w}{N.A_{eff}} \quad 4.21$$

$$T_{f,out} = T_{f,in} + \frac{q''_{eff}W.L}{\rho_f.Q_t.C_p.f} \quad 4.22$$

The thermal performance of the heat sink depends on the fluid flow characteristics and its velocity. The Reynolds number (Re) is used to characterize the flow inside the microchannel and is calculated by:

$$Re = \frac{\rho D_h V_{avg}}{\mu} \quad 4.23$$

Where ρ and μ are the density and viscosity of the fluid, respectively. They are evaluated at the mean fluid temperature [146]. V_{avg} is the average velocity of the fluid at each channel and is calculated by:

$$V_{avg} = \frac{\dot{V}}{N_c A_c} \quad 4.24$$

Where, $\dot{V}$ is the fluid volume flow rate at the manifold, N_c is the total number of channels in the heat sink, and A_c is the channel cross-sectional area. The fluid flow is considered to change from laminar to turbulent flow at Re=2300.The fluid flow development determines the thermal performance of the HTF. Generally, the heat transfer rate increases as the fluid flow rate increases. However, increasing the fluid velocity leads to an increase in the pressure drop and hence the power required to pump the HTF. The HTF pressure drop ΔP inside a rectangular channel is expressed by

$$\Delta P = 4 f_{app} \left(\frac{L}{D_h}\right)\left(\frac{\rho {V_{avg}}^2}{2\, g_c}\right) \quad 4.25$$

Where f_{app} is the apparent friction factor, L is the channel length and g_c is constant. The apparent turbulent friction factor [258] can be expressed as

$$f_{app} = A\,(Re^*)^B \quad 4.26$$

Where

$$A = 0.0929 + \frac{1.01612}{L/D_h} \quad , \quad B = -0.680 - \frac{0.31930}{L/D_h}$$

$Re^*$is called the laminar equivalent diameter of a rectangular channel and it is represented using:

$$Re^* = \left[\left(2/3\right) + \left(11/24\ \alpha\right) x \left(2 - 1/\alpha\right)\right] D_h \quad 4.27$$

Where, $(\alpha = b/W_c)$.

The heat transfer rate per unit area $(q")$ from the channel walls to the HTF is found by:

$$q" = h\Delta T \quad 4.28$$

Where h is the heat transfer coefficient and ΔT is the temperature difference between the channel wall and the HTF.

4.3 CPV-MLM numerical analysis

In this section, a numerical analysis of an MLM heat sink cooling system attached to a high concentration single solar CPV receiver has been carried out. The analysis includes various MLM heat sink configurations to determine the most efficient in terms of the solar cell temperature and the fluid pumping power. The geometry of the channel has also been explored.

4.3.1 Model description

The modelled system, illustrated in Figure 36, consists of a CPV multi-junction (MJ) solar cell assembly (AZURSPACE 3C42) attached to an MLM heat sink. The CPV MJ solar cell assembly consists of a solar cell located under a conductive layer made of copper. A ceramic layer placed under the copper layer is used as electrical insulation. Finally, the full arrangement is placed in a second copper layer for thermal conduction purposes. The assembly also consists of two by-pass diodes and two electrical terminals. However, for simplicity, the diodes are not considered in the model. All the CPV assembly dimensions, thickness and materials are listed in Table 9 [122]. The solar cell size is 10mmx10mm and is made of GaInP-GaInAs-Ge. The electrical efficiency of the solar cell under concentration ratio of 500x and standard test conditions (CSTC) is 41.2%.

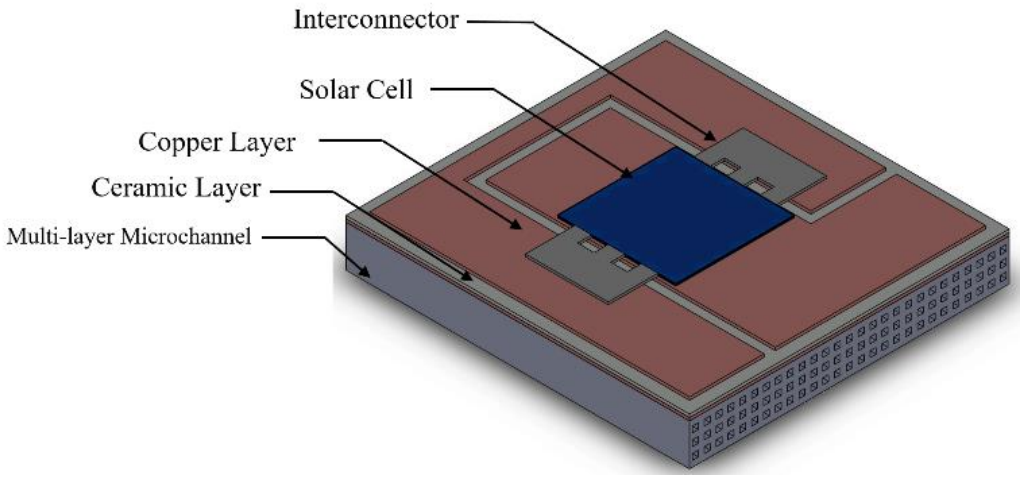

Figure 36. Schematic of a CPV receiver attached to a MLM heat sink.

A typical 3-layers MLM heat sink design is shown in Figure 37. All layers are stacked in an arrangement with parallel fluid flow. The overall heat sink dimension

is 29mm x27mm (LxW). Different heat sinks have been considered in terms of the channel width (W_c), channel height (H_c) and fins width (W_f) as shown in Figure 37 and Table 10. The top plate thickness (t_{b1}), bottom base thickens (t_{b2}) and plate thickness between layers (t_b) are kept the same for all heat sinks to 500µm.

Table 9. The dimensions and material properties of the CPV parts.

Layer	Dimension (mm)	Thickness (mm)	Thermal conductivity W/ (m.K)	Heat Capacity (J/kg.)	Density (kg/m³)
GaInP	10x10	0.066	73	370	4470
GaInAs	10x10	0.067	65	550	5316
Ge	10x10	0.067	60	320	5323
Copper I	27x25	0.250	400	385	8700
Ceramic	29x27	0.320	27	900	3900
Copper II	29x27	0.250	400	385	8700
Aluminium	-	-	160	900	2700
Solder	-	0.125	50	150	9000
Silver	-	0.20	430	235	10490

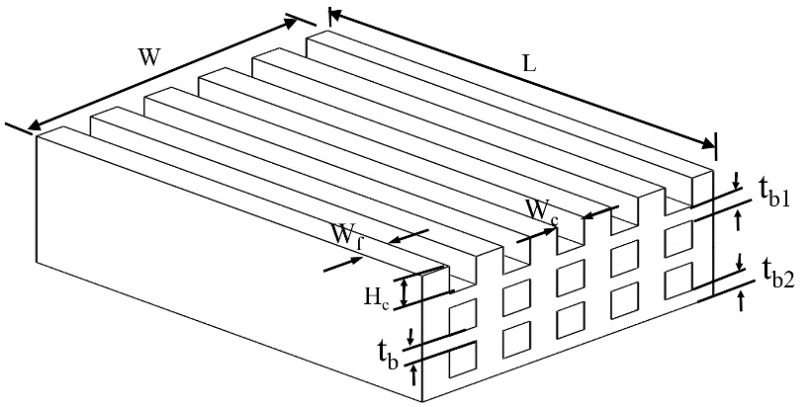

Figure 37. Dimensions of the MLM heat sink showing: spacing (W_c), fins height (H_c), thickness (W_f), length (L), base width (W), base thickness (t_b, t_{b1}, t_{b2}).

Table 10. The varied MLM heat sink dimensions.

Heat sink#	Width of fin W_f (µm)	Width of channel W_c(µm)	Depth of channel H_c(µm)
1	500	500	500
2	700	700	500
3	1000	1000	500
4	500	500	750
5	500	500	1000

The thermal boundary conditions of the studied model are shown Figure 38 and Table 11. Also, the following assumptions have been considered:

- The solar cell is subjected to a uniform solar irradiance of 1000W/m² and concentration ratio of 500x and all heat is produced by the Ge sub-cell [259].
- The ambient temperature is 25°C.
- Water is selected as the coolant fluid and its properties varies with temperature [260,261]. Its inlet temperature is 24°C.
- Water volume flow rate is 120ml/min. The flow is steady, laminar (Re<165) and fully developed in all channels.

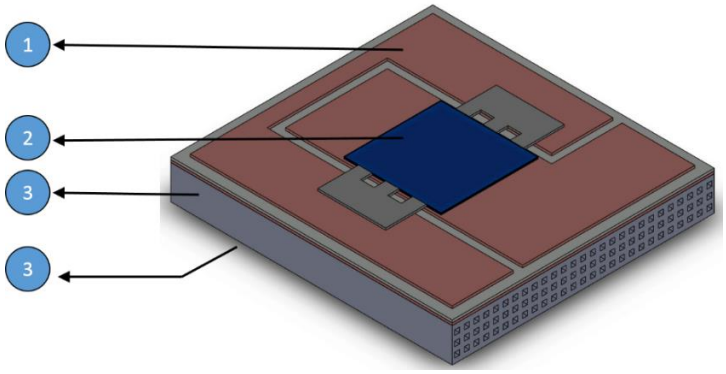

Figure 38. Schematic of the computational domains and boundary conditions.

Table 11. The model thermal boundary conditions.

No	Region	Boundary Condition
1	CPV top surfaces	Natural convection(15W/m²K)
2	Germanium Sub-cell	Heat source (Q_h)
3	Surfaces on bottom and sides of heat sink	Thermally insulated

4.3.2 Mathematical formulation

COMSOL Multi-physics (version 5.2) has been used to build a 3D numerical model using non-isothermal flow [262]. The simulations are conducted in steady state study conditions. Concentrated solar irradiance falls uniformly over the outer solar cell sub-cell. The lower solar cell sub-cell (germanium) is considered as the heat source [259]. The total heat generated by the system per m² (Q_h) can be expressed as:

$$Q_h = (1 - \eta_{elec})Q_o \qquad 4.29$$

Where Q_o indicates the total optical power in Watts at the outlet of the concentrator and η_{elec} is the electrical efficiency of the solar cell. The optical power considers both the concentration ratio and the concentrator efficiency. The solar cell manufacturer has specified the typical solar cell electrical efficiency at

500x versus temperature [250]. The electrical efficiency can be expressed using a linear relation with temperature as the following:

$$\eta_{elec}(T) = -5.09x10^{-4}T + 0.40227 \quad 4.30$$

Where T is the solar cell temperature between 25°C and 80°C, all CPV assembly top surfaces release heat to the environment using natural convection mode and the convection heat transfer rate (q_{conv}) is given by:

$$q_{conv} = h.A.\Delta T \quad 4.31$$

Where h is the convection heat transfer coefficient (W/m²K), A is the exposed surface area (m²) and ΔT is the temperature difference between the top surface and the ambient (K). Also, the heat is transferred to the environment by irradiance and its transfer rate (W) is expressed by:

$$q_{rad} = \varepsilon.\sigma.A.(T_{surf}^4 - T_{amb}^4) \quad 4.32$$

Where ε is the emissivity of the materials, σ is Stefan-Boltzmann constant, A is the radiated surface area, T_{surf} is the surface temperature and T_{amb} is the ambient temperature. However, most of the generated heat is transferred to the lower part of the CPV assembly and then to the heat sink by conduction phenomena. Under the above assumptions, the governing equations for this 3-D conjugated heat transfer problem are as follows [162][163].

Continuity equation for the HTF:

$$\frac{\partial u}{\partial x} + \frac{\partial v}{\partial y} + \frac{\partial w}{\partial z} = 0 \quad 4.33$$

Where u, v and w are the velocity components in the x, y and z directions, respectively.

Momentum equation for the HTF:

$$\rho_f\left(u\frac{\partial u}{\partial x} + v\frac{\partial u}{\partial y} + w\frac{\partial u}{\partial z}\right) = -\frac{\partial p}{\partial x} + \mu_f\left(\frac{\partial^2 u}{\partial x^2} + \frac{\partial^2 u}{\partial y^2} + \frac{\partial^2 u}{\partial z^2}\right) \quad 4.34$$

$$\rho_f\left(u\frac{\partial v}{\partial x} + v\frac{\partial v}{\partial y} + w\frac{\partial v}{\partial z}\right) = -\frac{\partial p}{\partial y} + \mu_f\left(\frac{\partial^2 v}{\partial x^2} + \frac{\partial^2 v}{\partial y^2} + \frac{\partial^2 v}{\partial z^2}\right) \quad 4.35$$

$$\rho_f\left(u\frac{\partial w}{\partial x} + v\frac{\partial w}{\partial y} + w\frac{\partial w}{\partial z}\right) = -\frac{\partial p}{\partial z} + \mu_f\left(\frac{\partial^2 w}{\partial x^2} + \frac{\partial^2 w}{\partial y^2} + \frac{\partial^2 w}{\partial z^2}\right) \quad 4.36$$

Where p is the HTF pressure, ρ_f and u_f are the density and dynamic viscosity of the HTF, respectively, and velocity components in the x, y and z directions, respectively.

The energy equation for the HTF:

$$\rho_f C_{p,f}\left(u\frac{\partial T_f}{\partial x}+v\frac{\partial T_f}{\partial y}+w\frac{\partial T_f}{\partial z}\right)=k_f\left(\frac{\partial^2 w}{\partial x^2}+\frac{\partial^2 T_f}{\partial y^2}+\frac{\partial^2 T_f}{\partial z^2}\right) \quad 4.37$$

Where T_f , $C_{p,f}$ and k_f are the temperature, specific heat and thermal conductivity of the HTF, respectively. The energy equation for the solid domain:

$$0=k_s\left(\frac{\partial^2 T_s}{\partial x^2}+\frac{\partial^2 T_s}{\partial y^2}+\frac{\partial^2 T_s}{\partial z^2}\right) \quad 4.38$$

Where T_s and k_s are the temperature and thermal conductivity of the solid domain. The associated boundary conditions for the governing equations for the channels in all surfaces as follows:

HTF inlet:

$$u_{x=0}=u_{in}, \quad v_{x=0}=0, \quad w_{x=0}=0, \quad T_{x=0}=T_{in} \quad 4.39$$

HTF outlet:

$$p_{x=l_x}=p_{atm} \quad 4.40$$

HTF-solid interface:

$$u=v=w=0, \quad T_f=T_s, \quad T_f=T_s\,, \quad -k_{eff}\frac{\partial T_f}{\partial n}=-k_s\frac{\partial T_s}{\partial n} \quad 4.41$$

The correlations of the HTF density (ρ_f), specific heat $(C_{p,f})$, thermal conductivity (k_f), and dynamic viscosity (u_f), as functions of HTF temperature are described as follows [174] [261]:

$$\rho_f(T_f)=838.46+1.40T_f-3.01x10^{-3}T_f^2+3.71x10^{-7}T_f^3 \quad 4.42$$

$$C_{p,f}(T_f)=12010.14-80.40T_f+30.98x10^{-2}T_f^2-5.38x10^{-4}T_f^3+3.62x10^{-7}T_f^4 \quad 4.43$$

$$k_f(T_f)=-86.90x10^{-2}+8.94x10^{-2}T_f-1.58x10^{-5}T_f^2+7.97x10^{-9}T_f^3 \quad 4.44$$

$$u_f(T_f)=1.37-21.22x10^{-3}\,T_f+1.36x10^{-4}\,T_f^2-4.64x10^{-7}\,T_f^3+8.90x10^{-10}\,T_f^4-9.07x10^{-13}\,T_f^5+3.84x10^{-16}\,T_f^6 \quad 4.45$$

Where, T_f is the temperature in Kelvin (K).

4.3.3 Mesh study

The computational domain was meshed using a free tetrahedral grid system. In order to confirm that the solution is independent on the size of the mesh, the model has been meshed with different sizes. As an example, Figure 39 shows the average and maximum solar cell temperature changes with the number of elements for the two layers MLM heat sink. The number of elements (NoE) has been varied between $0.25x10^6$ and $2.5x10^6$. The maximum and average solar cell temperatures are constant for the NoE between $1.76x10^6$ and $2.5x10^6$. Therefore, the NoE with $1.76x10^6$ has been selected for the 2-layers MLM heat sink.

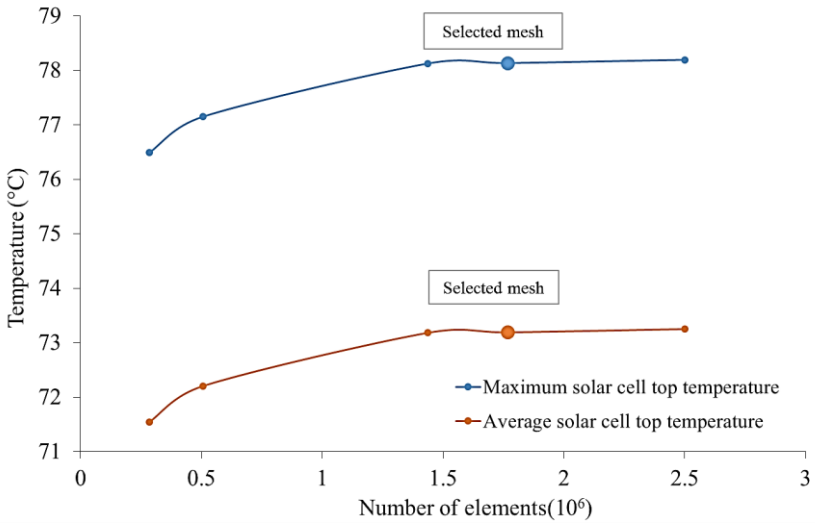

Figure 39. Grid Independence study for 2-layers MLM heat sink with channel cross section of 500x500μm.

4.3.4 Data analysis

As pointed out earlier, the solar cell efficiency decreases with the increase of its temperature. Therefore, a trial and error iteration approach has been used to find the solar cell temperature at the steady state condition, the solar cell temperature being initially assumed equal to the ambient temperature. Equations above are used to find the solar cell efficiency and the generated heat by the solar cell. The model is then solved based on this assumption and a new solar cell temperature is found. The new temperature is used to calculate the electrical efficiency and hence the generated heat and the model is solved again. The process is repeated until the solar cell temperature difference reaches the allowable limit of ≤0.01°C. Figure 40 shows the variations in the average solar cell temperature with iterations for the various number of layer heat sinks for the channel size of

500x500μm. The temperature difference becomes below the limit after the 4th iteration in all cases.

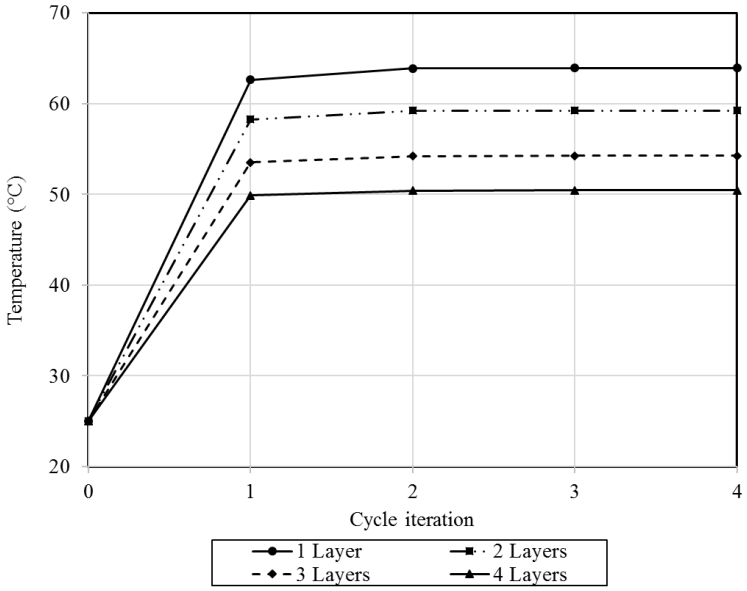

Figure 40. Variation of solar cell average temperature with cycle iteration for 500x500μm channel cross section and 120 ml/min HTF flow rate.

Any water-cooled heat sink performance is usually characterized using two parameters such as thermal resistance and pumping power. The effect of the numbers of layers in the heat sink has been investigated for the same channel cross section (500x500μm) and 120ml/min HTF flow rate. As shown in Figure 41(a), both the heat sink thermal resistance and the solar cell maximum temperature both decrease with the increase of the numbers of layers for the same water mass flow rate. The maximum solar cell temperature was maintained below 69°C for all the heat sink arrangements.

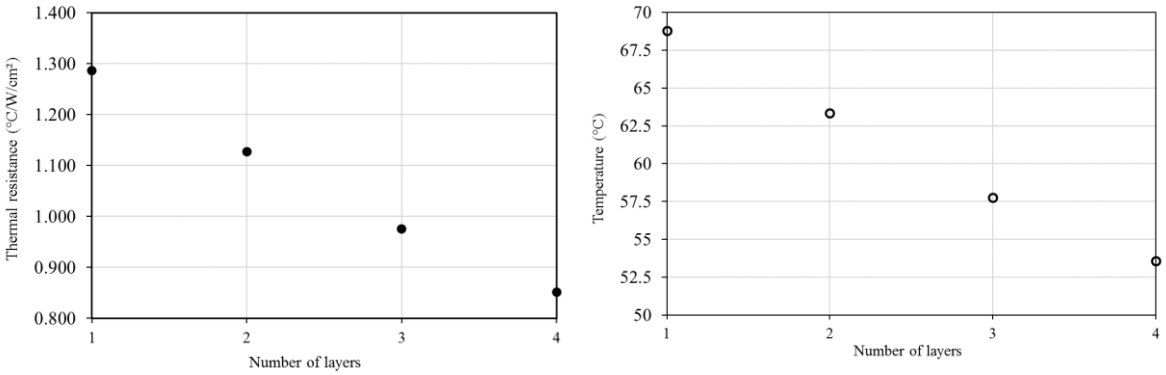

(a) (b)

Figure 41. The MLM heat sink using 500x500μm channel cross section (a) thermal resistance and (b) maximum solar cell temperature

The temperature on the solar cell surface has to be uniform for maximum electrical efficiency. Figure 42 shows the temperature distribution in the solar cell surface for different number of layer heat sinks. It can be observed that the maximum temperature zone in the solar cell surface is located at the outlet fluid side. Also, the increase of the number of layers reduces the temperature non-uniformity of the solar cell by 6°C between the 1-layers and 3-layers arrangement.

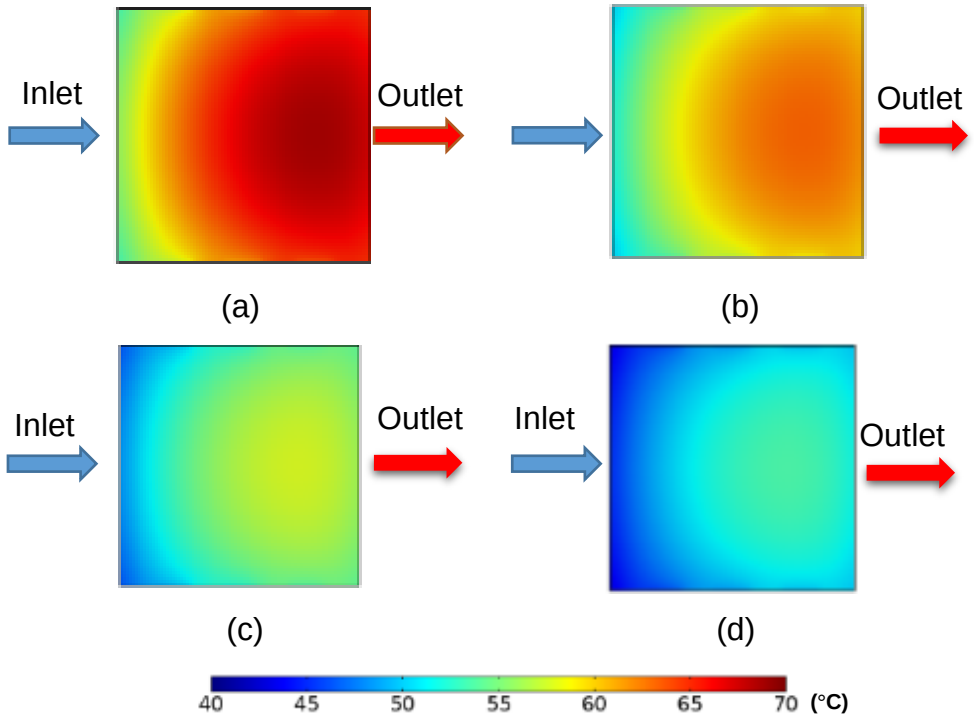

Figure 42. Solar cell surface temperature using MLM heat sink with 500x500μm channel cross section and 120ml/min flow rate for (a) 1-layer, (b) 2-layers, (c) 3-layers and (d) 4-layers.

The increase of the number of layers in the heat sink leads to a lowering in the fluid mass flow rate in each channel and reduces the pressure drop along the channel. Figure 43 (a) shows that the heat sink total pressure drop has been reduced by 50% when using the two-layer MLM heat sink compared to the single layer heat sink pressure drop. However, the pressure drop starts to decrease slightly for the 3-layers and 4-layers heat sinks. In addition, the pumping power has been reduced significantly for the double layer heat sink compared to the single heat sink layer but the change in the pumping power is slightly decreased for the three and four layers compared to double number of layer heat sink.

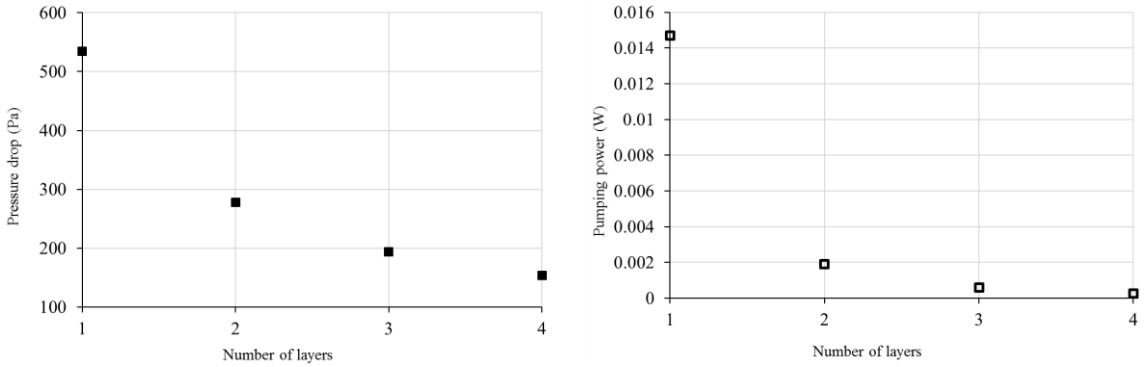

(a) (b)

Figure 43. Effects of the number of layers of MLM heat sink for 500x500µm channel cross section (a) pressure drop and (b) pumping power.

4.3.4.1 Geometry

The aspect ratio value is defined as the ratio between the height of the channel to its width. Three channel heights have been considered: 500µm, 750µm and 1000µm for fixed channel width (500µm) i.e. the aspect ratios are 1, 1.5 and 2 respectively. Hence, the number of channels in each layer remains the same. The effect of variation of the channel height and width on the heat sink thermal resistance and solar cell maximum temperature has been investigated using the 3-Layers MLM heat sink as shown in Figure 44. It shows that increasing the channel height decreases the thermal resistance of the heat sink from 1.092K/W to 1.01K/W for 500µm and 1000µm, respectively. Concurrently, the maximum solar cell temperature decreases by 3°C as the channel height increases by the double.

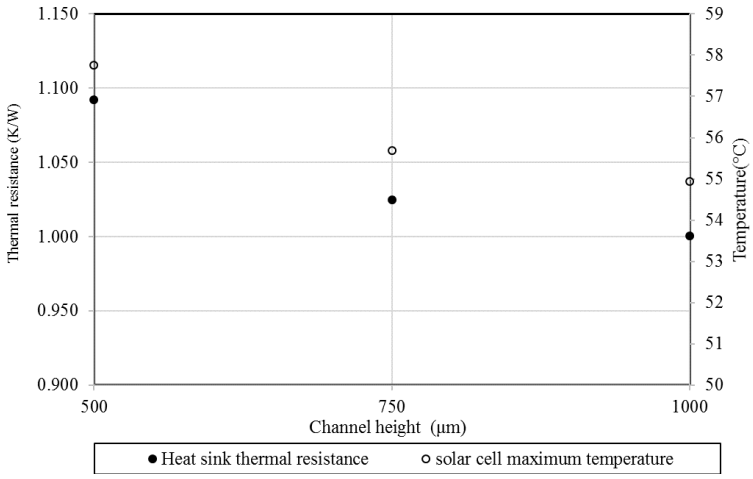

Figure 44. The thermal resistance and solar cell maximum temperature for various MLM heat sink channel heights and 120ml/min HTF flow rate.

The temperature uniformity of the solar cell surface is another measure for a maximum electrical efficiency. Figure 45 shows the temperature distribution in the solar cell surface for different number of layer heat sinks. It can be observed that the maximum temperature zone in the solar cell surface is located at the HTF outlet side. Also, the increase of the number of channel height reduces the temperature non-uniformity of the solar cell by 2°C as the channel height increases from 500 µm to 1000 µm by the double.

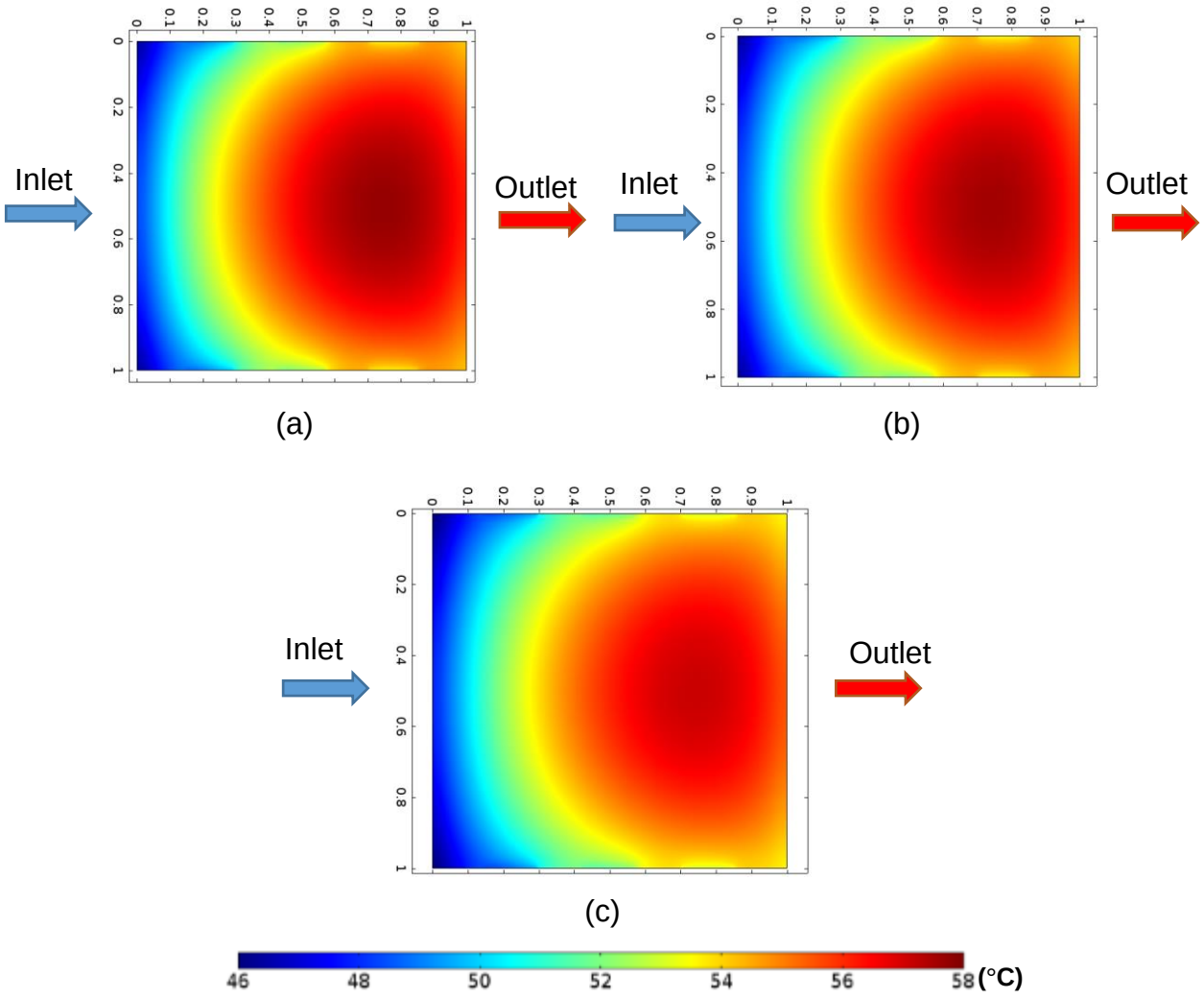

Figure 45. Solar cell surface temperature distribution for the MLM heat sink of 500µm channel width and a channel height of (a) 500µm, (b) 750µm and (c) 1000µm for 120ml/min HTF flow rate.

The pressure drop and the pumping power of the HTF for various channel heights are shown in Figure 46. It noticed that the fluid pressure drop decreases dramatically from around 200 Pa for 500µm microchannel height to just 50 Pa for 1000µm microchannel height. This decrease in the pressure drop leads to a

reduction in the power required for the fluid pumping. This is very important in increasing the overall system efficiency of the CPV-MLM system.

The effect of the channel width has been investigated by considering three channels widths of 500μm, 750μm and 1000μm for a fixed channel height of 500 μm. In this case, the number of channels in each layer increases with the decrease of the channel width. The effect of variation of the channel height and width on the heat sink thermal resistance and solar cell maximum temperature has been investigated using the 3-Layers MLM heat sink as shown in Figure 47. It shows that thermal resistance reduces slightly by 0.02 K/W as the channel width is increased from 500μm to 1000μm. Also, the figure shows that the channel width has a slight effect on reducing the maximum solar cell temperature from 57.76°C to 57.14°C as the channel's widths increased from 500μm to 1000μm, respectively.

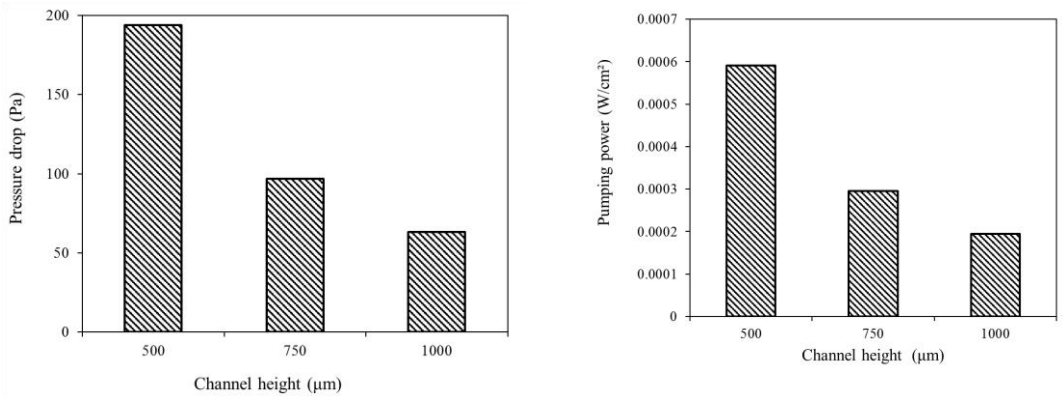

(a) (b)

Figure 46. Effect of the channel height for the MLM heat sink in the (a) Pressure drop and (b) Pumping power for 500μm channel width at HTF flow rate of 120ml/min.

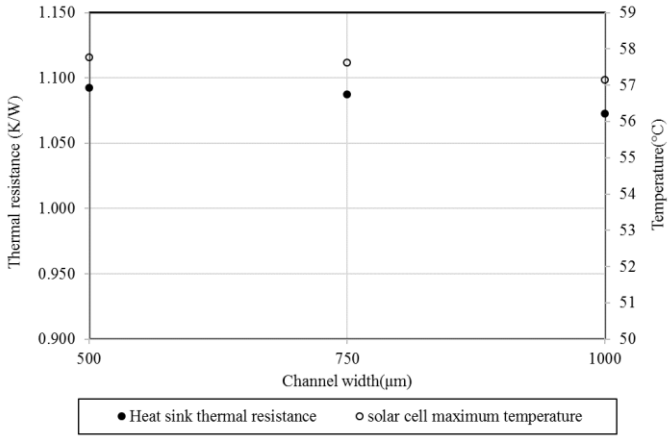

Figure 47. The thermal resistance and solar cell maximum temperature for 500μm channel height and various channels widths for 120ml/min HTF flow rate.

Figure 48 show the pressure drop and the pumping power of the HTF for various channel widths for HTF flow rate of 120ml/min. It can be seen that the pressure drop decreases as the channel width increased. However, the wider channel impact of the pressure drop is less in the channel width compared to the channel height due to the change of the fluid flow characteristics. An interesting observation is that the fluid pumping power increases as the channel width increases although the pressure drop decreases. This could be understood by the fact that the velocity of the fluid at the channel inlet increases as the channel width increases.

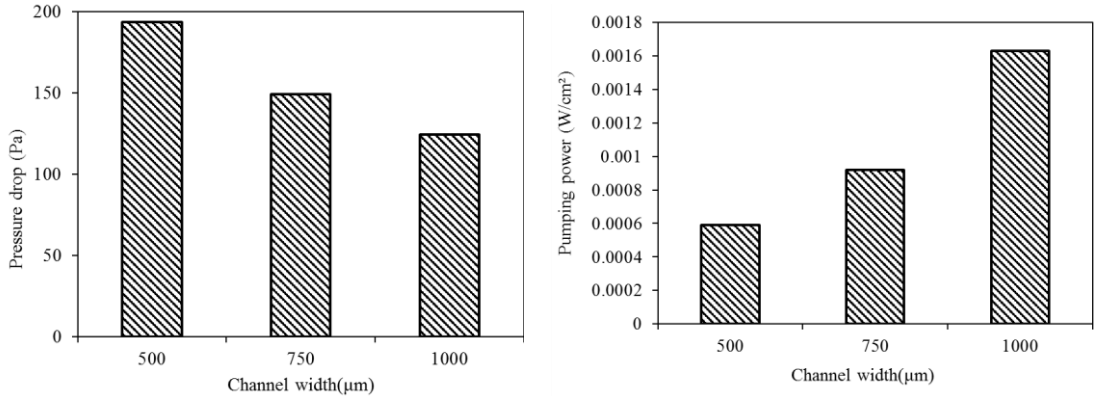

(a) (b)

Figure 48. The effect of the channels width on the pressure drop for the MLM heat sink of channel height of 500μm for 120ml/min HTF flow rate.

4.3.4.2 Materials

The effects of thermal conductivity of the microchannel materials used in the 3-layers MLM heat sink has been studied in the current work. The thermal conductivities studied are 50 W/ (m.K), 283 W/(m.K), 400 W/(m.K) and 160 W/(m.K), corresponding to steel, silicon carbide, copper and aluminium, respectively. As can be seen from Figure 49 that using copper is the most appropriate materials due to its low thermal resistance and the solar cell temperature of 0.488K/W and 41.53°C, respectively. However, a slight difference between the copper and silicon carbide has been noticed in their heat sink thermal resistance and the solar cell temperature. The MLM heat sink of microchannel plates made by steel experience the highest thermal resistance and solar cell temperature.

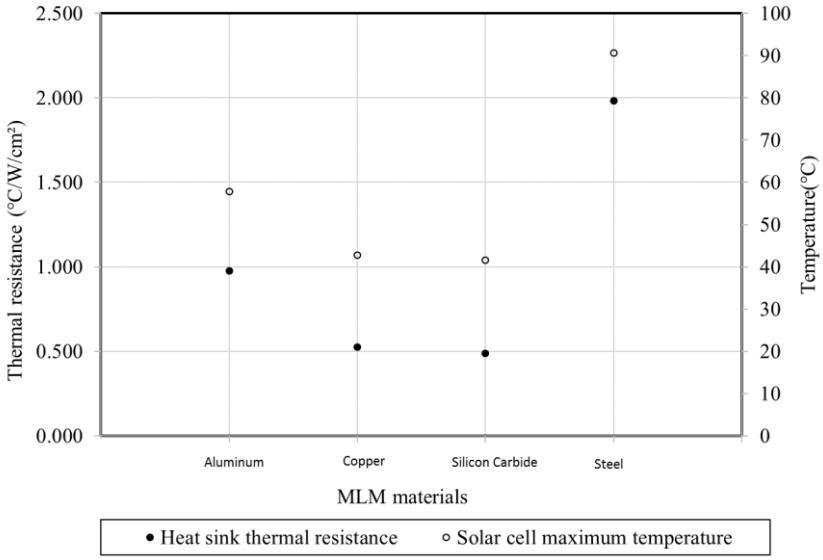

Figure 49. Variation of thermal resistance and solar cell temperature for different materials for 3-layers MLM heat sink for 120ml/min HTF flow rate.

4.4 Experimental work

The numerical analysis showed the ability of the proposed MLM heat sink to regulate the temperature of the CPV system. In this section, an experimental work has been conducted to examine the CPV-MLM system using various working conditions.

4.4.1 Microchannel plate fabrication

Microchannel plate can be fabricated by several methods depending on the channel dimensions and materials. Micro-sawing is used to fabricate rectangular channels in metal or silicon of channels ranges of 0.1-1mm with high or low aspect ratios [120]. Also, the micro-sawing is classified as low cost method in the microchannel fabrication and offers a better surface finish compared to other the manufacturing techniques [120]. In this study, a very precise cutting disk of a thickness similar to the desired channel width has been used. The channel height is controlled by moving the disc up and down. The machine is equipped with a 3 axis digital readout kit for a better cutting accuracy with a resolution from 0.1 μm to 500μm .The machines was operated manually so every channel has been cut individually and after completing the channel cut, the disc is moved to the other channel and so on.

In this study, the microchannel plates have been made from aluminium and its width (W) and length (L) are 32mmx30mm, respectively. The other microchannel dimensions are shown in Figure 50 and Table 12. A microscope scan has been

used to inspect the channels shape to ensure that the sides of the channels are straight and of right angles. As can be seen in Figure 50 (b) the channels vertical walls are properly achieved, and no significant inclination is visible. Moreover, the bottom surfaces of the channels are relatively smooth.

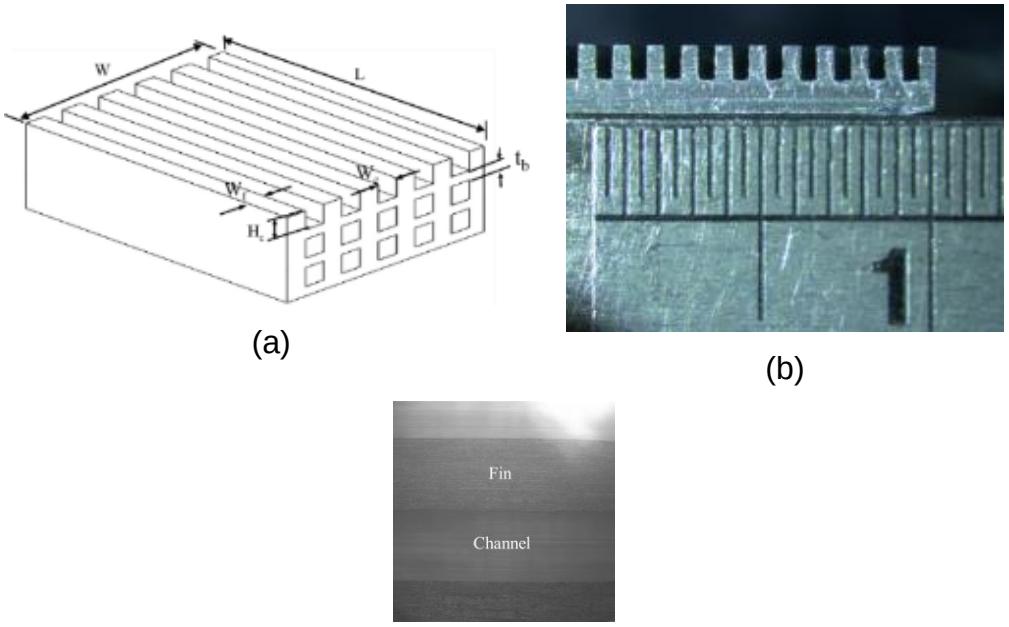

(a) (b)

(c)

Figure 50. Schematic of (a) 3-layers MLM heat sink, (b) Microscopic image of the side of the microchannel plate and (c) surface finish under the microscope.

Table 12. The dimensions of the MLM heat sink microchannel plates.

thickness of fins W_f (μm)	Width of channel W_c(μm)	Height of channels and fins H_c(μm)	Base thickness t_b(μm)
500	500	1000	1000

4.4.2 MLM heat sink test module

The test module, illustrated in Figure 51, is designed to stack the microchannel plates between 1 and 4 layers. The test module case is made of a transparent acrylic and consists of two pieces; top and bottom. Bolts are used to join the case pieces and to stand to any pressure forces. A rubber sealing is place between the top and bottom parts to prevent any fluid leakage during the testing. The HTF inlet and outlet ports are at the sides of the test module case using 8mm diameter copper connectors. The space between the inlet and the MLM entrance are kept for a fully developed HTF flow. The HTF inlet and outlet temperatures are measured using 1mm K type stainless steel thermocouples, which are inserted

just after the inlet and just before the outlet ports; respectively. The pressure drop across the MLM heat sink is captured using two pressure ports using 8mm copper connectors. A 0.5mm K type stainless steel thermocouple has been inserted into the middle channel of the first layer to measure the temperature at this location. The other thermocouples are distributed in according to the experiment type of either using the ERH heat source or CPV and this will be detailed at each section separately.

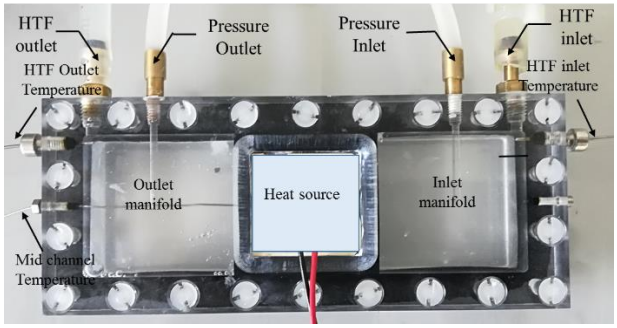

(a)

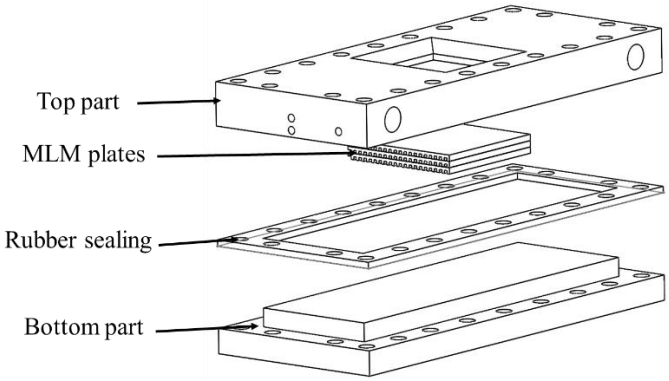

(b)

Figure 51. The MLM heat sink moudle (a) the photograph (top view) and (b) the schematic (isometric view).

4.4.3 HCPV single solar cell module

The HCPV module design used in this study was developed with the help of Dr. Katie Shanks at the University of Exeter [251,263–266]. The module was modified to accommodate the MLM heat sink at the back of the CPV receiver for the thermal regulation purpose. Therefore, this section will present a brief theoretical description of the main design parameters and dimensions for the selected HCPV module. Then, the characteristics of the materials such as

transparency and reflectance are investigated. Finally, the manufacturing process of the module is described.

4.4.3.1 Design concept

The selected HCPV module is a two-stage reflector. The main advantage features of the two-stage reflector is the compressed size and the upward facing receiver [264]. The two-stage reflector uses a cassegrain set up [267]. This system is considered to have lower acceptance angles than the Fresnel lens system but can reach higher concentration ratios. The system as proposed by Shanks et al. [264] consists of primary reflector, secondary reflector, homogeniser, solar cell assembly and a heat sink as shown in Figure 52. In the cassegrain setup, the light rays from the sun are firstly received by the primary reflector and then concentrated to the secondary reflector. Then, the concentrated rays are reflected to the homogeniser and finally to the solar cell.

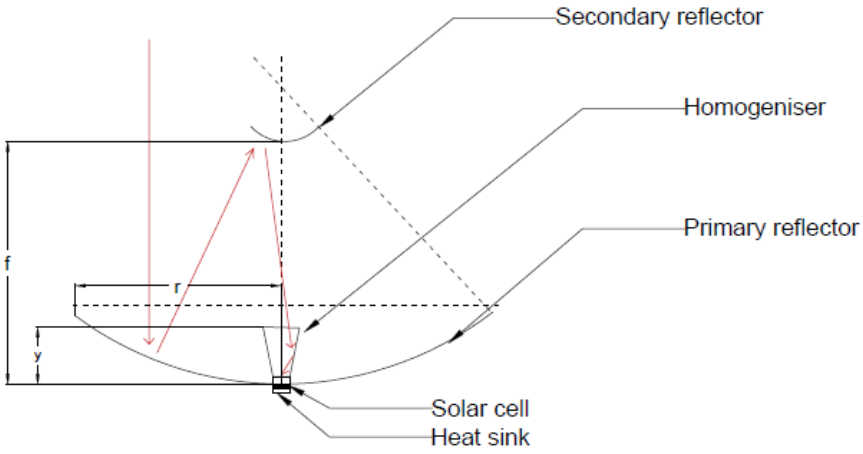

Figure 52. Cassegrain concentrator parts and light path.

The aimed geometric concentration ratio for the setup was 529x with a solar cell area of 1cm^2. Therefore, the design of the primary reflector should consider this concentration ratio, the divergence of the sun rays (approximately ±0.27°), and the shading caused by the secondary reflector. The secondary reflector allows the height of the module to be shortened and the receiver to be upward facing with cooling management at the back of the module. The use of homogeniser is to improve the irradiance uniformity on the solar cell surface. So, the homogeniser has been proposed as square pyramid shape made of solid transparent materials.

The primary reflector geometry is defined using the focal point, f, radius, r and depth, y of a parabola and are related using the following:

$$r^2 = 4fy \quad 4.46$$

The primary and secondary reflectors have been selected with square cuts [264]. The primary width is hence 230mm although the full uncut diameter (2r) is 325.27mm and the depth (y) is 31.64mm. The secondary reflector has been chosen of width 50mm. The pyramid homogeniser has a height of 75mm, input width of 30mm and an output width of 10mm.

The optical efficiency of the module depends on the optical properties of the cover glass, the primary reflector, the secondary reflector, and the homogeniser. This is controlled by the materials used in the manufacturing and their degradation with time. This is easily found using transparency and reflectance measurements as investigated in section 4.4.3.2.

The tracking error is also a source of optical loss for the concentrating system. In this setup the tracking error for ±1° is estimated to have an optical efficiency ranged between 84.82-81.89%. An increased tracking error of 1.5° causes an estimated optical efficiency drop to 55.49%. A possible source of error due to module dimensions could also affect the optical efficiency. This includes the perfect alignment between the solar cell and the homogeniser exit aperture. A 0.1mm alignment tolerance produces a maximum optical efficiency of 84.82%.

4.4.3.2 Materials characteristics

The materials used to build the module have been characterized in this study. This includes the transparency of both the cover glass and the homogeniser, reflectance of the primary and the secondary reflectors. The low iron glass cover transmittance has been measured of approximately 90% in the wavelength ranged between 400-1500nm as shown in Figure 53. In this module, the selected material of the primary reflector is plastic due to its light weight compared to the metallic ones. Also, the plastic can be shaped accurately using CNC machining and achieve a higher degree of smoothness after post-polishing processes. This material is recommended to a maximum working temperature of 60°C. However, due to the expected high temperature on the secondary reflectors which receive concentrated light, a plastic secondary would not be able to sustain the high

temperatures. So, aluminium has been selected as the best to use for this application. The reflectance percentage of the primary and secondary are shown in Figure 53. The figure shows a higher reflectance percentage of the primary reflector of more than 90% compared to the secondary reflector.

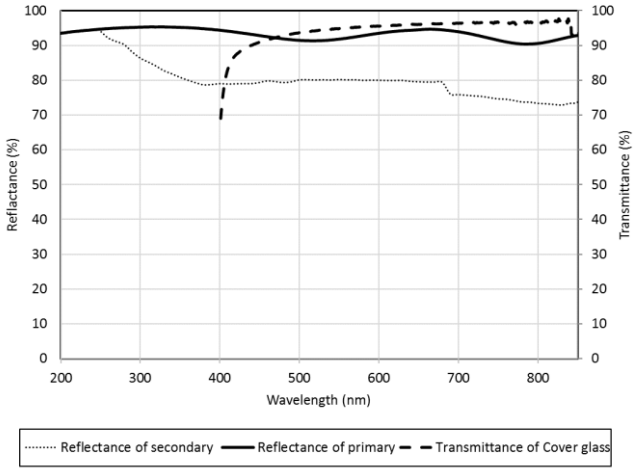

Figure 53. Transmittance and reflectance of the HCPV components.

Two types of homogeniser materials have been tested; crystal resin and glass. As expected, the glass transparency is better than the crystal resin homogeniser. The glass homogeniser experiences a transparency of more than 90% in the wavelength range between 400 and 850nm whereas the crystal resin transparency is of 70% in the wavelength range between 400nm and 850nm.

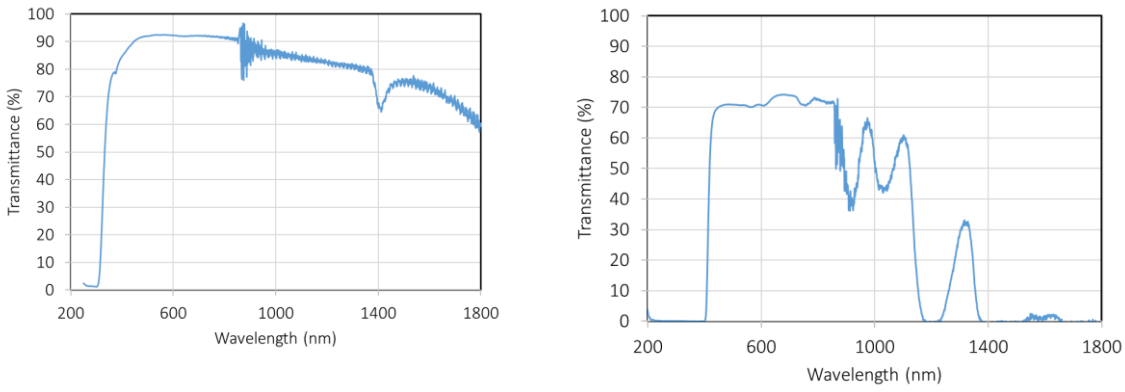

(a) (b)

Figure 54.Transmittance spectra of (a) glass and (b) crystal resin.

The transmittance of the homogeniser made of crystal resin is expected to degrade with time and hence effects the concentration ratio. During the indoor experiments of the HCPV-MLM system, it has been noticed that the homogeniser made of the crystal resin started melting/burning from the top due to the high concentration as shown in Figure 55. On the other hand, no burns marks have

been noticed on the homogeniser made from glass. Therefore, crystal resin is not a good selection of materials to be used for the homogeniser in a high concentration application.

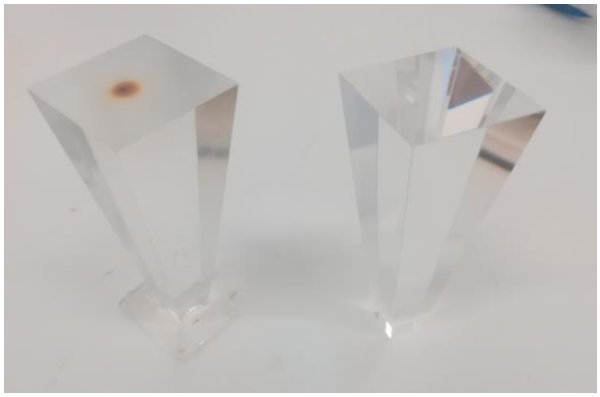

Figure 55.Burn marks in the crystal resin homogeniser (left) and the glass homogeniser (right).

The transmittance of the glass homogeniser is noticed not affected by the high temperature and during running the HCPV-MLM experiments of using the glass homogeniser, it could withstand the high temperature with no visible effects on its structure and finish. Therefore, both the indoor and the outdoor experiments have been run using the glass homogeniser.

The homogeniser was supported using a structure similar to the one proposed by Shanks et al. [251]. For simplicity, a 3D printer was used to produce this structure. The main desired property of the materials is to be able to withstand the load of the homogeniser weight and the high temperature due to the effect of the high solar concentration. The material was ABSplus-P430. It deflects at 96°C under 66psi and at 82°C under 264psi. The optical losses summary from the different optical components are shown in Table 13. The table shows the optical efficiency of the system varies between 55.49% and 84.89% depending of the tracking error angle.

Table 13. Optical loses from different optical stages.

Stage	Optical efficiency
Cover glass transparency	90%
Primary reflectance	90%
Secondary reflection	80%
Homogeniser transparency	92%
Sylgard (1mm) thickness	95%
Tracking error (1.5°)	55.49%
Tracking error (1°)	84.82-81.89%
Misalignment(0.1mm)	84.82%

4.4.3.3 HCVP-MLM module assembly

The first step to assemble the module was attaching the homogeniser to the CPV assembly. Sylgard 184 was used to attach the two pieces together. Five thermocouples were fixed at this stage located at the middle of the solar cell surface and four thermocouples to measure the corners of the copper plate substrate. Firstly, aluminium foil was used to create a barrier around where the homogeniser was to be placed to avoid sylgard leakage during the curing. Then, the thermocouples were place at their positions and the homogeniser laid at the top of the solar cell surface. Finally, the sylgard was injected using a syringe with a fine needle to fill the space between the solar cell and the homogeniser. The sylgard should be injected carefully to the system so that no air is trapped between the homogeniser and the solar cell. The needle was place at one corner of the solar cell and then a small amount of sylgard was injected to the system and left to flow within the area. The displacement of the air by the sylgard should be visible at the top of homogeniser. When needed, more sylgard was applied to ensure a full cover over the solar cell area. Finally, the setup was left to cure at room ambient temperature for 24 hours. Figure 56 shows the final setup of the CPV assembly and the homogeniser.

Figure 56. Photo of refractive homogeniser attached to the CPV assembly.

Figure 57 shows the side view and top view of the supported structure attached to CPV-homogeniser assembly. The top view shows that the homogeniser is accurately fixed at the top of the solar cell and the sylgard is properly distributed without any visible trapped air bubbles. Also, the thermocouple can be seen from this view at the middle of the solar cell.

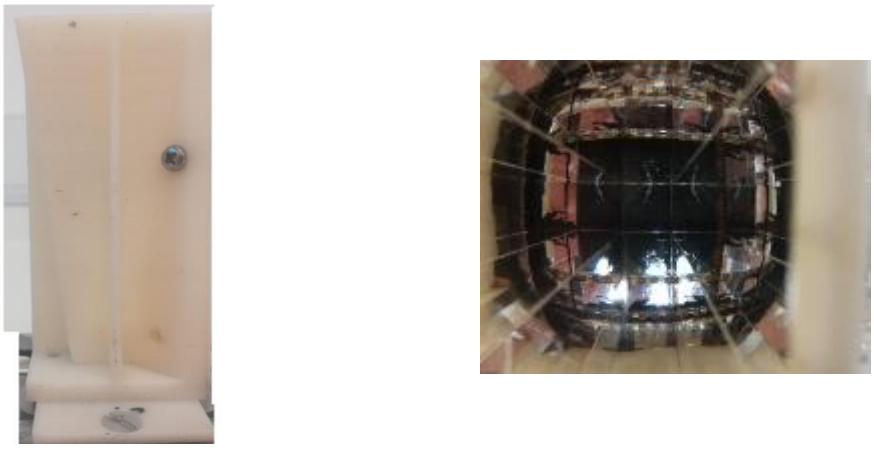

(a) (b)

Figure 57. Photographs of the 3D printed support structure (a) side view, (b) the view from the entry aperture of the homogeniser

The next step to assemble the module is by attaching the heat sink to the previously assembled system (CPV assembly and homogeniser). For thermal conductivity enhancement and to fill any air gap between the CPV-homogeniser assembly and the microchannel top plate produced by the bended surface for both sides, a heat sink compound from RS was used. It is a metal oxide paste of thermal conductivity of 0.65 W/m.K. The compound was applied equally across the surface of a thickness of less than 0.5mm. The assembled CPV-MLM without the optical part is shown in Figure 58.

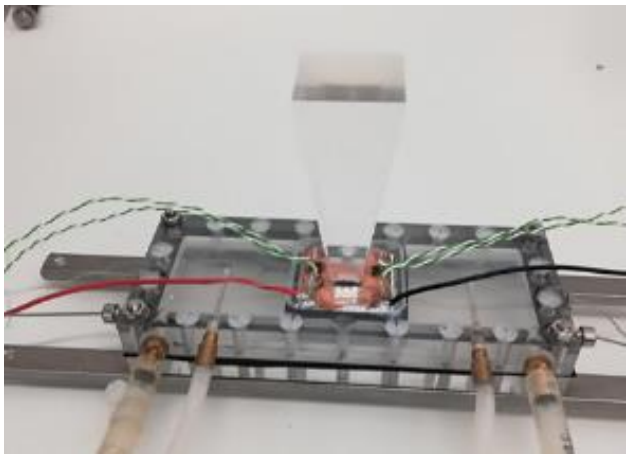

Figure 58.CPV-MLM heat sink assembly.

Attaching the optical case (the primary and secondary reflectors) to the previous assembly was another critical part of the assembly to ensure that all the concentrated rays fall onto the top of the homogeniser and in a uniform pattern. So, a laser beam device was used to ensure that a proper reflectance of rays onto the solar cell could be seen. Figure 59 shows the laser beam reflectance at

various locations. It can be noticed that beam is reflected at the top of the homogeniser even at the extreme corner of the primary reflector which means a proper concentration across the homogeniser surface.

Figure 59. A photograph showing the laser beam reflection at the top of the homogeniser.

The final HCPV-MLM setup is shown in Figure 60. The side view shows the MLM heat sink at the bottom of the HCPV module with all thermocouples, electrical terminal and HTF pipe connections.

(a) (b)

Figure 60. Photograph of the HCPV-MLM heat sink (a) side view and (b) top view.

4.4.4 Experimental setup

As explained earlier, three types of experiments have been conducted to evaluate the MLM heat sink into different working conditions; non-uniform heat test for a heating load of less than 30W, HCPV-MLM indoor experiments and HCPV-MLM

outdoor experiments. In this section, the experimental setup of each experiments is descried individually because of their difference at each condition.

4.4.4.1 Non-uniform heat source-MLM experiments setup

A schematic and a photograph of the experimental setup of the non-uniform heat source-MLM heat sink are shown in Figure 61. The experimental setup consists of a heat sink testing module, HTF circulation bath with a built-in pump, a variable area glass flowmeter, differential pressure meter, K-type thermocouples, data logger and a desktop computer. A HTF with constant volume flow rate and inlet temperature is supplied using the circulation bath at a temperature of 24°C. The HTF volume flow rate is measured using the variable area flowmeter and controlled using a built-in needle valve. The cold HTF picks up the heat from the MLM heat sink and passes to the circulation bath. K-type thermocouples are placed in the inlet, outlet and within the test module in different locations as shown in Figure 62(b). The temperature is recorded with an interval of 10 seconds until the steady state is reached.

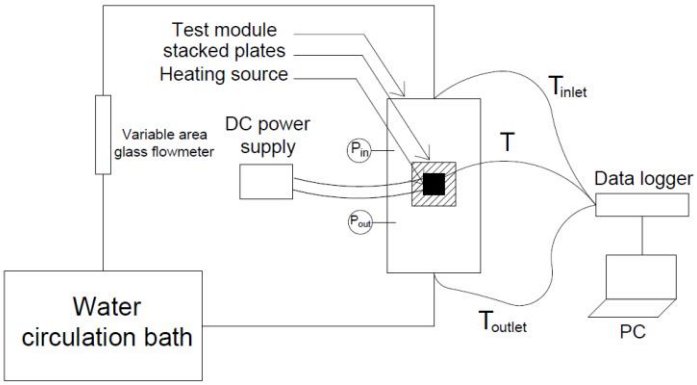

(a)

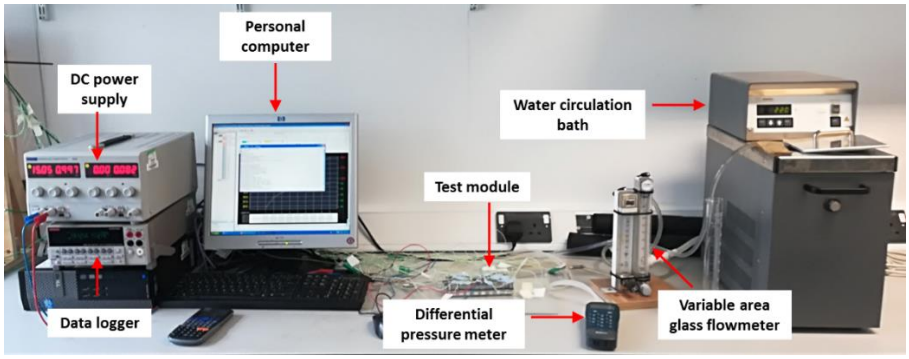

(b)

Figure 61. The non-unifrom heat source-MLM heat sink experimental setup(a) schematic and (b) photograph.

As explained above that, this study is dealing with thermal behaviour of the MLM heat sink under non-uniform heat source. Therefore, the solar cell in the CPV assembly has been replaced by an electrical resistance heater (ERH) to simulate the heat load generated by the CPV. The ERH power rating is 30W and its size of 10mmx10mm and is operated using a DC power supply.

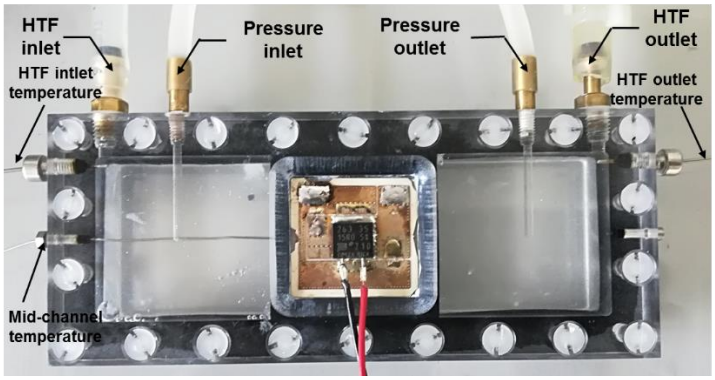

Figure 62. modified CPV assembly attached to the MLM heat sink module.

A typical test run is started when the test module was assembled and all instruments were connected. The modified CPV assembly was attached to the top layer of the heat sink and a thin layer (<1mm) of thermal transfer paste was used for better thermal conductivity between the two plates. The de-ionized water was used as the HTF throughout the experiments. Before starting any test, he de-ionized water was circulated from the right to left direction at a temperature of 24°C and to the desired flow rate for 1 hour to ensure the temperature of the heat sink is uniform, at its initial temperature conditions and to remove any trapped air from the loop. Throughout the experiments, water inlet temperature was allowed to vary between 24±0.1°C. The experiments were started by switching on the DC power supply and the data logger. Then, the experiment was monitored to reach the temperature steady state condition. The steady state was to be achieved when the temperature variations in all thermocouple's measurements are of less than 0.1°C. The pressure drop measurements were recorded manually. The HTF flow measurements were verified manually using a conventional glass water column and stop watch method.

4.4.4.2 HCPV-MLM indoor experiments setup

A photograph of the HCPV-MLM heat sink indoor experimental setup is shown in Figure 63. It consists of the solar simulator, I-V tracer, the HCPV-MLM heat sink module, water circulation bath, a variable area glass flowmeter, a differential

pressure meter, K-type thermocouples, data logger and two desktop computers. The electrical terminals of the HCPV module were connected to the I-V tracer and the HTF connections were connected to the flowmeter, the differential pressure meter. K-type thermocouples were placed at the HTF inlet, outlet, solar cell temperature and the four corners of the substrate. The temperature was recorded with an interval of 10 seconds until the steady state reached.

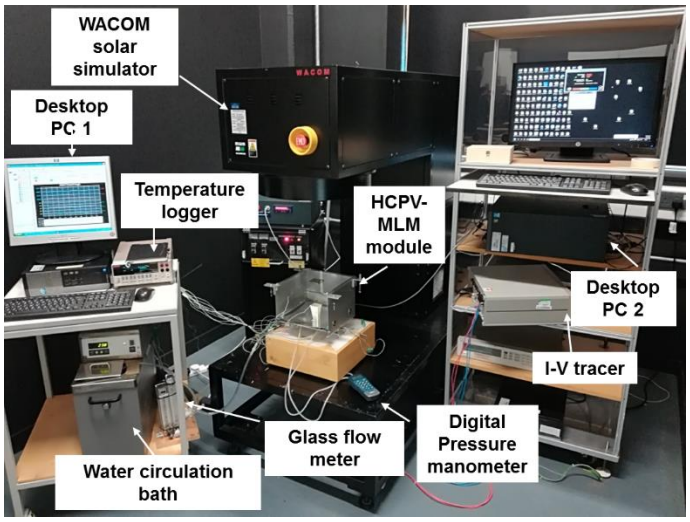

Figure 63. Indoor HCPV-MLM experimental setup.

Before starting any tests, the solar simulator irradiance was adjusted and calibrated to the desired irradiance output. This was controlled by varying the light intensity and measuring using the calibrated silicon cell. The calibration process was detailed in chapter 3.

A typical test run was started when the both the electrical and the fluid connections were connected as shown in Figure 63. In order to protect the solar cell from any sudden increase in its temperature, water was circulated from at a temperature of 24°C and to the desired flow rate. Similar to the non-uniform heat source-MLM heat sink experiments, throughout the experiments, water inlet temperature was allowed to vary between 24.1°C and 23.9°C. The experiments were started by opening the lamp shutters of the solar simulator and by switching the data logger to the scanning mode. The output electrical power and the I-V curve were scanned in 1 minute interval. The experiment was monitored for reaching the temperature steady state condition of temperature variations in all thermocouple measurement of less than 0.1ºC. The volume flow measurements were verified manually using a conventional glass water column and stop watch method.

4.4.4.3 HCPV-MLM outdoor experiments setup

The outdoor test location was selected at the roof of the ESI building (50°10’15.8” N, 50°07’40.4” N) at the university of Exeter, campus Penryn, UK. The selected days of running the outdoor tests were with fully sunny or partly clouded. All the outdoor tests were run during September. The solar group at the university has their own weather station than can take the measurements of the global, direct and diffused solar irradiance continuously. In addition, the ambient temperature and wind speed and direction measurements were recorded.

A schematic and a photograph of the HCPV-MLM outdoor experimental setup is shown in Figure 64. The experimental setup consists of the HCPV-MLM module, solar tracker, I-V tracer, HTF circulation bath, variable area glass flowmeter, differential pressure meter, K-type thermocouples, data logger and a desktop computer. The electrical terminals of the solar cell are connected to the I-V tracer, the HTF inlet connection is connected to the outer flowmeter side and the outlet HTF heat sink side is connected to the circulation bath.

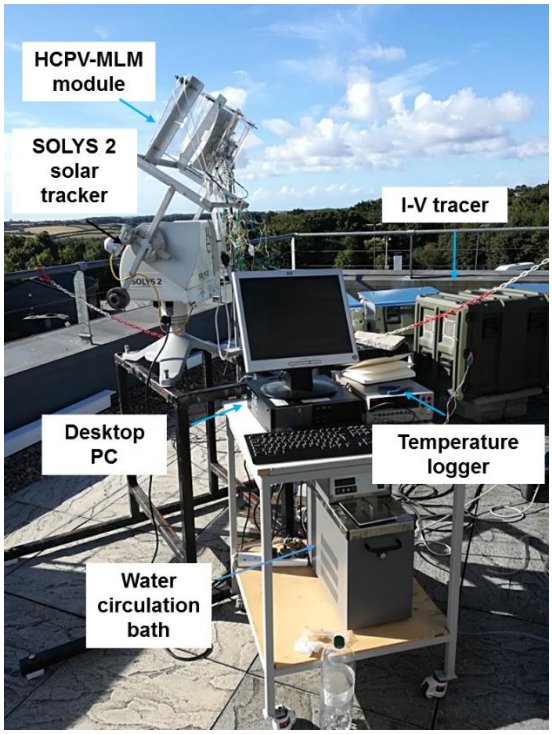

Figure 64. Outdoor HCPV-MLM experimental setup.

The solar tracker is considered as a very sensitive to the level and to the weight of the module, so a special attention has been taken for a precise sun tracker. The level of the tracker has been adjusted using the level instrument to the acceptable level. Also, the HCPV-MLM module has been attached to the solar

tracker with the right alignment and surface level. Finally, the weight of the HCPV-MLM module has been balanced using a counter weight in the other side of the solar tracker support.

A typical test run is started when all the instruments are connected and the solar tracker is switched on to track the sun. The electrical and thermal output are recorded simultaneously where the I-V curve is recorded every 1 minute and the temperature measurements are recorded every 10 seconds.

4.5 Results and discussion

In this section, the results of experimental and numerical work are presented for the different three experiments; MLM-non-uniform heat source experiments; HCPV-MLM indoor experiments and HCPV-MLM outdoor experiments.

4.5.1 MLM thermal analysis using non-uniform heat source

The actual solar cell heating map is non-uniform over the centre of the top surface MLM heat sink. So, the current experimental study illustrates how the thermal performance of the MLM heat sink change with this non-uniformity. The constant heat source power enables to reach the study state and hence to evaluate the heat sink under this state.

4.5.1.1 Test matrix for the non-uniform heat source-MLM heat transfer experiments

A list of controlling parameters is shown in Table 14. It shows that the number of the stacked layers in the heat sink was varied of 1, 2, 3 and 4 layers. For a fixed layer, the heating power was varied in a range between 5W and 30W and the HTF flow rate was varied from 30ml/min to 60ml/min.

Table 14. Non-uniform heat source on MLM heat source testing matrix.

Parameters	Value
Heating power(W)	5, 10, 15, 20, 25 & 30
HTF flow rate (ml/min)	30, 40, 50 & 60
Number of layers	1, 2, 3 & 4

In the current experiments, the flow pattern was maintained in a parallel flow in all layers. The HTF flow rate was closely monitored during the test in case of any change to the sited amount due to the pump pressure drop. Also, the HTF inlet temperature was monitored and adjusted accordingly due to the effect of the

change of the ambient temperature. For each flow rate, the power input was increased from 5W to the maximum output of 30W using the DC power supply. The DC power supply has a limit of 80 V and 5 A. As the characteristic ERH was around 15 Ω. A small voltage/current fluctuation during the experiments was noticed and this had been adjusted at that time.

For each layer test run, the test case was opened for changing the layers, so a special attention was taken to setup all the layers, thermocouples and test case parts to their original place to allow a valid comparison between all the cases under same conditions.

4.5.1.2 Numerical model validation

The computational domain was meshed using the free tetrahedral grid system. In order to confirm that the solution is independent of the size of the mesh for each case, the domains were meshed using different mesh elements sizes. Table 15 shows the variation of the maximum heat source temperature and the HTF outlet temperature with the number of elements (NoE). The number of elements has been varied between 560765 and 1669580. The maximum heat source temperature remains constant for the number of elements between 1510497 and 1669580. On the other hand, it is noticed that no change of the maximum heat source temperature and the HTF outlet temperature when using the NOE between 879992 and 1669580. Therefore, the mesh of NoE with 1510497 was selected for numerical analysis.

Table 15. Calculated temperatures with the variation of number of elements for the 3-layers MLM heat sink, 30ml/min and 15W power rate.

Number of elements		560765	712539	879992	1510497	1669580
Element size of domain	Water (fluid dynamics)	Normal	fine	Fine	Finer	Extra fine
	Remaining (general physics)	Normal	fine	Extra fine	Extra fine	Extremely fine
Calculated parameters	Maximum heat source temperature(ºC)	49.31	49.31	49.29	49.29	49.29
	Fluid outlet temperature(ºC)	31.70	31.70	31.70	31.70	31.70

Next, the CFD model has been validated using experimental results of the same parameters. The HTF outlet temperature and the temperature for the heat source have been used for the validation for all the layers arrangements and of heater powers ranged from 5W to 30W. Figure 65 compares between the experimental and the simulation results of the heat source temperature and the HTF outlet

temperature for the MLM heat sink with varied layers ranged between 1 and 4 and a HTF volume flow rate of 30ml/min and HTF inlet temperature of 24°C. The average difference between the numerical and experimental of the HTF outlet temperature is 1.25°C and a maximum difference of 3.30°C occurred at 25W of the 3-layers heat sink. However, more average difference of the heat source temperature between the numerical and experimental is found of 2.58°C. This shows a good estimation of the numerical model and will be used to explore the thermal characteristics of the system.

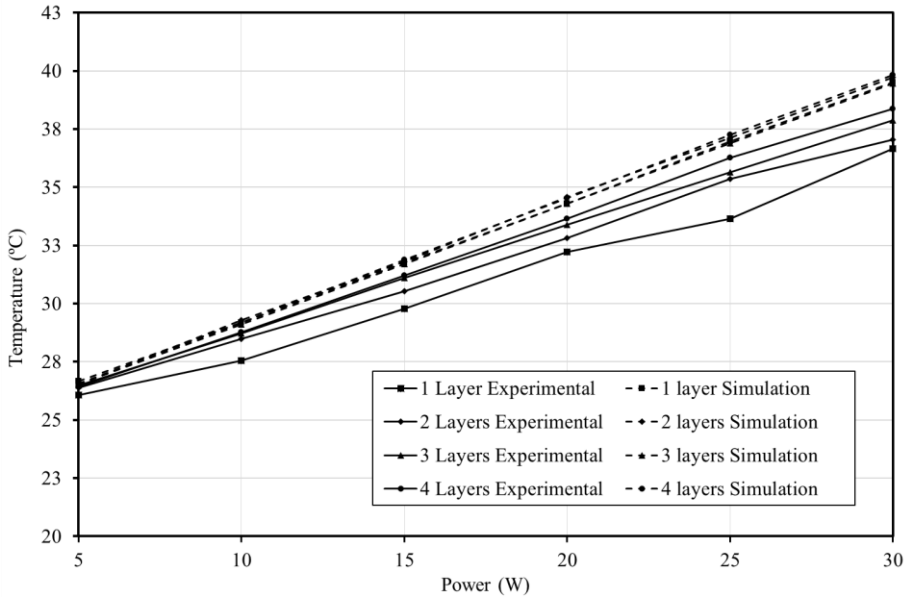

(a)

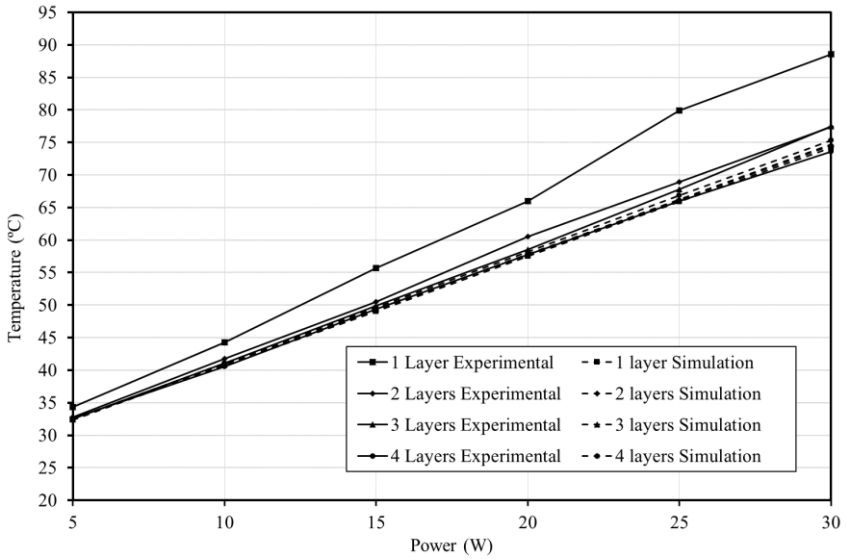

(b)

Figure 65. The simulation and experimental results for 30ml/min HTF flow rate of varied layers for (a) the temperature of the heat source at the middle top surface and (b) HTF outlet temperature.

4.5.1.3 Effects of number of layers on MLM performance

The effect of number of layers on the performance of the MLM heat sink is investigated in this section for variable number of layers ranged between 1 and 4. Figure 66 shows the thermal resistance of MLM heat sink and heat source surface temperature for different number of layers of a HTF flow rate of 30ml/min and 15W power rate. The thermal resistance decreases by 17% as the number of layers increases from 1-layer to 2-layers. However, a slight decrease of the thermal resistance of 2% is noticed when the number of layers increased to 3 and 4 layers. Also, the figure shows the heat source surface temperature for the various number of layers arrangement. The temperature decreases as the number of layers increases from 1-layer to 2-layers by 5.21°C and less temperature reduction is noticed when increasing the number of layers from 3 to 4.

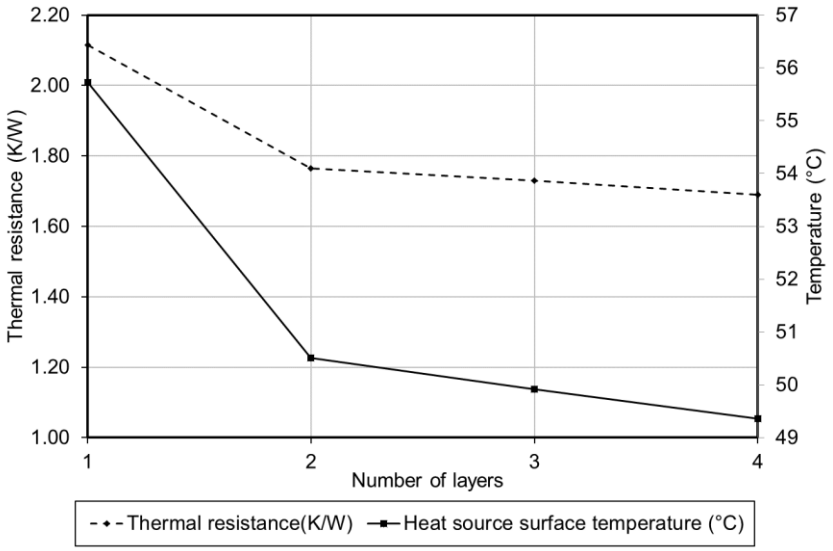

Figure 66. The thermal resistance and heat source temperature of the MLM heat sink versus the number of layers of 30ml/min HTF flow rate and 15W power rate.

A more investigation on the temperature uniformity on the heat source top surface temperature has been conducted. Figure 67 shows the measured temperature distributions of the surface of the heat source in 9 sections for the different number of layers heat sinks. The results show that the average and the standard deviation of the measured temperatures decreases as the number of layers increases. It can be clearly noticed that the centre of the heat source (section 1) suffers the maximum temperature of all the other sections and a wide difference between this temperature and the other locations within the heat source of a maximum difference of 12.01°C in the 2-layers MLM heat sink. This temperature

difference causes an increase of temperature non-uniformity across the heat source surface and hence the standard deviation. Despite the maximum temperature value (section 1), the single layer MLM heat sink is the most temperature variable around the heat source (sections 2-9) of a standard deviation of 4.30. Interestingly, 2-layers MLM heat sinks experiences less temperature non-uniformity compared to the 3-layers MLM heat sink of a standard deviation of 3.86 and 4.05, respectively.

41.61	43.51	45.40
42.37	55.71	46.76
43.14	45.82	48.50

Standard deviation: 4.30

Average: 45.87°C

(a)

38.49	38.84	39.19
38.53	50.50	39.13
39.08	39.08	39.08

Standard deviation: 3.86

Average: 40.22°C

(b)

38.18	38.37	38.57
39.34	49.91	37.63
37.76	37.23	36.70

Standard deviation: 4.05

Average: 39.30°C

(c)

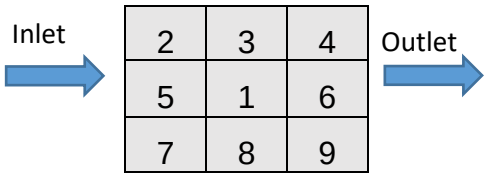

Figure 67. The heat source temperature distribution of 30ml/min HTF flow rate and 15W power rate for (a) 1-layer, (b) 2-layers and (c) 3-layers MLM heat sink.

A close look into the temperature distribution across the heat source surface is obtained using the contour representation from the numerical solution and it is shown in Figure 68. It can be noticed that the hot spot shifted to the centre of the heat source as the number of layers increases. In addition, the temperature distribution of the heat source edge near to the downstream becomes more uniform as the number of layers increased. Not much visible difference between the 3-layers and 4 layers heat sinks in terms of the hot spot distribution and the temperature uniformity.

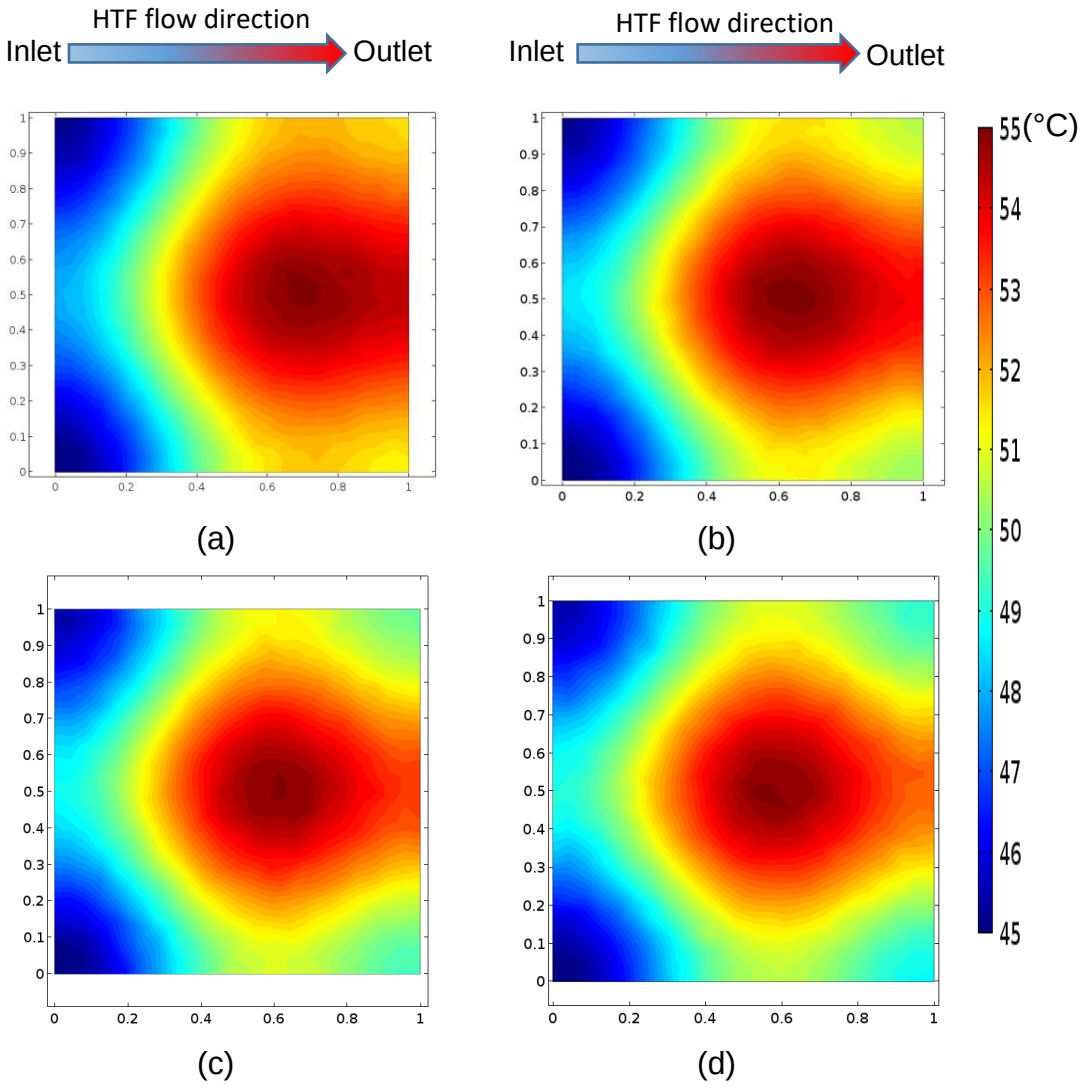

Figure 68. The heat source surface temperature contours MLM heat sink of 30ml/min HTF flow rate and 15W power rate for (a) 1-layer, (b) 2-layers and (c) 3-layers and (d) 4-layers.

An isotherm of the full heat sink module for the different layer heat sinks is shown in Figure 69. It can be noticed that less temperature is experienced by the microchannel plates especially at the edges. This implies an opportunity of using the MLM heat sink in the CPV applications by decreasing of the CPV receiver assembly in smaller size so that less heat sinks materials used and less fluid flow.

The thermal efficiency of the MLM heat sink and the HTF outlet temperature are shown in Figure 70. As seen from the figure, the thermal efficiency has been improved significantly by 20% when the number of layers increases from 1 to 3-layers. This is due to the increase of the HTF outlet temperature from 29.7°C to 31.1°C for the 1-layer and 3-layers MLM heat sinks, respectively. However, no effect on the thermal efficiency and the HTF outlet temperature have been noticed when the number of layers increased from 3-layers to 4-layers.

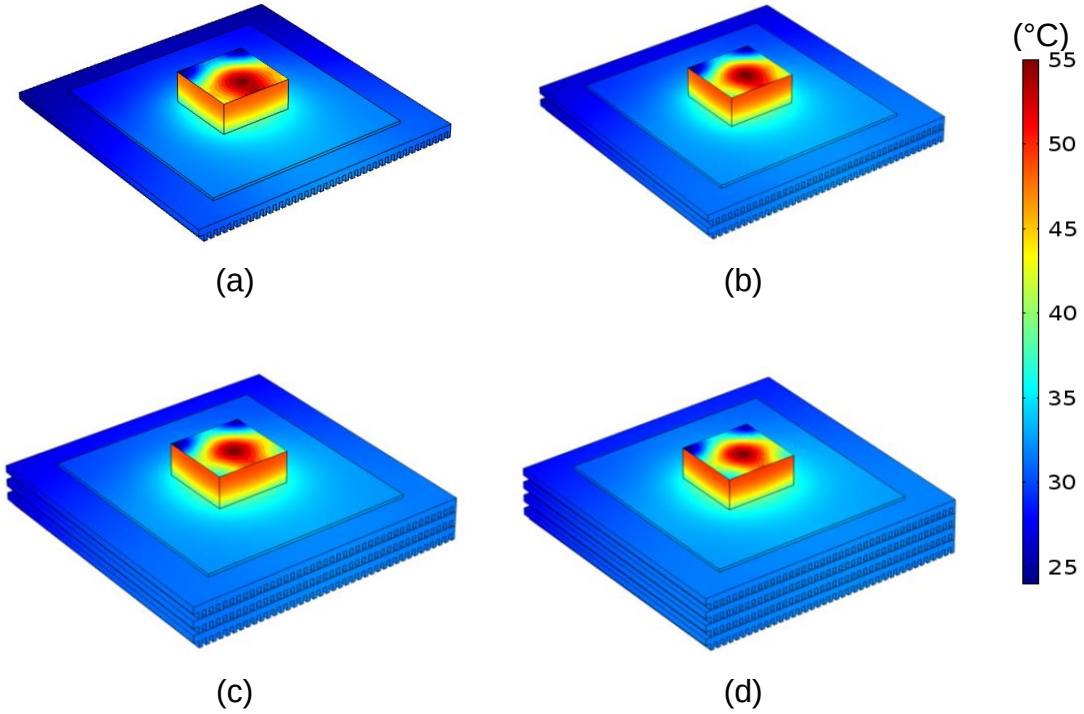

Figure 69. The MLM heat sink isotherms of 30ml/min HTF flow rate and 15W power rate for (a) 1-layer, (b) 2-layers and (c) 3-layers and (c) 4-layers.

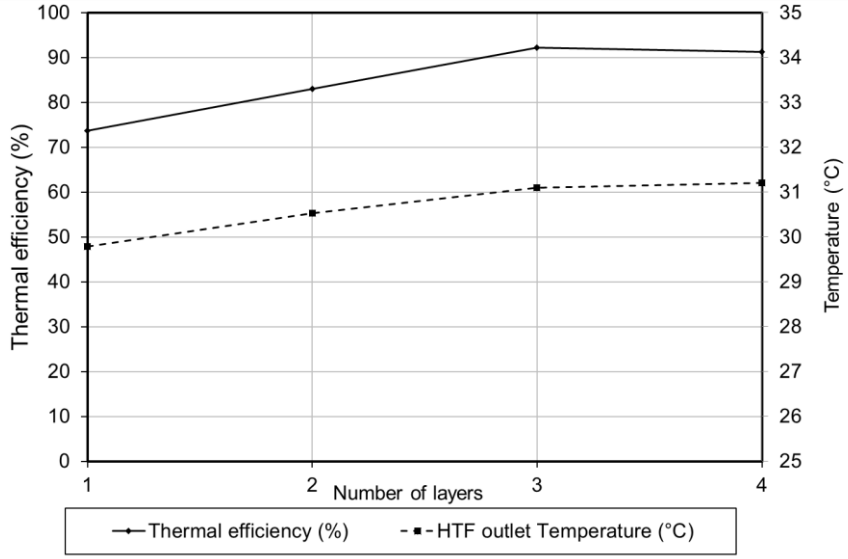

Figure 70. The thermal efficiency and the HTF outlet temperature of the heat sink versus the number of layers of 30ml/min HTF flow rate and 15W power rate.

The hydrodynamic characteristics are as important as the thermal performance in evaluating the effect of the number of layers in the MLM heat sink. Pressure drop across the heat sink is one of these characteristics in which it effects the pumping power. Figure 71 shows the effect of layers in the pressure drop. It can be noticed that the pressure drop decreased as the number of layers increased.

An approximate 4 mm H_2O pressure drop reduction of increasing of each layer where the pressure for the MLM heat sink of 1-layer and 3-layers are 16.6 and 8.29mm H_2O, respectively.

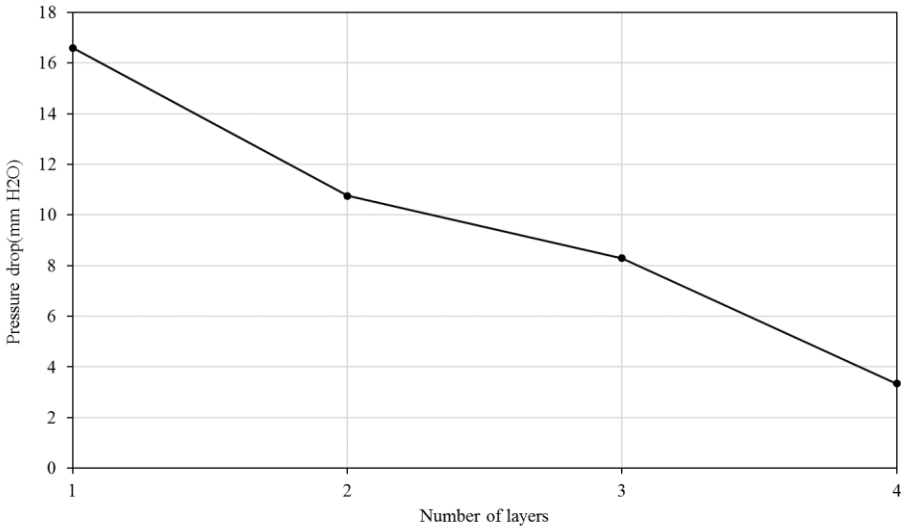

Figure 71. The HTF pressure drop across the MLM heat sink versus the number of layers of 30ml/min HTF flow rate and 15W power rate.

4.5.1.4 Effect of the power rate

Total thermal resistances for different power input rate for the 3-layers MLM heat sink with 30ml/min flow rate are shown in Figure 72. As can see from the figure, the total thermal resistance of the heat sink increases slightly with increasing the power rate from 5W to 30W for the same HTF flow rate of a difference of 0.08 K/W. This shows the ability of the heat sink to undertake a wide range of power rate with a slight change in the thermal resistance.

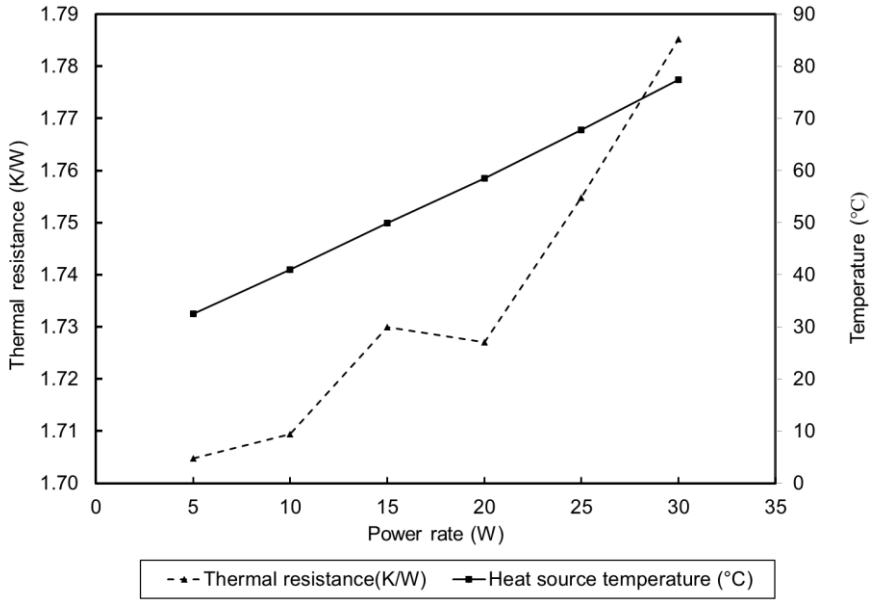

Figure 72. The thermal resistance and heat source temperature versus the power rate of 3-layers MLM heat sink of 30ml/min HTF flow rate.

As expected, a significant increase of the heat source temperature as heat source power rate increases from 5W to 30W for the same HTF flow rate. The temperature of the heat source is doubled when the power rate increases from 5W to 30W of a difference of 45°C. However, the heat source temperature on the worst case at 30W is 77.48°C which is within the recommended temperature of the solar cell manufacturer (80°C).

Figure 73 shows the temperature distributions on the surface of the heat source, average temperature and standard deviation for 3-layers MLM heat sink of 30ml/min HTF flow rate for various power rates. The results show an increase of the temperature non-uniformity within the heat source as the power rate increases and this is the same for the standard deviation. For 5W power rate, the temperature varies with a standard deviation of 1.25°C and with an average temperature of 29.18°C. A significant increase of the standard deviation in the 30W power rate of 9.03°C in the 30W power rate and of an average temperature of 54.09°C.

28.63	28.74	28.86
29.11	32.49	28.67
28.93	28.71	28.48

Standard deviation: 1.25°C

Average: 29.18°C

(a)

38.19	38.38	38.57
39.35	49.91	37.64
37.77	37.24	36.71

Standard deviation: 4.05°C

Average: 39.31°C

(b)

52.61	52.80	52.99
54.15	77.48	50.33
49.96	48.81	47.66

Standard deviation: 9.03°C

Average: 54.09°C

(c)

Figure 73. The heat source temperature distribution for the 3-layers MLM heat sink of 30ml/min HTF flow rate for a power rate of (a) 5W, (b) 15W and (c) 30 W.

The thermal efficiency of the heat sink and the HTF outlet temperature for various power rates for the 3-layers MLM heat sink of 30ml/min HTF flow rate are shown in Figure 74. As can be seen from the figure, the thermal efficiency drops significantly by 6% when the power rate increases from 5W to 10W. However, the thermal efficiency decreases slightly when the power rate increases from 10 to 30W and reach to 90% for the 30W power rate. Also, the HTF outlet temperature increases as the power rate increases from 5W to 30W of 26.45°C to 37.88°C. This shows a higher heat dissipation of a higher power rate.

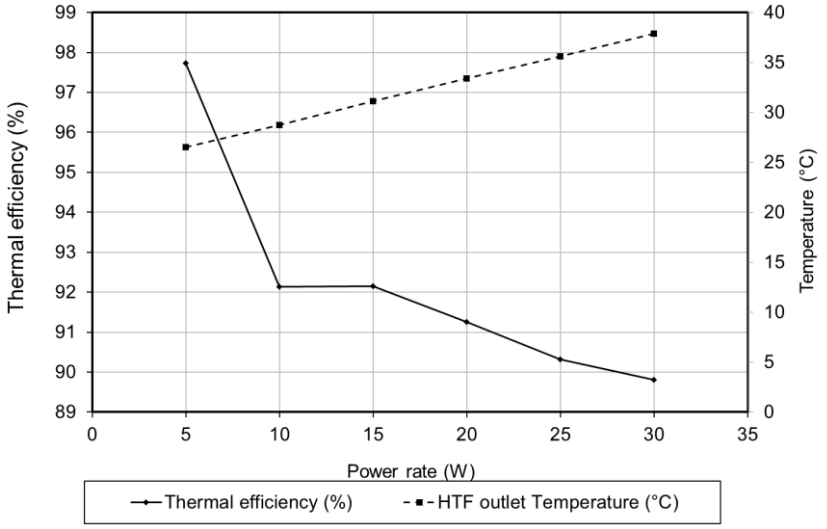

Figure 74. The MLM heat sink thermal efficiency and the HTF outlet temperature versus the power rates of the 3-layers MLM heat sink of 30ml/min HTF flow rate.

4.5.1.5 Effect of HTF flow rate

In this section the effect HTF flow rates on the thermal performance of the heat source is presented for various number of layers MLM heat sinks. Figure 75 shows effect of the HTF flow rates on the thermal resistance of the MLM heat sink for the 5W power rate. For a single layer heat sink, the thermal resistance decreases from 2.04 K/W to 1.78K/W as HTF flow rate increases from 30ml/min to 60ml/min, respectively. A significant decrease of the thermal resistance is noticed as the HTF flow rate increases from 30ml/min to 40ml/min of the 3-layers and 4 layers heat sink of a difference of 0.15K/W and 0.14K/W, respectively. An interesting note that increasing the number of layers from 3 to 4 has a slight effect on the thermal resistance for the HTF flow rate of 30ml/min, 40ml/min and 60ml/min and this shows that the optimum number of layers in the 5W power rating is 3-layers.

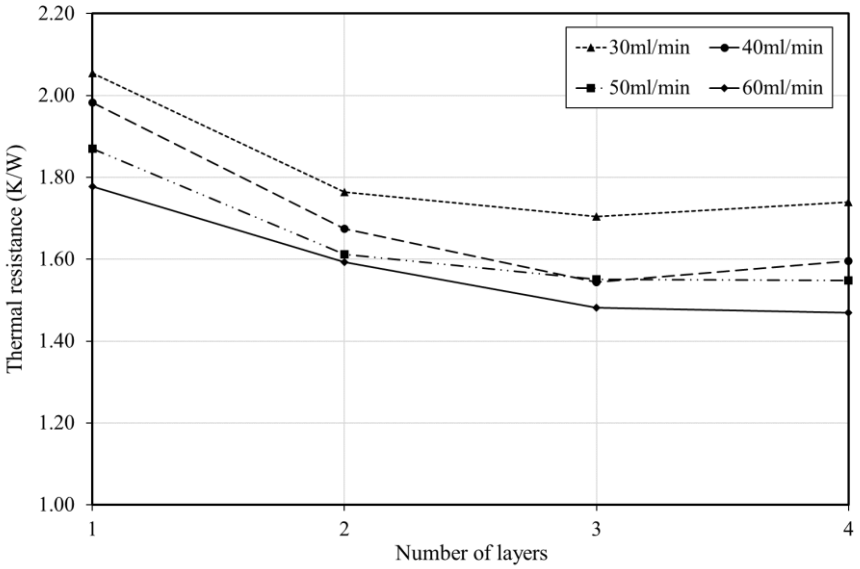

Figure 75. Heat sink thermal resistance versus the number of layers for different HTF flow rates for power rate of 5W.

Figure 76 shows the effect of the number of layers and HTF flow rates in reducing the heat sink thermal resistance for a higher power rate of 30W. At this power rating, both the increase of the number of layers and HTF flow rate have a major impact in reducing the thermal resistance of the heat sink HTF. The thermal resistance reduces by 23.26% and 10.25% when the number of layers increases from 1 to 4 layers for 30ml/min to 60ml/min, respectively. This shows that the power rate is critical in determining the optimum number of layers for the lower thermal resistance.

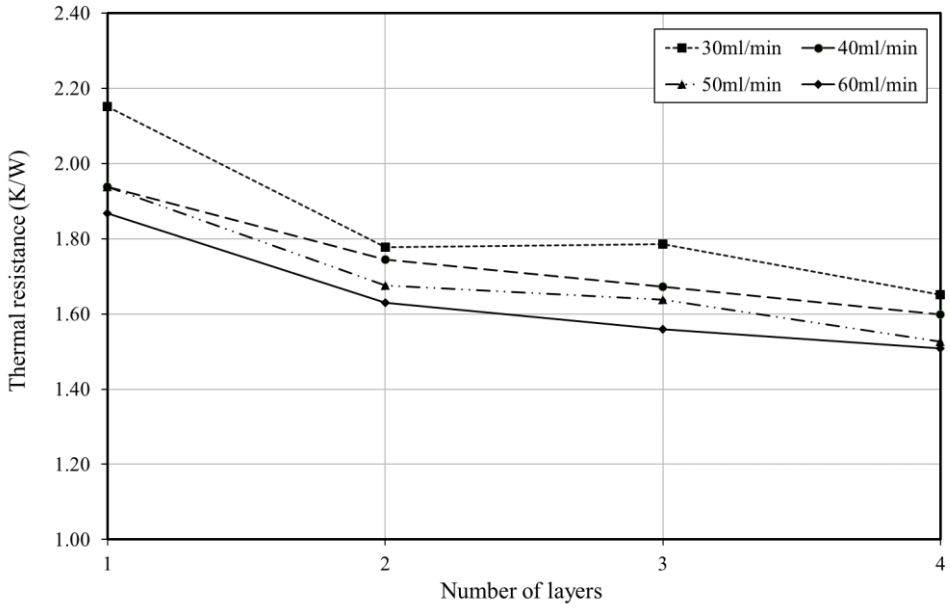

Figure 76. The MLM heat sink thermal resistance versus the number of layers for different HTF flow rates for power rate of 30W.

A summary of the measurements of the heat source temperature for various HTF flow rates are shown in Table 16. It is noticed that the heat source temperature decreases significantly as the HTF flow rate increases for all the MLM heat sinks arrangements for power rates of more than 15W. In additions, the heat source experiences a temperature of more than 80°C when using a single layer heat sink for power rate of 30W for all the tested HTF flow rates ranged from 30ml/min to 60ml/min which is more than the recommended maximum temperature specified by the CPV assembly manufacturer for performing a high electrical efficiency.

Table 16. The heat source maximum temperature for various HTF flow rates and power rates for the different layers MLM heat sinks.

Number of layers	HTF flow rate(ml/min)	Power rate (W)					
		5	10	15	20	25	30
		Temperature (°C)					
1	30	34.32	44.27	55.72	65.98	79.93	88.55
	40	33.91	43.49	53.44	62.51	74.11	82.27
	50	33.41	42.52	52.18	61.80	71.78	82.15
	60	32.77	42.03	51.18	60.95	70.30	80.02
2	30	32.79	41.76	50.51	60.52	68.91	77.39
	40	32.43	40.46	49.03	56.98	66.60	76.32
	50	32.12	39.95	48.21	56.60	65.56	74.30
	60	31.94	39.69	47.60	54.77	64.26	72.88
3	30	32.49	41.04	49.91	58.50	67.81	77.48
	40	31.78	40.15	48.47	56.06	64.88	74.16
	50	31.73	39.58	47.73	55.88	64.29	73.23
	60	31.38	38.94	46.86	54.67	62.16	70.70
4	30	32.63	40.55	49.35	57.75	66.00	73.57
	40	31.87	39.41	46.98	55.30	63.06	71.99
	50	31.66	39.13	46.38	53.62	60.83	69.74
	60	31.42	38.94	45.75	53.07	60.99	69.31

A summary of the HTF outlet temperature i.e. the dissipated heated for the different flow rates is presented in Table 17. Increasing the HTF flow rate decreases the HTF outlet temperature where the HTF outlet temperature in the 30ml/min reaches the maximum among all the flow rates. The is more noticeable in the high-power rates where the HTF outlet temperature difference is around 3.5°C when the HTF flow rate increases from 30ml/min to 40ml/min for all number

of layers. The maximum HTF outlet temperatures reaches its maximum in the 4 layers heat sink of 38.36°C.

Table 17. The HTF outlet temperature for various HTF flow rates and power rates for the different layers MLM heat sinks.

Number of layers	HTF flow rate(ml/min)	Power rate (W)					
		5	10	15	20	25	30
		Temperature (°C)					
1	30	26.08	27.54	29.79	32.22	33.66	36.66
	40	25.59	26.87	28.23	29.55	30.72	31.81
	50	25.18	26.03	26.90	27.89	29.03	29.74
	60	24.82	25.70	26.41	27.15	27.91	28.82
2	30	26.38	28.47	30.53	32.83	35.35	37.03
	40	25.82	27.30	28.69	30.23	31.84	33.24
	50	25.52	26.61	27.68	28.77	29.84	31.11
	60	25.19	26.05	26.95	27.96	28.95	29.98
3	30	26.49	28.72	31.10	33.39	35.63	37.88
	40	25.78	27.50	29.24	30.97	32.85	34.77
	50	25.37	26.81	28.22	29.74	31.25	32.95
	60	25.23	26.35	27.54	28.75	29.96	31.16
4	30	26.43	28.77	31.20	33.65	36.26	38.36
	40	25.80	27.39	29.26	31.12	32.89	34.71
	50	25.49	26.68	28.15	29.71	31.25	32.66
	60	25.30	26.35	27.50	28.75	30.01	31.26

The pressure drop of the MLM heat sink for different number of layers is shown in Figure 77. It is observed that the pressure drop for the flow rate of 30ml/min is the maximum at the single layer MLM heat sink of 16.6mm H_2O and its minimum in the 4 layers heat sink of 3.34mm H_2O which is a reduction of 3 times compare to the single layer heat sink. The heat sink of single layer experiences a significant increase of the pressure drop when the HTF flow rates is increased from 30ml/min to 60ml/min of an increase of 4.5mm H_2O. However, a slight increase of the pressure drop is noticed when the flow rate is increased for the MLM heat sink of the 2-layers, 3-layers and 4 layers MLM heat sinks of an increase of only of 1.51, 1.01 and 1.58mm H_2O, respectively.

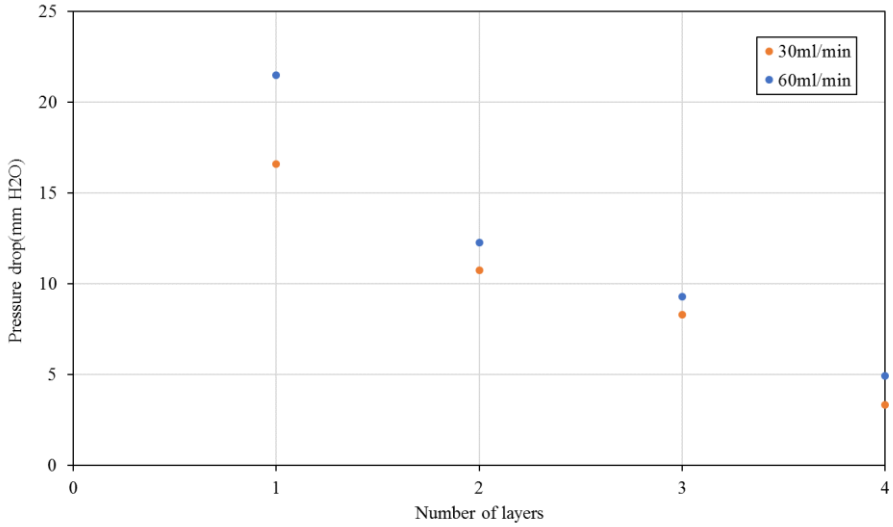

Figure 77. The pressure drop versus the number of layers for the different HTF flow rates.

4.5.2 HCPV-MLM heat sink indoor experiments results

This section presents the indoor experimental characterisation of the HCPV-MLM to investigate the electrical and thermal efficiencies. The reported performance parameters are the I-V curve analysis and the extracted heat from the system.

4.5.2.1 Test matrix for the HCPV-MLM experiments

A list of controlled parameters of the experimental work for the CPV-MLM system are shown in Table 18. It shows that the number of layers stacked in the heat sink was varied of 1, 2 and 3-layers. For a fixed layer, the HTF flow rate was varied from 30ml/min to 300ml/min.

Table 18. HCPV-MLM experiment testing matrix.

Parameters	Values
HTF flow rate (ml/min)	30, 40, 50, 60, 100, 200 & 300
Number of layers	1, 2 & 3

In the current experiments, the simulator intensity has been set for an output of 1000W/m^2. This was monitored using the calibration method as explained in chapter 3. The HTF flow rate was closely monitored during the test in case of any change to the setting amount due to the sudden change in the pump pressure drop. The HTF inlet temperature was kept to 24°C. However, it was monitored and adjusted manually because of the effect of the change of the ambient temperature. For each layer test run, the experiment test module was opened for changing the layers, so a special attention was taken to the setup all the layers,

thermocouples and test case parts to their original place to allow a valid comparison between all the cases under same conditions.

4.5.2.2 Effects of homogeniser materials

This part provides details of the indoor experimental characterisation of the HCPV-MLM module to investigate the electrical and thermal analysis and the optical loss for the different tested homogeniser materials under the solar simulator. The results including the IV characterisation of the HCPV, the thermal extracted heat and the improvements due to the MLM heat sink.

The effect of the homogeniser materials on the I-V characterization on the solar cell performance is shown in Figure 78 for the 2-layers MLM heat sink and 30ml/min under 1000W/m^2 irradiance intensity. The maximum power of the HCPV module with glass homogeniser is found 3.46W which is higher to the module with crystal resin homogeniser (0.97W higher). The short circuit current for the HCPV module with glass homogeniser is found 1.403A, which is 0.323A higher than the crystal resin homogeniser module. The fill factor is increased slightly from 81% to 84% for the crystal resin and the glass, respectively. Less optical loss and uniformity in the intensity distribution on the solar cell may be the cause of the high fill factor as observed in the glass homogeniser module.

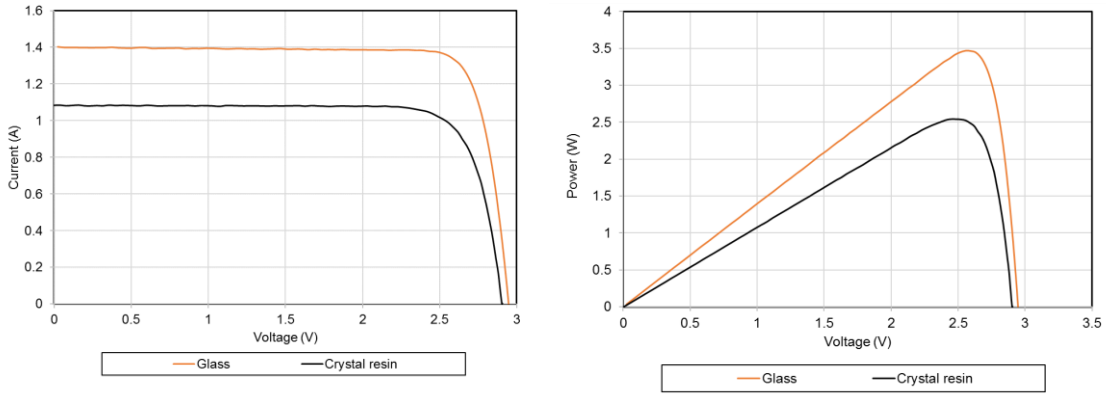

(a) (b)

Figure 78. The glass and the crystal resin homogeniser of a HTF flow rate of 30ml/min with 1000W/m^2 irradiance intensity of 2-layers MLM heat sink (a) I-V and (b) power curve.

The electrical and thermal analysis for the different homogeniser materials is summarized in Table 19. For the 2-layers MLM heat sink and 60ml/min under 1000W/m^2 irradiance intensity, it is observed that the module with glass homogeniser experiences a higher short circuit current of 1.39A and a maximum

power of 3.47W compared to the crystal resin homogeniser of a short circuit current and a maximum power of 1.09A and 2.60W, respectively. The increase in the generated electricity by the solar cell causes a noticeable increase in the solar cell temperature. In addition, the table shows a significant increase of the optical efficiency of the HCPV when using the glass homogeniser compared to the crystal resin homogeniser. Also, a slight increase in the HTF outlet temperature is noticed when using the glass homogeniser which increases the thermal efficiency and hence the overall system efficiency.

Table 19. HCPV-MLM electrical and thermal parameters with 1000W/m^2 irradiance intensity of 2-layers MLM heat sink.

Flow rates (ml/min)	Glass					Crystal resin				
	Isc (A)	Voc (V)	Power (W)	Tcell (°C)	HTF outlet temp (°C)	Isc (A)	Voc (V)	Power (W)	Tcell (°C)	HTF outlet temp (°C)
30	1.34	2.95	3.46	63.26	30.34	1.08	2.90	2.55	59.21	29.04
40	1.40	2.96	3.48	61.49	28.63	1.09	2.91	2.58	58.10	27.75
50	1.40	2.96	3.48	60.79	27.86	1.09	2.91	2.58	57.62	26.99
60	1.39	2.96	3.47	59.81	27.06	1.09	2.92	2.60	57.10	26.58

The electrical and thermal efficiency of the HCPV-MLM system for the both homogeniser materials is shown in Figure 79. The electrical efficiency is increased when using the glass homogeniser where the calculated electrical efficiency of the glass homogeniser is 6.87% and 5.05% for the crystal resin homogeniser for the HTF flow rate of 30ml/min. In addition, the overall efficiency of the HCPV-MLM module when using the glass homogeniser is 30.66% and 23.70% for the crystal resin homogeniser. However, this difference of the overall efficiency remains constant with the increase of flow rates.

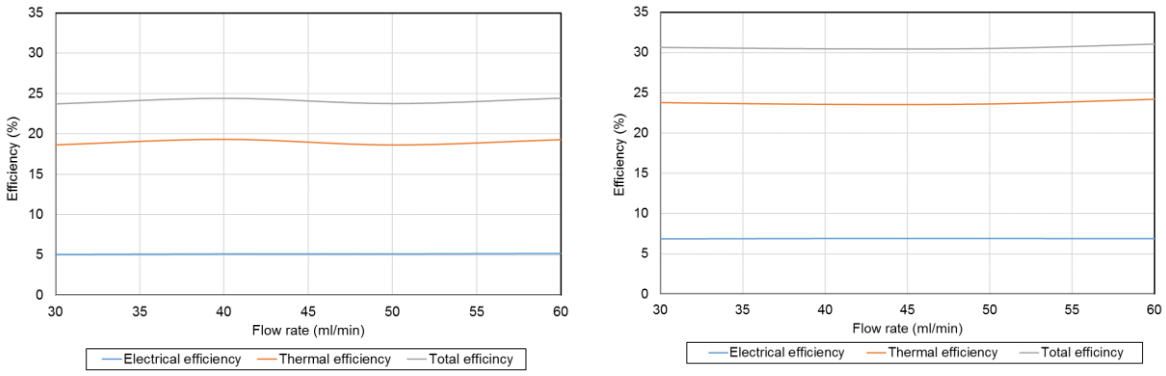

Figure 79. The thermal, electrical and total efficincies of the HCPV-MLM using the homogeniser materials made from (a) Crystal resin and (b) Glass for a HTF flow rate of 30ml/min with 1000W/m^2 irradiance intensity.

4.5.2.3 *Effects of number of layers*

Because of its higher optical and electrical performance and not affected by the high concentration, the HCPV with glass homogeniser was used in the further investigations for the HCPV-MLM. Further experiments were carried out with irradiance of 1000W/m^2 to estimate the I-V characterisation and the thermal efficiency of the HPCM-MLM module with the increase of the number of layers. Figure 80 shows the I-V characterisation of the HCPV module of a HTF flow rate of 30ml/min. The short circuit current of the 1-layer MLM heat sink is 1.319A and it increases to the maximum of 1.445A when using the 3-layers MLM heat sink. Similarly, the maximum power increases from 3.298W for the 1-layer MLM heat sink to 3.608W of 3-layers heat sink. However, a slight increase of the open circuit voltage is noticed when using the 3-layers MLM heat sink compared to the 1-layer of a difference of 20mV. It is observed that the change of the filling factor of the HCPV system is almost neglected of around 84.45%. Also, the results show that number of layers has no effect on the filling factor due to similar level of homogenous distribution of light intensity on the solar cell in the HCPV system.

The increase of the electrical performance of the HCPV under similar optical setup could be referred to the thermal performance of the heat sink in controlling the solar cell temperature. The results show an increase in the solar cell temperature by 3.15°C of the 1-layer MLM heat sink compared to 3-layers heat sink. This gives a reduction in the maximum electrical power of 98.4mW/°C. Figure 81 shows the temperature distribution within the HCPV assembly where the solar cell temperature is represented in section 1 and the corner temperatures

of the top of the HCPV assembly is represented by sections from 2 to 4. It can be observed that the maximum temperature at the corner is decreased as the number of layers is increased from 41.55°C in 1-layer heat sink to 36.58°C in 3-layers heat sink.

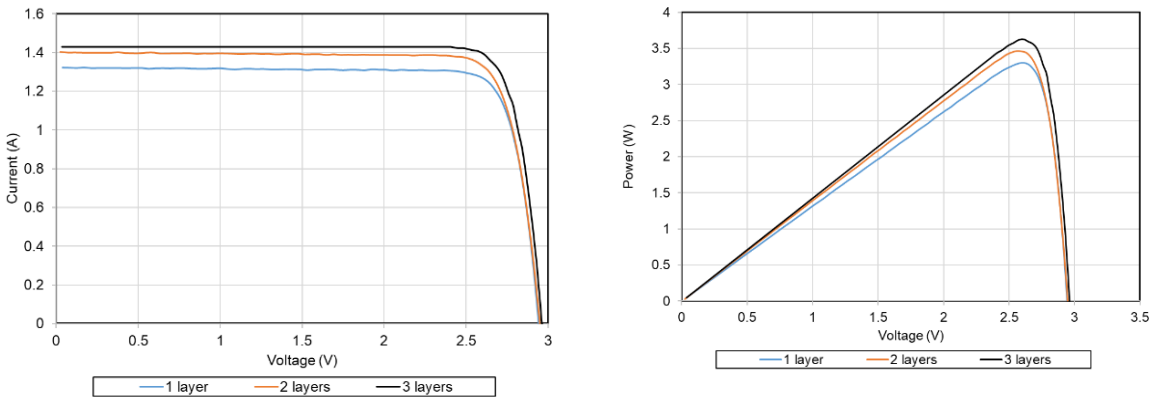

(a) (b)

Figure 80. The effect of the number of layers on the HCPV of a HTF flow rate of 30ml/min under 1000 W/m² irradiance intensity incident (a) I-V and (b) power curve.

37.45		41.55
	62.96	
35.31		37.23

(a)

36.93		41.03
	61.26	
35.69		37.28

(b)

34.32		36.58
	59.81	
34.89		35.25

(c)

Inlet

4		2
	1	
3		1

Outlet

Figure 81. The surface temperature distribution of the copper substrate of 60ml/min HTF flow rate with 1000 W/m^2 irradiance intensity for for the MLM heat sink of (a) 1-layer, (b) 2-layers and (c) 3-layers.

Further experiments have been carried to demonstrate the effect of the number of layers in the I-V characterisation and the thermal performance of the HCPV-MLM module with irradiance intensity of 1000W/m². Figure 82 shows the I-V characterisation of the HCPV module of the HTF flow rate of 60ml/min. It can be noticed that the short circuit current of the 1-layers MLM heat sink is 1.321A, and it is increased to the maximum of 1.432A when the number of layers is increased to 3. Also, the maximum power is increased from 3.315W for the 1-layer MLM

heat sink to 3.624W of 3-layers heat sink. This gives a reduction in the maximum electrical power of 100mW/°C which is similar rate found in the 30ml/min HTF flow rate. A slight increase in the open circuit voltage in the 3-layers MLM heat sink compared to the 1-layer heat sink of only of 18mV. Similar to the 30ml/min HTF flow rate, it is observed that the change of the filling factor of the HCPV system is almost neglected of around 85%. This result demonstrates that number of layers have a significant effect on increasing on the maximum power of the solar cell.

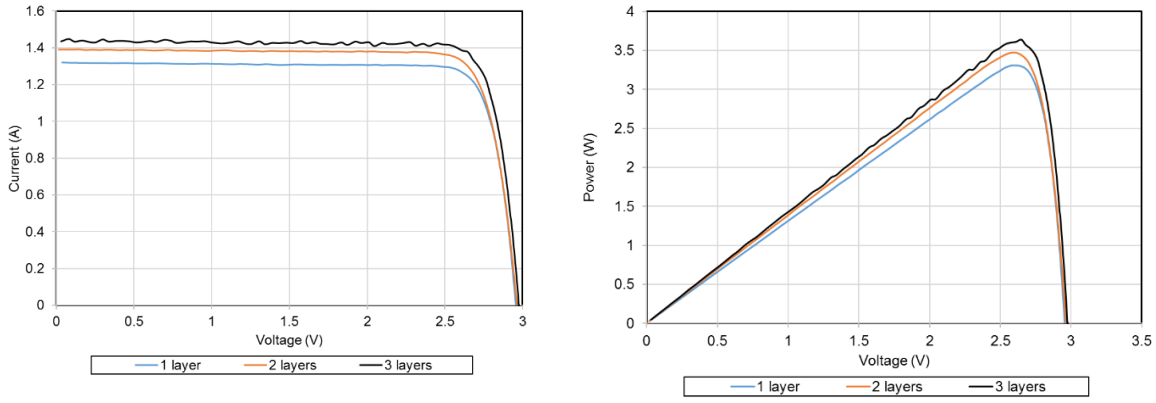

(a) (b)

Figure 82. The effect of the number of MLM layers on the HCPV of a HTF flow rate of 60ml/min under 1000 W/m² irradiance intensity incident (a) I-V and (b) power curve.

The measurements of the solar cell temperature show a reduction in the solar cell temperature by 3.08°C of the 3-layers MLM heat sink compared to 1-layer MLM heat sink. This difference is similar to that in 30ml/min HTF flow rate. Figure 83 shows the surface temperature distribution of the HCPV assembly of 60ml/min HTF flow rate with 1000 W/m² irradiance intensity for the MLM heat sink. It can be observed that the maximum temperature at the corner is decreased as the number of layers is increased from 38.5°C in the 1-layer MLM heat sink to just 33.96°C in the 3-layers heat sink. This clearly indicates a significant impact of the number of layers on the temperature reduction in the CPV substrate.

The electrical, thermal and the total efficiencies are calculated in Table 20. It can be noticed that the electrical efficiency is increased by 0.29% when the number of layers is increased from 1-layer to 3-layers for the 30ml/min HTF flow rate. However, the total efficiency is decreased by 1.03% as the number of layers is increased from 1-layer to 3-layers. This can be referred due to the decrease of

the amount of the heat generated by the solar cell when using the 3-layers MLM heat sink.

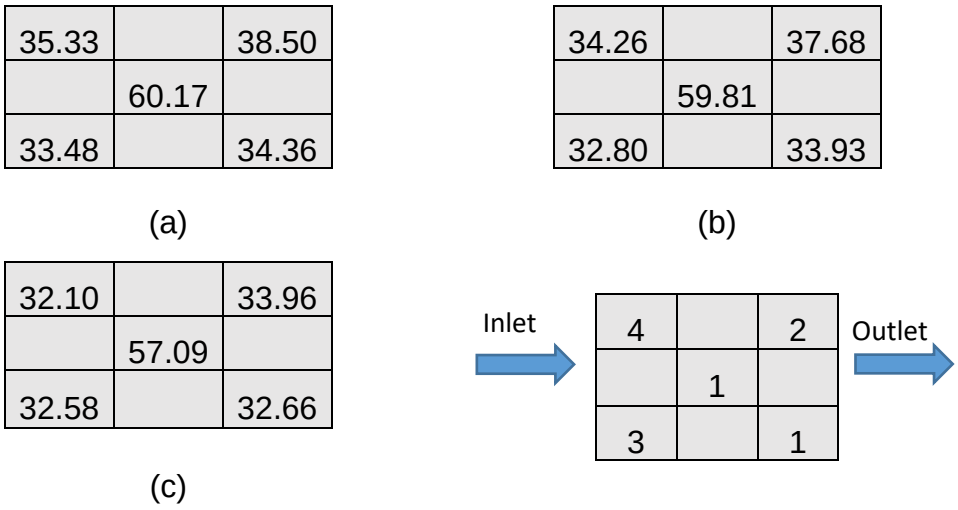

Figure 83. The surface temperature distribution of the copper substrate of 60ml/min HTF flow rate with 1000 W/m² irradiance intensity for the MLM heat sink of (a) 1-layer, (b) 2-layers and (c) 3-layers.

Table 20. HCPV-MLM electrical, thermal and total efficiencies with 1000W/m² irradiance intensity of different number of layers.

HTF flow rate (ml/min)	Number of layers								
	1-layer			2-layers			3-layers		
	η_{elec}	η_{th}	η_{tot}	η_{elec}	η_{th}	η_{tot}	η_{elec}	η_{th}	η_{tot}
30	6.87	24.01	30.88	6.89	23.79	30.68	7.16	22.69	29.85
40	6.90	25.23	32.13	6.93	23.59	30.52	7.21	22.40	29.61
50	6.90	25.13	32.03	6.93	23.63	30.56	7.25	21.40	28.65
60	6.89	26.30	33.19	6.89	24.19	31.08	7.19	20.15	27.34

4.5.2.4 Effects of HTF flow rate

In this section, the effects of the HTF flow rate on the I-V characterisation and thermal performance is analysed for the HTF flow rates ranged between 30ml/min to 300ml/min. Figure 84 shows the HCPV's maximum electrical power and solar cell temperature for the 2 and 3-layers MLM heat sinks. The maximum power of the 2-layers MLM heat sink for the HCPV is found to be 3.462W for the HTF flow rate of 30ml/min, with a maximum power of 3.536W at the 300ml/min HTF flow rate. This is considered as an improvement of 2.09%. For the 3-layers MLM heat sink, the maximum power is 3.608W for the 30ml/min HTF flow rate, with a maximum power of 3.75W at the HTF flow rate of 300ml/min and improvement of

3.93%. In Figure 84, the solar cell temperature with the different HTF flow rate for the 2 and 3-layers MLM heat sink. For the 2-layers MLM heat sink, the solar cell temperature is decreased from 63.26°C to 57.2°C for the 30ml/min and 300ml/min, respectively. Similar trend on reducing the solar cell temperature is noticed in the 3-layers heat sink of a decrease from 59.8°C to 55.5°C for the HTF flow rate of 30ml/min and 300ml/min, respectively. The reduction of the solar cell temperature is slightly when the HTF flow rate varied from 200ml/min to 300ml/min for the 2 and 3-layers MLM heat sinks.

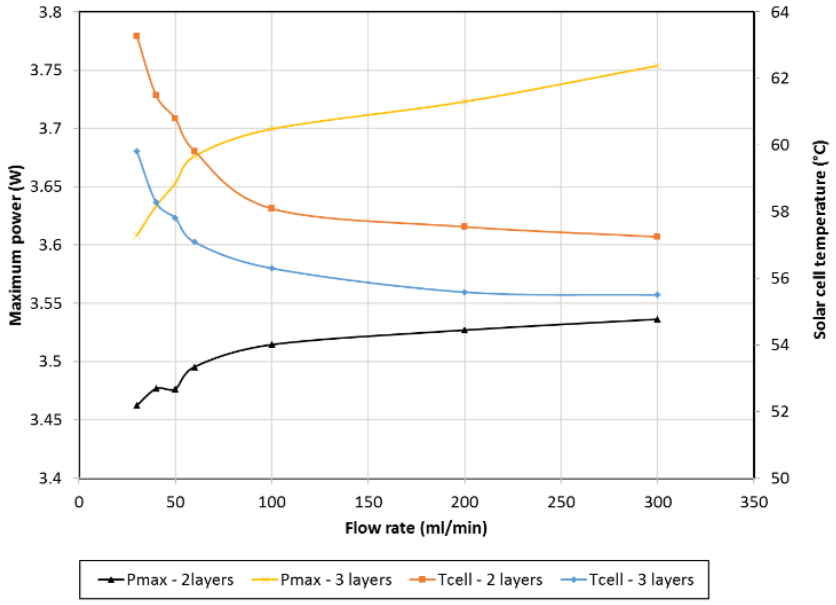

Figure 84. The effect of the HTF flow rate on the HCPV's maximum electrical power and solar cell temperature for 2-layers and 3-layers MLM heat sinks.

The heat rate extracted from the HCPV-MLM is calculated using the HTF mass flow, the heat capacity and the temperature difference between the inlet and the outlet. Figure 85 shows the calculated heat extracted by the HTF and the electrical power for the 2-layers MLM heat sink for the HTF flow rate ranged from 30ml/min to 300ml/min. It is observed that with the increase in the HTF flow rate, the discharged heat increased significantly from 12W in 30ml/min HTF flow rate to 16.33W in the 300ml/min. whereas a slight increase in the electrical power of 74mW between the two flow rates. In terms of percentage, the amount of heat removed from the MLM heat sink of 77.5% compared to 22.4% of the electrical generation at 30ml/min. For the 300ml/min HTF flow rate, the discharged heat is 82.2% where the electrical power reduces to 17.8%.

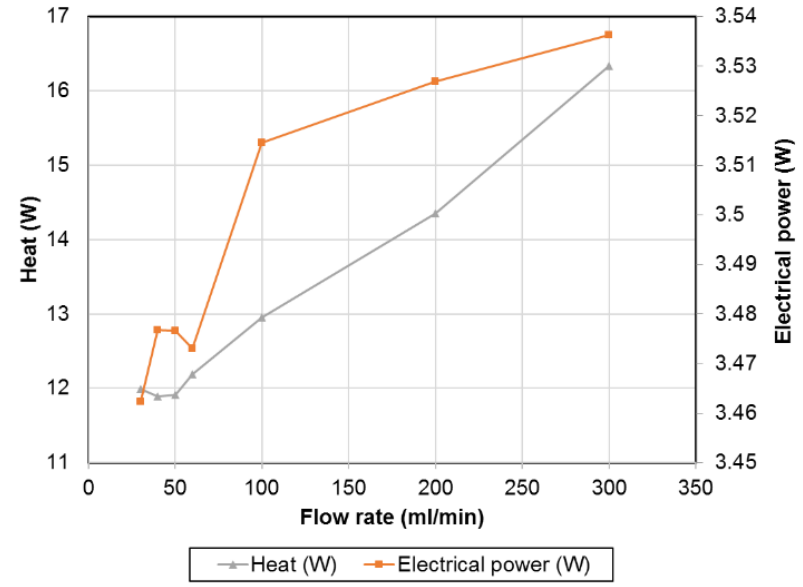

(a)

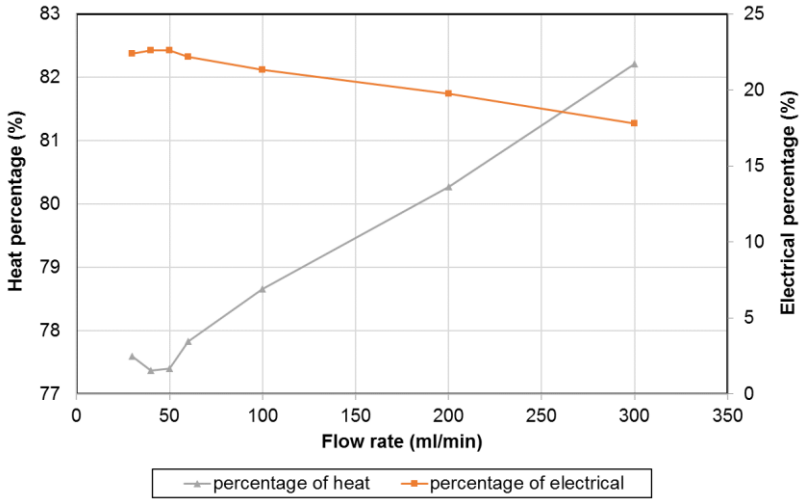

(b)

Figure 85. The electrical and heat powers of the HCPV-MLM using 2-layers for various flow rates and 1000 W/m² irradiance intensity for (a) powers and (b) their percentage.

Also, the effect of HTF flow rate on the electrical and thermal efficiency for each layer arrangement is shown in Table 20. It can be noticed a slight reduction of the electrical efficiency when the HTF flow is increased from 50 to 60ml/min for all the MLM heat sink arrangements. This might be referred to the experimental measurement error especially they have been done at the same day.

4.5.3 HCPV-heat sink outdoor test results

This section details the outdoor characterisation of HCPV-MLM module to evaluate its performance in ESI, Penryn campus location (50°10'15.4"N 5°07'40.2"W), UK. It provides a real performance data in collecting irradiances of

the I-V characterisation of the HCPV module. Because of the module degradation with long term exposure to the outdoor environment due to the weather variation throughout the year, this will require a long-term testing and needs to be taken into consideration for a detailed analysis in the future.

The fabrication details of the HCPV-MLM module used for the outdoor characterisation was discussed in section 4.4.3 and as per the setup described in section 4.4.4.3. The modules were characterised on the roof to avoid any objects shading effect. The solar irradiance logging period was every 5-seconds whereas the logging period for the I-V curve was every 5-minutes throughout the day. The solar cell temperature, HTF inlet temperature, HTF outlet temperatures was measured in 1-minute intervals to understand the effect of temperature and the amount of the collected heat. The ambient temperature and wind speed data were collected and reported using the weather station located at the same roof. A 3-layers MLM heat sink of 60ml/min HTF flow rate was selected due to their criteria of reducing the solar cell temperature as explained in sections 4.4.4.1 and 4.4.4.2. The weather during the planned period of outdoor testing was a typical Cornish summer day, with sunshine, rain and clouds. There was not a sunny day during September 2018, after several attempts the outdoor experiments were carried out in 3 days on 15th, 26th and 27th of September 2018.

4.5.3.1 First day (26th September 2018)

The weather during the first day of experiment was mostly sunny day and hence a high solar irradiance throughout the day. The variation of the direct solar irradiance and the output power of the HCPV system throughout is shown in Figure 86. It can be noticed a fluctuation in the direct solar irradiance this is due to short logging period of 5 seconds whereas the logging period for the I-V curve was every 5 minutes. The test was started at 11:30:00, the electrical output power of the system was 3.75W, corresponding to the solar irradiance of 751W/m² with a fill factor of 77.5%, short circuit current of 1.62A and an open circuit voltage of 2.99V. The maximum output power output of the system was 4.49W, corresponding to maximum solar irradiance of 896 W/m² reached at 14:11:00. The fill factor was calculated as 76% and the maximum short circuit current was 1.97A at this maximum solar irradiance. Then, the system output was decreased gradually as the solar irradiance decreased and reached to 1.59W at a solar

irradiance of 181W/m^2 at 18:30:00 by the end of the test. The outdoor experimental investigation shows an expected increase of the power produced by system compared to the indoor results due to the increase of the optical efficiency.

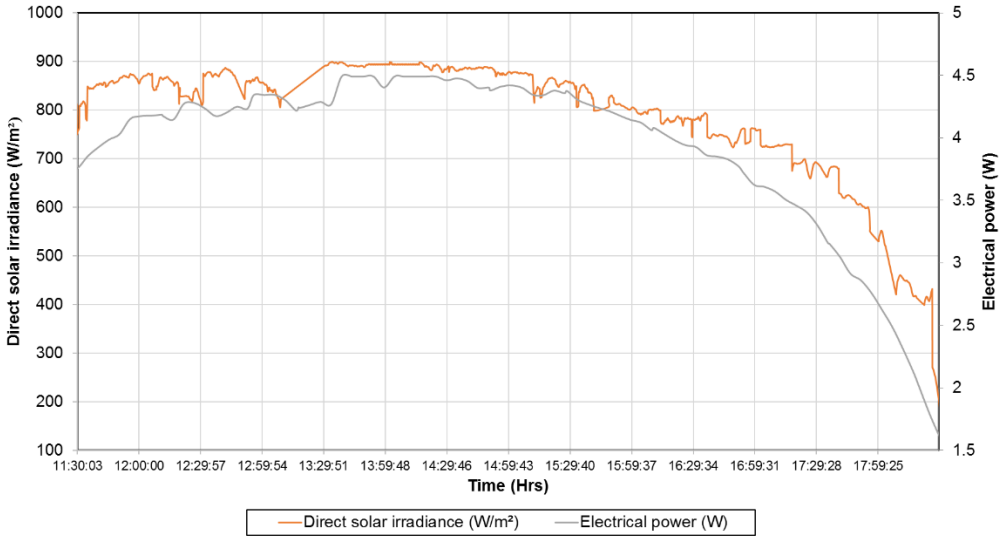

Figure 86. Variation of the direct solar irradiance and the electrical power throughout the day.

The electrical power output versus the direct solar irradiance is shown in Figure 87. A linear approximation was plotted between the two parameters. It can be noticed that most of the contribution results is from the higher intensities of more than 800W/m^2. This is due to high intensity of the solar throughout the day and the only the low solar irradiance intensity occurred by the end of the day.

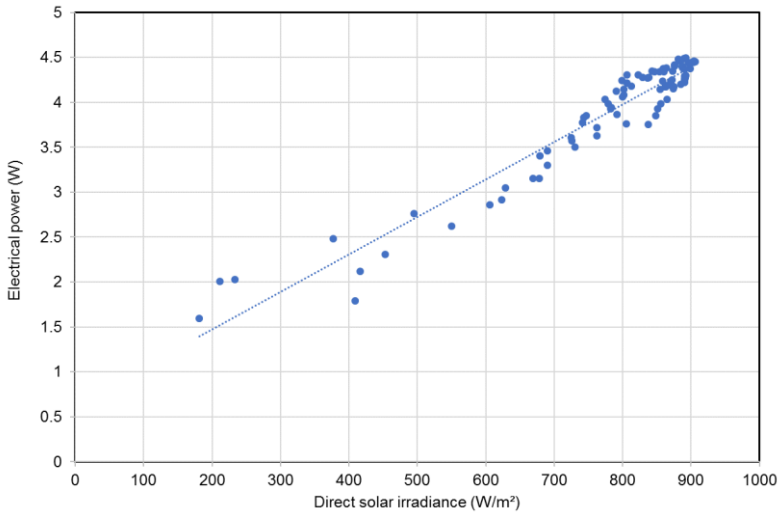

Figure 87. The output power of the HCPV versus direct solar irradiance.

The linear approximation of the short circuit current and open circuit voltage versus the direct solar irradiance is shown in Figure 88 and Figure 89,

respectively. Similar to the output power an approximation, the high intensities point contributed more than in the lower intensities. It is noticed that the short circuit current is more than 1.5A in the high intensity part. However, a small variation of the open circuit voltage is noticed of within of 0.1V.

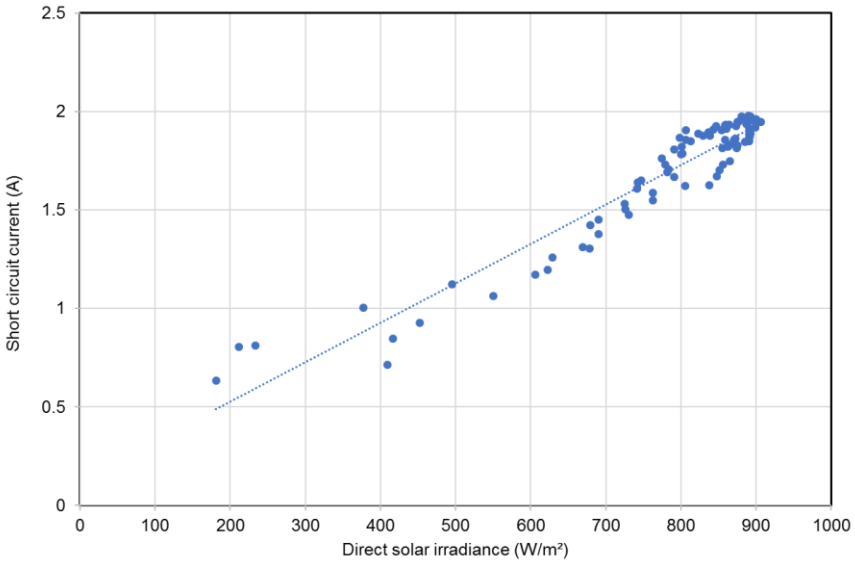

Figure 88. The short circuit current of the HCPV versus the direct solar irradiance.

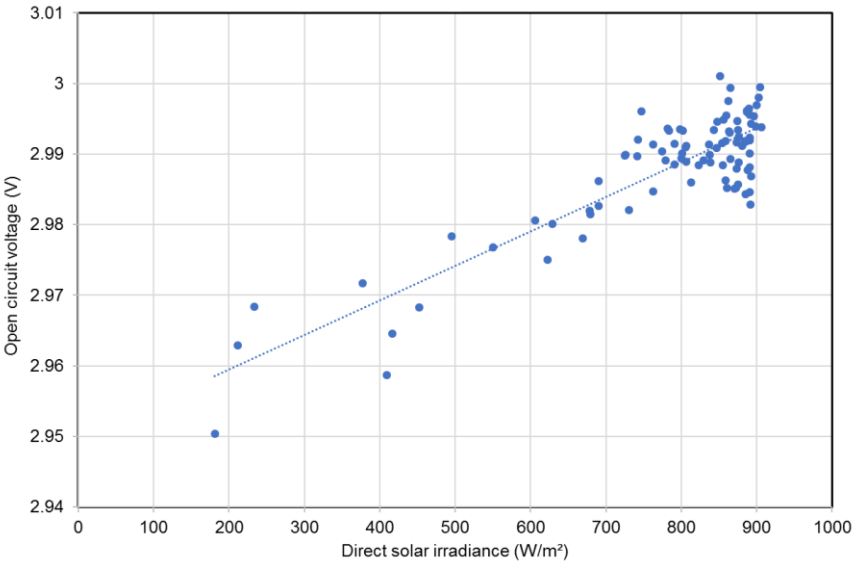

Figure 89. The open circuit voltage of the HCPV versus the direct solar irradiance.

The thermal analysis of the system is an important part and this is investigated using the solar cell temperature and the extracted heat. As explained before that the heat extracted from the HCPV-MLM is calculated using the HTF mass flow, heat capacity and HTF temperature difference. Figure 90 shows the solar cell temperature and the calculated heat extracted by the HTF. It is observed that the maximum solar cell temperature reached during the day is of 62.99°C, which is

considered within the solar cell manufacturer limit. A lower temperature could be achieved for a higher HTF flow rate but this will mean a higher pressure drop and hence more pumping power. As expected, the extracted heat increases with the increase of the solar irradiance. Throughout the day, the amount of extracted heat varies between 13.69W to 6.20W. At the maximum electrical output power, the amount of the extracted heat was 12.12W which represents of around 63%.

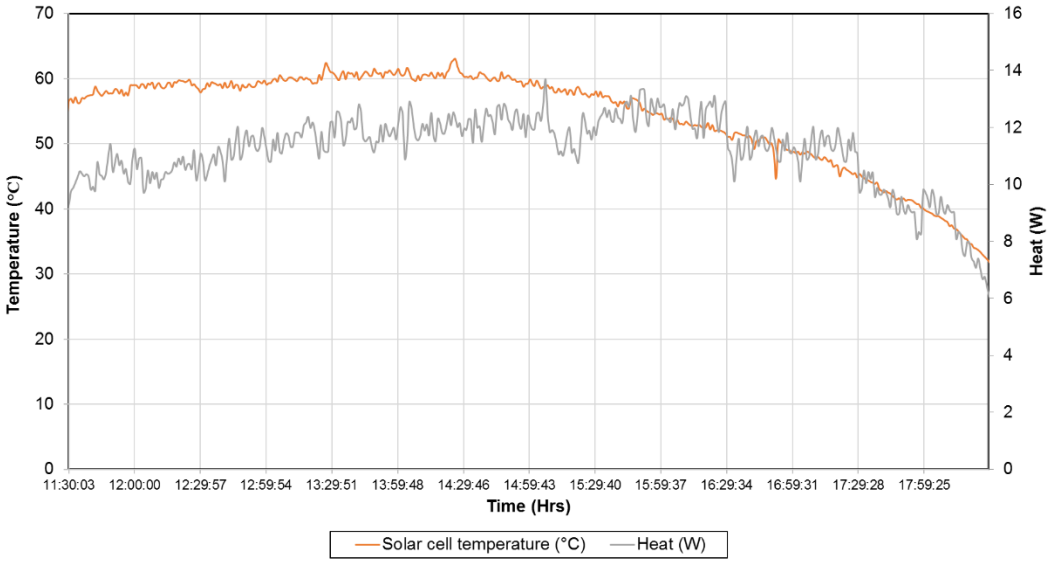

Figure 90. Variation of the solar cell temperature and the extracted heat by the HTF throughout the day.

4.5.3.2 Second day (27th September 2018)

The second day of the outdoor experiment was carried out on the 27th of September 2018. During this day, there was a clear sunny day without any clouds. This explains as on the first day the high electrical generated by HCPV-MLM module. The variation of the solar irradiance and the electrical power generated by the HCPV module is shown in Figure 91. The experiment was started at 11:30:00 and ended at 18:30:00. At the beginning of the experiment, the module received a large amount of solar irradiance of 851W/m² which caused a power generation of 4.45W. The filling factor was 75.5%, short circuit current of 1.959A and an open circuit voltage of 3.0V. During the day, the maximum output power output of the system was found to be 4.59W, corresponding to maximum solar irradiance of 881W/m² at 13:21:00. The fill factor was recorded as 75.1% and the maximum short circuit current was 1.96A during the time of maximum solar irradiance. After, that the direct solar irradiance decreased and reached its minimum by the end of the experiment of 226W/ m2 where the power generated reached to 0.88W.

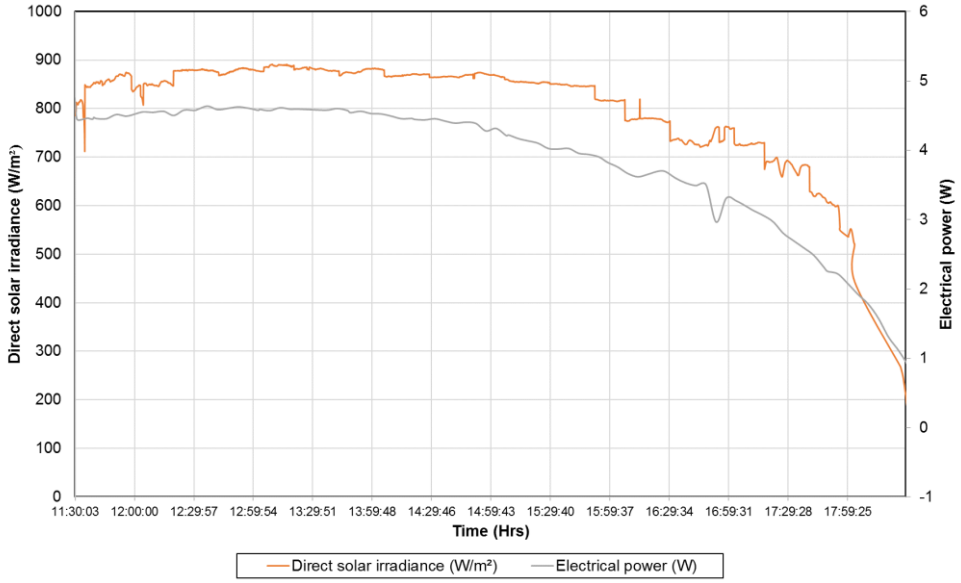

Figure 91. Variation of the direct solar irradiance and the electrical power throughout the day.

The electrical power output versus the direct solar irradiance is shown in Figure 92. Similar to the previous day, most of the linear approximation contribution is from the higher intensities of more than 800W/m^2 where better power output of the system is achieved. This is due to high intensity of the solar throughout the day and the low solar irradiance intensity occurred only by the end of the day.

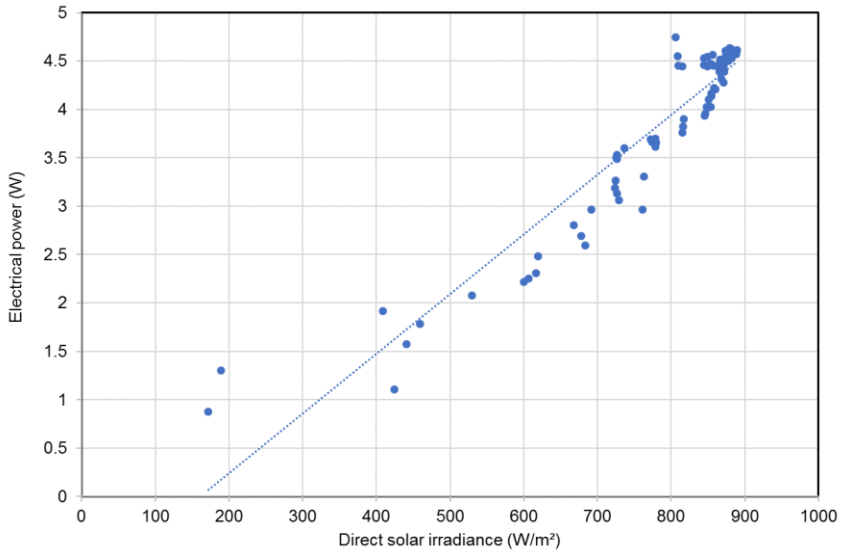

Figure 92. The maximum power of the HCPV versus the solar irradiance.

The linear approximation of the short circuit current and open circuit voltage versus the direct solar irradiance is shown in Figure 93 and Figure 94, respectively. Similar to the output power an approximation, the high intensities points contributed more than in the lower intensities. It is noticed that the short

circuit current is more than 1.5A in the high intensity part. However, a small variation of the open circuit voltage is noticed of within of 0.1V.

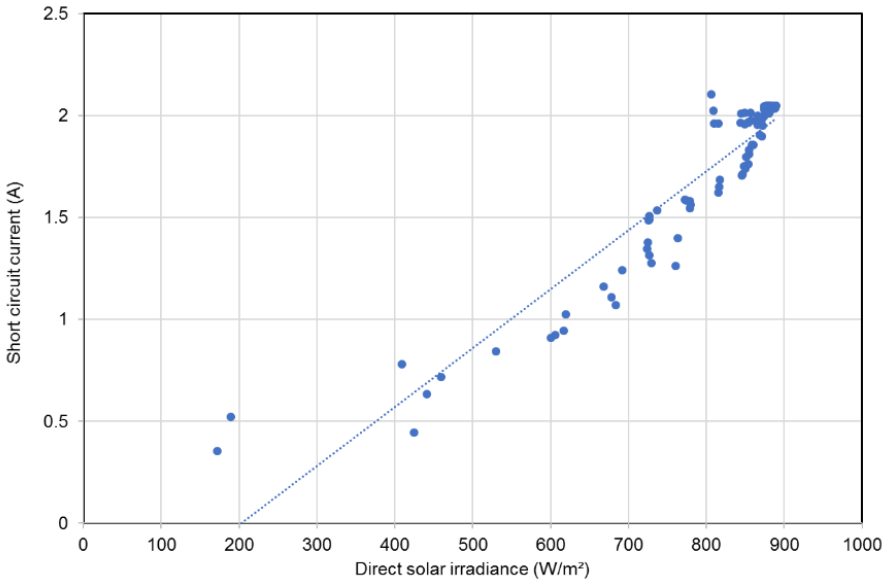

Figure 93. The short circuit current of the HCPV versus the direct solar irradiance.

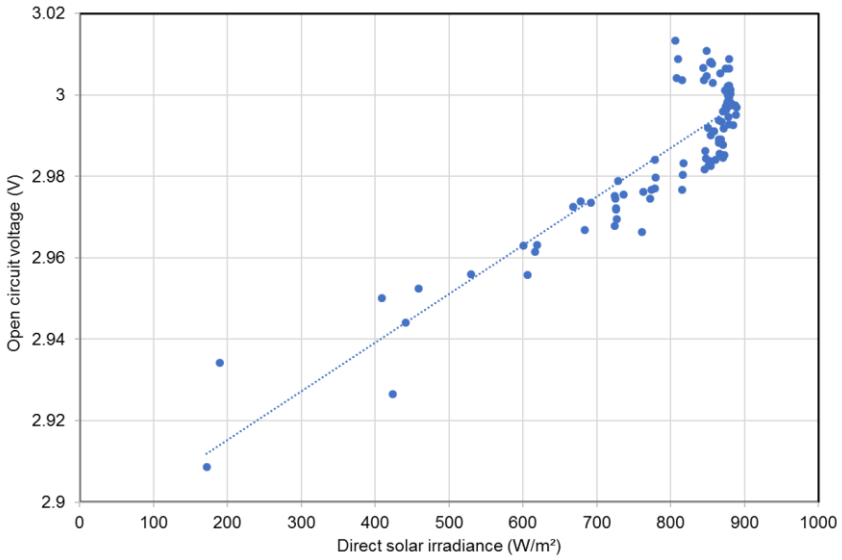

Figure 94. The open circuit voltage of the HCPV versus the direct solar irradiance.

Figure 95 shows the solar cell temperature and the calculated extracted heat by the HTF. The maximum solar cell temperature reached during the day is of 60.25°C, which is considered within the solar cell manufacturer limit. As expected, the extracted heat increases with the increase in the solar irradiance. Throughout the day, the amount of extracted heat varies between 12.84W to 4.185W which represents to the total absorbed energy of 83% and 74.9%, respectively.

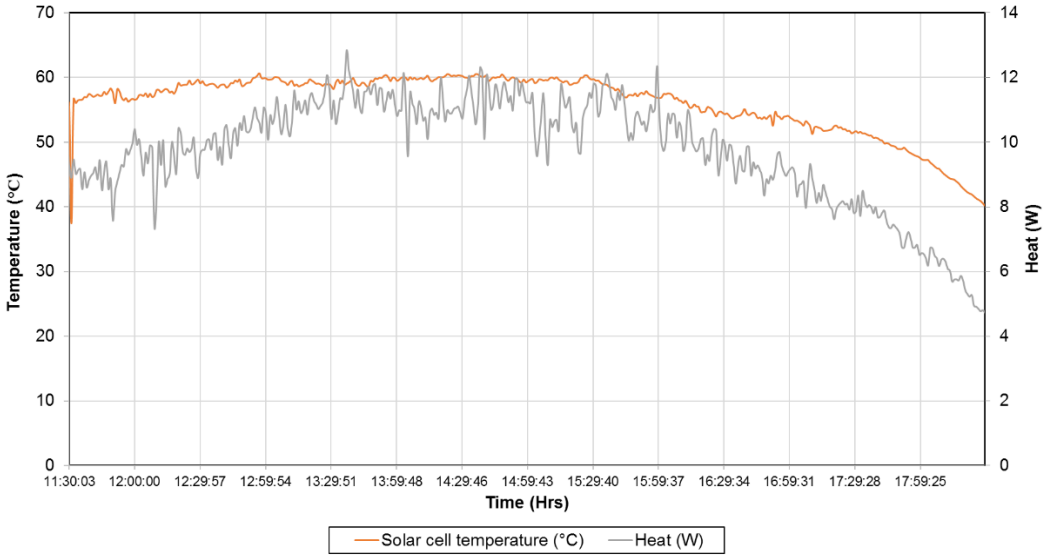

Figure 95. Variation of the solar cell temperature and the extracted heat by the HTF throughout the day.

4.5.3.3 Third day (15th September 2018)

The HCPV-MLM module was tested in a rapid changing weather which is considered as a typical weather day here in the UK. Figure 96 shows the maximum power generated by the module and the DNI from 11:30:00 to 17:05:00. It can be seen that the DNI is lower than the discussed previous two days where its maximum is 800W/m². At the beginning of the day, the DNI is very low and this is due to the cloudy weather condition. More sunny is noticed at 12:41:00 is noticed reaching at 746W/m². At this time, the power generated by the HCPV-MLM is still low due to the rapid change in the weather. The maximum power generated by the solar cell was 2.977W occurred at 13:42:00. The low generation of the power at some of the higher DNI is believed due to the difference in the logging time between the DNI and the I-V tracer as explained before.

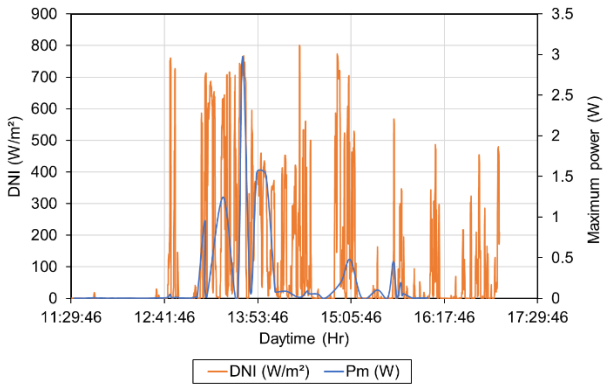

Figure 96. Variation of the direct solar irradiance and the electrical power throughout the day.

The variation of the solar cell temperature throughout the day is shown in Figure 97. It can be noticed that when no DNI reaching to the solar, its temperature is almost fixed to 19°C. The maximum solar cell temperature reached to 45.19°C when the direct solar irradiance reached to 746 W/m².

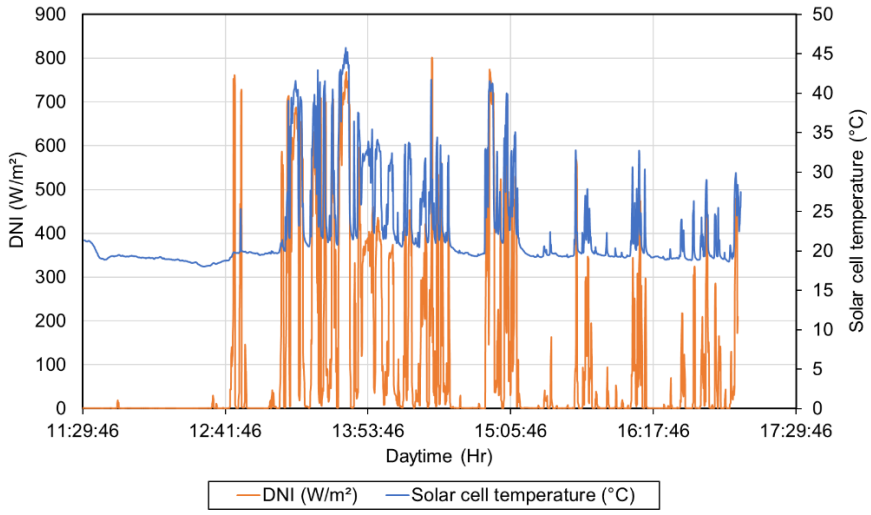

Figure 97. Variation of the direct solar irradiance and the solar cell temperature throughout the day.

4.6 Conclusions

The MLM heat sink for the HCPV applications has been carried out and analysed in terms of the electrical and thermal parameters. Different numerical and experimental investigations were conducted. First of all, the concept of multi-layer microchannel heat sinks for CPV applications was studied numerically using the entire domain (the heat sink and CPV) and three-dimensional model. The effect of variation of the number of layers and the channel width and height was investigated. The electrical and thermal model was coupled for an accurate calculation of the generated thermal heat of the solar cell. The results show a significant improvement of the heat sink performance in terms of the solar cell temperature, the thermal resistance and the fluid pumping power as the number of layers increases for the same HTF flow rate. The 3-layers microchannel heat sink was considered for the investigation of the channel height and width on the heat sink performance. The results show that the variation of the height of the channel height and the width has no effect on the maximum solar cell temperature. However, the fluid pressure drop along the channel is reduced significantly as the channel height was increased from 500μm to 1000μm i.e. a reduction in fluid pumping power consumption. The effectiveness of multi-layer

microchannel heat sink also depends on other design parameters such as the fluid inlet/outlet manifold and the fluid mass flow rate.

The non-uniform heat source on the MLM heat sink was investigated for a power rate of 30W. The results show a reduction of the heat sink thermal resistance by 17% as the number of layers increases from 1-layer to 2-layers. The results also show that the single layer MLM heat sink experiences the highest temperature difference between the centre of the heat source surface and the other locations causing a large temperature non-uniformity and a high standard deviation compared to the 2-layers and 3-layers MLM heat sinks. The numerical model shows that the hot spot in the heat source surface shifts to the centre as the number of layers increased and more temperature uniformity is achieved to the edge of the heat source near to the downstream side.

The indoor IV-characterisation of the HCPV-MLM heat sink module has been carried out for the different heat sink layers and HTF flow rates. The experiments show an increase on the maximum power produced by the module of 0.97W when using the homogeniser made from glass compared to the one made from crystal resin material. In terms of the effect of the number of layers, the results show an increase of 9.4% of the electrical power generated by the module when using the 3-layers MLM heat sink compared to the 1-layer MLM heat sink. In addition, the solar cell temperature decreased by 3.15°C when the number of layers increased from 1-layer to 3-layers.

At end of the chapter, the I-V and thermal characterisation of the HPCV-MLM module in the outdoor environment was presented. The module was mounted in the solar tracker for two sunny days and one mostly cloudy day at ESI Penryn campus location in the UK. A better electrical performance of the module was achieved in the outdoor compared to the indoor tests. The maximum electrical power of the module is 4.59W at a direct solar irradiance of 881W/m^2. The results show a high solar cell performance where the solar cell temperature was kept under 60°C.

Chapter 5 : PCM thermal storage: design, fabrication and experimental characterization

The PCM storage system is one of the major components of the CPV-PCM. This chapter presents a standalone study and analysis of a PCM thermal storage system. The system of the PCM storage analysis is first evaluated using a numerical analysis of the computational fluid dynamics (CFD) modelling technique using COMSOL. The simulations analyse various effects of system variables such as the geometry and materials. After that, an experimental assessment of a single PCM storage system is conducted to validate the model and to study in depth the effect of various operating conditions such as Heat Transfer Fluid (HTF) flow rate, its inlet temperature, the storage orientation, PCM melting temperature and its heat storage density as influence of performance. Following this, an experimental study of multi-stage PCM thermal storage is conducted to explore the enhancement parameters of using this technique. Additionally, the detailed parametric study of multi stage storage are discussed using the numerical approach.

5.1 Fundamentals of CFD on PCM modelling and data analysis

5.1.1 Introduction

Computation Fluid Dynamics (CFD) is the analysis of systems involving fluid flow and heat transfer using computer-based simulation. At present, the CFD approach is considered as a powerful tool for a wide range of heat transfer applications [268] due to its unique advantages:

- The CFD technique is considered as faster and cheaper compared to the experimental approach especially in a high-quality setup.
- In a very complicated system, it is very difficult to run it in ideal boundary and initial conditions such as uniform heat density, flow and adiabatic surfaces. These conditions are ideally controlled when using the CFD approach.
- Some measurements are very hard to obtain in the experimental approach due to confined space to insert an instrument or inaccessible locations whereas, the CFD approach has the ability to evaluate the parameters in those locations.

In this thesis, CFD approach has been used in the design to geometry, selection of PCM, selection of system construction materials, etc. The CFD is used as an important tool in the design stage to maximize the amount of the stored heat and hence improve the efficiency of the heat storage system. Also, the validated CFD model offers to explain the behaviour of the PCM along with the experimental results such as the heat transfer using the natural convection.

Modelling of PCMs is complicated due to the complexity of the behaviour of the PCMs during the phase transition [269]. The common features of PCMs are the change in the thermo-physical properties, the boundary movement of the solid-liquid during phase transition, convection heat transfer mode during the melting and the volume change(expansions or contraction) [270]. This section aims to provide an overview of the modelling of a cylindrical PCMs thermal storage system.

5.1.2 Mathematical modelling of PCM

Various methods have been founded to solve the PCM boundary problems. Among them, the two main methods are the fixed-grid and the moving deformable-grid [271]. The fixed-grid method uses similar conservation equations and boundary conditions for both solid and liquid phases. The interface conditions are described as source terms in the governing equations and latent heat value is assigned to each element according to the enthalpy or temperature. In this method, a large force is added to PCM (infinite viscosity) in the solid phase and this force is eliminated to zero for the PCM in the liquid phase. The moving deformable-grid method is based on the classical Stefan formulation on the governing equations and the solid-liquid phase interface is explicitly solved. The phase change is tracked continuously and the latent heat is treated as a moving boundary [272].

There are two modelling approaches available for the analysis of the PCM heat transfer problems, namely temperature-based method (TBM) and the enthalpy-based method (EBM) [273]. The enthalpy method is considered as the most popular approach in the PCM numerical modelling to solve the boundary problem [13] [274]. The main advantage of this method is to obtain the solution on the fixed space grid [275]. This means that the enthalpy method solves the enthalpy as a temperature dependent variable through the integration of the volume

elements. There are two common formulations of the enthalpy method using the apparent heat capacity formulation and the source based formulation [275]. In the present investigation the apparent heat capacity formulation for a fixed grid was used the modelling of PCMs.

In a solid PCM undergoing to a liquid phase transformation (i.e. melting), the conservation of energy equation can be written in terms of the mixture enthalpy L (J/kg) as [275]:

$$\frac{\partial(\rho L)}{\partial t} + \nabla.(\rho u L) = \nabla.(k \nabla T) \quad 5.1$$

where ρ, u, T and k are PCM density, velocity, temperature and thermal conductivity, respectively. The general definition of the mixture enthalpy (L) is as the following [276]:

$$L = (1 - f) \int_{T_{ref}}^{T} C_s \, dx + f \int_{T_{ref}}^{T} C_l \, dx + fH \quad 5.2$$

where f, T_{ref}, C_s and C_l are the liquid volume fraction of liquid phase, reference temperature, and the specific heat of solid, specific heat of liquid, respectively. The two common enthalpy methods are the apparent heat capacity method (AHCM) and the source-based method (SBM). The enthalpy function used in the apparent heat capacity is not included in the governing equation and the phase change is not simultaneously tracked but derived afterward from the calculated temperatures [277]. This causes faster solution in the general heat transfer packages. In the SBM method, the latent heat evolution is represented by a suitable source term [271].

In this study, the AHCM is used to model the PCM problem. Therefore, instead of adding a latent heat L in the energy balance equation when the material reaches its melting temperature (T_m), it is derived from its temperature. Therefore, it is assumed that the melting of PCM occurs in a temperature interval of ΔT and between $T_m - \Delta T/2$ and $T_m + \Delta T/2$. In this interval, the liquid fraction of PCM (f) is modelled by a smoothed function which is represented by:

$$f(T) = \begin{cases} 0, & T \leq (T_m - \frac{\Delta T}{2}) \\ \frac{T - T_m + \frac{\Delta T}{2}}{\Delta T}, & \left(T_m - \frac{\Delta T}{2}\right) < T < (T_m + \frac{\Delta T}{2}) \\ 1, & T \geq (T_m + \frac{\Delta T}{2}) \end{cases} \quad 5.3$$

Therefore the PCM heat capacity is expressed as [278]:

$$C_p = \frac{1}{\rho}\left[(1 - f(T))\rho_s C_{ps} + f(T)\rho_l C_{pl}\right] + C_L(T) \quad 5.4$$

Where $C_L(T)$ is expressed as:

$$C_L(T) = L\frac{d\alpha_m}{dT} \quad 5.5$$

And

$$\alpha_m = \frac{1}{2}\frac{f(T)\rho_l - (1-f(T))\rho_s}{\rho(T)} \quad 5.6$$

The changes in the other PCM thermo-physical properties during the phase transition are expressed as the following:

$$\rho(T) = f(T).\rho_{solid} + (1 - f(T)).\rho_{liquid} \quad 5.7$$

$$k(T) = f(T).k_{solid} + (1 - f(T)).k_{liquid} \quad 5.8$$

5.1.3 Modelling of cylindrical PCM storage

The modelled PCM storage system consists of three domains: PCM, HTF and the tube. The model domains and its boundary conditions are shown in Figure 98. The HTF is set as an inlet boundary condition with a constant temperature (T_{in}) and a constant water volume flow rate. The outlet HTF is set as heat outflow boundary with a normal flow fluid outlet. The following assumptions have been considered in the model:

- The flow of the HTF is fully developed.
- The PCM is pure, homogeneous, and isotropic.
- The PCM melting process occurs over a range of phase transition temperature (ΔT)
- The ambient temperature is 24°C.
- The outer wall of the storage is exposed to a natural convection of a heat transfer coefficient (h) is 5.8W/m^{2}K.
- Adiabatic walls are in the storage top and bottom.

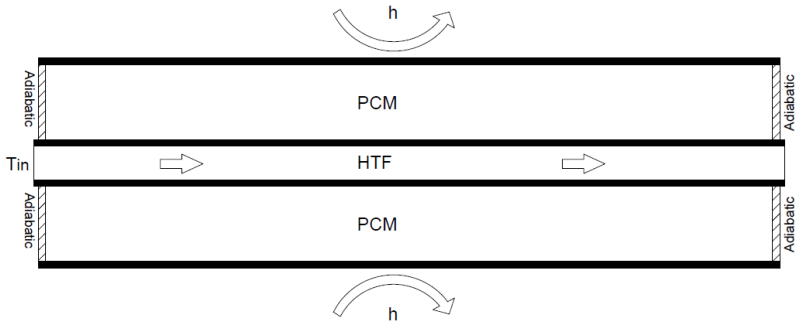

Figure 98.Schematic of model domain showing the boundary conditions

The heat transfer processes involved in the system are the heat transfer by conduction and convection. The general heat conduction equation used in this analysis for a cylindrical geometry with no circumferential variation, constant materials properties and without internal heat generation is expressed as [279]:

$$\rho C_p \frac{\partial T}{\partial t} = \frac{1}{r}\frac{\partial}{\partial r}\left(kr\frac{\partial T}{\partial r}\right) + \frac{\partial}{\partial z}\left(k\frac{\partial T}{\partial z}\right) \quad 5.9$$

The heat transfer due to convection is between the HTF and the tube wall, the energy equation is given by[215]:

$$\rho C_p \left(\frac{\partial T}{\partial t} + v_r\frac{\partial T}{\partial r} + v_z\frac{\partial T}{\partial z}\right) = k\left[\frac{1}{r}\frac{\partial}{\partial r}\left(r\frac{\partial T}{\partial r}\right) + \frac{\partial^2 T}{\partial z^2}\right] + q \quad 5.10$$

where ρ and k represent the density and the thermal conductivity of the HTF respectively. During the phase change, the PCM absorbs heat in forms of latent heat (L). The apparent PCM heat capacity (Cp) used in the heat equation is given by:

$$C_p(T) = C_{p,solid} + \left(C_{p,liquid} - C_{p,solid}\right).f(T) + L.D(T) \quad 5.11$$

where D(T) is a smoothed Gaussian function which is zero everywhere except in the melting interval and is expressed:

$$D(T) = \frac{e^{\frac{-T(T-T_m)^2}{\Delta T^2}}}{\sqrt{\pi\Delta T^2}} \quad 5.12$$

In this model, the PCM is assumed to be in liquid phase. The mass, momentum and energy conservation equations are coupled with the heat transfer diffusion. The momentum conversion equation is modified to model the phase change using two forces: buoyancy force (F_b) and the force to control the solid phase (F_a). These are expressed as the following:

$$\overrightarrow{F_b} = -\rho_{solid}(1 - \beta(T - T_m))\vec{g} \quad 5.13$$

$$\overrightarrow{F_a} = -A(T)\vec{u} \quad 5.14$$

where β is the coefficient of thermal expansion (K^{-1}) and A(T) is expressed as:

$$A(T) = \frac{-C(1-B(T))^2}{(B(T)^3+q)} \quad 5.15$$

where C and q are constants and equal to 10^5 and 10^{-3}, respectively.

5.1.4 Modelling results

The PCM storage performance is evaluated using different parameters such as temperature distribution, melting time and melting profile. In addition, some derived parameters such as average heat transfer coefficient and thermal resistance can be used to express the system performance.

5.1.4.1 Average heat transfer coefficient

The convection heat transfer coefficient (h) is defined as the rate of heat transfer between a tube surface and a fluid per unit surface area per unit temperature difference [280] and it is important in representing the amount of heat transferred to the PCM. Because of the temperature variation between the outer surface of the HTF tube and the PCM along both the axial and radial directions, the heat transfer coefficient is very difficult to be calculated accurately for the PCM storage system. However, the average heat transfer coefficient for the melting process is calculated instead [281]. The heat transfer rate (q) to the PCM storage can be calculated through the enthalpy reduction rate in the HTF [199] and can be calculated through the following equation:

$$q = \dot{m}C_p(T_{in} - T_{out}) \quad 5.16$$

Where, $\dot{m}$ is the HTF mass flow rate, T_{in} and T_{out} are the temperature of the inlet and outlet of the HTF, respectively. The convection heat transfer coefficient (h) is expressed by:

$$h = \frac{q}{A\,.\,\Delta T_{LMTD}\,.t} \quad 5.17$$

The average heat transfer coefficient during the charging period is calculated using the following equation:

$$\bar{h} = \frac{Q_{total}}{A\,.\,\Delta T_{LMTD}\,.t} \quad 5.18$$

Where, Q_{total} is the total heat absorbed by the PCM during the charging time. The logarithmic mean temperature difference (LMTD) is represented by:

$$\Delta T_{LMTD} = \frac{T_{inlet} - T_{outlet}}{\ln\left[\frac{T_s - T_{outlet}}{T_s - T_{inlet}}\right]} \quad 5.19$$

Where, T_s is the tube surface temperature of HTF. The performance of the PCM heat exchanger can also be represented by its effectiveness. The instantaneous effectiveness at any point of time over the phase change period is presented by [209]:

$$\varepsilon = \frac{(T_{in} - T_{out})}{(T_{in} - T_{PCM})} \quad 5.20$$

The average effectiveness is presented by:

$$\bar{\varepsilon} = \int_0^t \varepsilon \, dt \quad 5.21$$

5.1.4.2 Thermal resistance network

The PCM heat exchanger consists of two mediums (PCM and the HTF) separated by the tube wall. The heat transfer starts as soon as the HTF enters the tube and the temperature profile starts developing in the system in the axial and radial directions. The heat is first transferred from the HTF to the tube wall by forced convection, through the tube wall by the conduction and from the tube wall to the PCM by the natural convection [280]. Three thermal resistances are associated with the heat transfer in the PCM heat exchanger storage, HTF convective heat resistance (R_f), conduction thermal resistance across the tube thickness (R_w) and the PCM convective heat resistance (R_l) as shown in Figure 99 [280]. It is more convenient to represent the thermal resistances in mK/W due to its change with the length of the tube in the PCM medium. The values of R_f,R_w and R_{PCM} are determined using the following equations:

$$R_f = \frac{1}{\pi h_f D_i} \quad 5.22$$

$$R_w = \frac{1}{2\pi k_w} \ln\left(\frac{D_o}{D_i}\right) \quad 5.23$$

$$R_{PCM} = \frac{1}{2\pi k_{PCM}} \ln\left(\frac{D_{PCM}}{D_o}\right) \quad 5.24$$

More heat transfer rate between the HTF and the PCM is achieved by decreasing the thermal resistance values. Therefore, the resistance of the HTF can be reduced by increasing the heat transfer coefficient (h_f) or increasing the inner tube

diameter (D_i). In addition, decreasing the thermal resistance of the tube wall and the solid PCM is by increasing the materials thermal conductivity or reducing the thickness of the tube and the PCM.

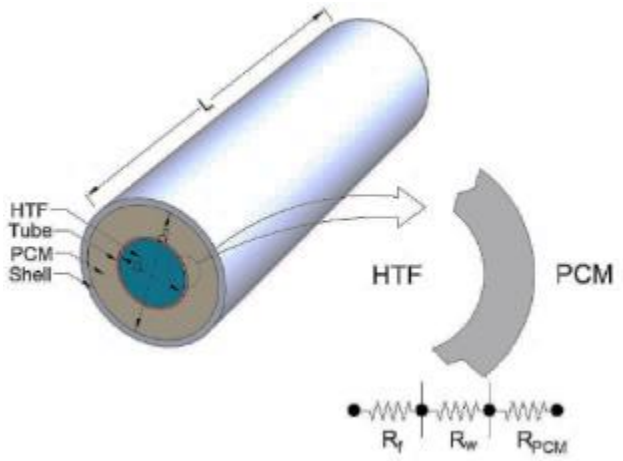

Figure 99. PCM heat exchanger thermal resistance network.

5.1.4.3 Dimensional analysis

Characterization of a fluid flow inside a tube is an important and this can be done using the Reynolds number (Re), which is presented by the following equation:

$$\mathrm{Re} = \frac{\rho_f . u_f . D}{\mu_f} \qquad 5.25$$

Where u_f is the mean fluid velocity in the tube cross section, D is the tube diameter, μ_f and ρ_f are the fluid's dynamic viscosity and density, respectively.

The natural convection takes place as the PCM melts and this can be quantified using the Grashof number. It represents the natural convection effect and presented by the following equation [212]:

$$\mathrm{Gr} = \frac{g\,\beta\,(T_s - T_f)\,r_e}{v_{pcm}^2} \qquad 5.26$$

Where, g is the gravity (m/s²), β is the coefficient of volume expansion (1/K), T_s is the temperature of the solid surface, T_f is the temperature of the liquid, r_e is the characteristic length of the geometry and v_{pcm} is the kinematic viscosity of the fluid (m²/s). The Nusselt number is used to quantify heat transfer and calculated using [228]:

$$\mathrm{Nu} = \frac{h\,r_e}{k_{pcm}} \qquad 5.27$$

Where, k_{pcm} is the thermal conductivity of the PCM. Nu_m is the mean Nusselt number and calculated by:

$$\overline{Nu} = \frac{\bar{h}\, r_e}{k_{pcm}} \qquad 5.28$$

5.1.4.4 The experimental case study by Longeon

Longeon et al.[194] experimentally has studied the process of melting of the PCM in the shell-and-tube storage unit with the PCM on the shell side, and the HTF flows inside the tube. Additionally, they have conducted a series of experiments to study the effect of heat charging scenarios on the heat transfer process.

5.1.4.5 The experimental setup description

Test rig proposed by Longeon consists cylindrical PCM storage with a HTF tube placed inside the PCM storage. The test rig is placed vertically and the PCM is filled in the shell with the diameter of D_o, whereas the HTF flows through the tube with diameter of D_i. The HTF tube is made of stainless steel and has an inner diameter of 15mm and a thickness of 2.5 mm. The outside tube is made of Plexiglas and of an inner diameter of 44 mm and length of 400 mm. The amount of the used PCM is 480g with an estimated thermal storage capacity of 120kJ (from 28^{o}C to 46^{o}C). A paraffin RT35 is used as the PCM with a melting temperature of 35 °C and its physical and thermal properties as given by the manufacturer are presented in Table 21.

The experimental loop studied by Longeon is shown in Figure 100. Thermobath is used to control water temperature. Hot water at temperature of 54^{o}C is circulated through the stainless-steel tube with an average inlet velocity of 0.01 m/s. several thermocouples have been installed at various locations to monitor the PCM and water temperature during the testing duration. Thermocouple signals are recorded in a PC using a data acquisition unit. As per the authors, the heat loss effect from the PCM to the ambient is minimized due to the PCM melting temperature is close to the ambient temperature.

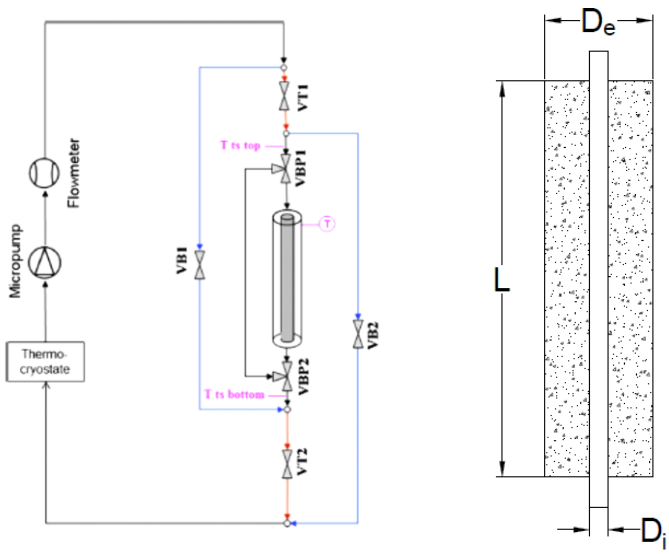

(a) (b)

Figure 100. Schematic of (a) experimental loop and (b) test section [194].

Table 21.Thermo-physical properties of RT35 by Rubitherm®.

Property	Value
Melting Temperature, Tm	35 ºC
Liquid density, ρ_l	760 kg/m^3
Solid density, ρ_s	880 kg/m^3
Thermal conductivity, k	0.2 W/(m.K)
Liquid specific heat, C_{pl}	2400 J/kg.K
Solid specific heat, C_{ps}	1800 J/kg.K
Latent heat, L	157 KJ/Kg
Viscosity, μ	3.3x 10-3 m^3/s
Thermal expansion coefficient, β	0.00091 1/K

5.1.4.6 Validation of the CFD model

A Model to represent the Longeon's PCM thermal storage heat exchanger experiment was conducted using COMSOL multi-physics software. The PCM test section was modelled using a 2D axisymmetric geometry. The model domains were the PCM, the HTF and the HTF tube. The PCM container was neglected for simplicity reason and the thermal loss was presented using the natural convection rate.

The appropriate mesh used in the numerical model was an important for accurate results and saving the computational time and effort. Because of the fluid behaviour of most of the domains (water and PCM), all domains were meshed using the triangular fluid dynamics meshing because of the PCM behaviour. Five different meshing sizes (coarse, normal, fine, finer and extra fine) were selected to investigate its effect on this PCM storage model. The details of the examined

meshes sizes are shown in Table 22. The simulations ran using PARDISO (Parallel Direct Sparse Solver) which is a direct solver to solve non-linear system.

Table 22.The computational mesh sizes.

Mesh#	Mesh type	Number of elements (NoE)	Minimum/ maximum size (mm)	Mesh distribution
Mesh 1	Coarse mesh	7526	0.096/2.14	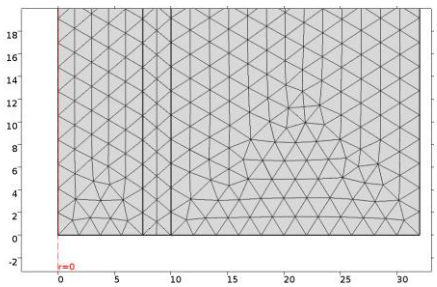
Mesh 2	Normal mesh	15640	0.064/1.44	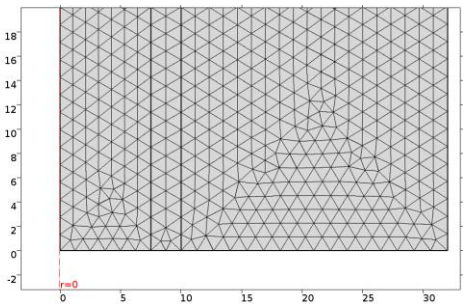
Mesh 3	Fine mesh	26544	0.032/1.12	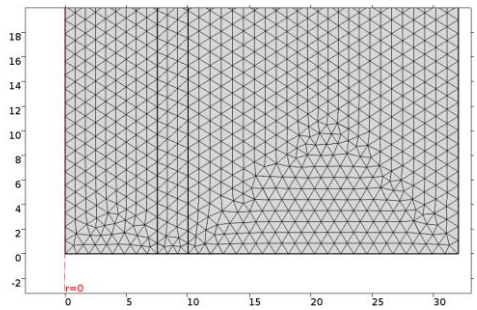
Mesh 4	Finer mesh	41182	0.0128/0.896	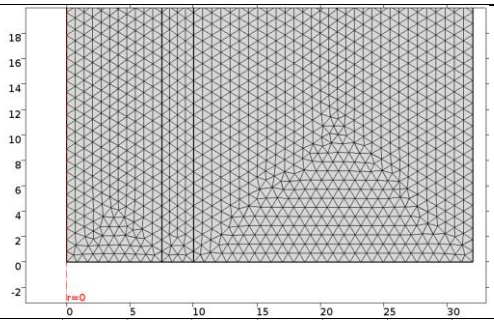
Mesh 5	Extra fine mesh	187476	0.0048/0.416	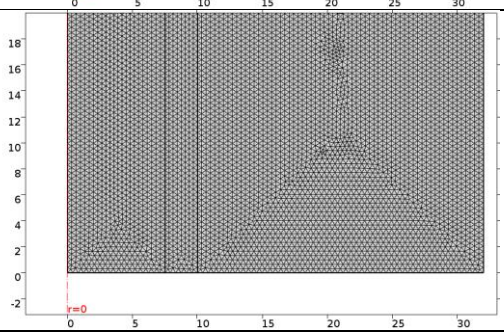

The melting fraction of the PCM liquid fraction with time was used to investigate the effect the mesh size. The study was conducted using Longeon initial and boundary conditions and RT35 as the PCM for 54°C HTF inlet temperature and with an average inlet velocity of 0.01 m/s. Figure 101 shows the PCM melting fraction variation with time for the different meshes. It is noted that the PCM melting fraction is almost the same for all the five meshes up to the 1130 seconds where 22% of the PCM is melted. Apparently from the graph, the model that uses mesh 1 and 2 exhibits a slower melting rate for the rest of the charging period. The magnifying window in the figure shows that the model of mesh 3 delays the melting by 0.8% for the rest of the charging period. Also, the difference of the melting fraction between mesh 4 and mesh 5 is less than 0.2%. This implies that using mesh 4 has the advantage of less computing time with similar results to when using mesh 5. Therefore, mesh 4 has been used throughout the study.

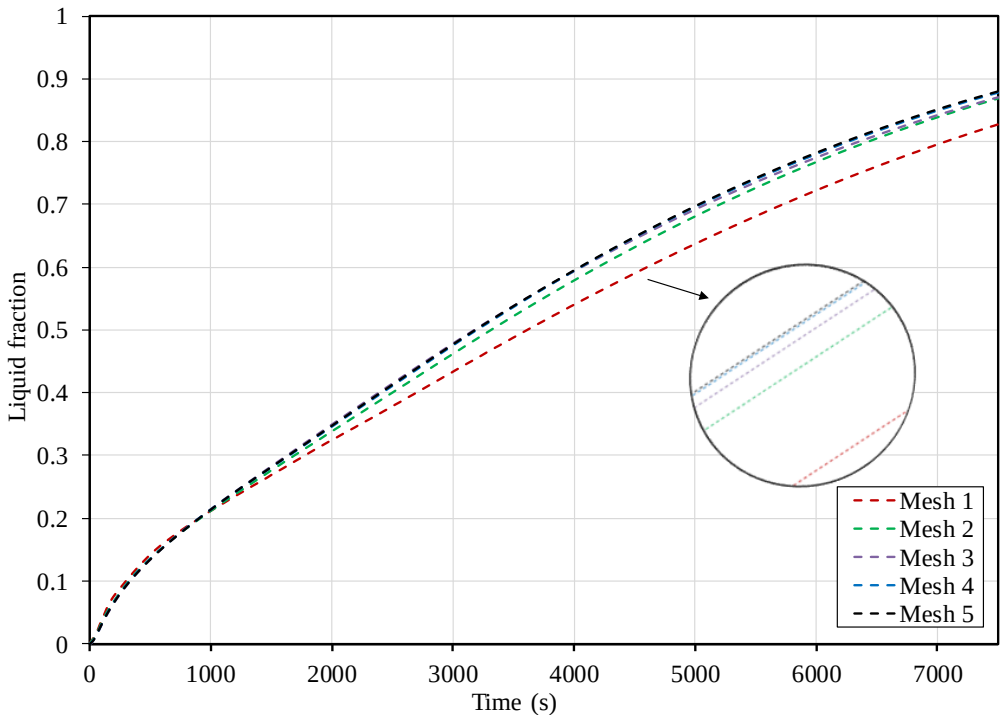

Figure 101.Liquid fraction variation using different meshes.

The validation of the computational model was carried out by comparing numerical results obtained from COMSOL to the experimental data obtained by Longeon et al.[194] . The CFD model were validated using the experimental results of the PCM temperature measurements on location T1 and T2 as shown in Figure 102. In addition, the comparison was taken place for the HTF outlet temperature.

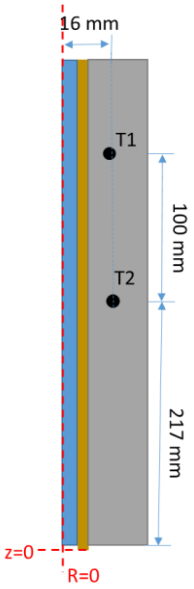

Figure 102.The PCM storage symmetric view showing the locations and coordinates of the compared PCM temperatures.

Figure 103 and Figure 104 show the predicated temperatures of the PCM using the numerical solution and the experimental found by [194]. In Figure 103, the predicted temperature of PCM at T1 has the lowest temperature difference compared to the experimental measurements before the 1000s and after 4500s of a maximum temperature difference of 1.26°C only. However, the maximum temperature difference between 1000s and 4500s is at 5.18°C. The predicted temperature of T2 follows the same pattern of T1 where the lowest temperature difference compared to the experimental measurements before the 3000s and after 6000s is of a maximum temperature difference of 0.705°C only and the maximum temperature difference between 3000s and 6000s is increased at maximum temperature of 5.18 °C.

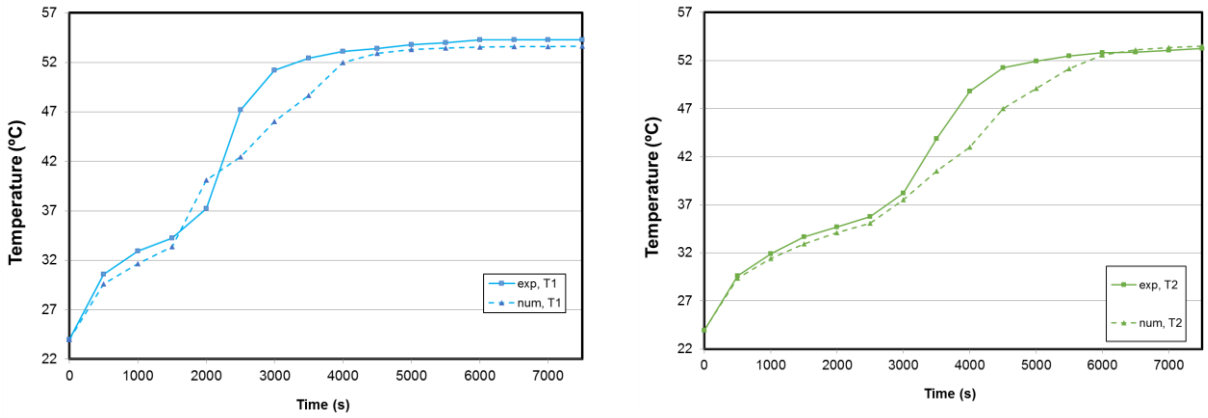

Figure 103.The variation of the predicted and experimental temperature at locations of T1 and T2.

Figure 104 shows the predicted HTF outlet temperature and the experimental of a maximum difference of 4.22°C at 1000s. In general, the comparison of the numerical results with the experimental results found in [194] demonstrate that the developed numerical model accurately describes processes taking place in the experimental test rig. Therefore, this model can be used with confidence for further heat transfer simulations analysis in the shell-and-tube PCM storage.

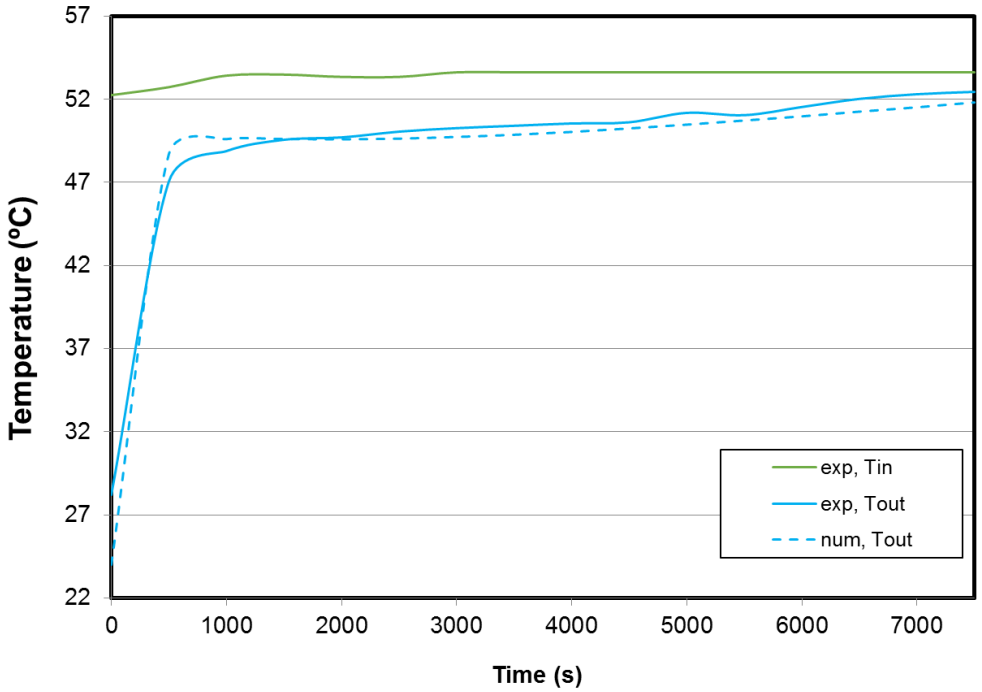

Figure 104.The predicted and experimental temperature for the HTF outlet temperature.

5.1.4.7 Heat transfer characterization inside the PCM storage

A thermal analysis of the validated numerical CFD model was further performed to examine the performance of the shell and tube PCM storage unit during the heat charging mode using RT35 with a HTF inlet temperature and an average inlet velocity of 54°C and 0.01 m/s, respectively. Figure 105 shows the PCM temperature distribution and melting profiles in the PCM computational domain in 1875s, 3750s and 5625s. It can be seen that the PCM temperature gradually rises in the regions close to the tube walls and the highest temperature is observed at the domain's top region close to the inlet of the HTF. As a result, the top part of the domain turns into liquid first and later, the melted PCM expands to the lower regions on the PCM domain. However, the melting rate in the axial direction is higher than in the radial direction.

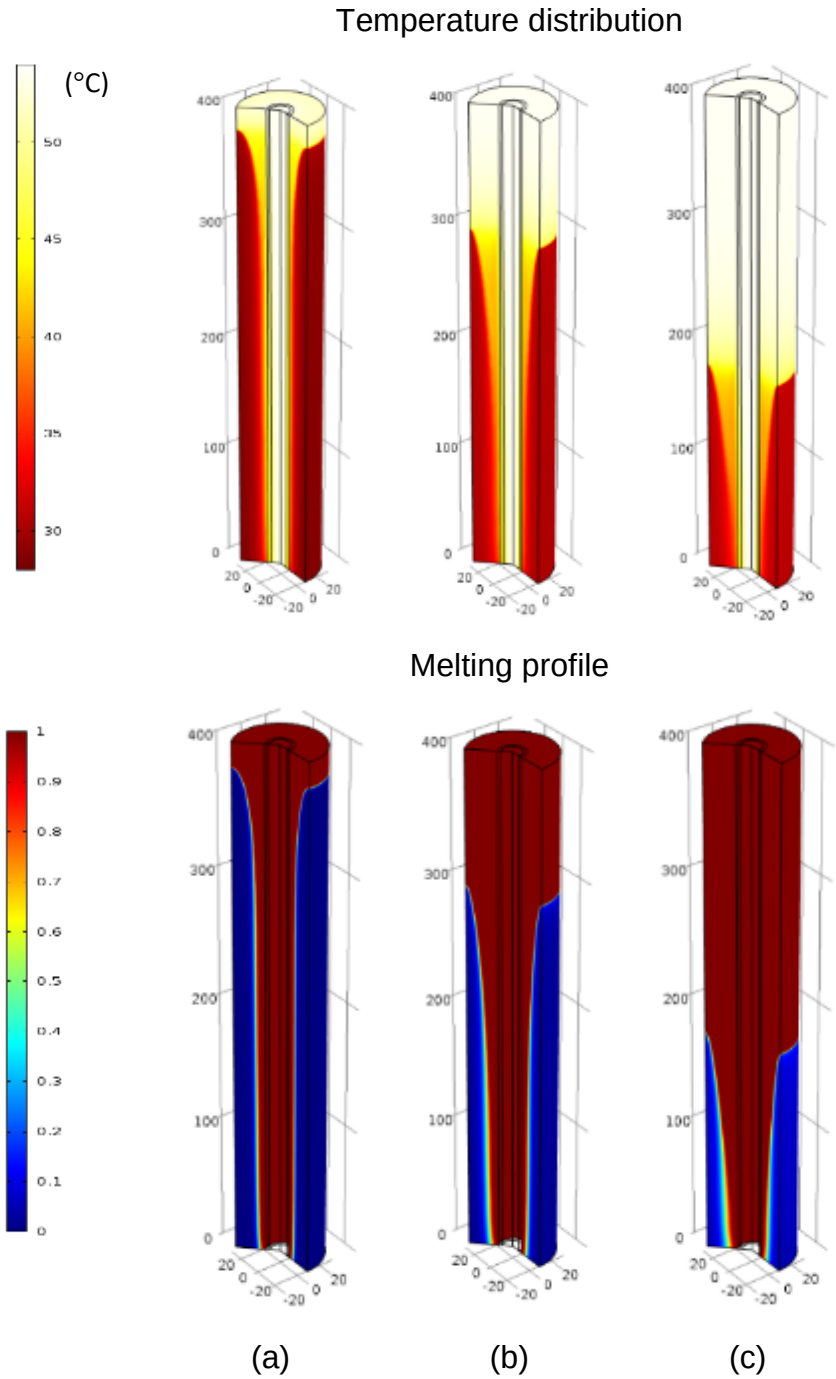

Figure 105. The PCM temperature distribution and melting profile at (a) 1875s, (b) 3750s, and (c) 5625s (T_i=54°C, V_{HTF}=0.01m/s).

Figure 106 shows the melting fraction of the PCM inside the storage where the PCM melts in an approximately constant rate. During the two hours of charging, 93.14% of the PCM turns into a liquid phase where, the melting of the 50% of the PCM occurs during the first third of the charging time.

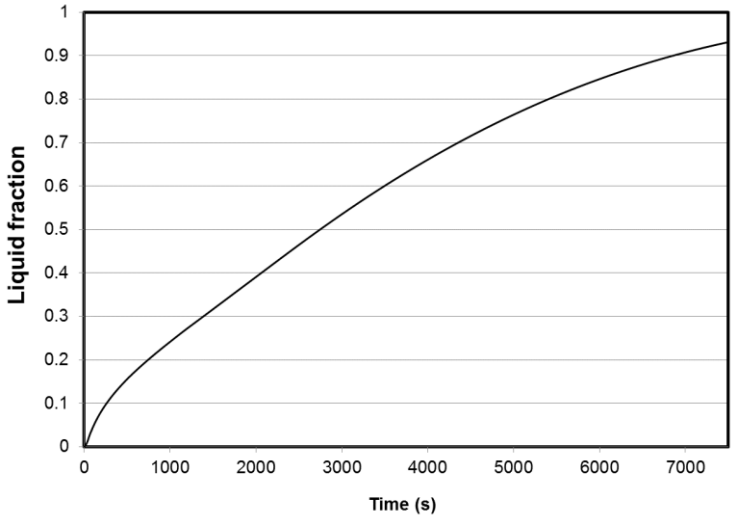

Figure 106. The PCM melting fraction versus time (T_i=54°C, V_{HTF}=0.01m/s).

Figure 107, Figure 108 and Figure 109 present the temperature variation along radial direction in different periods for axial height of 3L/4, L/2 and 0, respectively. The Figure 107 and Figure 108 show that the temperature of the PCM remains constant during the melting at a temperature of around 42°C due to the latent heat effect. Then, the PCM temperature rises suddenly after the 3000s and the 5000s at location 3L/4 and L/2, respectively. By the end of charging process, the PCM temperature is uniform across the radial section which is close to the temperature of the HTF. However, the temperature of PCM remains low at Z=0 due to the incomplete PCM melting. The figures show also a negligible temperature difference across the tube thickness which implies a very low conduction thermal resistance of the tube.

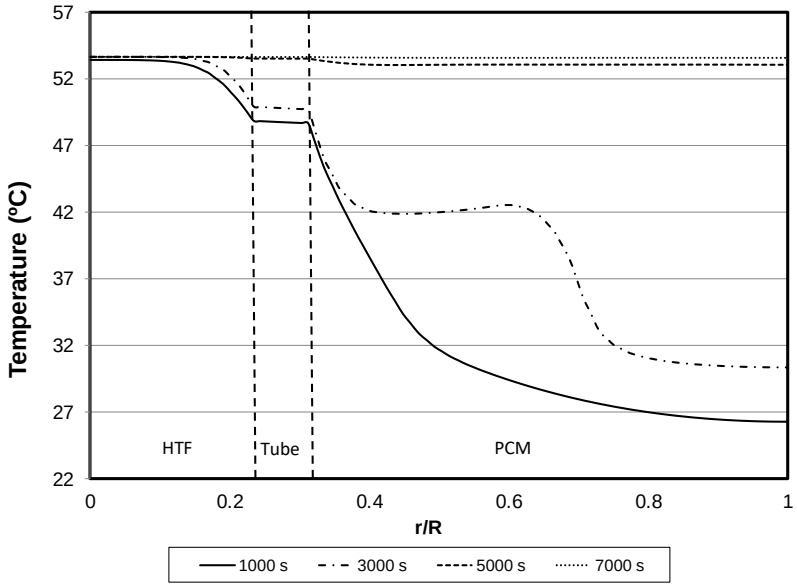

Figure 107. Temperature gradient along the radial axis at z=3L/4 at various times (T_i=54°C, V_{HTF}=0.01m/s).

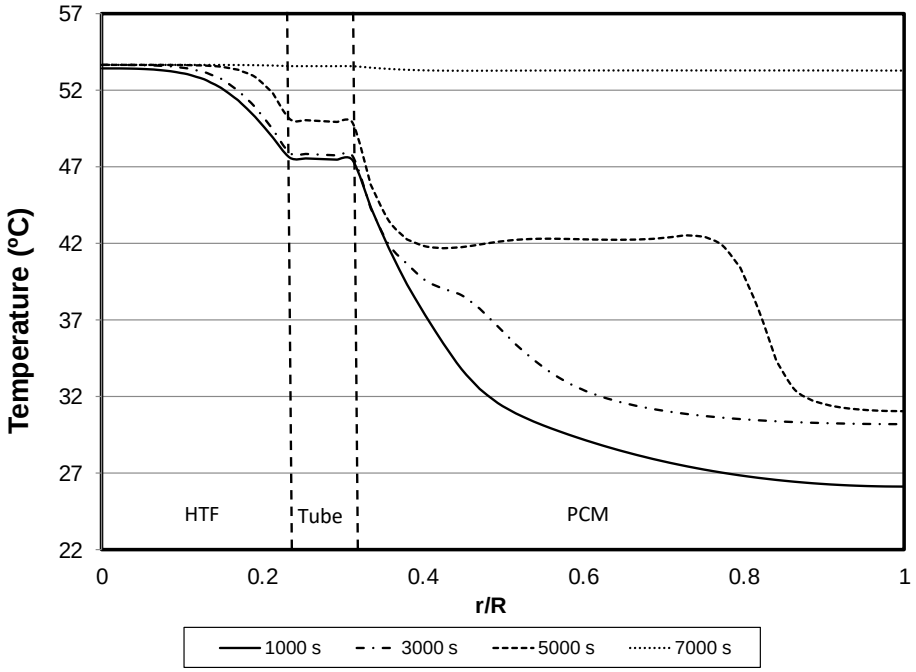

Figure 108. Temperature gradient along the radial axis at z=L/2 at various times (T_i=54ºC, V_{HTF}=0.01m/s).

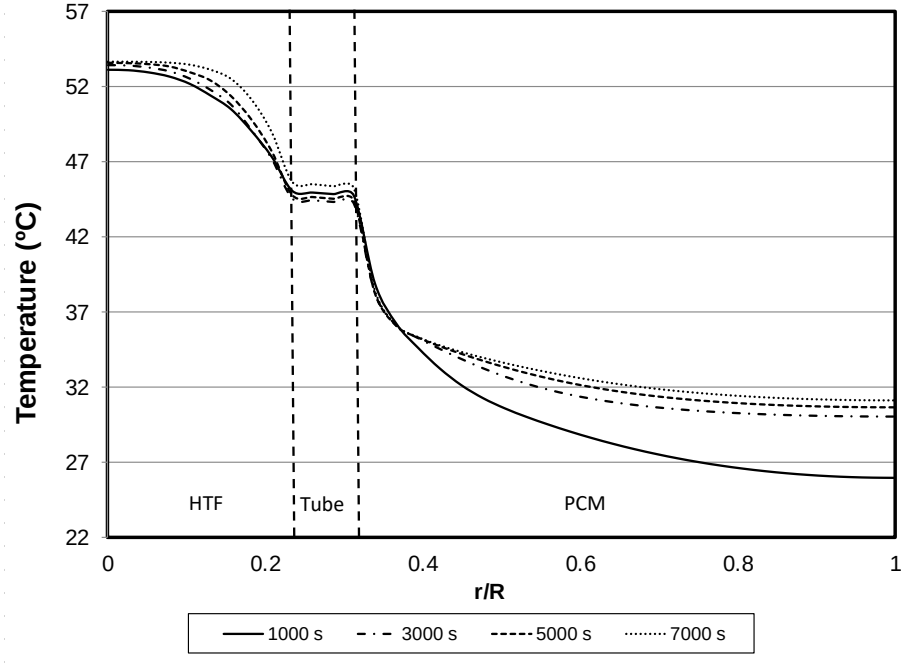

Figure 109.Temperature gradient along the radial axis at z=0 at various times (T_i=54ºC, V_{HTF}=0.01m/s).

Figure 110 shows the temperature variation of the PCM along the axial axis at the 21mm radial distance. It can be noticed that, the PCM temperature along the axial axis follows the same pattern at different times and reached to the same saturation temperature along the axial axis after the melting of 53ºC. Also, the figure shows a constant PCM melting volume rate in the interval between 3000s to 7000s of a rate of 56mm/1000s.

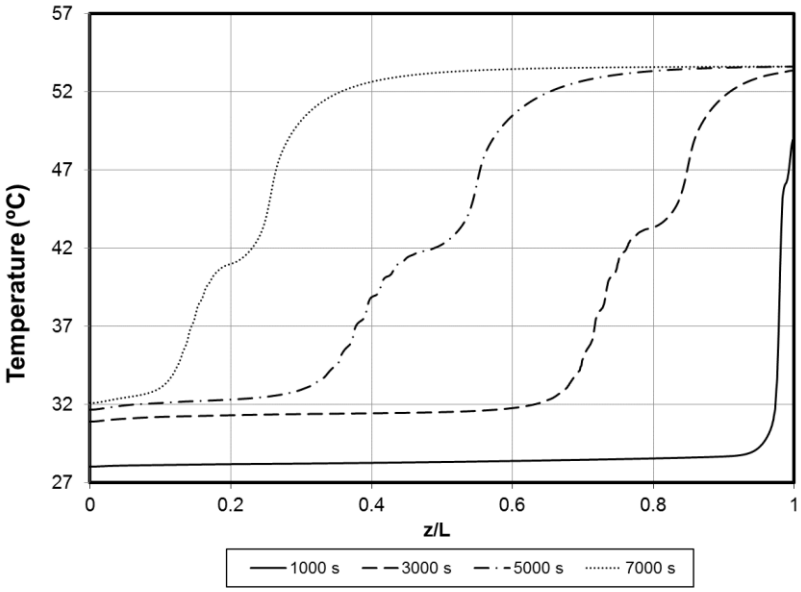

Figure 110. PCM temperature along the axial positions at the r=21mm at various times (T_i=54°C, V_{HTF}=0.01m/s).

The heat transfer rate and the total stored heat in the PCM are shown in Figure 111. The rate of stored heat is decreased dramatically from 120J/s to 46J/s in the first 1000s due to difference between the HTF inlet temperature and initial temperature of the PCM. Then, it is decreased gradually during the rest of the charging time due to the melting of the PCM. On the other hand, the total stored heat is increased with time and reached to 179kJ/kg by the end of the charging period.

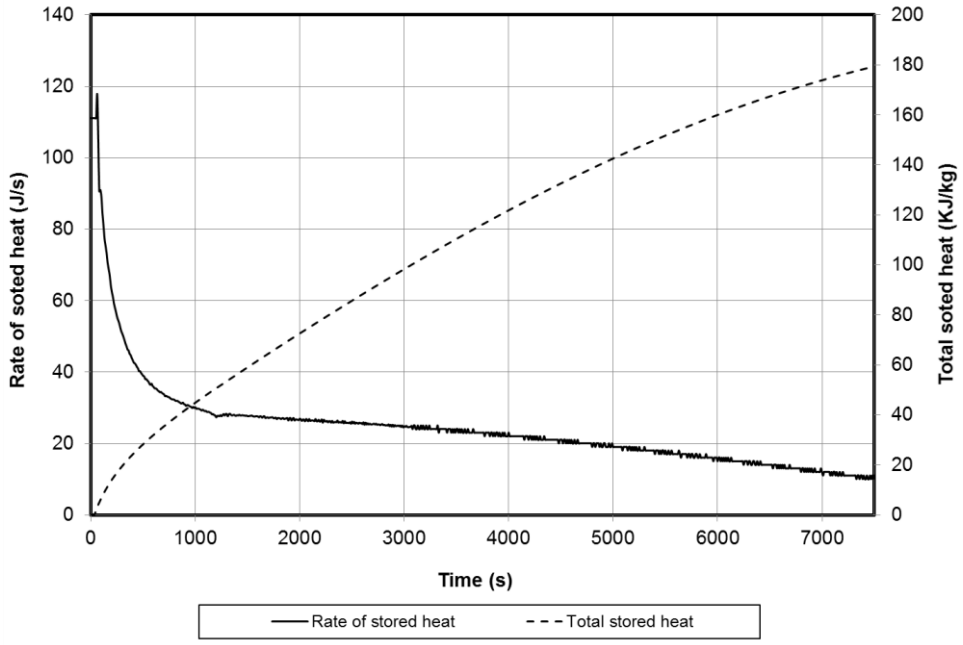

Figure 111. The rate and the total stored heat versus time (T_i=54°C, V_{HTF}=0.01m/s).

5.1.5 Heat transfer maximisation of PCM storage using geometry

The objective of this section is to maximize the heat transfer performance of the system at a fixed HTF flow rate and inlet temperature. For a PCM storage using shell and tube configuration, the heat transfer performance effects the PCM melting time, the temperature distribution of the PCM and the wasted energy. Since the HTF tube thickness is usually thin and the used materials, such as copper, have a very high thermal conductivity, the thermal resistance is normally small and it has a negligible thermal resistance on the overall heat transfer. However, the increase of the tube diameter leads to an increase in the outer area and hence increasing the convective heat transfer rate. For the PCM domain, as the PCM diameter increases, for a fixed PCM volume or mass, the length decreases. However, the conduction thermal resistance of the PCM increases because now the PCM is thicker. Therefore, there is an optimum PCM dimensions for the maximum heat transfer. The optimization problem to be investigated for two cases are for a fixed PCM volume/mass as Longeon study and a variable PCM volume. In both cases, the charging time was extended to 14000s to allow full PCM melting.

For the fixed PCM volume case, two parameters are to be optimized; the PCM thickness and the length. These two dimensions control the heat flow inside the PCM and hence the rate of heat transfer and the amount of heat. The HTF flow rate, the tube dimensions and thickness are fixed throughout the optimization process. The optimization problem is summed up to the following:

Objective function: increase heat transfer rate, reduce the melting time and increase the average PCM temperature.

Constraints:

- The average HTF velocity=0.01m/s, Re<2300
- HTF inner diameter= 15mm
- HTF tube thickness=2.5mm

Variables: the new PCM radius (r) was varied in ratios of 0.5 and 2 of the Longeon study (R=22mm). Hence the height of PCM storage dependent equation is expressed as:

$$H = \frac{m_{PCM}}{\rho_{PCM}} * \frac{1}{\pi({r_{PCM}}^2 - {r_{tube}}^2)} \quad 5.29$$

The effect of the radius ratio on the PCM melting rate with time is presented in Figure 112. The results show a reduction on the total melting time by approximately of 6.5% when the PCM radius ratio is reduced from 1 to 0.5 and is increased by 33% when the PCM radius ratio is increased from 0.5 to 1.5. The PCM could not melt completely in the case of radius ratio of the 2.

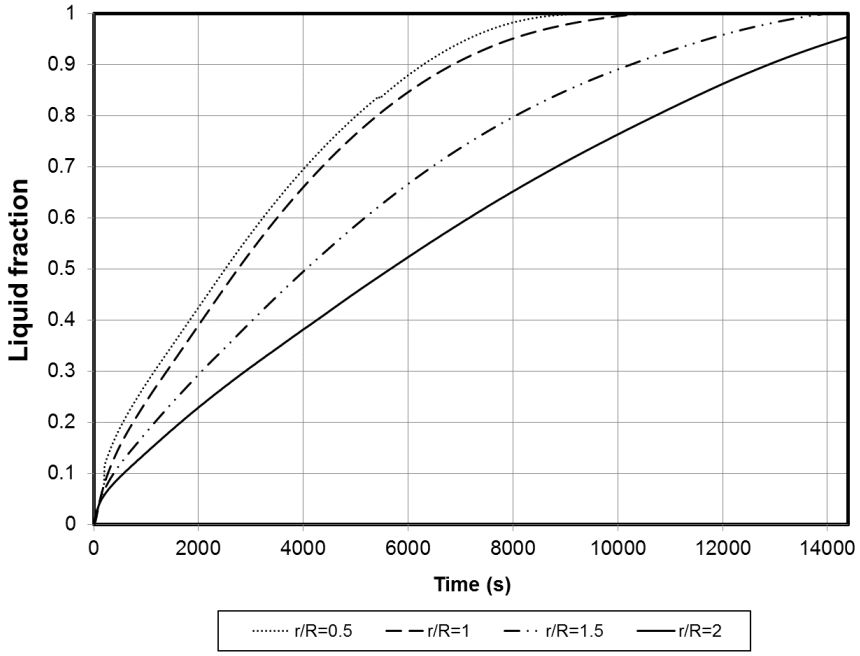

Figure 112. The PCM liquid fraction versus time for various PCM radius ratios (T_i=52°C, V_{HTF}=0.01m/s).

The variation of the average of the PCM temperature versus time for different radius ratio is presented in Figure 113. It can be noticed that the PCM average temperature for the radius ratios of 0.5 and 1 reach their saturated temperature of 53.6 C° at 10000s and 105000s, respectively. However, the radius ratio reaches its saturation temperature by the end of the charging period and the radius ratio of 2 could not reach its saturation temperature due to the incomplete of the PCM. Also, no change on the PCM average temperature is notice for all radius ratios after the complete melting of 53.6C° which implies a uniform temperature of PCM at this point. This shows a strong relation between the charging period and the amount of the PCM to be used in the storage. For instance, for the charging period of 10000s, the system of the radius ratio of 1 is the best selection. However, the radius ratio of 1.5 is considered the best for the charging period of 14000s.

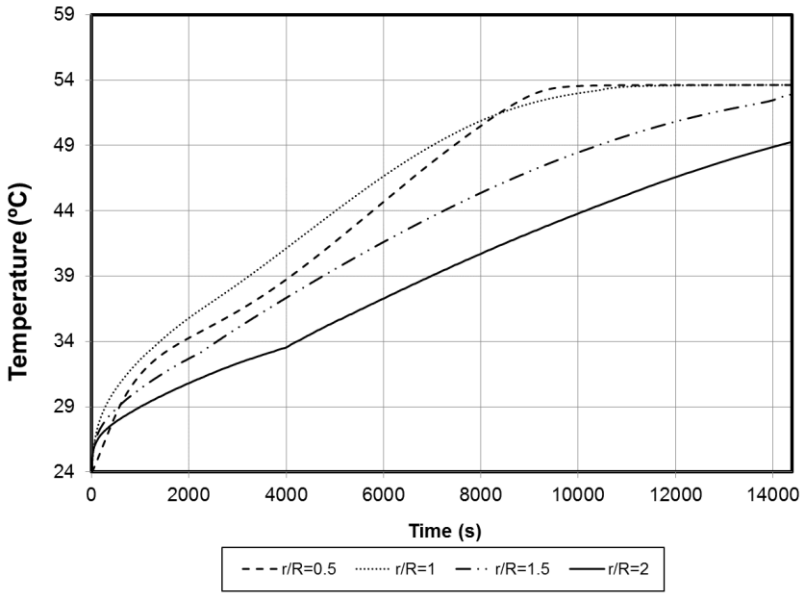

Figure 113. The average temperature of PCM versus time for various PCM radius ratios (T_i=52°C, V_{HTF}=0.01m/s).

Figure 114 shows the HTF outlet temperature with time for the different radius ratio. It can be noticed that the HTF outlet temperature for the radius of 0.5 is the lowest compared to the other radius ratios. This shows a high heat transfer rate is experience at this radius ratio. However, a slight difference is noticed after the 7000s for the 0.5 radius ratio due to the complete melting of the PCM. Also, the HTF outlet temperature varies slightly for the radius ratio varies between 1.5 and 2.0 and this indicates a low heat transferred to the PCM. In addition, it shows that longer storage leads to more heat transfer area between the PCM and the outer surface of the tube.

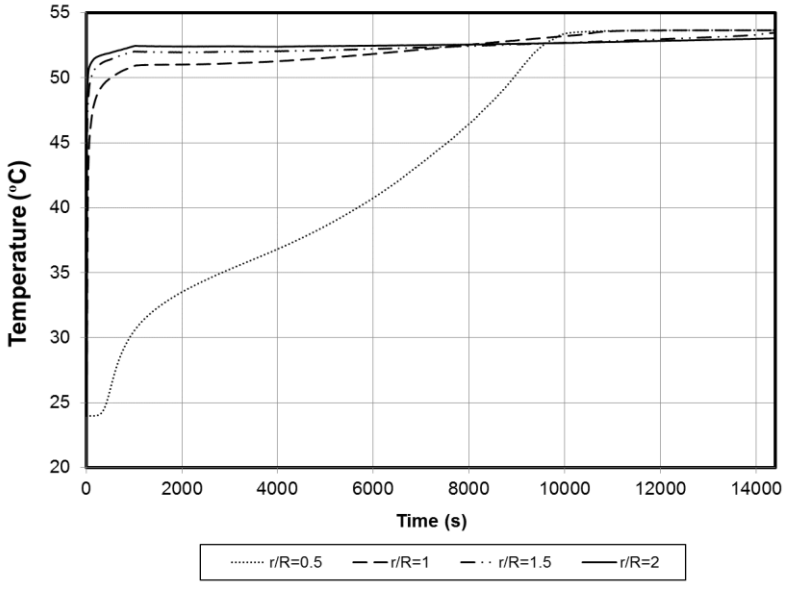

Figure 114. HTF outlet temperature versus time for various PCM radius ratios (T_i=54°C, V_{HTF}=0.01m/s).

The effect of the increase of the amount of PCM in the storage performance is investigated here. A survey of the literature of the PCM geometry shows that conducted studies on the PCM storage geometry parameters are by varying the PCM to the tube radius ratio (Ro/Ri) between 3 and 6 and also the ratio of the storage length to the inner radius (L/Ri) varied between 55 and 200 [282]. So, the effect of the PCM radius and the storage length ratio on the performance of the PCM storage system is studied using this ratio ranges and the rest of the parameters are kept constant as shown in Table 23 .

Table 23. The geomatry parameters cases

Case #	Fixed variables (mm)	Ratio range	Varied parameter range (mm)
Case 1	L=400 Ri=7.5	3<Ro/Ri<6	22.5<Ro<45
Case 2	Ro=22 and Ri=7.5	55<L/Ri<200	412.5 <L<1500

Case 1 as shown in Table 23 investigated the effect of increasing the ratio of the outer PCM radius to the inner tube radius between 3 and 6. Therefore, four ratios were selected to conduct the study, 3, 4, 5 and 6. The considered PCM outer radius were 22.5mm, 30mm, 37.5mm and 45mm. The mass of the PCM filling and the stored heat (from 24^{o}C to 54^{o}C) in each radius ratios are shown in Figure 115.

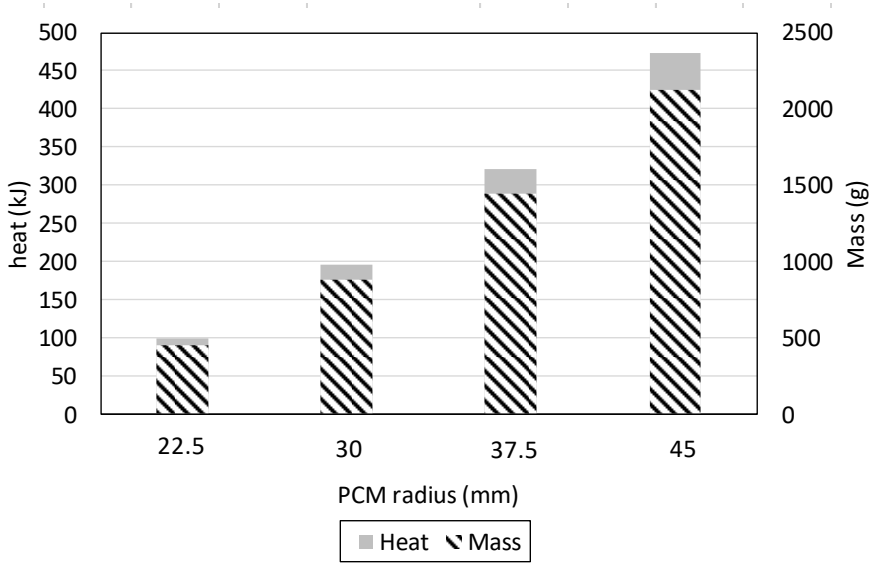

Figure 115. The amount of PCM and the maximum heat stored at the PCM to the tube radius ratios.

The melting fraction of PCM for the various PCM to the tube radius ratios is shown in Figure 116. It can be noticed that the PCM of the 3 radius ratio is melted completely in 10920s and the other radius ratios are not melted completely by

the end of the charging period and more time is required for complete melting where doubling the radius ratio (6) is caused only melting 70% of the total of PCM. However, the PCM to the tube radius ratio of 4 is considered as the best ratio for the charging period of 14500s.

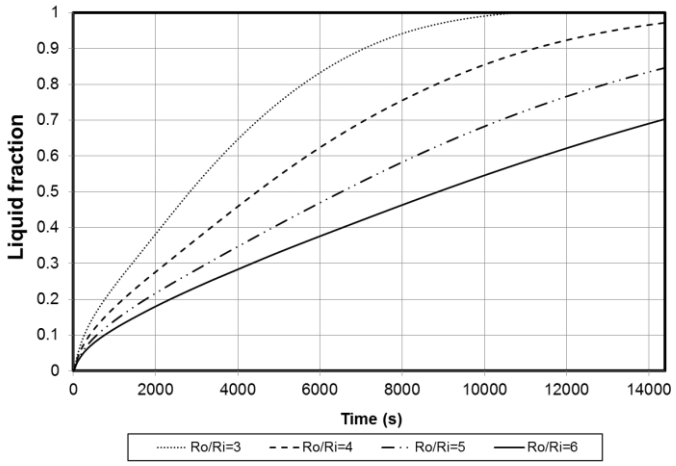

Figure 116. The liquid fraction versus time for various PCM to the tube radius ratios.

The average temperature of the PCM for the different radius ratios is shown in Figure 117. The PCM at the storage of radius ratio of 3 experiences the highest average temperature at all the time of charging due to the its fastest rate of the PCM melting and it reaches to the HTF inlet temperature by the end of charging period of 54^{o}C. In addition, the average temperatures of the other radius ratios are higher than the melting temperature of PCM and reach to 42.3^{o}C by the end of the charging period for the largest radius ratio.

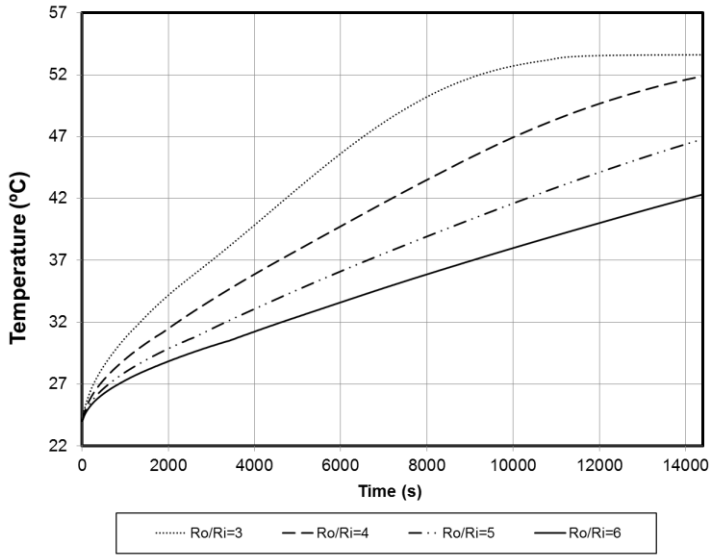

Figure 117. The average temperature of PCM versus time for various PCM and tube radius ratio.

The rate of the stored heat for the various the PCM to the tube radius ratios is represented in Figure 118. At the beginning of the charging, the stored heat rate decreases sharply from 90J/s to 26.9J/s for all the radius ratios due to heating up of the materials such as the tube and HTF. Then, the stored heat rate varies different of each radius ratios. The PCM storage with higher radius ratios (i.e. more PCM mass) absorbs the heat faster compared to the PCM storage of lesser radius. It is also noticed that the PCM storage of the radius ratio of 3 has reached to its saturation at the 11780s at which the temperature of the PCM reaches to the same to the HTF inlet temperature.

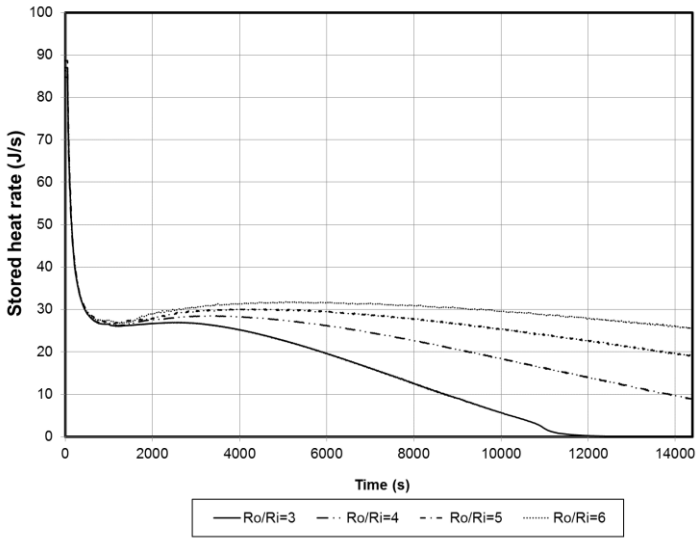

Figure 118. The rate of the stored heat versus time for various PCM to the tube radius ratio.

The investigation of the effect of increasing the length of the PCM storage (Case 2) as shown in Table 23 is presented here. The ratio of the storage length to the HTF tube radius is varied between 55 and 200. Five ratios are selected to conduct the study, 53, 75, 100, 150 and 200. The considered PCM storage lengths are 400mm, 562.5mm, 750mm, 1125mm and 1500mm. The calculated mass of the PCM filling and stored heat (from 24^{o}C to 54^{o}C) in each is presented in Table 24.

Table 24. The amount of PCM and the maximum heat stored for various PCM storage length to the HTF tube radius ratios.

Ratio	Length (mm)	PCM mass (g)	Heat (kJ)
53	400	424.43	84.88
75	562.5	596.85	119.37
100	750	795.80	159.16
150	1125	1269.75	253.95
200	1500	1794.62	358.92

The liquid fraction of PCM for the different length to tube radius ratios are shown in Figure 119. It can be noticed that the PCM in the storages with length of 400mm, 562.5mm and 750mm melted completely whereas the PCM in the storage of the length of 1125mm and 1500mm melted by a fraction of 0.998 and 0.992, respectively. In addition, increasing the storage length from 400mm to 750 increases the total melting time of PCM by 2510s. This concludes that for this specific HTF inlet temperature and flow rate are more suitable for the 1500mm PCM storage due to the ability of the PCM to absorb the heat.

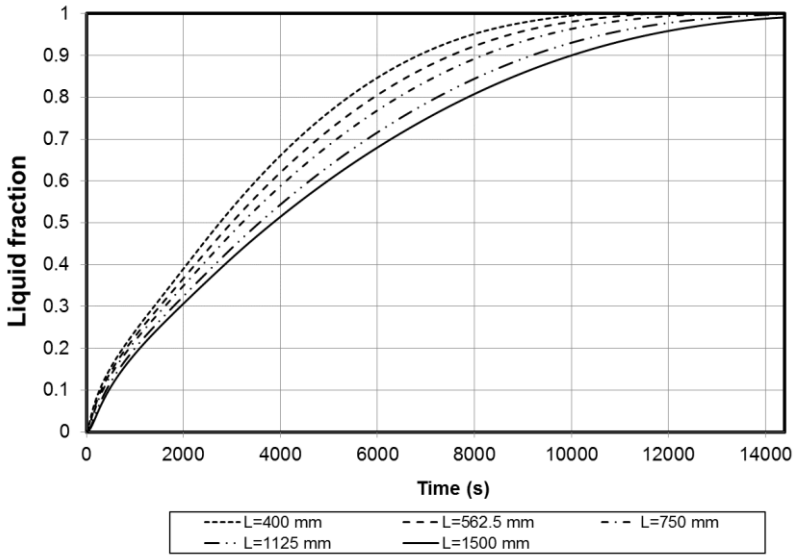

Figure 119. The liquid fraction versus time for various PCM storage lengths.

Figure 120 represents the average temperature of PCM for the different storage lengths. It can be noticed that the PCM for the storage length of 400mm experiences the highest average temperature at all the time of charging due to the faster melting of PCM and it reaches along with the other storages lengths of 562.5mm and 750mm to the HTF inlet temperature by the end of the charging period of 54^{o}C. Also, the average temperatures of the other lengths of 1125mm and 1500mm reach the saturation temperature of 52.9^{o}C.

The rate of stored heat for different PCM storages length is shown in Figure 121. The figure shows clearly the dependency of the amount of stored heat on the storage length. The difference of the rate of the stored heat is more organized after the 2000s of charging. After this time, the difference is constant until the 10000s of charging. Beyond this point, the heat rate starts decreasing as the PCM was nearly in complete melting at the storage of the length of 400mm, 562.5mm and 750mm.

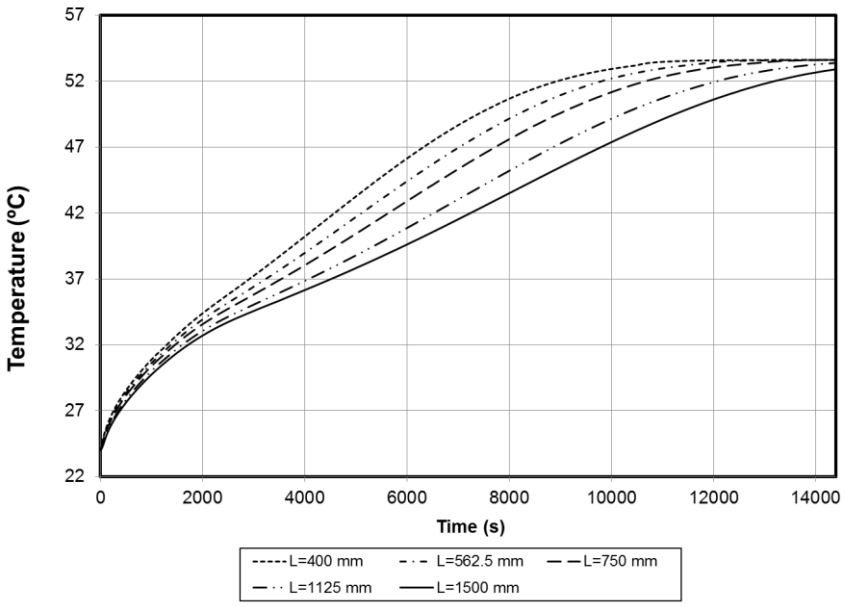

Figure 120. The average temperature of PCM versus time for various PCM storage lengths.

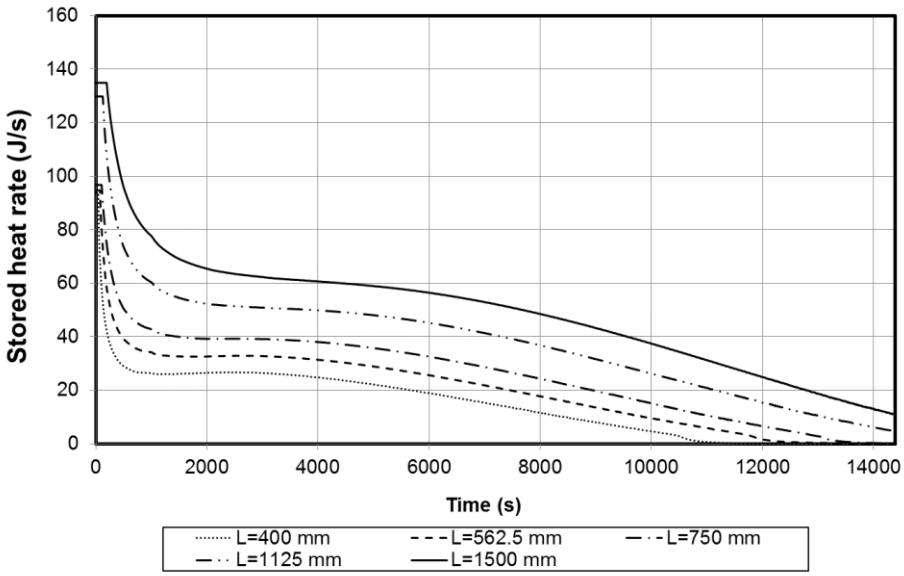

Figure 121. The rate of the stored heat versus time for various PCM storage lengths.

5.2 Experimental study of the PCM thermal storage system

The main objective of the experimental study is to examine the performance of a PCM storage system filled by a PCM. The experiment setup is designed so that it is able to investigate on the performance of:

- A single PCM storage using different PCM melting temperature, orientations and under different working conditions such as the HTF flow rates and HTF inlet temperatures.

- Using multi-stage PCM storages technique for enhancing the thermal conductivity of the PCM and the effect of working conditions.

5.2.1 PCM storage design and materials selections

As discussed earlier, the cylindrical PCM storage is the most convectional geometry for the thermal storage applications. Therefore, the cylindrical configuration for the PCM thermal storage system is used. The PCM storage consists of elementary parts of a shell and tube heat. The PCM is placed inside the shell whereas the heat transfer fluid (HTF) is circulated inside the tube. Selection of materials of the container is another critical parameter for the PCM storage. The main three materials to be selected are the PCM, outer container and the tube. The main characteristics of the material of the outer container is the low thermal conductivity, withstand the required storage temperature, to prevent any PCM leaking during the operation and transparent for the PCM melting visualization purposes. The most convenient material is the acrylic material in which it offers low thermal conductivity (0.21 W/m·K) [119]. The heat loss to the environment could also be eliminated using a thermal insulation around the outer surface. The HTF tube materials must be made from high conductive materials such as copper, aluminium and stainless steel to increase the heat transfer rate. The photograph of the PCM container and the HTF tube are shown in Figure 122.

(a) (b)

Figure 122. Photographs of (a) the PCM container and (b) HTF tube.

A photograph of the assembled PCM storage test section is shown in Figure 123. It consists of a single copper tube enclosed by a transparent acrylic shell for PCM melting profile visualisation. The HTF flows through the tube and exchange the thermal energy to the PCM in the shell. The inner diameter of the tube (Dt) is 8mm with a thickness of 2mm. The inner diameter of the PCM container is 40mm with thickness of 4mm and its height (L) is 183mm and it can be filled with 170g of PCM. All parts of the test section are tightly joined to avoid any HTF and PCM leakage.

Five thermocouples of 0.5mm dia with a measuring accuracy of ±0.1°C are fixed near to the tube to measure the temperature of the PCM. The temperatures are distributed along the container of 45.7mm apart and in the middle radial of the PCM as shown in Figure 123 (C). In addition, a single thermocouple is placed at the corner edge of the container to capture the complete melting time of the PCM. The thermocouples have been calibrated using the constant temperature water bath of a temperature range between 0ºC and 100ºC with an accuracy of ±0.1ºC.

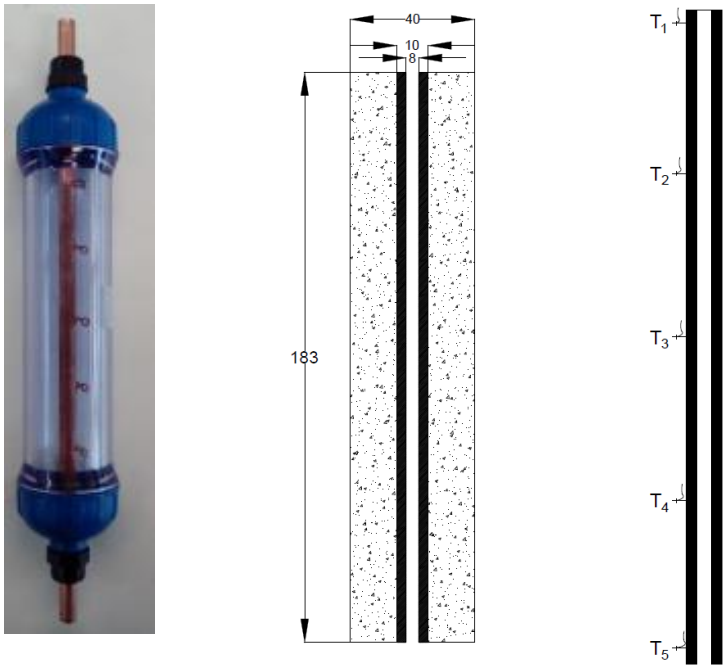

(a) (b) (c)

Figure 123. The final arrangement of the PCM storage test section (a) Photograph (b) dimensions and (c) Thermocouples distribution.

5.2.2 Experimental setup and procedure

As stated above, two investigations have been carried out to study the PCM storage under different working conditions; the single stage PCM storage and the

multi-stage PCM storage. The experimental setup for the investigations of the single PCM storage is shown in Figure 124. The test section of the single PCM storage is designed such as it is equipped with an adjustable-tilt mechanism for the PCM storage inclination study.

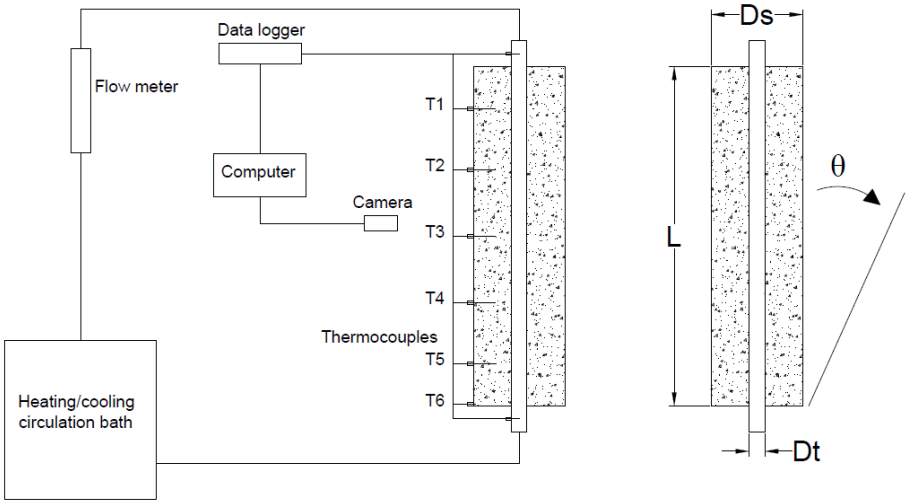

Figure 124. Schematic of the single PCM storage experimental setup.

The multi-stage PCM storage experimental setup photograph and its schematic are shown in Figure 125 and Figure 126, respectively. The three PCM storage stage are placed in parallel where the HTF flows from the high PCM melting temperature storage to the lower PCM melting temperature storage.

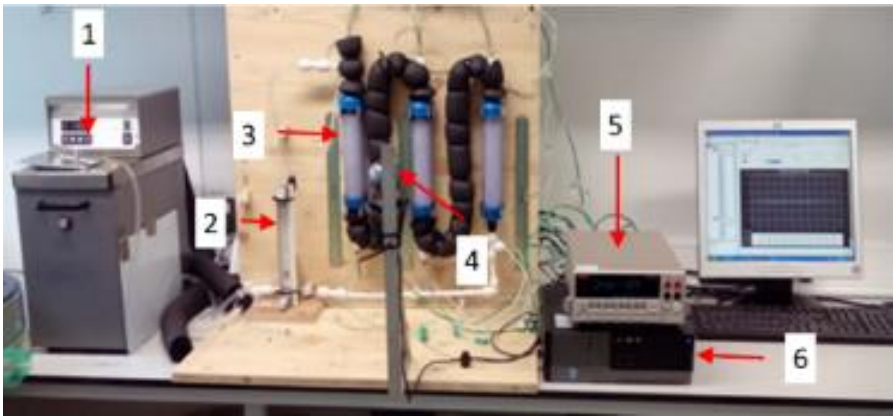

Figure 125. Photograph of experimental setup; (1) HTF circulation bath, (2) variable area glass flowmeter, (3) Test module, (4), (5) Data logger and (6) Personal computer.

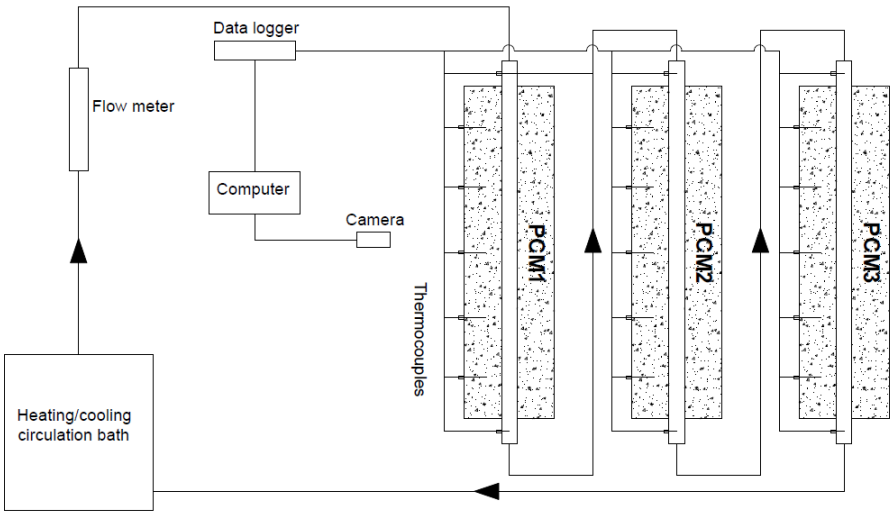

Figure 126. Schematic of the multi-stage PCM experimental setup.

For the fluid heat load, the fluid entered the tube at an inlet temperature (T_{in}) and the inlet temperature and the outlet temperature (T_{out}) were captured using an inline thermocouple of pro type. The HTF exchanged the heat with the PCM at a controlled volume flow rate using a variable area flowmeter and varied by a built-in valve at the inlet of the flowmeter. The HTF was heated in a constant inlet temperature (T_{in}) using a constant temperature water bath and circulated using a built-in pump. In the present study, De-ionized water was selected as the heat transfer fluid (HTF). The data acquisition system for temperature readings was a 40-channel Keithley 2700. A digital camera was used to capture the melting profile images for every 1-minute time interval.

The filling of the PCM inside the container is the same for all experimental tests. The PCM quantity of 170g is melted using a hot plate of temperature of 60^{o}C. Then, the liquid PCM is poured inside the container. An air gap is noticed at the top of container, this is due to the volume contraction of the solid PCM by 15% compared to the PCM in liquid phase. Before starting each experiment, it is very important to ensure that the PCM temperature is homogenous and in the specified initial temperature of 20°C. Therefore, the HTF is circulated at a temperature of 20°C using the circulation bath for 3 hours. Subsequently, the experiment is started by circulating the constant temperature HTF of a fixed flow rate. The inlet and outlet HTF temperatures, as well as the PCM temperature across the PCM storage and the external temperature are measured and recorded in an interval of 30 seconds.

5.3 Results and discussion

This section presents the results of the thermal characteristics of both the single PCM storage and multi-stage PCM storage under different conditions. The numerical results from COMSOL simulations were carried out for the understanding the behaviour of the PCM and to conduct a parametric study.

5.3.1 Single PCM storage thermal analysis

This section investigates the effect of the HTF flow rate and inlet temperature on the PCM storage performance. Then, the effect of the storage inclination in three different inclination positions on the thermal behaviour of the PCM storage system such as the temperature distribution across the storage system, the PCM melting profile, the motion of the liquid PCM.

5.3.1.1 Thermal characterization of PCM storage using RT35

The influence of the HTF inlet temperature and flow rate on the charging rate is investigated in this section. The PCM charging period starts with the first PCM melting and ends with the complete melting of PCM. In this study, the complete PCM melting time was found using the system photograph analysis and the temperature measurements simultaneously. T6 represents the last PCM melting point in the system and its behaviour can be used as an indication for complete melting of the PCM. Figure 127 shows the temperature distribution of the PCM along the test section and the melting profile photograph for RT35 of 60°C HTF inlet temperature of flow rate of 120ml/min. At the beginning of the charging period, the temperature of PCM in the locations between T2 to T5 are the same until the 10^{th} minute, this indicates that the PCM is solid phase and the absorbed heat is stored in sensible form which causes a gradual increase in the PCM temperature of up to 34^{o}C. However, T6 experiences less temperature raise due to its location at the edge of the storage and less heat is transferred because of the low conductivity of the PCM. After that, a gradual increase of the PCM temperature in each location. Once the PCM melts completely, the PCM temperature reaches to the steady state condition. This steady state condition is proportional to the location of the PCM i.e. PCM at the top has a higher temperature than the PCM at bottom. By the end of the charging period, the PCM temperature range is between 50^{o}C to 58^{o}C. This PCM temperature variation inside the storage can be referred to fluid convection phenomena which is

explained later in more details. In ideal condition the temperature of the PCM at the steady state condition has to match the HTF inlet temperature. The current different can be explained due to the heat transferred to the ambient as waste heat. The PCM temperature at T6 shows a sudden increase from 34 ^{o}C to 43 ^{o}C within 15 minutes which indicates that the melting occurs within this period. The photograph confirms the complete PCM melting time is in approximately in the 96 minute.

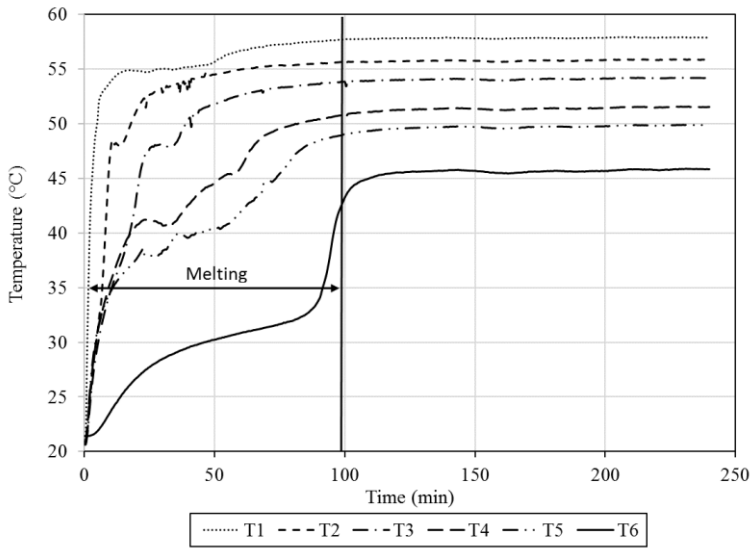

(a)

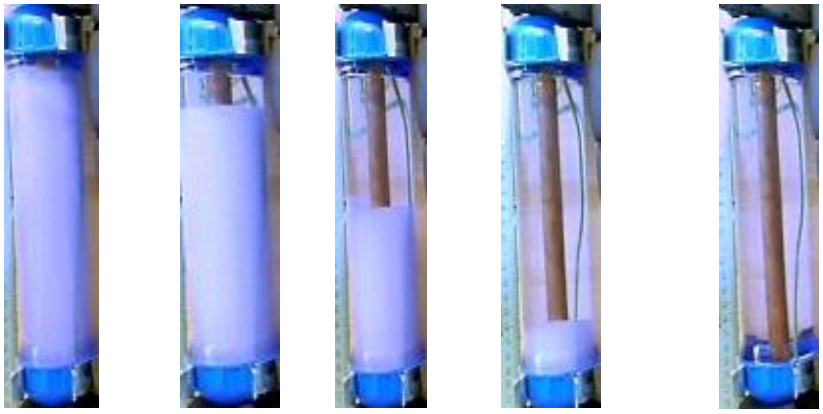

t=0min t=25min t=50min t=75min t=100min

(b)

Figure 127. Experimental (a) PCM temperature along the storage versus time (b) Photographs of the PCM storage at different time points of 60°C HTF inlet temperature of a flow rate of 120ml/min.

The heat transfer rate to the PCM is shown in Figure 128. At the beginning of the charging process, heat transfer rate is decreased sharply from 23.6J/s to 12.5J/s

in 5.5 minutes due to system components heating up such as the copper tube. Then, the stored heat decreases gradually between the 13 minutes and the 52 minutes of charging of rate of 7.4J/s. This shows the maximum melting rate of the PCM occur in this period of charging. After that, the stored heat rate is further reduced until the 96 minutes where full PCM melting is expected at this point and the heat absorbed beyond this point is for the sensible heat for the PCM and the wasted heat to the ambient.

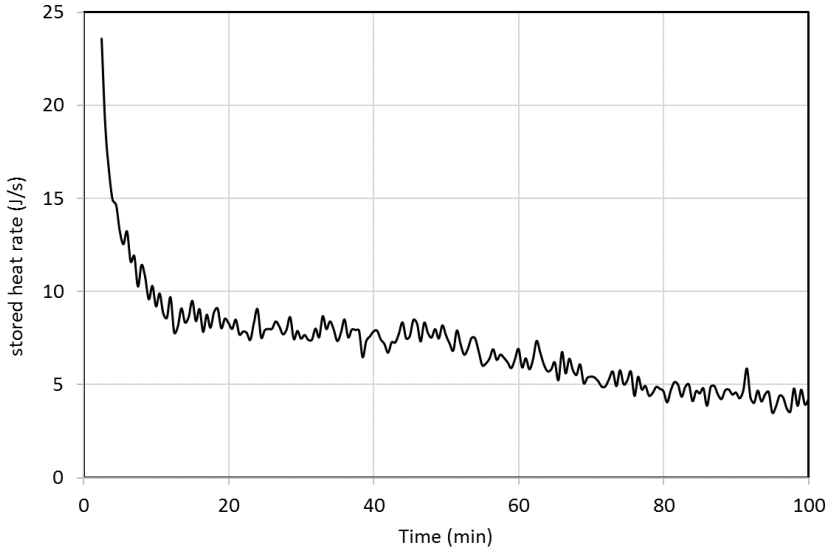

Figure 128. The stored heat rate of the PCM storage for RT35 of HTF inlet temperature of 60^{o}C and HTF flow rate of 120ml/min.

5.3.1.2 Effect of the HTF inlet temperature

The effect of HTF inlet temperature is investigated using various HTF inlet temperatures of 60^{o}C, 55^{o}C and 50^{o}C using the PCM storage filled by RT35. Figure 129 shows the PCM temperature at T6 for various HTF inlet temperature for 120ml/min fluid flow rate. The figure shows clearly that the melting time of PCM is reduced when the fluid inlet temperature is increased from 50^{o}C to 60^{o}C. The results show also that the complete melting time of the PCM is 96, 146 and 240 minutes for HTF inlet temperature of 60^{o}C, 55^{o}C and 50^{o}C, respectively. This indicates that the HTF inlet temperature plays an important role in reducing the complete melting time. In addition, the photographs show no effect of the HTF inlet temperature in the general PCM melting profile where the PCM melts in horizontal line perpendicular to the axial axis from the inner to the outer side.

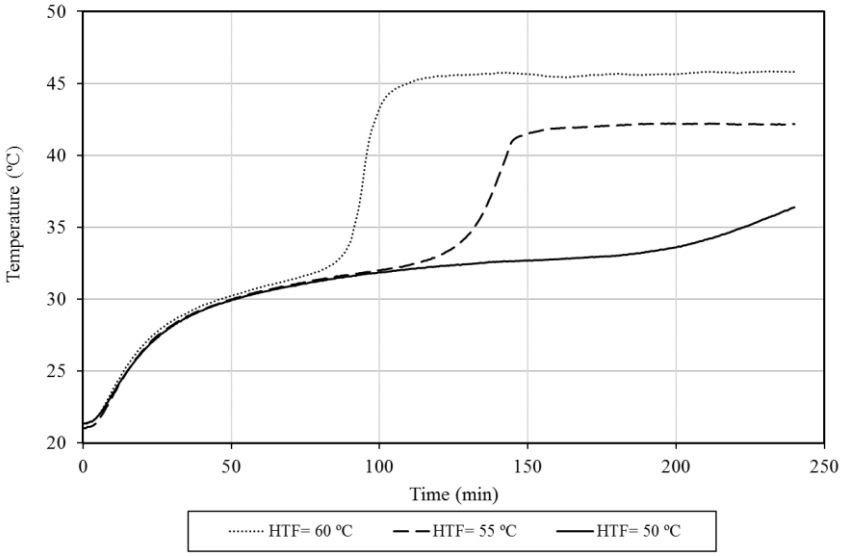

Figure 129. PCM temperature at the lower bottom of the PCM storage (T6) for 120ml/min HFT flow rate and different HTF inlet temperatures.

Also, the temperature of the PCM at locations of T1 and T5 is compared for the different HTF inlet temperatures as shown in Figure 130. By the end of the charging period, the results show a noticeable increase of the PCM temperature at T1 by11.3^{o}C and 7.5^{o}C when the HTF inlet temperature is increased from 50 ^{o}C to 55^{o}C and 60^{o}C, respectively. Also, By the end of the charging period, the results show an increase of the PCM temperature at T5 by 3.5^{o}C and 8^{o}C when the HTF inlet temperature is increased from 50 ^{o}C to 55^{o}C and 60^{o}C, respectively.

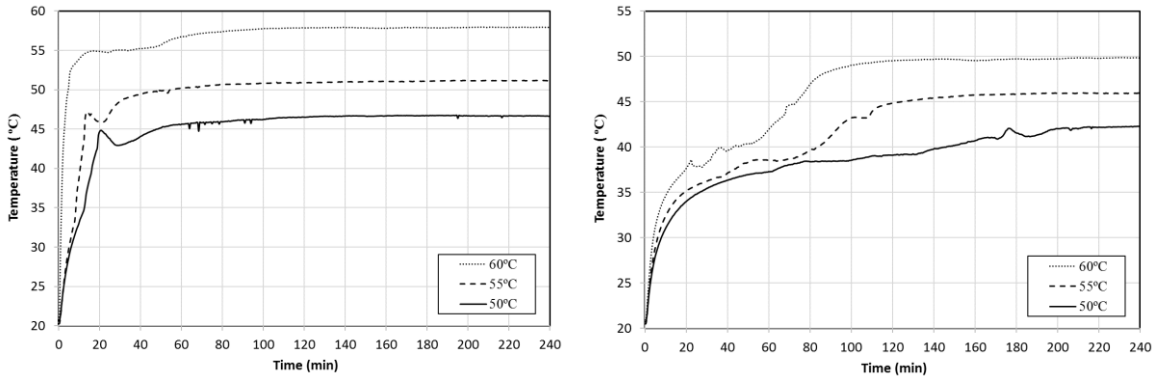

(a) (b)

Figure 130. The heat stored rate of the PCM storage for RT35 of HTF inlet temperature of 60^{o}C and HTF flow rate of 120ml/min at (a) T1 and (b) T6.

5.3.1.3 Effect of the HTF flow rate

The effect of the HTF flow rate on the PCM storage performance is investigated here by varying the HTF flow rate between 60ml/min to 120ml/min. Figure 131 shows that the HTF flow rate has relatively an insignificant effect on the complete

PCM melting time. This might be due to nature of the PCM storage where the optimum HTF flow rate is reached. Also, this indicates that the heat charging rate is not affected by the HTF flow rate i.e. similar melting profile is expected for both HTF flow rates at the same HTF inlet temperature.

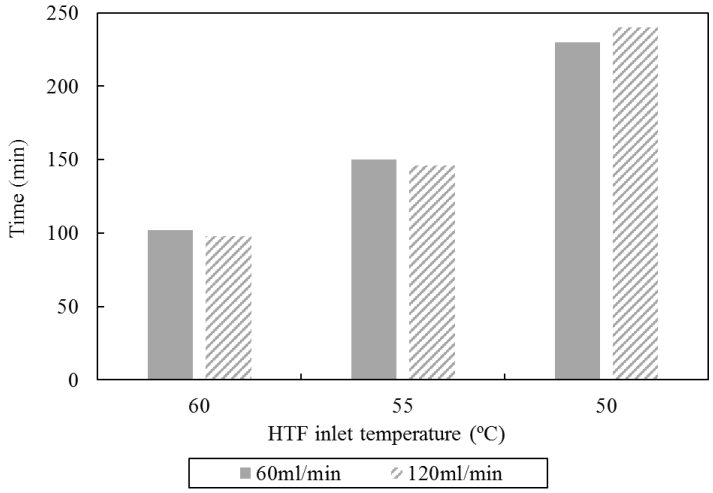

Figure 131. PCM melting time for different HTF inlet temperatures and flow rates.

5.3.1.4 Effect of the PCM storage inclination

The influence of the PCM storage inclination is investigated in three positions of 0º, 45º and 90º. Figure 132 shows the temperature distribution of PCM in the storage system along the axial direction of storage at inclination positions of 0º, 45º and 90º. In the 0º (Figure 132 (a)), the temperatures of the PCM at the different locations are the same at the beginning of the charging except for the PCM at T1. This continue until the 10 minutes of charging where the temperature of the PCM reaches 34ºC i.e. close to the PCM melting temperature. This shows that the absorbed heat is used to raise the temperature of the PCM (sensible heat) where the PCM requires only a small amount of heat to increase its temperature from 20 ºC to 34ºC. Then, the temperature of PCM at each location starts to deviate from each other's depending on their location where the top PCM temperature increases faster than the PCM in the lower part of the storage. The temperature of PCM at T1 shows that the start of latent heat period is after 14.5 minutes of charging at temperature of 54.65ºC and continue until the 47.5 minutes of charging. The latent heat period for the PCM in the other locations (T2 to T5) vary on the time and temperature. Theoretically, the temperature of PCM in the latent heat period is constant and interestingly it is almost unclear in T4 and T5 and this is due to slow melting rate effect. In the final stage of charging, the

PCM temperature in all locations reach their steady state and the temperatures of the PCM vary from each other approximately in a linear increment. By the end of the charging process, the maximum PCM temperature at T1 is 57.9°C and the lowest is at T5 of 49.8°C.

The PCM temperature distribution inside the storage in the 45° inclination is shown in Figure 132 (b). Unlike, the 0º inclination, the PCM temperature distribution inside the storage in the 45° inclination during the sensible heat vary at each location. By the end of the charging duration, the PCM temperature reaches its steady state condition and the temperature of PCM in T1 is lower than the 0° inclination by 1.2°C and the temperature of PCM in T5 is higher than the 0° inclination by 0.6°C. Also, the temperature gradients of the PCM in this inclination are more uniform compared to the 0° inclination by the end of the charging period.

A more interesting temperature distribution of the PCM inside the PCM storage is in the 90º inclination (Figure 132 (c)) where the temperature is similar in all the axial locations. By the end of the charging period, the PCM temperature is the same in all locations along the axial axis of approximately of 55.5°C. This shows that heat is transferred equally in the axial and further analysis of PCM temperature in the T6 is required for more understanding of the temperature distribution.

It is expected the last PCM will melt in the lower corner at T6 and the comparison of the temperature of T6 in all inclination positions could be used to find out the complete melting of the PCM. Figure 133 shows the temperature of PCM at T6 of storage inclination of 0 º, 45º and 90º. At the beginning of charging, the figure shows a similar temperature for all inclination positions until the PCM temperature reaches 30°C at 54 minutes. After that, the temperature of PCM at T6 in the storage of the 45° inclination is increased compared to the other inclinations until it reaches to 45°C at the 85 minutes. Then the temperature raises gradually and reaches its steady state in the 92 minutes of charging at temperature of 46.1°C. The behaviour of PCM's temperature in T6 in the storage of 0° inclination is similar to that in the 45° inclination but the complete melting is estimated at 98 minutes and the steady state is delayed to the 110 minutes of charging at temperature of 45.8°C. The temperature of PCM at T6 in the storage at 90° shows a slow increase and does not reach to the steady state by the end of the charging

period of 240 minutes. In conclusion from this figure, the temperature of the PCM at the lower edge of the PCM storage gives an approximate time of complete melting of the PCM. Also, the PCM storage at 45° inclination is the fastest in melting the PCM followed by the 0° inclination and the longest PCM melting time is at the 90° inclination. The melting rate could be explained extensively by a close look into the solid-liquid melting profile as detailed below.

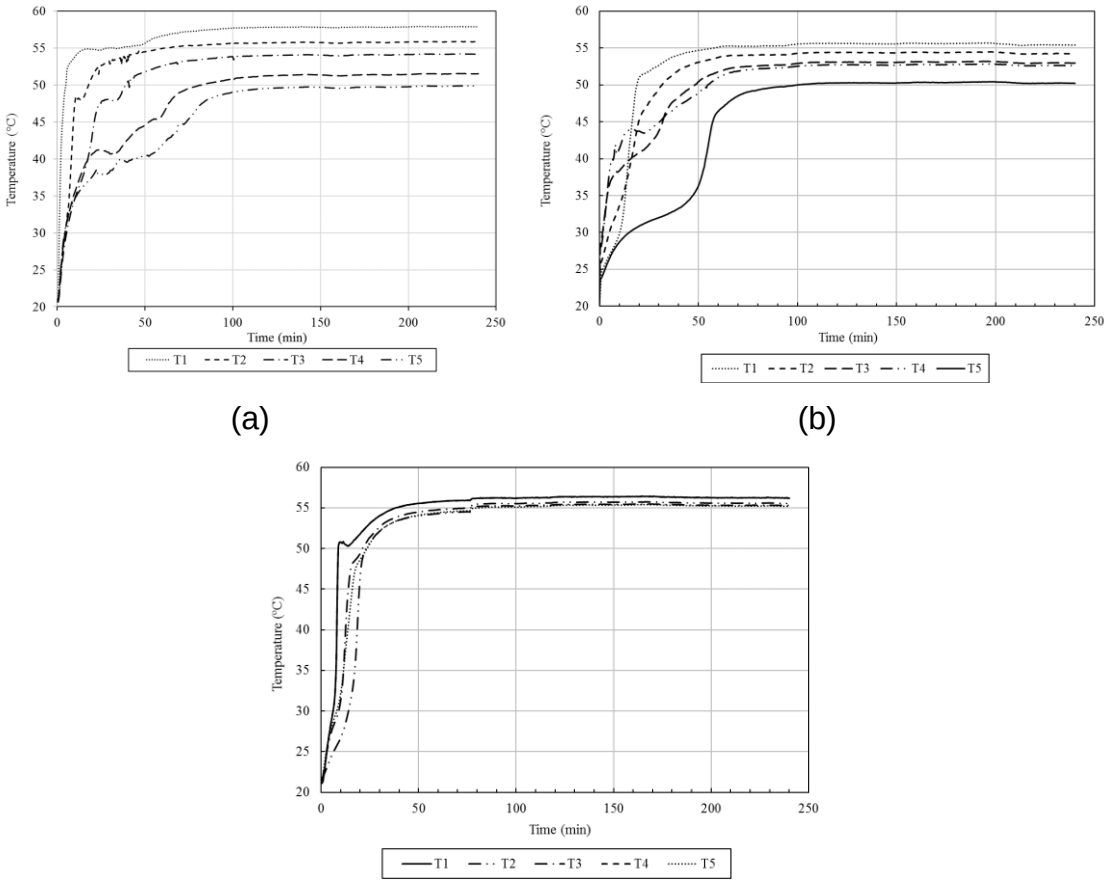

Figure 132. PCM temperature distribution in the axial direction inside the PCM straoge for storage inclination positions, 0º, 45º and 90º (a, b, and c) for RT35 of HTF inlet temperature of 60ºC and flow rate of 120ml/min.

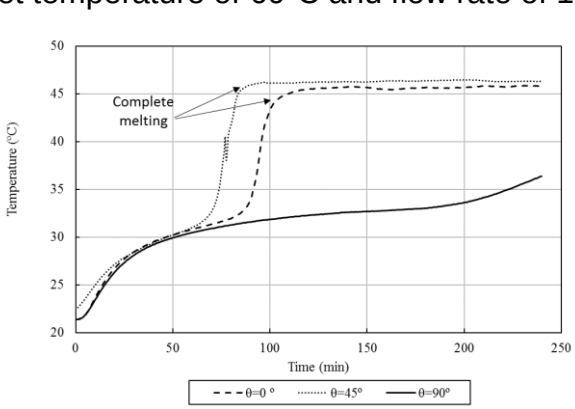

Figure 133. The PCM temperature in the lower bottom (T6) inside the PCM storage of inclinations of 0º, 45º and 90º.

- Effects of inclination on solid-liquid melting profile

Visualizing the solid-liquid interface progression with time inside the PCM storage is important for better understanding of the PCM melting behaviour inside the PCM for all the inclinations. Figure 134, Figure 135 and Figure 136 show the experimental photograph of the PCM melting progression, the simulation melting progression and the simulation PCM temperature inside the PCM storage at the three inclinations for a constant HTF inlet temperature of 60ºC and a flow rate of 120ml/min. In the figures, the white and transparent colours represent the solid and liquid PCM, respectively. At the beginning of the charging, the heat transfer mode within the PCM is only using conduction heat transfer. The visual observation of the melted PCM inside the storage starts in the 14, 5 and 13min for the 0^{o}, 45^{o} and 90^{o} inclination, respectively.

The outer photographs of the PCM melting profile for the storage in the 0^{o} inclination is seen from Figure 134(a)-(d). The PCM solid-liquid interface occurs in horizontal line starting from the top of the storage to the bottom until the complete melting of PCM in all the sides of the storage. The photographs show that the PCM has melted completely in the 98 minute which matches with the melting time approximation using the T6 measurements. The simulation diagrams of the PCM melting profile is very useful tool since the internal behaviour can be investigated. The diagrams of simulation melting profile of the PCM as in Figure 134 (e)-(h) show that during the initial period of melting, the PCM adjacent to the hot pipe is melted first making in a thin layer of the liquid PCM from the top to the bottom. The melting process initiates the natural convection heat transfer mode. Also, the buoyant force effect increases due to the fact of PCM tends to expand, reduce its density. The development of buoyant force resulting a faster melting of PCM at the top of the storage compared to the bottom and causes upwardly convex shape. During the melting period, the axial PCM melting rate is considered faster than the radial melting rate in terms of length measurement at this inclination.

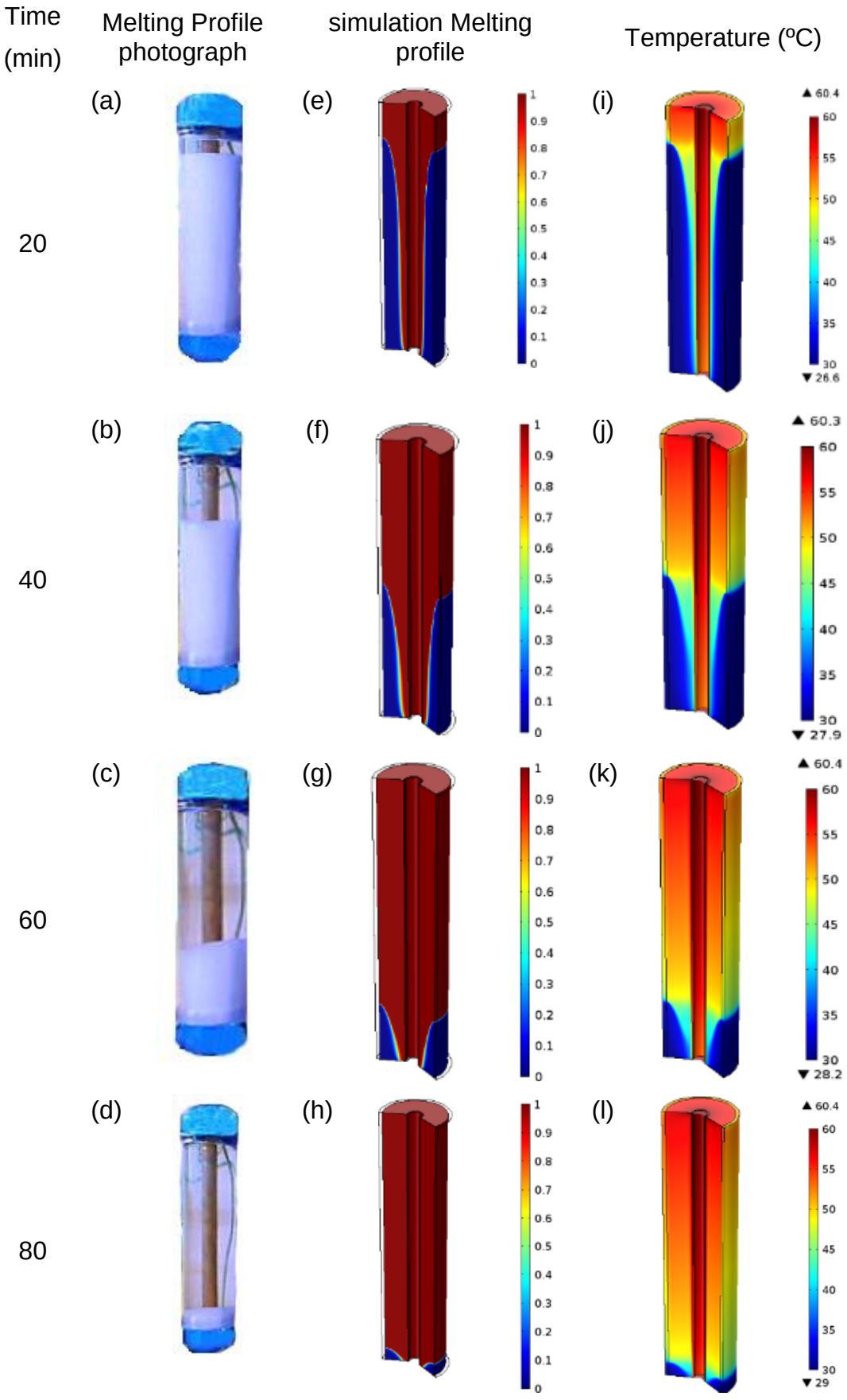

Figure 134. Experimental PCM melting photographs (left), simulation melting profile (centre) and simulation PCM temperature (right) for the PCM storage in 0º inclination at different time.

Figure 135 shows the PCM melting profile (experimental and simulation) and temperature distribution inside the PCM storage in the 45^{o} inclination. Unlike the melting of the PCM at the inclination of 0^{o}, the experimental photographs show a faster PCM melting rate at the top part of the container compared to the lower part and only a small portion of solid PCM is found after 80 minutes of charging. This difference in melting can be referred to the movement of the hot liquid PCM buoyant in the direction opposite to the gravity and impinges to the solid PCM at the top part opposite to the gravity direction which means that the PCM melting rate will be the fastest among all other directions in the storage. The melting of PCM in this inclination has been explained by others for rectangular container as three-dimensional flow structures and vortex motions in the liquid PCM and this is valid as well for the cylindrical PCM storage [192,193].

The PCM melting profile and temperature distribution inside the PCM storage in an inclination 90^{o} are shown in Figure 136. As shown from the figure, the PCM solid-liquid interface is in a straight horizontal line along the container starting with the upper side of the axial axis and the same reason can be referred of the hot liquid PCM movement in the direction opposite to the gravity. Melting of PCM in straight line profile continue until the last portion of PCM left in bottom of the container. One thing to note here is that the PCM at the bottom of the container could not be melted completely even when the test period extended up to 240 minutes and this is considered as a drawback of selecting this position.

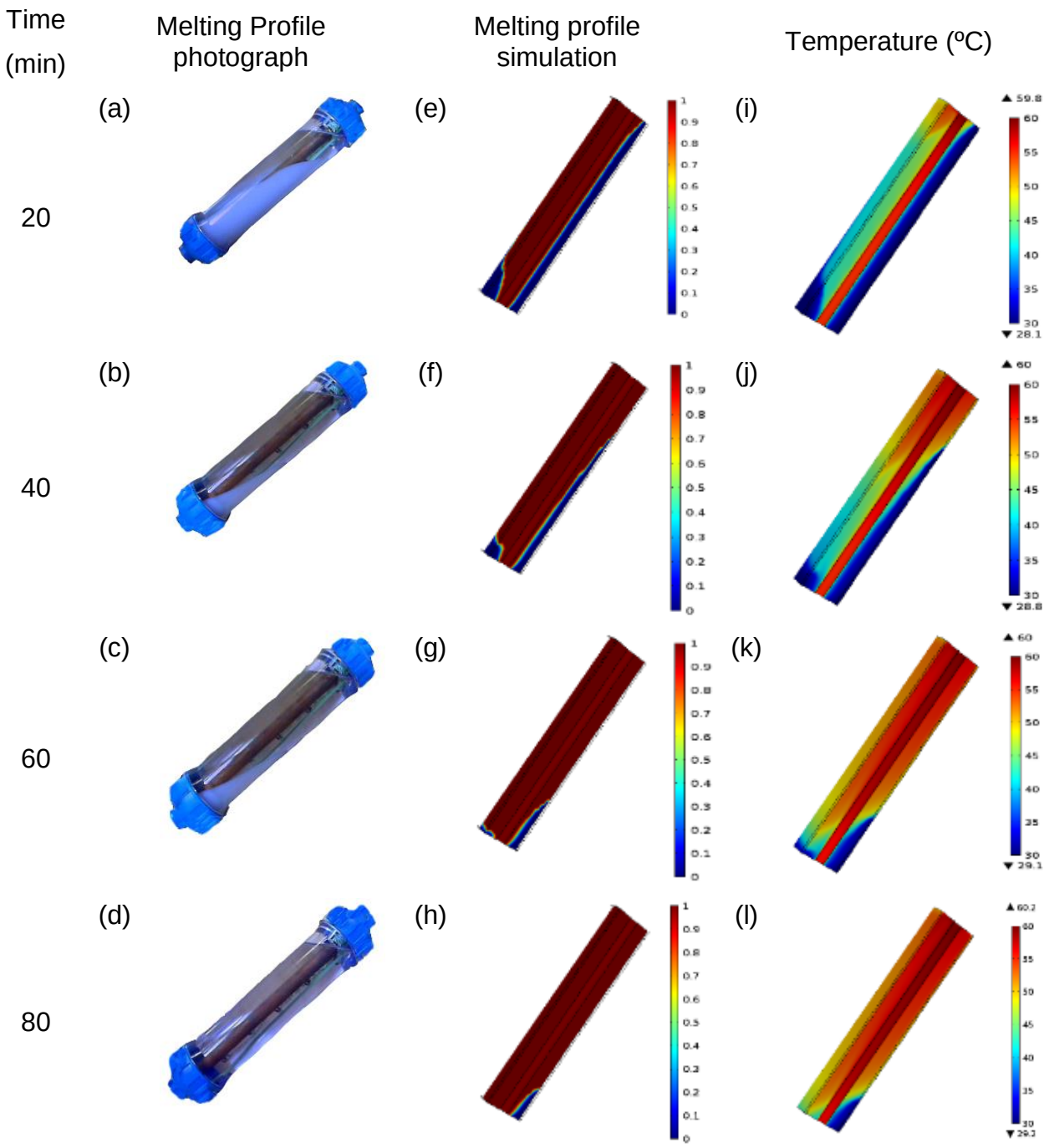

Figure 135. Experimental PCM melting photographs (left), simulation melting profile (centre) and simulation PCM temperature (right) for the PCM storage in 45º inclination storage at different time

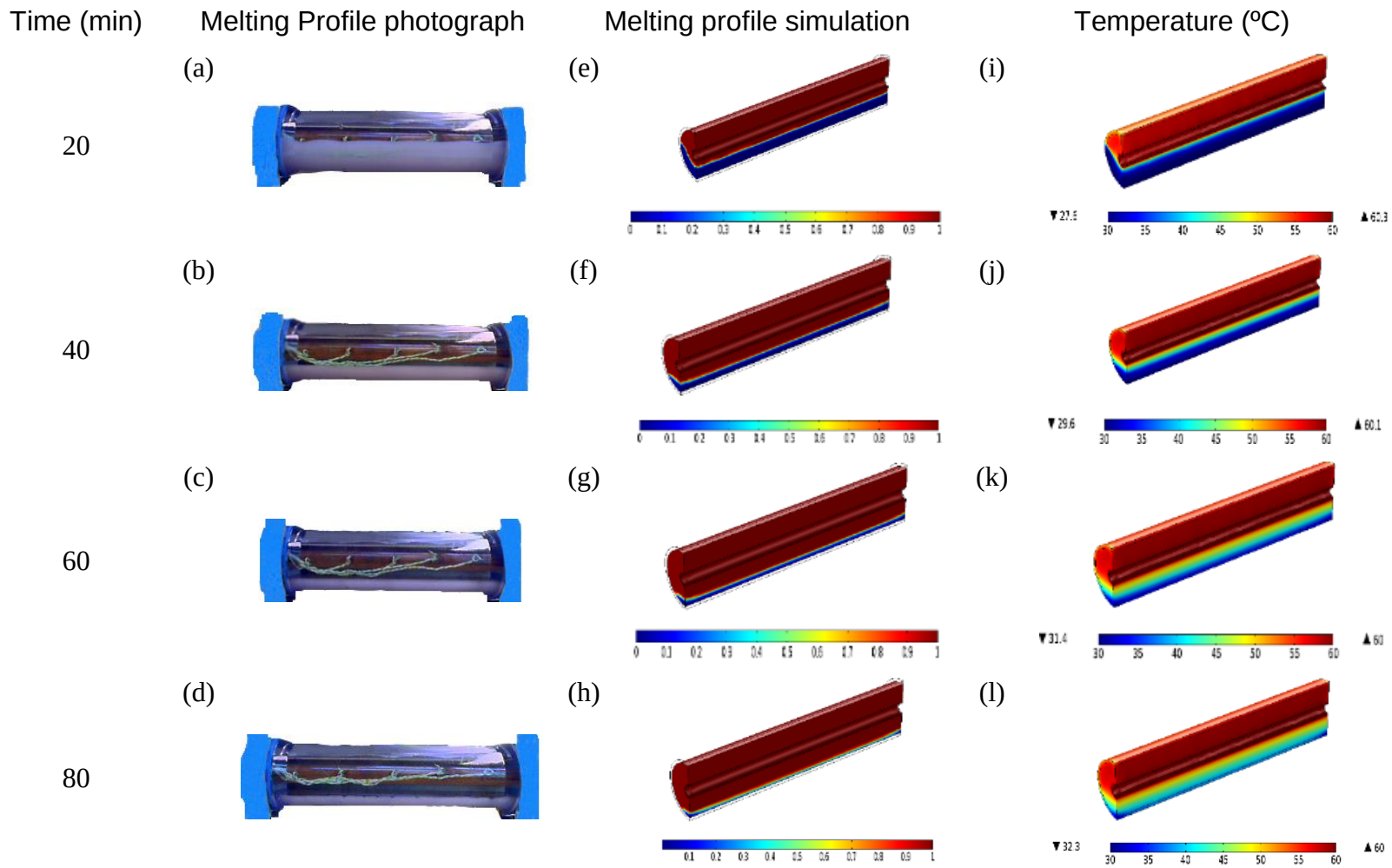

Figure 136. Experimental PCM melting photographs (left), simulation melting profile (centre) and simulation PCM temperature (right) for the PCM storage in 90º inclination at different tim

- Effects of inclination on the PCM flow

To further evaluate the effect of the storage inclination position on the convection within the PCM, the PCM flow using the numerical model is investigated. Figure 137, Figure 138 and Figure 139 show the PCM flow and velocity vector distribution within the PCM storage for the storage in the inclinations of 0°, 90° and 45°, respectively. Figure 137 shows the melted PCM adjacent to the HTF pipe surface experiences the highest velocity at the beginning of charging period (20min) and very few PCM flows downwards due to the system start up condition. The high flow of PCM near to the hot pipe causes a large non-uniform PCM flow within the container and explains the high melting rate in the axial direction compare radial direction [204]. With the proceeding of the melting process, the PCM adjacent to the container wall travels downward faster (blue colour indicates the flow in the opposite to gravity direction).

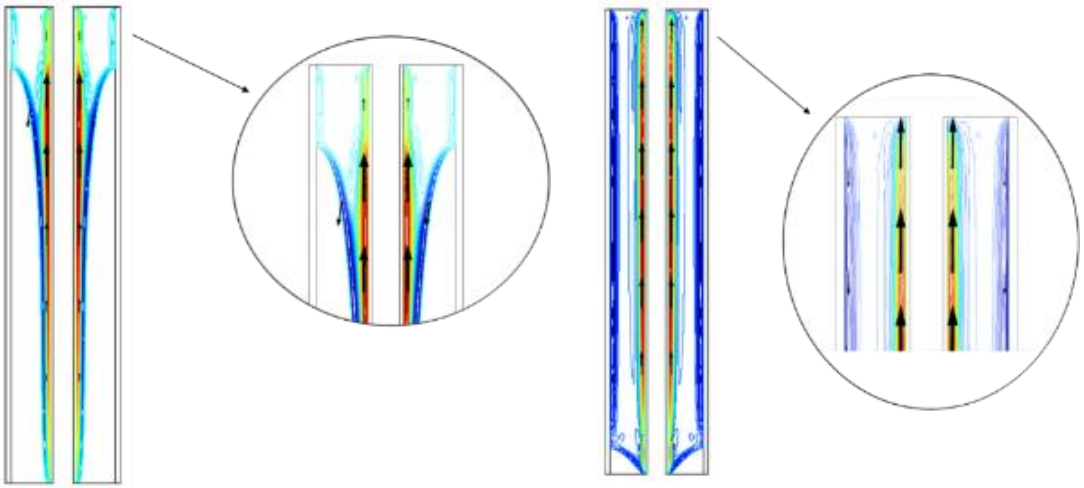

Time=20min Time=80min

Figure 137. PCM flow inside the PCM storge in 0º inclination cross section.

Figure 138 shows the PCM flow distributions in liquid phase in the cross section in the middle of the container (0.5L) at the storage of 90° inclination. In the 20 minute of charging process, the liquid PCM flows in the upper direction and making a vortex at the top of the container and the cooled liquid PCM flows in the direction adjacent to the inner wall of the container. This means that most of the absorbed heat is stored in the upper part of the storage. As the melting continue, the liquid PCM vortex is still active and more liquid PCM movement in the lower part is noticed.

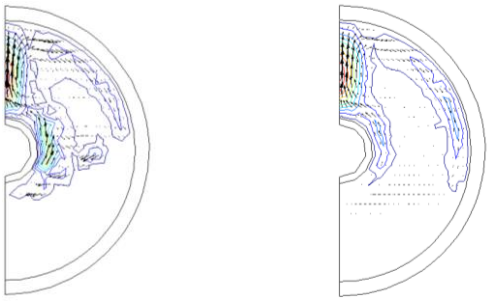

Time=20min Time=80min

Figure 138. PCM flow inside the heat exchanger in 90° inclination cross section at length=0.5L.

The liquid PCM flow for the storage in 45° inclination as shown in Figure 139 is different from the two other inclination positions (0° and the 90°) where the liquid PCM flows in more uniformity along the top axial and radial directions. This behaviour explains the fast melting rate of PCM in the upper side of the storage in both radial and axial directions. At later stage of melting (80min), the PCM located in the lower part of hot pipe flows toward the base container which helps overall PCM melting rate.

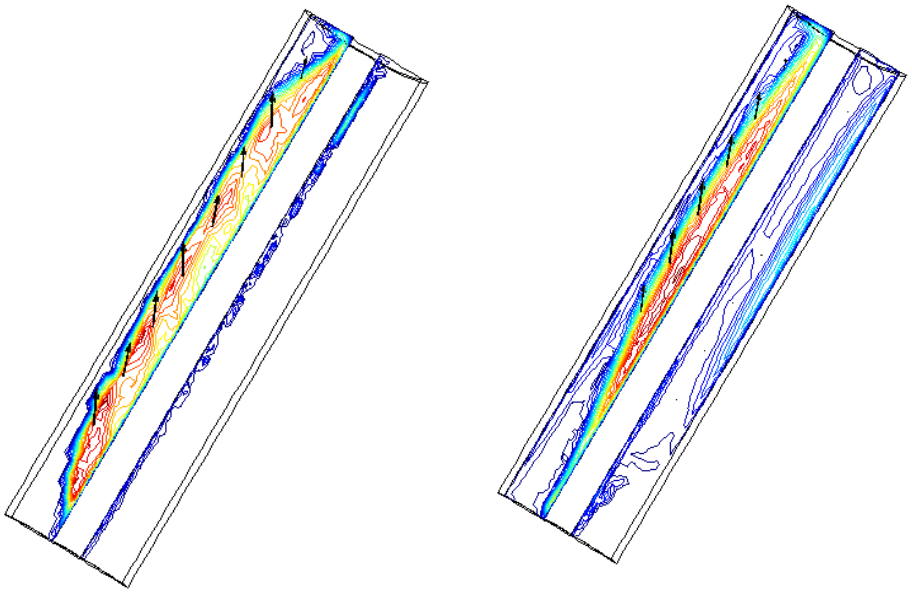

Time=20min Time=80min

Figure 139. PCM flow inside the heat exchanger in 45° inclination cross section at length=0.5L.

- Effects of inclination on the charging rate

Figure 140 illustrates the HTF temperature difference between the inlet and outlet during the melting process for the storage at different inclination. The results are

shown from the fifth minute for visualization purposes where the difference at the beginning of the chagrining is significant compared to the period after the 5th minute. Also, the figure shows that the HTF temperature difference in of the storage in the 0º inclination is more stable than of the storage in the 45º inclination. According to this figure, when the PCM storage is positioned at 45º, the HTF temperature difference is the maximum among the other two inclination positions until the 50.5 minute of charging. This means that the heat stored rate in the system is more in the 45º and followed by the storage in the 0º inclination. This observation is severely due to the complete PCM melting in the upper side of the tube where the natural convection is more significant as explained in the previous sections. After this period of charging, the situation is changed where the PCM storage in the 0º inclination stores heat at higher rate than the storage in the other two inclination positions.

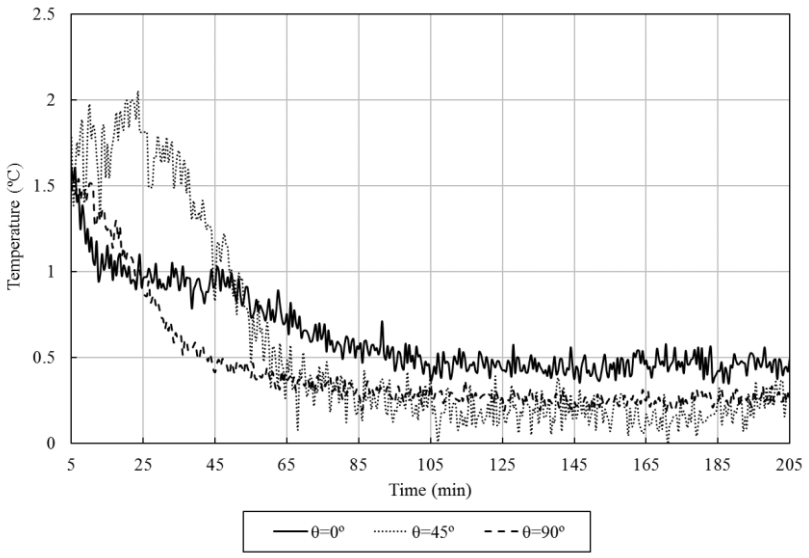

Figure 140. HTF inlet and outlet temperature difference for the PCM storage at different inclination positions for RT35 of HTF inlet temperature of 60ºC and HTF flow rate of 120ml/min.

5.3.1.5 Effect of the PCM latent heat density

The effect of latent heat on the thermal behaviour of the PCM storage was investigated using similar PCMs melting temperature with different latent heat capacity. In this case, RT27 and RT28HC was selected of heat capacity of 179kJ/Kg and 250kJ/kg, respectively. Their melting temperature difference was only 1ºC different and can be neglected due its low value. The results show that the melting time for RT27 PCM storage is less than the melting time for RT28HC by 35%. This can be realized by referring to Figure 141. Also, the PCM in the

RT28HC could not capture all the heat provided by the HTF due to the limit in the thermal conductivity of the PCM.

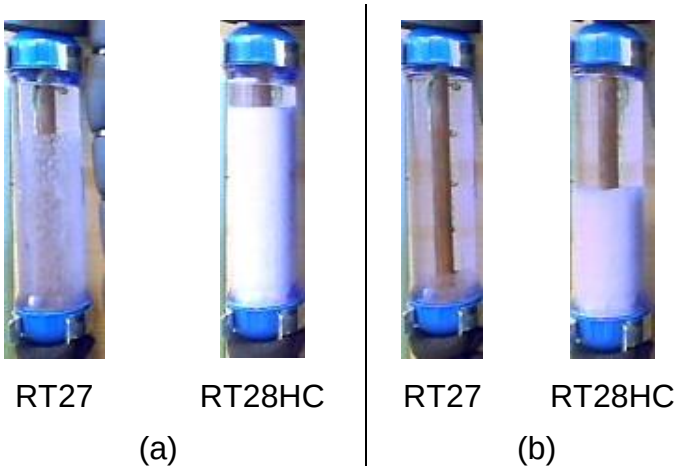

Figure 141. PCM melting photograph for RT27 and RT28HC with HTF inlet temperature of 55°C and flow rate of 60ml/min at (a) 20min and (b) 55min.

The temperature distribution of the PCM for both PCM storages is shown in Figure 142. It can be seen that the temperature distribution of the PCM in the 20 minute of charging when using the RT27 is higher at the middle of storage (T3, T4 and T5) than when using the RT28HC. At the same time of charging, the temperature of PCM when using RT28HC at T1 is higher than when using the RT27. This is because that slower heat rate is transferred to the PCM in the RT28HC case due to its high latent heat capacity. By the end of the complete of melting of RT27 (55min), the temperatures of T1, T2 and T3 of RT28HC are higher than in RT27 whereas the temperature of T4 and T5 in RT27 are higher than in RT28HC. The same reason of the high density can be referred to explain this increase.

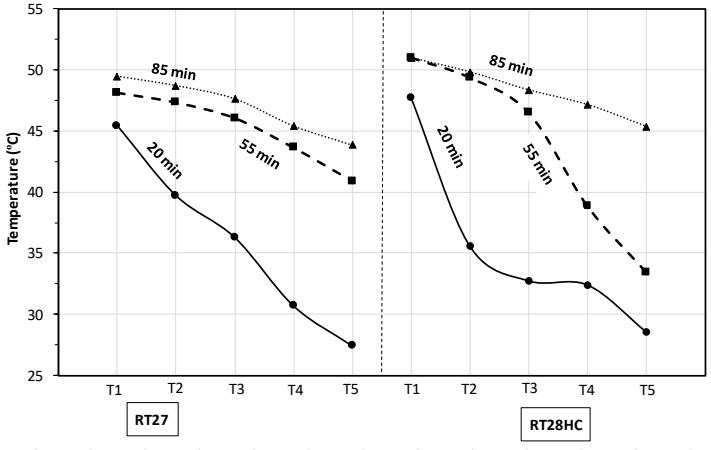

Figure 142. Temperature distribution within the PCM storage for RT27 and RT28HC for 60ml/min HTF flow rate and 55°C HTF inlet temperature in different times.

5.3.2 Enhancement of TES using multi-stage technique

This section reports experimental results of multi-stage PCM storage systems. The investigation includes the overall characteristics of a multi-stage system by examining the PCM temperature distribution, stored heat rate and PCM melting profiles. Then, the effect of several parameters is investigated experimentally such as the HTF flow rate and inlet temperature. The considered PCM arrangements are as the following:

- Case 1: PCM1: RT27, PCM2: RT27, PCM3: RT27
- Case 2: PCM1: RT42, PCM2: RT35, PCM3: RT27
- Case 3: PCM1: RT42, PCM2: RT42, PCM3: RT42

5.3.2.1 Overall multi- stage PCM system performance

The overall performance of multi-stage PCM storage is presented in this section. The HTF flow rate and inlet temperature are 120ml/min and 60^{o}C, respectively. Table 25 shows the melting time of each arrangement. In the case of same PCM filling with RT27 (case 1), all the PCM storages are melted in less than 50 minutes of charging with an interval difference of 5 minutes of each other. In the case of same PCM filling with RT42 (case 3), the PCM melting time is extended up to 411 minutes for the last PCM storage tank. More different melting time is noticed for each storage at each of the storage compared to the case. This can be explained due to fact that the HTF outlet temperature is higher than the melting temperature of the PCM in case 1 compare to the melting temperature of PCM in case 3. In addition, the HTF temperature after each stage is reduced more in case 1 compared to case 3. In the case of different PCM storage of RT42, RT35 and RT27 (case 2), it is noticed that the last storage stage PCM 3 melts faster than PCM1 and PCM 3 due to its lower melting temperature compared to the other two PCMs. It is good to note that the melting time for PCM 3 in case 1 and case 2 is kept unchanged for the both cases of 50 minutes. However, the melting time for the PCM 1 decreases slightly between the two cases (case 2 & case 3). This is due to the slight fluctuations of both HTF flow rate and inlet temperature.

In order to visualize the PCM melting profile and fraction, Figure 143, Figure 144 and Figure 145 show the melting profile for cases 1, 2 and 3, respectively. It is noticed that all cases follow the same type of melting profile of a horizontal line.

Also, a clear PCM gradual melting is noticed in the case 2 in Figure 144 due to the large PCM melting temperature difference between the stage between the RT27 and the other two PCMs (RT42 and RT35). Also, the difference in the melting progress is noticed in the same PCM type (case 3), this is due to the slight difference HTF inlet temperature at each stage.

Table 25. The complete PCM melting time in minutes for different PCM arrangement.

Case 1			Case 2			Case 3		
RT27	RT27	RT27	RT42	RT35	RT27	RT42	RT42	RT42
40	45	50	245	108	50	265	390	411

(a) (b)

Figure 143. PCM melting photographs for case 1 (RT27) with HTF inlet temperature of 60°C and flow rate of 120ml/min at (a) 40min and (b) 240min.

(a) (b)

Figure 144. PCM melting photographs for case 2 (RT42-RT35-RT27) with HTF inlet temperature of 60°C and flow rate of 40ml/min at (a) 40min and (b) 240min.

(a) (b)

Figure 145. PCM melting photographs for case 3 (RT42) with HTF inlet temperature of 60ºC and flow rate of 240ml/min (a) 60min and (b) 240min.

The temperature distribution of the PCM in case 1, 2 and 3 is reported as shown in Figure 146. It can be seen that the temperature distribution of the PCM in case 1 at T1 is similar for all storages of a difference of 1°C. However, the temperature of PCM at the middle of the storage (T2-T5) is higher in PCM 2 and PCM 3 compared to PCM 1. The average temperature of PCM in case 2 is considered higher than in case 1 and case 3 and the maximum temperature reaches to 57.5°C, 56.5°C and 55.4°C, respectively. This concludes that the multi-stage PCM arrangement could be used to increase the PCM average temperature.

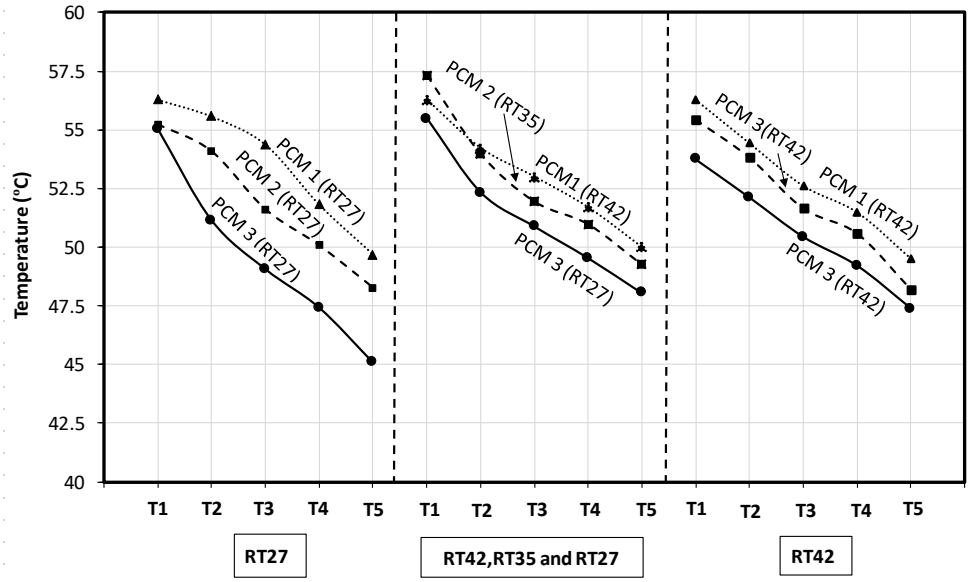

Figure 146. PCM temperature distribution inside the multi-stage storage at the melting time for different arrangements for HTF inlet temperature of 60ºC and flow rate of 120ml/min.

The rate of stored heat and the accumulated heat until the completed melting for case 1, case 2 and case 3 is shown in Figure 147. The heat transfer rate in the case 1 is more than to case 2 and 3 for the same period of complete melting of case 1 (50minutes), this is because of the lower PCM melting temperature in case

1 compared to case 2 and 3 with a total stored heat of case 1 of 168kJ. However, the larger the melting temperature difference between PCMs stages, the more sensible heat is stored in the PCM storage. This is due to the fact that the PCM with the lowest melting temperature melts quickly when the melting temperature difference between the PCMs stage becomes greater as seen in case 2 and case 3. The total heat stored in case 2 and case 3 are 408kJ and 425kJ, respectively.

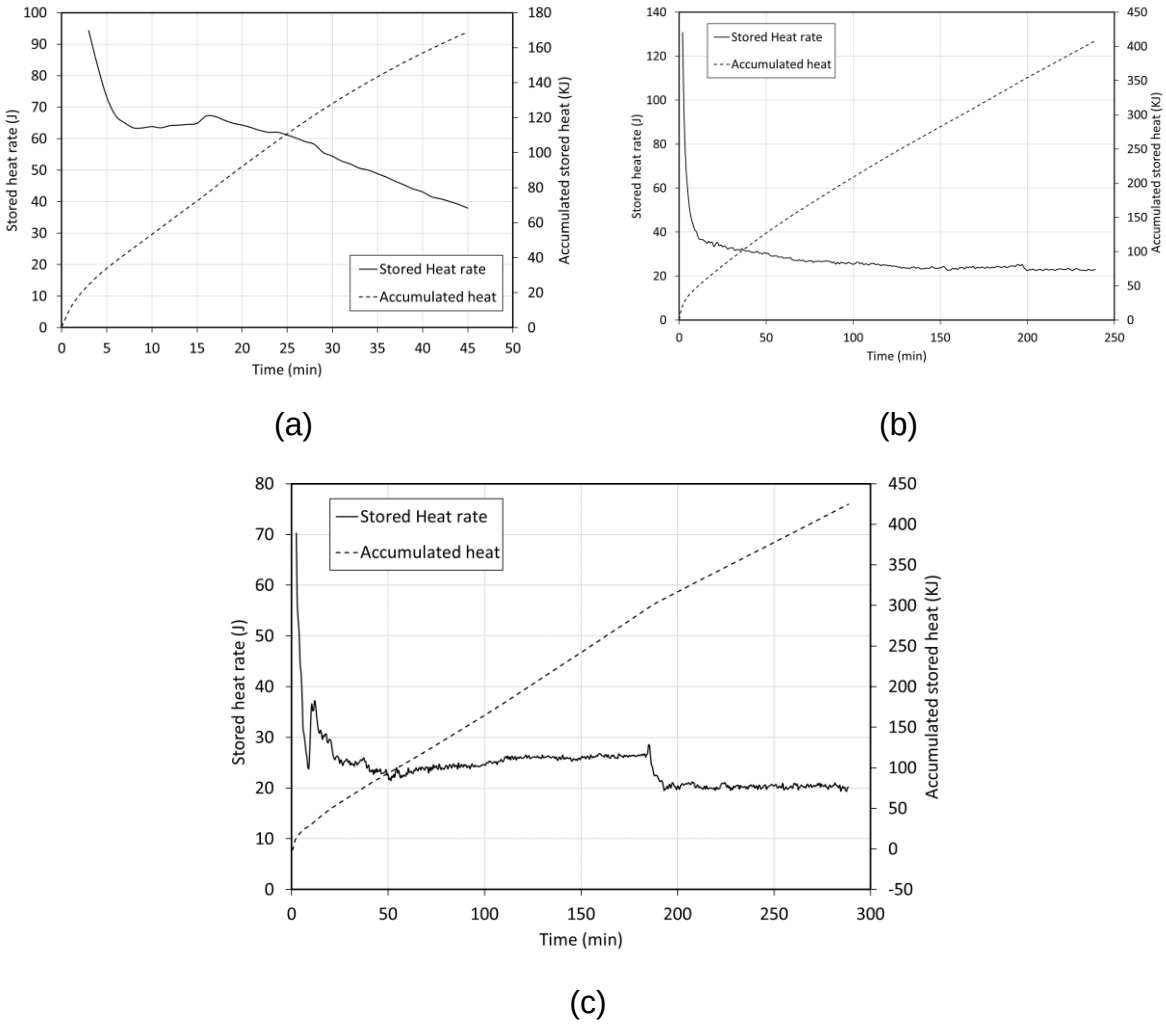

Figure 147. Heat storage rate and accumulated stored heat versus time with HTF inlet temperature of 60°C and flow rate of 120ml/min for multi-storage arrangement (a) Case 1, (b) Case 2 and (C) case 3.

5.3.2.2 Effect of HTF flow rate on the multi-stage PCM storage system

The effect of the HTF fluid flow on the melting time for the different PCM arrangement cases is shown in Table 26. It can be noticed that melting time is reduced by 10% of PCM 3 for the case 1 arrangement as the HTF flow rate is increased from 120ml/min to 240ml/min whereas no change of the melting time is noticed to the PCM 1 and PCM 2. A general reduction of the melting time for

the case 2 arrangement especially in the PCM 2 (8 minutes) and PCM 3 (4 minutes) as the increase of the HTF flow rate due to the high melting temperature of PCM 1. A dramatic decrease of the melting time as the HTF flow rate is increase for the case 3 arrangement by 57min, 133min and 122.5min for PCM 1, 2 and 3, respectively.

Table 26. PCM melting time for the different PCM arrangement at HTF inlet temperature of 60°C for various HTF flow rates.

HTF Flow rate (ml/min)	Case 1			Case 2			Case 3		
	PCM 1	PCM 2	PCM 3	PCM 1	PCM 2	PCM 3	PCM 1	PCM 2	PCM 3
120	40	45	50	240	108	50	276	390	411
240	40	45	45	239	100	46	219	257	288.5

The PCM temperature distribution inside the storages for the HTF flow rates of 120 and 240ml/min are shown in Figure 146 and Figure 148, respectively. The HTF flow rate has not effect of on the temperature distribution in PCM 1 and PCM 2 in case 1 and a slight increase in the temperature of the PCM 3. In case 2, it is noticed a slight increase of the PCM temperature in the locations from T2 to T5 as the HTF flow rate is increased. Similar increase pattern is noticed in case 3 but this includes all PCM locations (T1-T5).

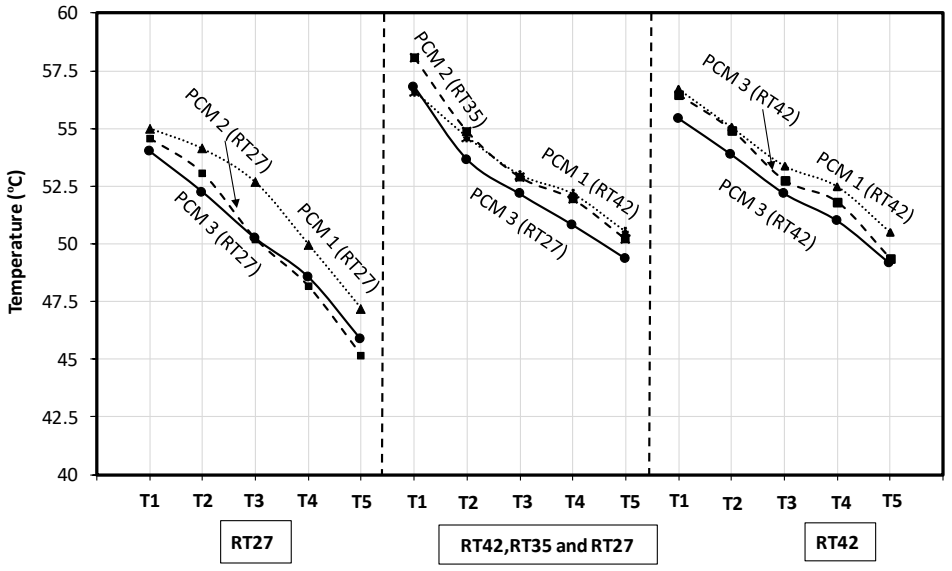

Figure 148. PCM temperature distribution inside the multi-stage storage at the melting time for different PCMs for HTF inlet temperature of 60°C and flow rate of 240ml/min.

5.3.2.3 Investigation geometrical parameters in the multi-stage PCM storage

This section investigates numerically the effect of geometry parameters on the multi-stage PCM storage system of charging and discharging process. Two systems are studied having the same and variable PCM volume.

Higher PCM storage volume was considered in this section with storage length of 750mm, 20mm PCM storage radius and inner tube diameter of 4mm with thickness of 2mm. Each storage has the capacity of 777g of PCM. The HTF flow rate was 60ml/min and its temperatures for charging and discharging were set to 60°C and 24°C, respectively. Both the charging and discharging durations were 18000s for each process. The arrangement of the PCMs in multi-stage system is sorted in descending order of melting temperature such that higher melting temperature is at the inlet side of the HTF i.e. RT42- RT35-RT27.

Figure 149 shows the liquid fraction for the PCM in the all the storages during the charging and discharging process. At the beginning of the charging, all the PCM storages melted at the same rate until the1880s where the liquid fraction reaches to 0.29. Then, the PCM 3 storage of RT27 is melted in faster rate compared to the others PCM storages due to its low melting temperature. By the end of the charging the PCM liquid fraction of PCM 1, 2 and 3 reach to 0.71, 0.82 and 0.99, respectively.

At the discharging process, the HTF was circulated at a temperature of 24°C. The figure shows clearly a slight increase on the liquid fraction of PCM at the beginning of charging of in stages of PCM 2 and PCM 3 and an immediate solidification of PCM 1 starts at this period. This is due to the effect of the released heat by the PCM 3. The PCM 3 continues to keep the high liquid fraction on 0.99 during the first 2480s of the discharging process (20480s of the total process). PCM 1 storage experiences a higher heat release and the complete release of the latent heat is achieved by 3440s. PCM 2 releases its latent heat at longer time than PCM 3 by 4368s. However, by the end of the discharging process, PCM 3 is able to release all the latent heat at a liquid fraction of 0.082.

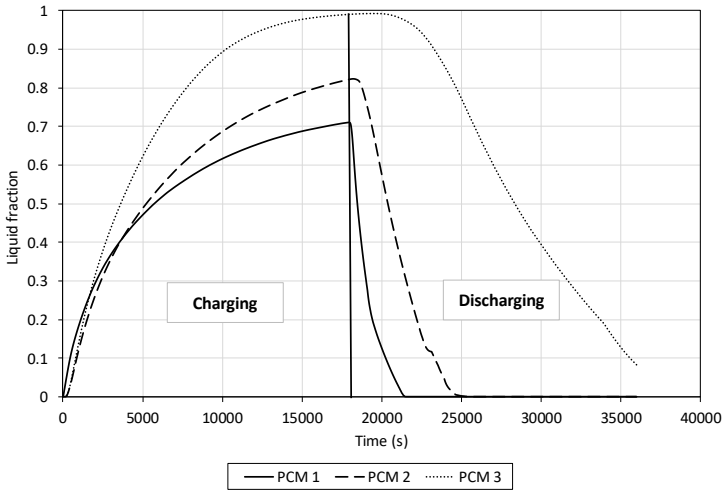

Figure 149. The PCM liquid fraction versus time for charging and discharging for PCM radius of 20mm of HTF inlet temperature of 60°C and flow rate of 60ml/min.

Figure 150 compares the PCM average temperature for the different storages. As expected, the average temperatures of the PCM increases with the charging time and the storage with the higher melting temperature i.e. PCM 1. This is due to the absorbed heat by PCM 1 is in the sensible form. By the end of the charging, the PCM average temperatures of the stages of PCM 1, PCM 2 and PCM 3 are 45.2°C, 40.67°C and 37.01°C, respectively. In the discharging mode, temperature of PCM in PCM 1 and PCM 2 decrease steeply and reached to its minimum in at 5640s and 8660s, respectively.

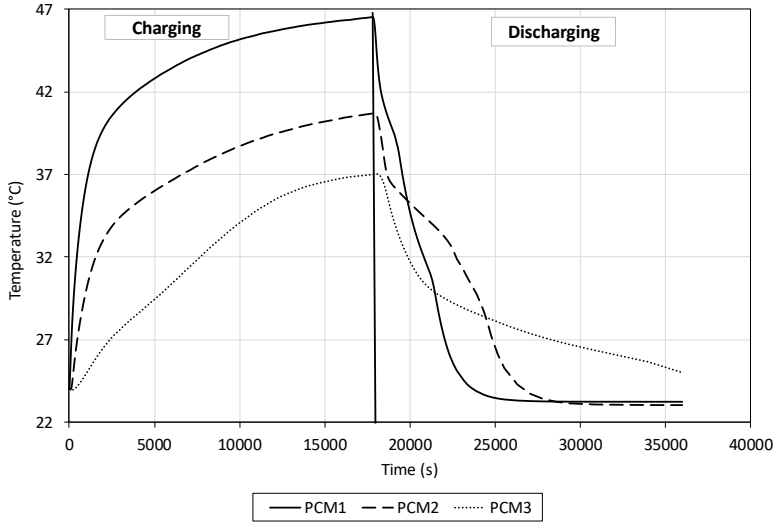

Figure 150. The average temperature of PCM versus time for charging and discharging for PCM radius of 20mm of HTF inlet temperature of 60°C and flow rate of 60ml/min.

The HTF outlet temperature is shown in Figure 151 for the three storage stages. The HTF outlet temperature at the outlet of PCM 3 is 37°C by the end of the

charging process with a difference from the inlet temperature of 23°C. The outlet temperature of HTF increases in PCM 3 due to the effect of absorbing the heat in the latent heat form which causes a complete melting of PCM as pointed out earlier.

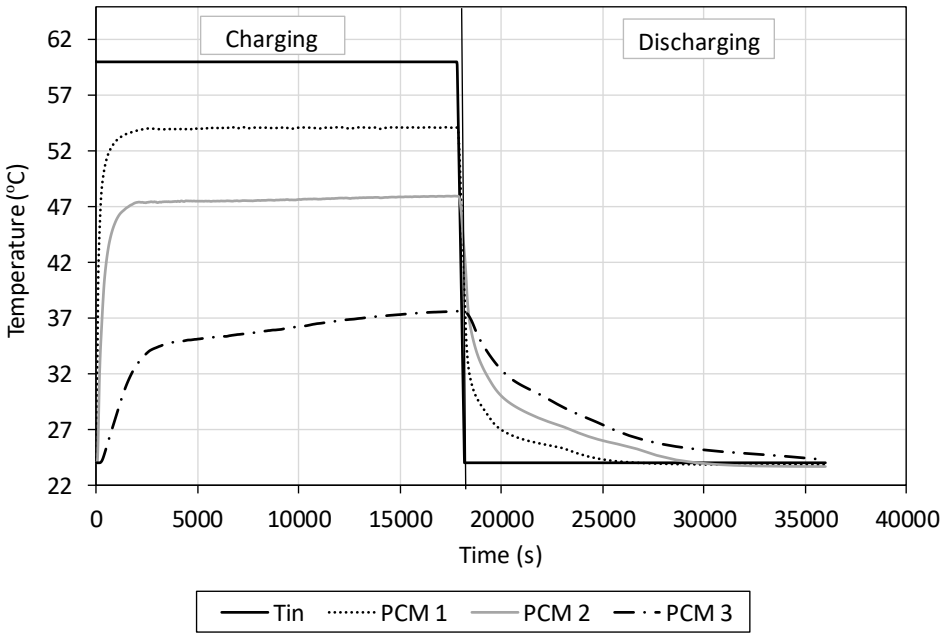

Figure 151. The HTF outlet temperature versus time for charging and discharging for PCM radius of 20mm of HTF inlet temperature of 60C and flow rate of ratio of 60ml/min.

For a fixed PCM volume case, two parameters to be varied; the PCM thickness and the storage length. These two geometry dimensions control the heat flow inside the PCM and hence the rate of the heat transfer and the accumulated stored energy. The HTF flow rate, the tube radius and thickness are fixed throughout the maximization process. The maximization problem is summed up to the following:

Objective function: increase the total stored/released heat and increase the melting process.

Constraints:

- The average HTF velocity=0.01m/s, Re<2300
- HTF inner radius= 4mm
- HTF tube thickness=2mm

Variables: r/r_{PCM} : 1.5, 2

The PCM radius ratio is varied in a range between 1.5 and 2 where the PCM thickness of 20mm is as radius ratio of 1. Hence the length PCM diameter dependent equation is expressed as:

$$H = \frac{m_{PCM}}{\rho_{PCM}} * \frac{1}{\pi({r_{PCM}}^2 - {r_{tube}}^2)} \quad 5.30$$

Figure 152 compares the liquid fraction of each of the PCM storages stages during the charging and discharging process for PCM radius ration of 1.5 and 2.0. As shown in Figure 152 that increasing the PCM radius ratio by 1.5 reduces the PCM liquid fraction at the end of the charging period by 0.13 and 0.05 compared to radius ratio of 1 in the PCM 1 and PCM 2, respectively. However, a slight decrease on the PCM liquid fraction is noticed for PCM 3 of less than 0.02. A further reduction in the PCM liquid fraction is noticed when the radius ratio is doubled as shown in Figure 152 (b) where it reaches to 0.37, 0.58 and 0.83 of PCM 1, 2 and 3, respectively.

The increase of liquid fraction of PCM 3 at the beginning of the discharging process is noticed in Figure 152 due to the cascaded storage effect as the radius ratio is increased and it is estimated to nearly of 1%. Also, a faster heat release by the PCM 3 stage in all the radius ratios compared to PCM 1 and PCM 2 due to the incomplete melting of PCM at this storage stage and the high difference in temperature between the HTF inlet temperate and the melting temperature. Also, higher PCM radius reduces the amount of heat released by the PCM and this is shown by higher liquid fraction for PCM 3 of 0.46 on the radius ratio of 2.

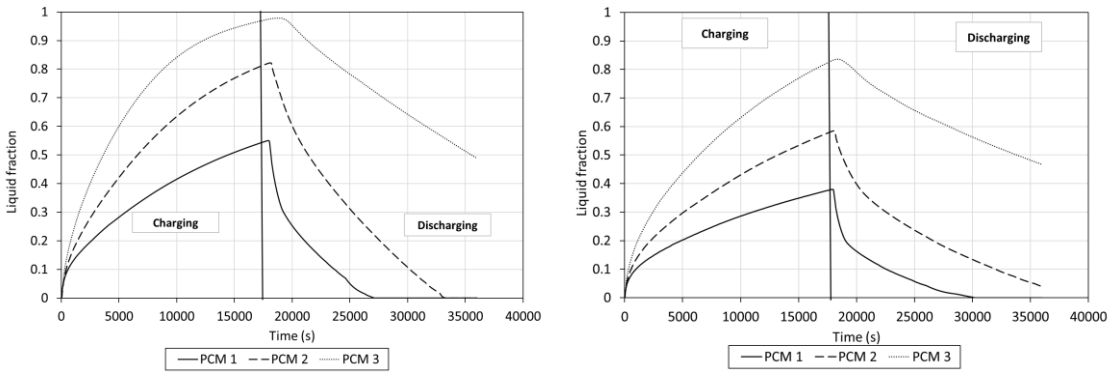

Figure 152. The PCM liquid fraction versus time for charging and discharging for the PCM radius ratios of (a) 1.5 and (b) 2.

Figure 153 compares the average temperature of the PCM in the different stage storages for the different radius ratios. It is noticed increasing the radius ratio

decreases the average temperature of PCM for all the stages in the charging process. The average PCM temperature is reduced as the radius ratio is increased by 3.58°C, 4.86°C and 4.12°C for PCM 1, PCM 2 and PCM 3, respectively. However, a lower temperature drop of the PCM is noticed in PCM 1 and PCM 3 as the radius ratio is increased. The average temperature of PCM 1 is the same for both radius ratios by the end of the discharging process of 26.8°C.

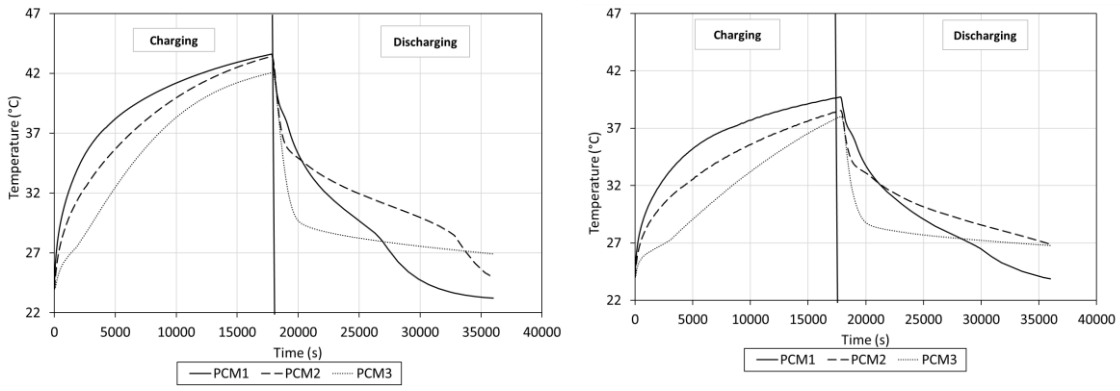

Figure 153. The average temperature of PCM versus time for charging and discharging for the PCM radius ratios of (a) 1.5 and (b) 2.

Figure 154 shows the HTF outlet temperature i.e. the heat storage rate for the different radius ratios. It clearly showing that at the beginning of charging process, less outlet HTF temperate is at the PCM radius ratio of 1.5 compared to the radius ratio of 2. This difference is reduced to 1.5°C in radius ratio of 1.5 compared to 2. Also, more heat is realised by the PCM in the radius ratio of 2 compare 1.5 and no difference of the HTF outlet temperature is noticed by the end of discharging process.

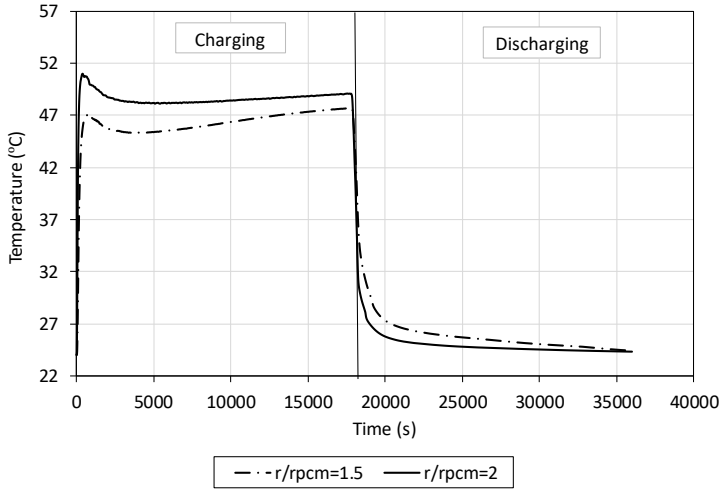

Figure 154. The HTF outlet temperature versus time for charging and discharging for various PCM radius ratios.

The multi-storage PCM was studied for different geometries by varying the PCM volume. So, two cases were considered; case 1 investigated the effect of the PCM radius for a variable PCM volume in the performance of the multi-storage system. So, the ratio of the PCM radius to the HTF inner tube radius was varied in the ratio of 3, 4, 5 and 6. In this case, the storages height were kept fixed at 750mm. Case 2 considered the effect of variation of the ratio of storage height to the HTF inner of 55, 100, 150 and 200 on the performance of the multi-storage system. For both cases, PCM 1, PCM 2 and PCM3 were filled by RT42, RT35 and RT27, respectively. The HTF outlet temperature was set to 60°C and of flow rate of 60ml/min. A summary for the cases geometry is summarized in Table 27.

Table 27. The geomatry parameters cases

Case #	Fixed variables	Ratio range	Varied parameter range
Case 1	L=750mm Ri=4mm	3<Ro/Ri<6	12<Ro<24
Case 2	Ro=20 and Ri=4mm	55<L/Ri<200	220 <L<800

Figure 155 shows the PCM liquid fraction for the multi-storage for various radius ratios (case 1). It clearly noticed a high melting rate for the radius ratio of 3 of complete melting of PCM 2, PCM 3 in 10000s and 6500s. In addition, the storage of PCM 3 experienced a liquid fraction of 0.89 by the end of charging process at this PCM radius ratio. Increasing the PCM radius ratio between 4 and 5 reduces the PCM liquid fraction of both PCM 1 and PCM 2 where PCM 3 is maintained at a full melting in those PCM radius ratios by the end of the charging process.

In the discharging process, it can be observed that a lower radius ratio increases the heat released by the PCM as in Figure 155 (a) where by the end of the discharging all the storages stages are in the solid phase. Also, the higher PCM radius ratios between the PCM radius and the HTF inner causes a slight delay of solidification of PCM in all stages. However, the PCM liquid fraction of PCM 3 increases by the end of the discharging process as the PCM radius ratio increases from 4, 5 and 6 of 0.11, 0.28 and 0.37, respectively.

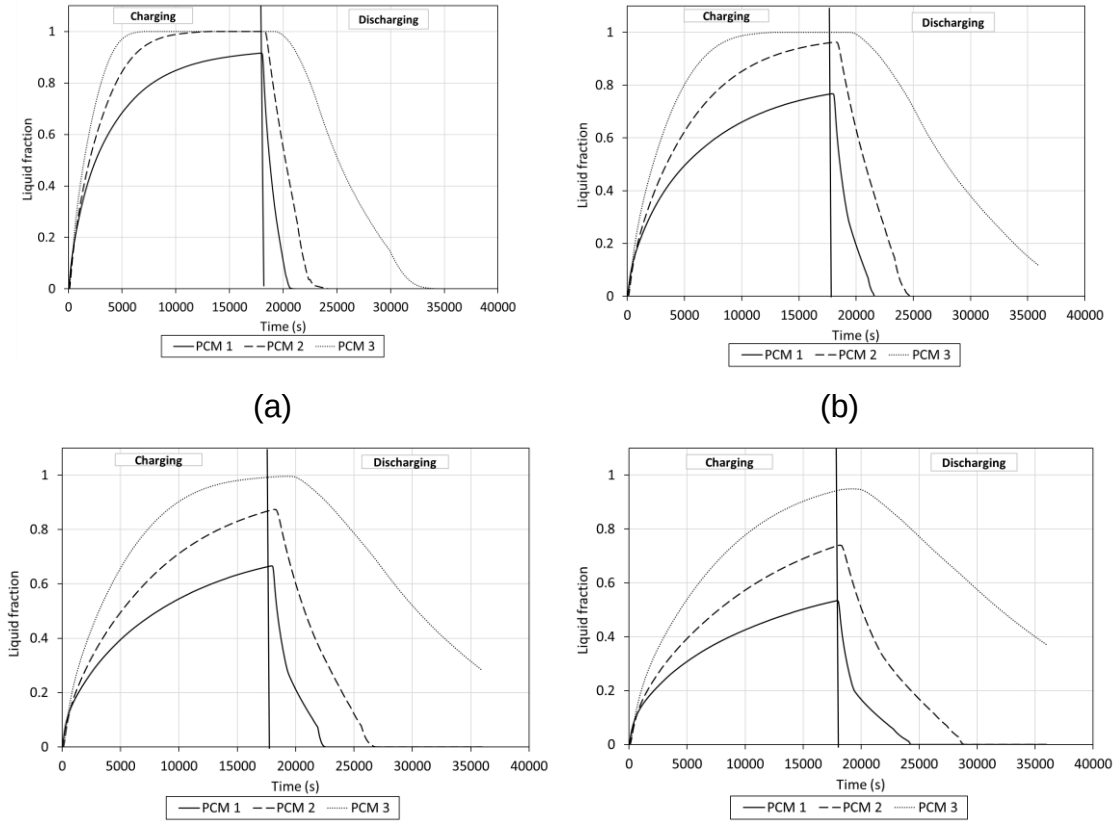

Figure 155. The PCM liquid fraction versus time for charging and discharging for radius ratio of (a) 3 ,(b) 4, (c) 5 and (b) 6.

Figure 156 compares the average temperature of the PCM storages for the different PCM radius ratios. It can be clearly notice that increasing the radius ratio decreases the PCM average temperature during the charging process. For instance, increasing the PCM radius ratio from 3 to 6 reduces the temperature by the end of charging process of PCM 1, PCM 2 and PCM 3 by 5.5°C, 6.49°C and 6.04°C, respectively. In the discharging process, faster PCM temperature drop is noticed as the PCM radius ratio is decreased. The average temperature of the PCM is reached to the HTF inlet temperature of 24°C for PCM 1 and PCM 2 for all the radius ratios by the end of the discharging process.

Figure 157 shows the HTF outlet temperature for the different radius ratios. It clearly showing that the HTF outlet temperature at the highest radius ratio of 6 is maintained constant during the charging process and only a slight increase of 1.3°C is noticed by the end of the charging process and this shows that the heat stored at fixed rate. On the other hand, the lower PCM radius ratios decreases its heat stored rate with time and reaches to its steady state by the end of the

charging process. The steady state for the radius ratio of 3 is reached at time of 10640s.

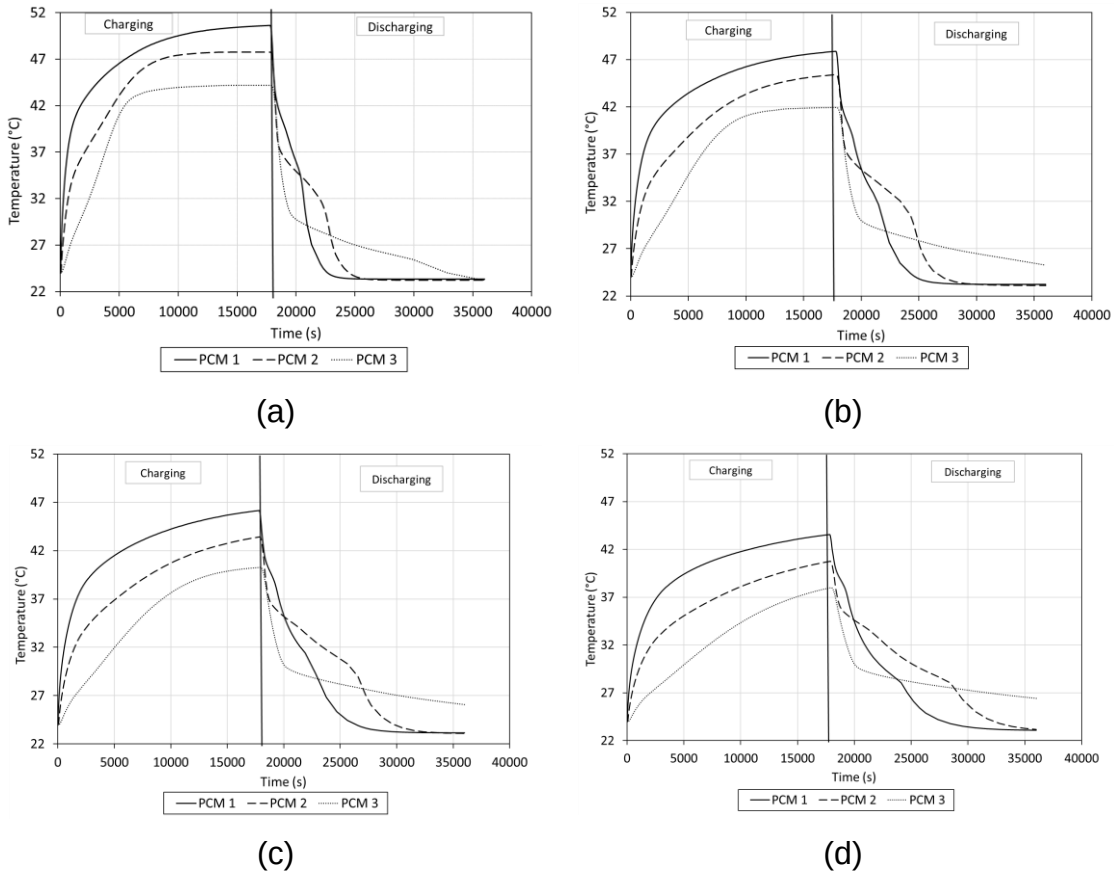

Figure 156. The average temperature of PCM versus time for charging and discharging for PCM radius ratio of (a) 3 ,(b) 4, (c) 5 and (b) 6.

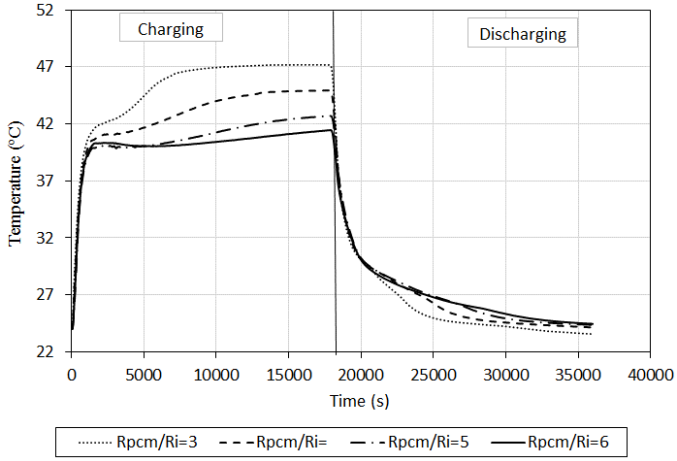

Figure 157. The HTF outlet temperature versus time for charging and discharging for various PCM radius ratios.

In the case 2 of maximizing the heat transfer rate for the PCM, the storage length is varied between 220mm and 800mm with a ratio to the inner tube diameter ratios of 55, 100, 150 and 200. Figure 158 shows the PCM liquid fraction for the

multi-storage for the various lengths. It clearly noticed that increasing the length of the storage is delayed the fully melting status of PCM 3 stage from 8140s in length ratio of 55 to 18000s in length ratio of 200. However, PCM 1 and PCM 2 could not complete its melting during the charging period for the length ratios ranged from 100 to 200 by the end of the charging period. The non-complete of the melting PCM in PCM 1 stage at all the lengths ratios has dropped the liquid fraction significantly with time. On the other hand, the longer PCM i.e. the more PCM volume results a gradual solidification of the PCM and by the end of the discharging process, the PCM is not fully solid.

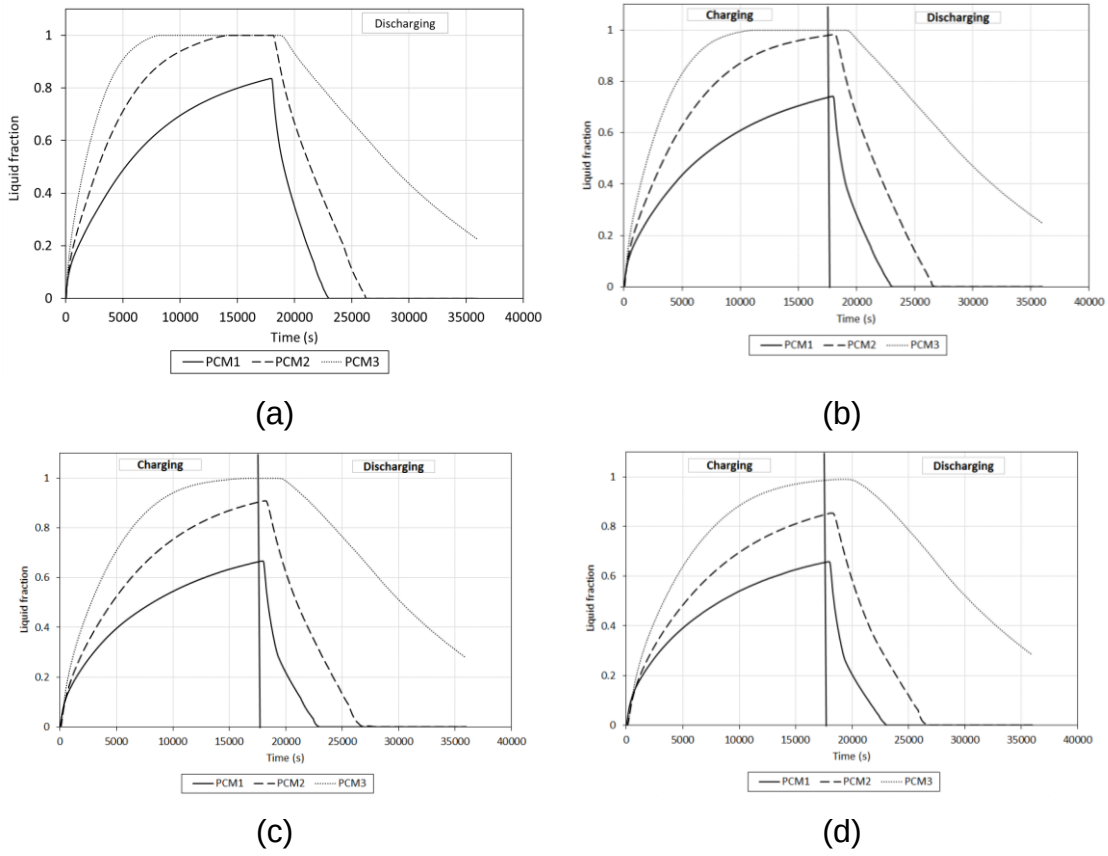

Figure 158. The liquid fraction versus time for charging and discharging for the storage length to tube radius ratio of (a) 55 ,(b) 100, (c) 150 and (b) 200.

Figure 159 shows the HTF outlet temperature for the different lengths. It clearly showing that the HTF outlet temperature at longest storage lengths absorbed most of the heat. Interestingly that HTF outlet temperature have similar pattern during the charging process and can be approximated in parallel. In addition, the storage with higher length radius produces a higher HTF outlet temperature during the discharging period. By the end of the charging period, the HTF outlet temperature for all the length ratios produce the same HTF outlet temperature.

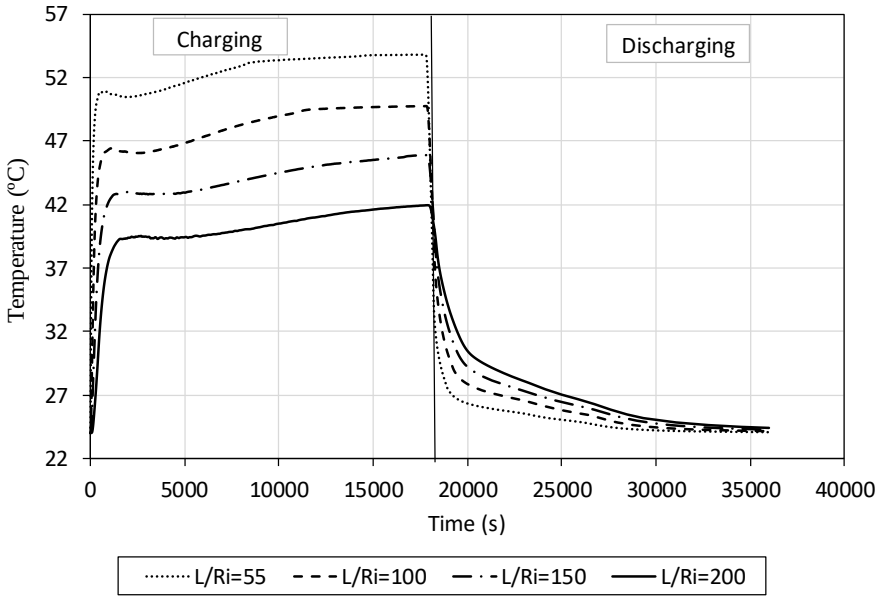

Figure 159. The HTF outlet temperature versus time for charging and discharging for various the storage length to tube radius ratio.

5.4 Conclusions

The present chapter reported experimental and numerical investigations on the thermal behaviour of a cylindrical PCM thermal storage system. The effects of different factors on the performance of the PCM storage were investigated such as the geometry, PCM melting temperature, PCM storage orientation, HTF inlet temperature and its flow rate. Finally, the multi-stage PCM storage technique was studied.

At the beginning of the chapter, a numerical model was developed for a PCM storage system. The model was validated using a case study from a published work. The results show a good agreement of the model results with the considered experimental case. Hence, the model was used to conduct a geometric parametric study of varying the PCM thickness and its height. The results show a reduction by 6.5% of the PCM melting time as its radius decreases from 22mm to 11mm and an increase by 33% when the PCM radius increased from 11mm to 33mm. Also, the effect of varying the PCM radius or its height was investigated. The results show that longer PCM storage does not necessarily lead to experience lower melting time.

In addition, an experimental and numerical study was presented for the influence of the storage inclination position on the melting characteristics of the melting process in a cylindrical PCM storage system at three inclination positions of 0º, 45º and 90º using an HTF flow rate of 120ml/min at inlet temperature of 60ºC. It

is clearly shown that inclination has a major impact on the melting characteristics of the PCM. The PCM in a storage at inclination position of 45º melts faster than the PCM in the heat exchanger in the vertical and horizontal position where the PCM melting time is reduced in the storage inclination position of 45º by 13% compared to the one in the vertical position. The PCM melting profile in the storage differs at inclination positions , for example, the PCM melts faster in the axial direction than the radial direction in the storage of 0º inclination position. The opposite PCM melting behaviour was observed in the storage of 90º inclination position where it melts faster in the radial direction than the axial direction. The PCM melting behaviour in the storage of 45º inclination position in both directions the axial and radial occurs with similar rate. The liquid PCM motion within the heat exchanger has an important influence on the PCM melting rate where the PCM facing the direction of the buoyant force is melted at a faster rate compared to the PCM located in all other directions. During the charging period, the PCM in the lower part of the storage in the 90º inclination position was not melted completely which is considered as a disadvantage on selecting this inclination position. It has been found that the melting time is not affected by the HTF increase from 60ml/min to 120ml/min. However, an HTF inlet temperature increase causes a reduction in the PCM but in contrast no change in the PCM melting profile is noticed due to the operating conditions.

At the end of the chapter, the enhancement of TES using the multi-storage technique was investigated by examining the temperature distribution, stored heat and melting profiles. The results show that arranging the PCM from higher to lower melting temperature, no increases the overall PCM temperature which is an advantage in terms of the heat quality. A greater reduction of the melting time was observed for the PCM with the higher melting temperature.

Chapter 6 : HCPV-MLM and PCM storage integration

In previous chapters, the performance of the two different systems the MLM and multi-stages PCM storage were analysed under different operating conditions. As pointed out in the literature review, very little attention has been given to the integration of the CPV and PCM storage system. For the HCPV-MLM, a fundamental factor of great importance for highly efficient operation is its integration with the PCM storage and the combination can represent interesting solutions for various domestic applications. The HCPV-MLM in such a system generates both electricity and thermal energy. The obtained experimental results for the heat discharged by the HCPV-MLM system is characterized as time dependent and the integrated PCM storage system must be able to accommodate this behaviour using the conventional control or using the maximization approach. This chapter presents the numerical analysis of the integration between the HCPV-MLM modules with the PCM storage system.

6.1 Description of the CPVT-MLM and PCM storage

In the previous chapters, the analysis of the two systems of the HCPV-MLM and the PCM storage has been performed. This study is very important for evaluating whether the integrated two systems have the potential to be useful for hybrid electrical and thermal generation based on the technical aspects. The combination of the HCPV-MLM system and PCM storage consists of a HCPV-MLM system that acts as both electrical and heat source, PCM storage that acts as thermal storage to store the heat. The multi-stage PCMs storage is used to enhance the heat transfer for the input thermal and the PCM thermal conductivity. A discharge heat load is connected to the system to be utilized for the domestic heating. The proposed system is shown in Figure 160.

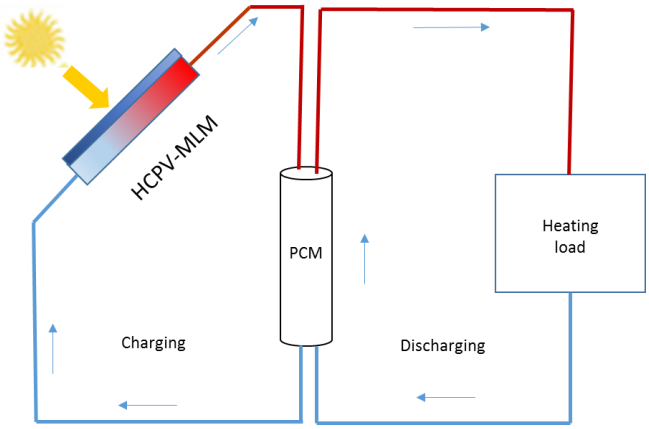

Figure 160. The schematic of the integration of the HCPV-MLM with the PCM storage and heating load.

6.1 Performance of the HCPV-MLM and PCM storage

Since the HCPV-MLM system can produce heat and electricity simultaneously, the evaluation criteria for the performance of the system includes the thermal efficiency η_{th} and the electrical efficiency η_{elec}, and they are calculated based on the following definitions [283]:

$$\eta_{th,CPV} = \dot{Q}_{th,HCPV}/\mathrm{A}_{ref}\mathrm{P}_{\mathrm{in}} \quad 6.1$$

where A_{ref} is the primary reflector area, P_{in} is the energy received by the primary reflector (W/m^2) and $\dot{Q}_{th,CPV}$ is the thermal energy collected by the HTF and it is calculated by:

$$\dot{Q}_{th,HCPV} = \dot{\mathrm{m}}\mathrm{C}_{\mathrm{p}}(\mathrm{T}_{out} - \mathrm{T}_{\mathrm{in}}) \quad 6.2$$

Where $\dot{\mathrm{m}}$ is the HTF mass flow rate (kg/s), C_{p} is the HTF heat capacity. The HCPV electrical efficiency ($\eta_{elec,HCPV}$) is calculated by:

$$\eta_{elec,HCPV} = \mathrm{P}_{\mathrm{elec,HCPV}}/\mathrm{A}_{ref}\mathrm{P}_{\mathrm{in}} \quad 6.3$$

Where $\mathrm{P}_{\mathrm{elec,HCPV}}$ is the electrical power of the HCPV. The total system efficiency ($\eta_{total,HCPV}$) is presented by expressed by:

$$\eta_{total,CPV} = \eta_{th,CPV} + \eta_{elec,CPV} \quad 6.4$$

However, the heat produced by the HCPV-MLM system is not fully stored by the integration of the PCM storage. This is due to the heat loss to the ambient and due to the inability of the system to absorb the heat presented at the HTF. Therefore, the energy balance of the thermal energy of the HCPV-MLM and the PCM storage is defined by:

$$\dot{Q}_{HCPV} = \dot{Q}_{HCPV-PCM} + \dot{Q}_{PCM} + \dot{Q}_{PCM-amb} \quad 6.5$$

Where $\dot{Q}_{HCPV-PCM}$ is the transferred heat to the ambient between the HCPV and PCM system and $\dot{Q}_{PCM-amb}$ is the transferred heat to the ambient as a result of not being absorbed by the PCM storage.

6.1 Mathematical HCPV-MLM and PCM storage formulation

A dynamic numerical model is needed to consider the variable heat produced by the HPCV-MLM during the daytime to the integrated PCM storage system. The following assumptions is made for the modelling:

- The HCPV-MLM setup is thermally insulated and the heat lost to the ambient is neglected.
- The HTF inlet temperature to the HCPV-MLM is constant.
- All the DNI that is not converted to electricity is converted to heat.
- The PCM storage is fully insulated and its temperature is homogeneous at the start of charging of 20°C.

6.2 HCPV-MLM and PCM storage system

In this section, the integration between the single solar cell HCPV module tested in chapter 4 and the PCM thermal storage model validated in chapter 5 is investigated. A single solar cell is attached to a PCM storage system. The HTF flow rate is 60ml/min and the HTF outlet temperature from the HCPV during the day is shown in Figure 161. The shown HTF outlet temperatures are for the two days of the outdoor tests. Analysing the HTF outlet temperature from the HCPV-MLM system is very important in terms of selecting the most appropriate PCM melting temperature. As the HTF inlet temperature is specified by 20°C, this is considered as the initial condition for the PCM storage. The upper limit of the system is the HTF outlet temperature where it reached up to 27.09°C and 29.60°C for the 26th and 27th of September, respectively.

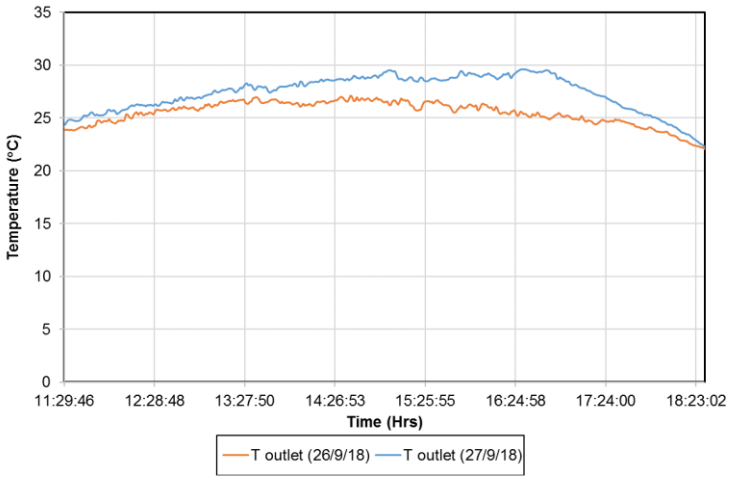

Figure 161. HTF outlet temperture for the two days of operation.

Based on the above facts, the PCM melting temperature of the storage should be in the range of the 20°C C and 29°C. Hence, the cases of the PCM arrangement that have been investigated in this study are shown in Table 28.

Table 28.List of PCM arrangements for the different cases.

Case #	PCM 1	PCM 2	PCM 3
Case 1	RT22HC	RT22HC	RT22HC
Case 2	RT28HC	RT25HC	RT22HC
Case 3	RT28HC	RT28HC	RT28HC

The thermo- physical properties of the selected PCM is presented in Table 29. It can be notice that high density PCMs are selected so that it can absorb heat. The latent heat capacity of the PCMs vary between 190 kJ/kg and 250kJ/kg.

Table 29. Thermal properties of PCMs

(Rubitherm® Technologies GmbH, Germany, http://www.rubitherm.de)

Product code	RT22HC	RT25HC	RT28HC
Melting temperature range (°C)	20-23	22-26	27-29
Solid density (kg/m³)	760	880	880
liquid density (kg/m³)	700	770	770
Latent heat(kJ/kg)	190	210	250
Specific heat (kJ/kg °C)	2	2	2
Thermal conductivity (W/m K)	0.2	0.2	0.2
Volume expansion (%)	12.5	12.5	12.5

The numerical model of the multi-stage PCM storage is shown in Figure 162. Therefore, the HTF of the specified flow rate enters in the PCM 1 stage storage

of an inlet temperature obtained by the HCPV-MLM system. The heat is absorbed by the PCM in the first stage and. Then, the HTF with a reduced temperature flows into the second storage stage to exchange the heat with the PCM 2. Finally, the HTF flows into the third storage stage.

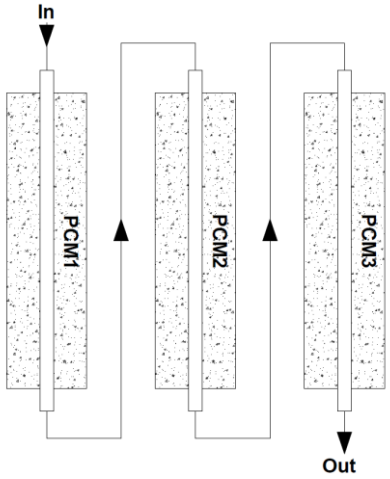

Figure 162. PCM arrengement in the multi-stage stoage.

6.3 Results and Discussion

This section presents the results of the thermal characteristics of the multi-stage PCM storage using the heat discharged by the HCPV-MLM module conditions using the numerical model that is verified in chapter 5.

6.3.1 HCPV-MLM and PCM storage (26th September 2018)

The overall performance of multi-stage PCM storage for the different proposed PCM arrangement using the HTF outlet temperature for the 26th September is presented. The HTF flow rate is 60ml/min with a variable inlet temperature to the PCM storage system during the day. Figure 163 shows the rate of the stored heat in each case. It can be noticed that for all the PCM arrangement cases that storage heat rate varied with time due to the variable temperature of the HTF at the inlet to the PCM storage system. The figure shows that the case 1 storage arrangement absorbs heat more than the other two cases at all the time of charging period. At the beginning of the day, the absorbed heat in case 1 is the highest of 12W due to initial heating of the PCM. Then, it is decreased to 4.51W at 12:40:00. Then, the absorbed heat is increased gradually until it reaches to its maximum of 7.59W at 15:04:00 and then it continues to absorb heat on the fluctuating rate until 16:32:00. After that, the amount of the absorbed heat

decreases gradually and reaches to its minimum by the end of the testing day. It can be noticed that no heat is discharged from the system due to the fluid inlet temperature fluctuating throughout the day.

Case 2 PCM arrangement follows the similar heat absorbing profile as case 1 but in less absorbed heating rate. At the beginning of the day, the absorbed heat in this case of PCM arrangement is the highest of 8W and it decreases to 3.29W at 12:38:00. After that, the absorbed heat increases gradually until it reaches its maximum of 7.8W at 16:46:00 and then it continues to absorb the heat at fluctuating rate until 16:30:00. After that, the amount of the absorbed heat decreases gradually and reaches to its minimum rate by the end of the testing day. It can be noticed that there is a discharging of heat by the system before 15minutes of the end of the testing which is considered as undesired thermal behaviour of the thermal storage.

Case 3 of PCM arrangement has the lowest heat absorption among the two cases due to the high melting temperature of the PCM. It can be noticed that the rate of the absorbed heat is less fluctuating in this case compared to the other cases. The rate of the absorbed heat is estimated by about of 1.85W between the 11:56:00 to 13:53:00.

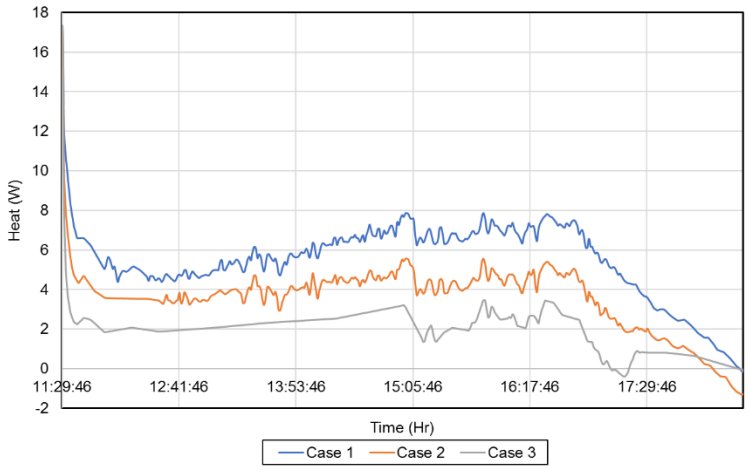

Figure 163. The absorbed heat by PCM in the three different PCM arragement cases througout the day.

Figure 164 shows the PCM liquid fraction for all the PCMs cases arrangements for the 26th September. It can be seen that all the PCMs storages in the case 1 melts gradually throughout the day. In this case (Figure 164 (a)), the PCM 1 storage stage experiences the highest melting rate compared to the other storage stages (PCM 2 and PCM 3) due to its first interact with the hot inlet HTF

temperature to the storage system. By the end of the day, the PCM melting fractions in the storages reach to 0.88, 0.81 and 0.76 for PCM 1, PCM 2 and PCM 3 respectively. This explains the continuous the absorption of heat by the PCM as not completing of melting of the PCM is performed. Also, the proposed volume of PCM is the ideal to store the heat in this profile because of the high melting fraction of the PCMs in the storage by the end of the day.

Because of higher melting PCM temperature used in case 2, a lower PCM melting rate is noticed in the case 2 PCM arrangements. It can be observed that the PCM1 storage stage (RT28HC) starts melting at 13:29:00 and reaches to its maximum of melting fraction of 0.06 at 16:53:00. However, the PCM in this storage starts to solidify during the rest of the day i.e. discharging. A continuous melting of PCM in the PCM2 storage (RT25HC) is noticed from the beginning of the day until it reaches its maximum of 0.42 liquid fraction at 17:23:00. Then it starts to solidify and reaches to 0.29 by the end of the day. Due to its lower melting temperature, PCM 3 storage stage (RT22HC) melts continuously throughout the day and 0.83 of the PCM melts by the end of the day. A very low quantity of the PCM melts in the all stages on the case 3 PCM arrangement and no PCM melted is observed by the end of the day. This concludes that the case 1 is the best selection in terms of the melting fraction.

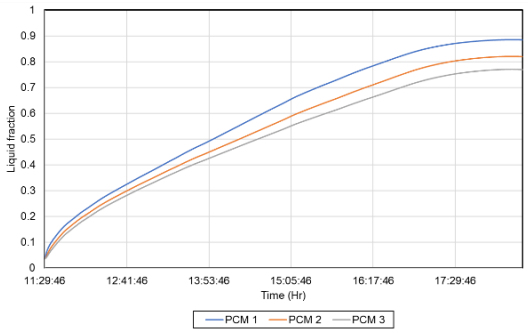

(a)

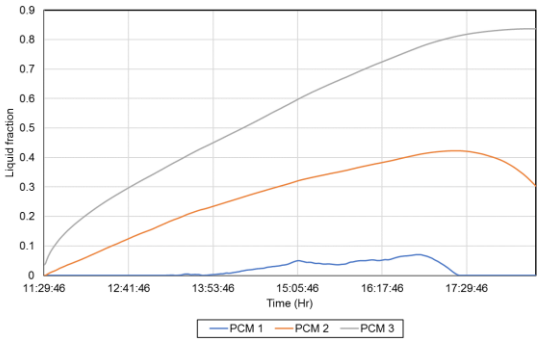

(b)

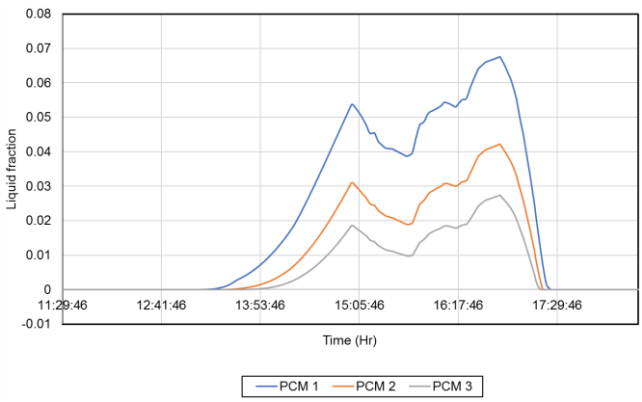

(c)

Figure 164. The PCM liquid fraction of the PCM arragements of (a) Case 1,(b) Case 2 and (b) Case 3.

6.3.2 HCPV-MLM and PCM storage (27th September 2018)

The overall performance of multi-stage PCM storage using the heat generated by the HCPV-MLM system on the 27th September is shown in Figure 165. It can be noticed that, the case 1 storage arrangement absorbs heat more than the other two cases at all the time of the charging. At the beginning of the testing, the absorbed heat in the case 1 of PCM arrangement is 10W and it decreases to 4W at 12:01:00 and then it continues to absorb the heat at this rate of fluctuating profile until 15:37:00. After that, the amount of the absorbed heat decreases gradually and reaches to its minimum at the end of the testing day. It is observed that no heat is discharged from the system throughout the day.

Case 2 of the PCM arrangement follows the same heat absorption profile as case 1 arrangement but in less absorbed heating rate. The fluctuating absorbed heat is estimated by about 3W. Also, it is noticed that the heat absorbed heat in this arrangement starts to be discharged from the 18:00. Case 3 arrangement is an interesting behaviour where its heat absorbing profile shows a nearly a straight line which is different from the other two cases. The rate of the absorbed heat is estimated by about of 1.71W between the 12:00 to 16:17.

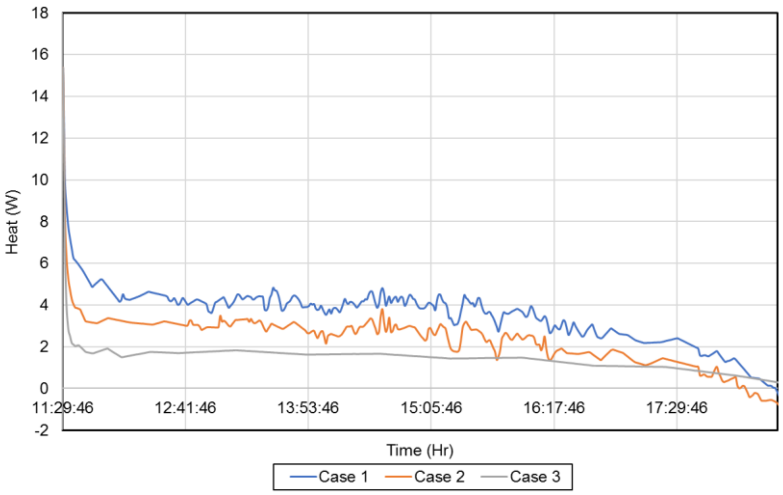

Figure 165. The absorbed heat by PCM in the three different PCM arragement cases througout the day.

Figure 166 shows the PCM liquid fraction for the case 1 and case 2 PCM arrangement and none of the PCM is melted in case 3. It is observed that all the PCMs storage stages in case 1 arrangement melts gradually throughout the day

disregard the fluctuation in the HTF inlet temperature. As expected, PCM 1 (RT22HC) storage experience the most melting fraction due to its first interact with the hot HTF inlet temperature. By the end of the day, the PCM melted fraction in the storages reached to 0.69, 0.63 and 0.60 for PCM 1, PCM 2 and PCM 3 respectively. Compared to the previous day of testing, less melting fraction of PCM was performed in this day i.e. less stored heat. On the other hand, a lower PCM melting rate is noticed in case 2 arrangement where no PCM melts at the PCM 1 storage (RT28HC) throughout the day. It could be noticed that PCM 2 storage melts gradually until 15:45:00 and then it starts to solidify throughout the day. This is due to lower HTF inlet temperature from the HCPV-MLM system. However, this did not stop the PCM 3 to continue to melt where its melting fraction reaches to 0.65 by the end of the day. This melting fraction is considered as lower than the case 1 PCM arrangement.

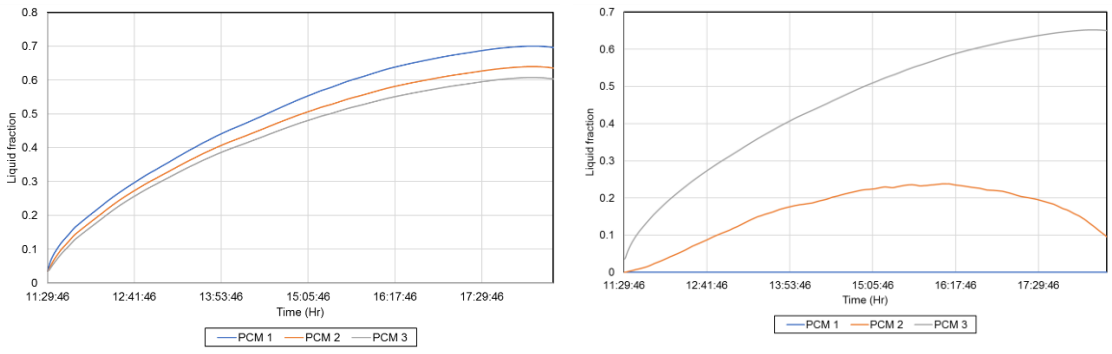

(a) (b)

Figure 166. The PCM liquid fraction of the PCM arragements of (a) Case 1 and (b) Case 2.

6.4 Conclusions

The previous two chapters 4 and 5 conduct an extensive study on the MLM system and PCM storage system, respectively and each system has been studied individually. This is to simplify the analysis of each system and to consider the various parameters. This chapter has presented the integration of the thermal behaviour of multi-stage PCM storage system using numerical approach for the heat supplied by the experimental setup of the HCPV-MLM system. Its importance is due to the fact that the heat discharged by the HCPV-MLM system is characterized as a variable throughout the day and different scenarios are expected.

The HTF inlet temperature from the experimental work for the HCPV-MLM system was used to select the PCM melting temperature for the investigation. As the temperature of the fluid was less than 30°C, three types of PCMs with high capacity were selected of RT22HC, RT25HC and RT28HC were selected. Three cases of PCM arrangements were tested using the heat generated by the HCPV-MLM for the two days of outdoor experiments and conclude the following:

- Higher heat absorption rate on PCM storage is observed when using a lower melting temperature PCMs compared to the higher PCM melting temperature arrangements.
- The multi-stages PCM with PCMs with different melting temperature shows a lower heat absorption compared to the PCM arrangement with one type of PCMs with a lower melting temperature.
- The rate of the absorbed heat fluctuation is less affected by the PCM arrangement with a higher melting temperature.
- Even though the heat generated by HCPV-MLM is produced at a fluctuating profile, the PCM with a lower melting temperature shows a constant PCM melting rate.

Chapter 7 : Conclusions and future recommendations

7.1 Conclusions

This thesis has presented numerical and experimental investigations on advanced solutions to enhance the performance of the HCPV system. The research was divided into three parts to investigate the HCPV-MLM system, PCM thermal storage system and the integration between the two systems. The three studies have been conducted with the aim to contribute to the development of an efficient, low-cost and reliable HCPV. The most important outcomes of the work are summarized in the following sections.

7.1.1 HCPV-MLM

The influence of the MLM on the performance of the HCPV module was investigated using both the numerical and experimental approaches. At the beginning of the study, the numerical analysis of an MLM heat sink cooling system for a high concentration single solar CPV receiver has been carried out. The analysis includes various MLM heat sink configurations to determine the most efficient in terms of cell temperature and fluid pumping power. The thermal modelling results show that increasing the microchannel height decreases the thermal resistance, the maximum solar cell temperature decreases and the temperature non-uniformity of the solar cell. However, increasing the microchannel width has less effect on the thermal resistance and the maximum solar cell temperature compared to the channel height effect.

The non-uniform heat source with the MLM heat sink experimental study illustrates the thermal performance of the system. The results show that increasing the number of layers has a major impact on reducing the heat sink thermal resistance and the heat source maximum temperature. The heat sink thermal efficiency increases from 75% to 92% as the number of layers increased from 1-layer to 3-layers respectively. In addition, the heat source maximum temperature decreases as increasing the number of layers from single to double layers and less temperature reduction is observed when increasing the number of layers to 3 and 4. Increasing the number of layers on the MLM heat sink reduces the temperature non-uniformity of the heat source which effects the performance of the electronics. Increasing the input power from 5W to 30W

increases slightly the heat sink total thermal resistance and the heat source temperature increases. This shows the ability of the heat sink to accommodate a wide range of power rate with a slight change in the thermal resistance.

The indoor experimental characterisation of the HCPV-MLM is to investigate the influence of the MLM under a real HCPV operation conditions. The reported performance parameters are the electrical (I-V curve) and the thermal analysis. The results show a significant influence of the homogeniser material on the system performance. The maximum power of the HCPV module with glass homogeniser considerably increases than when using the homogeniser made from the crystal resin. Also, the short circuit current for the HCPV module with glass homogeniser is slightly higher than when using the crystal resin homogeniser module due to the higher transparency, less optical loss and uniformity in the intensity distribution found in the glass material. The experiments show clearly that the high intensity damages the homogeniser made from the crystal resin and no effect of defect is noticed on the homogeniser made from glass.

The increase of the number of layers increases the short circuit current and the maximum power. This is considered as a good efficiency improvement of the system. In addition, increasing the number of layers decreases the solar cell temperature and the solar cell temperature uniformity.

In the last part of the experimental investigation, the outdoor characterisation of HCPV-MLM module to evaluate the performance in Penryn campus location has been studied. It provided real performance data under variable irradiances of the I-V characterisation, thermal behaviour of the HCPV module. In a sunny day, the proposed HCPV-MLM system shows a maximum output power of 4.49W, corresponding to a maximum solar irradiance of 906 W/m^2. The fill factor was 76% and the maximum short circuit current was 1.97A at this maximum solar irradiance. Using the MLM technique on the HCPV maintained maximum solar cell temperature during the day of 62.99°C, which is within the solar cell manufacturer limit. In addition, the extracted heat from the proposed HCPV-MLM system varied between 13.69W to 0.29W. During the maximum output power, the amount of the extracted heat was 12.12W which represents of around 63% of the total input power.

7.1.2 PCM thermal storage

The investigation of influencing the PCM thermal storage is summarized in this section. At the beginning, the numerical analysis of a PCM storage system for the thermal storage has been carried out to examine the geometric parameters on influencing its parameters. The model has been validate using an experimental result from a published reviewer. The thermal modelling results show decreasing the radius of the PCM storage increases the PCM average temperature during the melting. Also, more heat absorbed by the PCM in case of reducing the radius due to the increase area between the PCM and the surface of the HTF tube for the charging time. In addition, it has been shown the dependency of the storage length on the amount of the stored heat.

The thermal behaviour of the PCM storage system under different inclination positions and working conditions has been explored experimentally at constant HTF inlet temperature and flow rate. The study has investigated the effect of the HTF flow rate and inlet temperature on the PCM storage performance. The results show that HTF inlet temperature plays an important role in reducing the PCM melting time and increasing the overall PCM temperature where a slight effect of the HTF flow rate on the PCM melting time and the average temperature is noticed.

The results show a significant influence of the inclination of the PCM melting time, PCM profile and the temperature distribution. The PCM storage in 45º inclination position melts faster than the PCM in the storage in the 0 º and 90º inclination positions and the PCM melting time is reduced in the storage of 45º inclination compared to the storage at 0º inclination. In addition, the PCM temperature variation along the axial position is decreased as the storage inclination position is increased from the 0º to 90º. However, the PCM average temperature within the PCM storage is similar for all the inclination positions. Also, the melting profile of the PCM in the storages at the different inclination positions is different from each other where the PCM melts faster in the axial direction than the radial direction in the storage inclination position of 0º. The flow of the liquid PCM within the storage is an interesting finding and has an important in influencing on the PCM melting rate where the PCM faces the direction of buoyant force is melted in faster rate compared to the PCM located in all other directions.

This influence of the multi-stage PCM storage technique in enhancing the thermal conductivity of the PCM has been studied experimentally and numerically. The investigation has included the overall characteristics of a multi-stage system by examining the temperature distribution, stored heat and melting profiles. The thermal analysis shows that the multi-stage PCM arrangement could be used to increase the PCM average temperature. The larger the melting temperature difference between multiple PCMs, the more sensible heat is stored in the PCM storage. This is due to the fact that the PCM with the lowest melting temperature melts faster when the melting temperature difference between multiple PCMs becomes greater.

7.1.3 HCPV-MLM and PCM storage

At the last part of the investigation, a numerical model of the integration of the HCPV-MLM and PCM storage has been investigated. The study has considered different PCM arrangements. The results show a higher heat absorption rate on PCM storage in the lower melting temperature PCMs arrangement compared to the higher PCM melting temperature. In addition, the multi-stages PCM with the different melting temperature showed a lower heat absorption compared to the PCM arrangement with the lower melting temperature. The rate of the absorbed heat fluctuation is less affected by the PCM arrangement with higher melting temperature. Even though the heat produced by the HCPV-MLM produced at a fluctuating profile, the PCM with lower melting temperature showed a constant PCM melting rate.

7.2 Achievements

This thesis work provides an extensive study on enhancing the concentrating photovoltaic performance using the multi-layer heat sink technique and the PCM thermal storage. The detailed study also identified the scope of possible improvements in the integration of all the HCPV-MLM and the PCM storage.

The thesis has reported the application of a new technique in the thermal regulation of the HCPV. The experimental investigation carried out in this study has allowed the identification of the thermal behaviour of both systems the HCPV and the MLM heat sink. The thermal behaviour of the MLM heat sink has been examined using the experimental approach under a non-uniform heat source. This is very important due to the lack of investigation the MLM heat sink under

non-uniform heat source. In addition, the examination the performance of the HCPV-MLM heat sink in indoor and outdoor conditions is considered as one of the key achievements due to this being the first example of this kind of experiment. The outdoor tests are as one of the rare tests conducted in this part of UK and therefore this could be a valuable reference for the researchers in the future.

The investigations on the PCM storage have revealed and clarified more details mainly about two topics; the orientation effect and the multi-storage investigations. The study on the PCM storage orientation is one of the very few studies which has investigated experimentally and numerically the thermal behaviour of the PCM under those orientation positions. The multi-stages PCM storage investigation has achieved the testing of this technique as a thermal conductivity enhancement of the PCM using different PCM arrangements. The attempt of integrating the output thermal energy from the HCVP-MLM into a multi-stage PCM storage using the numerical approached has provided a solution in improving the overall system efficiency.

7.3 Recommendations for future work

The major objectives of the project have been achieved and have been reported in detail in the present thesis. However, some of the tasks have yet to be concluded and further investigations are required. The manufactured full HCPV-MLM with the PCM storage prototype has been tested experimentally at the University of Exeter, UK: a full-scale outdoor characterization would allow refining the design of the presented receivers, in order to enhance the electrical and the thermal performance of the system. Long term outdoor testing would also assess the durability of the developed system and highlight which modifications need to be introduced. Moreover, the fabrication on a larger scale with multi-solar cells high concentration would allow a full-scale characterization, in terms of electrical and thermal performance. Finally, new areas to be investigated emerged during the current study. Hence, a list of recommendations for future works is reported here:

HCPV-MLM heat sink:

- Improving the optical efficiency of the system to enhance electricity and thermal energy. This includes the developing new and lightweight optical

materials, optical interface between the optics and the solar cell, and minimise the losses from the system. This will be done through enhanced optical, thermal and electrical efficiency and Geometric experiments in order to establish light loss mechanism.

- Minimizing the non-uniform optical losses from the CPV module to improve the electrical performance. Non-uniformity can occur due to the imperfection of the optical device and system, which will be optimised with surface engineering.

- Manufacturing a light and compact module will reduce the required torque by the tracker and hence less power used by the system. Also, using less materials will lower the cost of the system. This is also enabled us to improve higher power to weight ratio of the modules, essentially reducing the overall costs of the electricity generation.

- Investigating the correspondence between the microchannel effectiveness and geometry to optimize the design of micro-finned heat sinks. Using other types of fluids including nano-fluids will be investigated to enhance the electrical and thermal performance of the system.

- Experimental verification of the behaviour of microchannel plates made of different materials will be conducted in future for various climatic conditions.

- Redesigning the heat sink case is considered as a potential improvement on the system performance and cost. This is due to the fact that the current heat sink case was designed for the experimental used only and no minimization of materials was conducted.

PCM storage system:

- Scale up PCM storage size should be investigated to accommodate the extracted heat with the different enhancement techniques such as the fins

- Test the multi-stages PCM techniques in scale up version.

- Discharge the extracted heat to a useful application such as a heating a room or green house for agriculture purposes.

Integration of the HCPV-MLM with the PCM storage:

- Develop a full integrated HCPV-MLM with the PCM storage to help understanding the system overall performance.
- On-field installation and continuous monitoring of the HCPV-MLM with the PCM storage in the UK weather condition to get more information on the long-term performance and on the durability of the components.
- Develop a cradle to incarnation life cycle analysis and cost analysis study.

These recommendations are expected to improve the performance and reduce the costs of CPV systems. These investigations have not been conducted because of time constraints or because they were beyond of the primary scope of the PhD project, but would definitely contribute to CPV cost-cutting and to its diffusion in the future power generation market. Moreover, the installation of the full HCPV-MLM and PCM storage will provide opportunities for the expansion on the knowledge of the topic.

References

[1] P. Energy, Statistical Review of World Energy, 2012.

[2] M.C. Browne, B. Norton, S.J. McCormack, Phase change materials for photovoltaic thermal management, Renew. Sustain. Energy Rev. 47 (2015) 762–782. doi:10.1016/j.rser.2015.03.050.

[3] International Renewable Energy Agency (IRENA), Renewable capacity statistics 2016 Statistiques de capacité renouvelable 2016 Estadísticas de capacidad renovable 2016, 2016. doi:10.1016/S2255-4971(15)30126-9.

[4] W.T. Twidell T, Renewable Energy Resources, second edi, Taylor & Francis Group, London and New York, 2006.

[5] V. Garboushian, D. Roubideaux, S. Yoon, Integrated high-concentration PV near-term alternative for low-cost large-scale solar electric power, Sol. Energy Mater. Sol. Cells. 47 (1997) 315–323. doi:http://dx.doi.org/10.1016/S0927-0248(97)00056-1.

[6] P. Pérez-Higueras, E. Muñoz, G. Almonacid, P.G. Vidal, High Concentrator PhotoVoltaics efficiencies: Present status and forecast, Renew. Sustain. Energy Rev. 15 (2011) 1810–1815. doi:10.1016/j.rser.2010.11.046.

[7] D.L. Talavera, P. Pérez-Higueras, J.A. Ruíz-Arias, E.F. Fernández, Levelised cost of electricity in high concentrated photovoltaic grid connected systems: Spatial analysis of Spain, Appl. Energy. 151 (2015) 49–59. doi:10.1016/j.apenergy.2015.04.072.

[8] E.F. Fernández, G. Siefer, M. Schachtner, a. J. García Loureiro, P. Pérez-Higueras, Temperature coefficients of monolithic III-V triple-junction solar cells under different spectra and irradiance levels, AIP Conf. Proc. 1477 (2012) 189–193. doi:10.1063/1.4753865.

[9] D.A.R. Barkhouse, O. Gunawan, T. Gokmen, T.K. Todorov, D.B. Mitzi, Device characteristics of a 10.1% hydrazine-processed Cu2ZnSn(Se,S)4 solar cell, Prog. Photovoltaics Res. Appl. 20 (2012) 6–11. doi:10.1002/pip.

[10] P. VERMA, VARUN, S. SINGAL, Review of mathematical modeling on latent heat thermal energy storage systems using phase-change material, Renew. Sustain. Energy Rev. 12 (2008) 999–1031. doi:10.1016/j.rser.2006.11.002.

[11] O.L. D'Ortigue, A. Whiteman, S. Elsayed, RENEWABLE ENERGY CAPACITY STATISTICS 2015, 2010.

[12] I. Dincer, Thermal energy storage systems and applications, Wiley, New York, 2003.

[13] A. Sharma, L.D. Won, D. Buddhi, J.U. Park, Numerical heat transfer studies of the fatty acids for different heat exchanger materials on the performance of a latent heat storage system, Renew. Energy. 30 (2005) 2179–2187. doi:10.1016/j.renene.2005.01.014.

[14] D. Chemisana, Building integrated concentrating photovoltaics: A review, Renew. Sustain. Energy Rev. 15 (2011) 603–611.

doi:10.1016/j.rser.2010.07.017.

[15] A.L. Luque, Concentrator photovoltaics, Springer, Berlin, 2006.

[16] G. Zubi, J.L. Bernal-Agustín, G.V. Fracastoro, High concentration photovoltaic systems applying III-V cells, Renew. Sustain. Energy Rev. 13 (2009) 2645–2652. doi:10.1016/j.rser.2009.07.002.

[17] S.P. Philipps, G. Peharz, R. Hoheisel, T. Hornung, N.M. Al-Abbadi, F. Dimroth, A.W. Bett, Energy harvesting efficiency of III–V triple-junction concentrator solar cells under realistic spectral conditions, Sol. Energy Mater. Sol. Cells. 94 (2010) 869–877. doi:10.1016/j.solmat.2010.01.010.

[18] K. Araki, M. Yamaguchi, Influences of spectrum change to 3-junction concentrator cells, Sol. Energy Mater. Sol. Cells. 75 (2003) 707–714. doi:10.1016/S0927-0248(02)00140-X.

[19] S. Lee, Thermal challenges and opportunities in concentrated photovoltaics, 2010 12th Electron. Packag. Technol. Conf. EPTC 2010. (2010) 608–613. doi:10.1109/EPTC.2010.5702711.

[20] L. Micheli, N. Sarmah, X. Luo, K.S. Reddy, T.K. Mallick, Opportunities and challenges in micro- and nano-technologies for concentrating photovoltaic cooling: A review, Renew. Sustain. Energy Rev. 20 (2013) 595–610. doi:10.1016/j.rser.2012.11.051.

[21] H.M.S. Bahaidarah, A.A.B. Baloch, P. Gandhidasan, Uniform cooling of photovoltaic panels: A review, Renew. Sustain. Energy Rev. 57 (2016) 1520–1544. doi:10.1016/j.rser.2015.12.064.

[22] D. Du, J. Darkwa, G. Kokogiannakis, Thermal management systems for Photovoltaics (PV) installations: A critical review, Sol. Energy. 97 (2013) 238–254. doi:10.1016/j.solener.2013.08.018.

[23] D. Aiken, M. Stan, C. Murray, Temperature dependent spectral response measurements for III-V multi-junction solar cells, … Rec. …. (2002) 828–831. http://ieeexplore.ieee.org/xpls/abs_all.jsp?arnumber=1190704.

[24] E. Radziemska, E. Klugmann, Thermally affected parameters of the current-voltage characteristics of silicon photocell, Energy Convers. Manag. 43 (2002) 1889–1900. doi:10.1016/S0196-8904(01)00132-7.

[25] E. Radziemska, The effect of temperature on the power drop in crystalline silicon solar cells, Renew. Energy. 28 (2003) 1–12. doi:10.1016/S0960-1481(02)00015-0.

[26] M.Y. Feteha, G.M. Eldallal, The effects of temperature and light concentration on the GaInP/GaAs multijunction solar cell's performance, Renew. Energy. 28 (2003) 1097–1104. doi:10.1016/S0960-1481(02)00211-2.

[27] A. Luque, G. Sala, J.C. Arboiro, Electric and thermal model for non-uniformly illuminated concentration cells, Sol. Energy Mater. Sol. Cells. 51 (1998) 269–290. doi:10.1016/S0927-0248(97)00228-6.

[28] F. Khan, S.N. Singh, M. Husain, Effect of illumination intensity on cell parameters of a silicon solar cell, Sol. Energy Mater. Sol. Cells. 94 (2010) 1473–1476. doi:10.1016/j.solmat.2010.03.018.

[29] J.L. Domenech-Garret, Cell behaviour under different non-uniform temperature and radiation combined profiles using a two dimensional finite element model, Sol. Energy. 85 (2011) 256–264. doi:10.1016/j.solener.2010.12.007.

[30] K. Ishaque, Z. Salam, H. Taheri, Syafaruddin, Modeling and simulation of photovoltaic (PV) system during partial shading based on a two-diode model, Simul. Model. Pract. Theory. 19 (2011) 1613–1626. doi:10.1016/j.simpat.2011.04.005.

[31] S. Moballegh, J. Jiang, Partial shading modeling of photovoltaic system with experimental validations, IEEE Power Energy Soc. Gen. Meet. (2011). doi:10.1109/PES.2011.6039281.

[32] H. Baig, K.C. Heasman, T.K. Mallick, Non-uniform illumination in concentrating solar cells, Renew. Sustain. Energy Rev. 16 (2012) 5890–5909. doi:10.1016/j.rser.2012.06.020.

[33] E. Cuce, P.M. Cuce, T. Bali, An experimental analysis of illumination intensity and temperature dependency of photovoltaic cell parameters, Appl. Energy. 111 (2013) 374–382. doi:10.1016/j.apenergy.2013.05.025.

[34] M.C. Di Vincenzo, D. Infield, Detailed PV array model for non-uniform irradiance and its validation against experimental data, Sol. Energy. 97 (2013) 314–331. doi:10.1016/j.solener.2013.08.030.

[35] M. Muller, T.J. Silverman, M. Deceglie, S. Kurtz, E. Menard, S. Burroughs, Optical cell temperature measurements of multiple CPV technologies in outdoor conditions, Conf. Rec. IEEE Photovolt. Spec. Conf. (2013) 3426–3430. doi:10.1109/PVSC.2013.6745184.

[36] G. Li, Q. Xuan, G. Pei, Y. Su, J. Ji, Effect of non-uniform illumination and temperature distribution on concentrating solar cell - A review, Energy. 144 (2018) 1119–1136. doi:10.1016/j.energy.2017.12.067.

[37] F. Almonacid, P.J. Pérez-Higueras, E.F. Fernández, P. Rodrigo, Relation between the cell temperature of a HCPV module and atmospheric parameters, Sol. Energy Mater. Sol. Cells. 105 (2012) 322–327. doi:10.1016/j.solmat.2012.06.043.

[38] E.F. Fernández, F. Almonacid, P. Rodrigo, P. Pérez-Higueras, Calculation of the cell temperature of a high concentrator photovoltaic (HCPV) module: A study and comparison of different methods, Sol. Energy Mater. Sol. Cells. 121 (2014) 144–151. doi:10.1016/j.solmat.2013.11.009.

[39] X. Zhang, X. Zhao, S. Smith, J. Xu, X. Yu, Review of R&D progress and practical application of the solar photovoltaic/thermal (PV/T) technologies, Renew. Sustain. Energy Rev. 16 (2012) 599–617. doi:10.1016/j.rser.2011.08.026.

[40] D.L. Evans, W.A. Facinelli, R.T. Otterbein, Combined photovoltaic/thermal system studies, 1978.

[41] Y. Nakata, T. Kobe, T. Machida, N. Shibuya, T. Takemoto, T. Tsuji, A 30kwp concentrating photovoltaic/thermal hybrid system application, 1982.

[42] P. Buffet, Hybrid Thermal and Photovoltaic Concentration Collector, in: R. Van Overstraeten, W. Palz (Eds.), Photovolt. Power Gener., Springer Netherlands, 1983: pp. 251–256. http://dx.doi.org/10.1007/978-94-009-7136-3_34.

[43] C. Gibart, S.E. De Propulsion, Study of an tests on a hybrid photovoltaic-thermal collector using concentrated sunlight, 4 (1981) 71–89.

[44] C. Kandilli, Performance analysis of a novel concentrating photovoltaic combined system, Energy Convers. Manag. 67 (2013) 186–196. doi:10.1016/j.enconman.2012.11.020.

[45] J. Zhao, Y. Song, W.-H. Lam, W. Liu, Y. Liu, Y. Zhang, D. Wang, Solar radiation transfer and performance analysis of an optimum photovoltaic/thermal system, Energy Convers. Manag. 52 (2011) 1343–1353. doi:10.1016/j.enconman.2010.09.032.

[46] M. Brogren, B. Karlsson, Low-Concentration water-cooled PV-Thermal hybrid system for high latitudes, Photovolt. Spec. Conf. 2002. Conf. Rec. Twenty-Ninth IEEE. (2002) 1733–1736.

[47] S. Krauter, Increased electrical yield via water flow over the front of photovoltaic panels, Sol. Energy Mater. Sol. Cells. 82 (2004) 131–137. doi:10.1016/j.solmat.2004.01.011.

[48] H. Bahaidarah, A. Subhan, P. Gandhidasan, S. Rehman, Performance evaluation of a PV (photovoltaic) module by back surface water cooling for hot climatic conditions, Energy. 59 (2013) 445–453. doi:10.1016/j.energy.2013.07.050.

[49] E. Wilson, Theoretical and operational thermal performance of a “wet” crystalline silicon PV module under Jamaican conditions, Renew. Energy. 34 (2009) 1655–1660. doi:10.1016/j.renene.2008.10.024.

[50] S. Zimmermann, H. Helmers, M.K. Tiwari, S. Paredes, B. Michel, M. Wiesenfarth, A.W. Bett, D. Poulikakos, A high-efficiency hybrid high-concentration photovoltaic system, Int. J. Heat Mass Transf. 89 (2015) 514–521. doi:10.1016/j.ijheatmasstransfer.2015.04.068.

[51] M. Li, X. Ji, G. Li, S. Wei, Y.F. Li, F. Shi, Performance study of solar cell arrays based on a Trough Concentrating Photovoltaic/Thermal system, Appl. Energy. 88 (2011) 3218–3227. doi:10.1016/j.apenergy.2011.03.030.

[52] H.A. Zondag, D.W. de Vries, W.G.J. van Helden, R.J.C. van Zolingen, A.A. van Steenhoven, The yield of different combined PV-thermal collector designs, Sol. Energy. 74 (2003) 253–269. doi:10.1016/S0038-092X(03)00121-X.

[53] J.K. Tonui, Y. Tripanagnostopoulos, Improved PV/T solar collectors with heat extraction by forced or natural air circulation, Renew. Energy. 32 (2007) 623–637. doi:10.1016/j.renene.2006.03.006.

[54] S. Janjai, P. Tung, Performance of a solar dryer using hot air from roof-integrated solar collectors for drying herbs and spices, Renew. Energy. 30 (2005) 2085–2095. doi:10.1016/j.renene.2005.02.006.

[55] K.E. Amori, H.M. Taqi Al-Najjar, Analysis of thermal and electrical

performance of a hybrid (PV/T) air based solar collector for Iraq, Appl. Energy. 98 (2012) 384–395. doi:10.1016/j.apenergy.2012.03.061.

[56] G. Mittelman, a Kribus, a Dayan, Solar cooling with concentrating photovoltaic/thermal (CPVT) systems, Energy Convers. Manag. 48 (2007) 2481–2490. doi:10.1016/j.enconman.2007.04.004.

[57] A. Al-Alili, Y. Hwang, R. Radermacher, I. Kubo, A high efficiency solar air conditioner using concentrating photovoltaic/thermal collectors, Appl. Energy. 93 (2012) 138–147. doi:10.1016/j.apenergy.2011.05.010.

[58] X. Zhao, X. Zhang, S.B. Riffat, Y. Su, Theoretical study of the performance of a novel PV/e roof module for heat pump operation, Energy Convers. Manag. 52 (2011) 603–614. doi:10.1016/j.enconman.2010.07.036.

[59] X. Ju, Z. Wang, G. Flamant, P. Li, W. Zhao, Numerical analysis and optimization of a spectrum splitting concentration photovoltaic-thermoelectric hybrid system, Sol. Energy. 86 (2012) 1941–1954. doi:10.1016/j.solener.2012.02.024.

[60] E. Ogbonnaya, A. Gunasekaran, L. Weiss, Micro solar energy harvesting using thin film selective absorber coating and thermoelectric generators, Microsyst. Technol. 19 (2013) 995–1004. doi:10.1007/s00542-012-1687-6.

[61] Thermal Management of Power Electronics using Thermoelectric Coolers Jan W . Vandersande and Jean-Pierre Fleurial Jet Propulsion Laboratory / California Institute of Technology f r o, (n.d.) 252–255.

[62] Y. Li, S. Witharana, H. Cao, M. Lasfargues, Y. Huang, Y. Ding, Wide spectrum solar energy harvesting through an integrated photovoltaic and thermoelectric system, Particuology. 15 (2014) 39–44. doi:10.1016/j.partic.2013.08.003.

[63] W.G.J.H.M. va. Sark, Feasibility of photovoltaic - Thermoelectric hybrid modules, Appl. Energy. 88 (2011) 2785–2790. doi:10.1016/j.apenergy.2011.02.008.

[64] A. ROYNE, C. DEY, D. MILLS, Cooling of photovoltaic cells under concentrated illumination: a critical review, Sol. Energy Mater. Sol. Cells. 86 (2005) 451–483. doi:10.1016/j.solmat.2004.09.003.

[65] K. Araki, H. Uozumi, M. Yamaguchi, a Simple Passive Cooling Structure and Its Heat Analysis for 500 X, (2002) 1568–1571.

[66] H.-F. Hong, T.-S. Huang, M.-H. Chiang, Z.-H. Shih, Degradation mechanism of concentrator solar receivers without protection layer., Microelectron. Reliab. 53 (2013) 1927–1932. doi:10.1016/j.microrel.2013.06.017.

[67] T. Cooper, G. Ambrosetti, A. Pedretti, A. Steinfeld, Surpassing the 2D Limit: A 600x High-concentration PV Collector Based on a Parabolic trough with Tracking Secondary Optics, Energy Procedia. 57 (2014) 285–290. doi:10.1016/j.egypro.2014.10.033.

[68] K. Araki, H. Uozumi, M. Yamaguchi, A simple passive cooling structure

and its heat analysis for 500× concentrator PV module, Conf. Rec. Twenty-Ninth IEEE Photovolt. Spec. Conf. 2002. (2002) 2–5. doi:10.1109/PVSC.2002.1190913.

[69] S.K. Natarajan, T.K. Mallick, M. Katz, S. Weingaertner, Numerical investigations of solar cell temperature for photovoltaic concentrator system with and without passive cooling arrangements, Int. J. Therm. Sci. 50 (2011) 2514–2521. doi:10.1016/j.ijthermalsci.2011.06.014.

[70] H. Lv, F. Sheng, J. Dai, W. Liu, C. Cheng, J. Zhang, Temperature-dependent model of concentrator photovoltaic modules combining optical elements and III–V multi-junction solar cells, Sol. Energy. 112 (2015) 351–360. doi:10.1016/j.solener.2014.12.005.

[71] L. Micheli, K.S. Reddy, T.K. Mallick, Plate micro-fins in natural convection: An opportunity for passive concentrating photovoltaic cooling, Energy Procedia. 82 (2015) 301–308. doi:10.1016/j.egypro.2015.12.037.

[72] L. Micheli, K.S. Reddy, T.K. Mallick, Thermal effectiveness and mass usage of horizontal micro-fins under natural convection, Appl. Therm. Eng. (2015). doi:10.1016/j.applthermaleng.2015.09.042.

[73] L. Micheli, K.S. Reddy, T.K. Mallick, Experimental comparison of micro-scaled plate-fins and pin-fins under natural convection, Int. Commun. Heat Mass Transf. 75 (2016) 59–66. doi:10.1016/j.icheatmasstransfer.2016.03.023.

[74] L. Micheli, E.F. Fernandez, F. Almonacid, K.S. Reddy, T.K. Mallick, Optimization of the least-material approach for passive Ultra-High CPV cooling, 2015 IEEE 42nd Photovolt. Spec. Conf. PVSC 2015. 2 (2015) 3–8. doi:10.1109/PVSC.2015.7355763.

[75] L. Micheli, K.S. Reddy, T.K. Mallick, General correlations among geometry, orientation and thermal performance of natural convective micro-finned heat sinks, Int. J. Heat Mass Transf. 91 (2015) 711–724. doi:10.1016/j.ijheatmasstransfer.2015.08.015.

[76] L. Micheli, K.S. Reddy, T.K. Mallick, Thermal effectiveness and mass usage of horizontal micro-fins under natural convection, Appl. Therm. Eng. 97 (2016) 39–47. doi:10.1016/j.applthermaleng.2015.09.042.

[77] L. Micheli, L. Micheli, E.F. Fernandez, F. Almonacid, Enhancing Ultra-High CPV Passive Cooling Using Least- Material Finned Heat Sinks, Cpv-11. (2015) 3–6.

[78] L. Micheli, K.S. Reddy, T.K. Mallick, Experimental comparison of micro-scaled plate-fins and pin-fins under natural convection, Int. Commun. Heat Mass Transf. 75 (2016) 59–66. doi:10.1016/j.icheatmasstransfer.2016.03.023.

[79] Y.A. Cengel, S. Klein, W. Beckman, Heat transfer: a practical approach, New York, 1998.

[80] W.G. Anderson, P.M. Dussinger, D.B. Sarraf, S. Tamanna, Heat pipe cooling of concentrating photovoltaic cells, 2008 33rd IEEE Photovolatic Spec. Conf. (2008) 1–6. doi:10.1109/PVSC.2008.4922577.

[81] a Cheknane, B. Benyoucef, a Chaker, Performance of concentrator solar cells with passive cooling, Semicond. Sci. Technol. 21 (2006) 144–147. doi:10.1088/0268-1242/21/2/007.

[82] A. Akbarzadeh, T. Wadowski, Heat pipe-based cooling systems for photovoltaic cells under concentrated solar radiation, Appl. Therm. Eng. 16 (1996) 81–87. doi:10.1016/1359-4311(95)00012-3.

[83] M.M. Farid, A.M. Khudhair, S.A.K. Razack, S. Al-Hallaj, A review on phase change energy storage: Materials and applications, Energy Convers. Manag. 45 (2004) 1597–1615. doi:10.1016/j.enconman.2003.09.015.

[84] Z. Ge, Y. Li, D. Li, Z. Sun, Y. Jin, C. Liu, C. Li, G. Leng, Y. Ding, Thermal energy storage: Challenges and the role of particle technology, Particuology. 15 (2014) 2–8. doi:10.1016/j.partic.2014.03.003.

[85] T. Ma, H. Yang, Y. Zhang, L. Lu, X. Wang, Using phase change materials in photovoltaic systems for thermal regulation and electrical efficiency improvement: A review and outlook, Renew. Sustain. Energy Rev. 43 (2015) 1273–1284. doi:10.1016/j.rser.2014.12.003.

[86] A. Sharma, V. V. Tyagi, C.R. Chen, D. Buddhi, Review on thermal energy storage with phase change materials and applications, Renew. Sustain. Energy Rev. 13 (2009) 318–345. doi:10.1016/j.rser.2007.10.005.

[87] W. ,Humphries, E. Griggs, A Design Handbook for Phase Change Thermal Control and Energy Storage Devices, NASA Tech. Pap. (1977).

[88] A. Hasan, H. Alnoman, A. Shah, Energy Efficiency Enhancement of Photovoltaics by Phase Change Materials through Thermal Energy Recovery, Energies. 9 (2016) 782. doi:10.3390/en9100782.

[89] A. Hasan, S.J. McCormack, M.J. Huang, B. Norton, Energy and cost saving of a photovoltaic-phase change materials (PV-PCM) System through temperature regulation and performance enhancement of photovoltaics, Energies. 7 (2014) 1318–1331. doi:10.3390/en7031318.

[90] S. Krishnan, S. V. Garimella, Thermal Management of Transient Power Spikes in Electronics—Phase Change Energy Storage or Copper Heat Sinks?, J. Electron. Packag. 126 (2004) 308. doi:10.1115/1.1772411.

[91] F.L. Tan, C.P. Tso, Cooling of mobile electronic devices using phase change materials, Appl. Therm. Eng. 24 (2004) 159–169. doi:10.1016/j.applthermaleng.2003.09.005.

[92] M. Hodes, R.D. Weinstein, S.J. Pence, J.M. Piccini, L. Manzione, C. Chen, Transient Thermal Management of a Handset Using Phase Change Material (PCM), J. Electron. Packag. 124 (2002) 419. doi:10.1115/1.1523061.

[93] K. Lafdi, O. Mesalhy, A. Elgafy, Merits of Employing Foam Encapsulated Phase Change Materials for Pulsed Power Electronics Cooling Applications, J. Electron. Packag. 130 (2008) 021004. doi:10.1115/1.2912185.

[94] S.K. Saha, Cooling of Electronics with Phase Change Materials under

Constant Power and Cyclic Heat Loads, 31 (2009). doi:10.1063/1.3516323.

[95] R. Kandasamy, X.Q. Wang, A.S. Mujumdar, Application of phase change materials in thermal management of electronics, Appl. Therm. Eng. 27 (2007) 2822–2832. doi:10.1016/j.applthermaleng.2006.12.013.

[96] R.D. Weinstein, T.C. Kopec, A.S. Fleischer, E. D'Addio, C.A. Bessel, The Experimental Exploration of Embedding Phase Change Materials With Graphite Nanofibers for the Thermal Management of Electronics, J. Heat Transfer. 130 (2008) 042405. doi:10.1115/1.2818764.

[97] R. Baby, C. Balaji, Experimental investigations on thermal performance enhancement and effect of orientation on porous matrix filled PCM based heat sink, Int. Commun. Heat Mass Transf. 46 (2013) 27–30. doi:10.1016/j.icheatmasstransfer.2013.05.018.

[98] S. Thapa, S. Chukwu, A. Khaliq, L. Weiss, Fabrication and analysis of small-scale thermal energy storage with conductivity enhancement, Energy Convers. Manag. 79 (2014) 161–170. doi:10.1016/j.enconman.2013.12.019.

[99] S. Khanna, K.S. Reddy, T.K. Mallick, Optimization of solar photovoltaic system integrated with phase change material, Sol. Energy. 163 (2018) 591–599. doi:10.1016/j.solener.2018.01.002.

[100] S.K. Saha, K. Srinivasan, P. Dutta, Studies on Optimum Distribution of Fins in Heat Sinks Filled With Phase Change Materials, J. Heat Transfer. 130 (2008) 034505. doi:10.1115/1.2804948.

[101] M. Jun Huang, The effect of using two PCMs on the thermal regulation performance of BIPV systems, Sol. Energy Mater. Sol. Cells. 95 (2011) 957–963. doi:10.1016/j.solmat.2010.11.032.

[102] S. Jegadheeswaran, S.D. Pohekar, Performance enhancement in latent heat thermal storage system: A review, Renew. Sustain. Energy Rev. 13 (2009) 2225–2244. doi:10.1016/j.rser.2009.06.024.

[103] X.Q. Wang, A.S. Mujumdar, C. Yap, Effect of orientation for phase change material (PCM)-based heat sinks for transient thermal management of electric components, Int. Commun. Heat Mass Transf. 34 (2007) 801–808. doi:10.1016/j.icheatmasstransfer.2007.03.008.

[104] B. Kamkari, H.J. Amlashi, Numerical simulation and experimental verification of constrained melting of phase change material in inclined rectangular enclosures, Int. Commun. Heat Mass Transf. 88 (2017) 211–219. doi:10.1016/j.icheatmasstransfer.2017.07.023.

[105] M. Avci, M.Y. Yazici, An experimental study on effect of inclination angle on the performance of a PCM-based flat-type heat sink, Appl. Therm. Eng. 131 (2018) 806–814. doi:10.1016/j.applthermaleng.2017.12.069.

[106] S. Poran, D.H. Ahmed, Effect of cavity shape and heat source/sink orientation on PCM melting, J. Therm. Energy Syst. 3 (2018) 1–22. http://www.matjournals.in/index.php/JoTES/article/view/2203.

[107] S. Khanna, K.S. Reddy, T.K. Mallick, Optimization of solar photovoltaic

system integrated with phase change material, Sol. Energy. 163 (2018) 591–599. doi:10.1016/j.solener.2018.01.002.

[108] S. Khanna, K.S. Reddy, T.K. Mallick, Optimization of finned solar photovoltaic phase change material (finned pv pcm) system, Int. J. Therm. Sci. 130 (2018) 313–322. doi:10.1016/j.ijthermalsci.2018.04.033.

[109] R. Kandasamy, X.Q. Wang, A.S. Mujumdar, Transient cooling of electronics using phase change material (PCM)-based heat sinks, Appl. Therm. Eng. 28 (2008) 1047–1057. doi:10.1016/j.applthermaleng.2007.06.010.

[110] R. Kandasamy, X.-Q. Wang, A.S. Mujumdar, Application of phase change materials in thermal management of electronics, Appl. Therm. Eng. 27 (2007) 2822–2832. doi:10.1016/j.applthermaleng.2006.12.013.

[111] S.C. Fok, W. Shen, F.L. Tan, Cooling of portable hand-held electronic devices using phase change materials in finned heat sinks, Int. J. Therm. Sci. 49 (2010) 109–117. doi:10.1016/j.ijthermalsci.2009.06.011.

[112] L.W. Fan, Y.Q. Xiao, Y. Zeng, X. Fang, X. Wang, X. Xu, Z.T. Yu, R.H. Hong, Y.C. Hu, K.F. Cen, Effects of melting temperature and the presence of internal fins on the performance of a phase change material (PCM)-based heat sink, Int. J. Therm. Sci. 70 (2013) 114–126. doi:10.1016/j.ijthermalsci.2013.03.015.

[113] S. Mahmoud, A. Tang, C. Toh, R. AL-Dadah, S.L. Soo, Experimental investigation of inserts configurations and PCM type on the thermal performance of PCM based heat sinks, Appl. Energy. 112 (2013) 1349–1356. doi:10.1016/j.apenergy.2013.04.059.

[114] M.J. Huang, P.C. Eames, B. Norton, Phase change materials for limiting temperature rise in building integrated photovoltaics, Sol. Energy. 80 (2006) 1121–1130. doi:10.1016/j.solener.2005.10.006.

[115] X.Q. Wang, C. Yap, A.S. Mujumdar, A parametric study of phase change material (PCM)-based heat sinks, Int. J. Therm. Sci. 47 (2008) 1055–1068. doi:10.1016/j.ijthermalsci.2007.07.016.

[116] A. Arshad, H.M. Ali, M. Ali, S. Manzoor, Thermal performance of phase change material (PCM) based pin-finned heat sinks for electronics devices: Effect of pin thickness and PCM volume fraction, Appl. Therm. Eng. 112 (2017) 143–155. doi:10.1016/j.applthermaleng.2016.10.090.

[117] S.K. Saha, K. Srinivasan, P. Dutta, Studies on optimum distribution of fins in heat sinks filled with phase change materials, J. Heat Transfer. 130 (2008) 34505. doi:10.1115/1.2804948.

[118] M. Emam, M. Ahmed, Cooling concentrator photovoltaic systems using various configurations of phase-change material heat sinks, Energy Convers. Manag. 158 (2018) 298–314. doi:10.1016/j.enconman.2017.12.077.

[119] Y. Tomizawa, K. Sasaki, A. Kuroda, R. Takeda, Y. Kaito, Experimental and numerical study on phase change material (PCM) for thermal management of mobile devices, Appl. Therm. Eng. 98 (2016) 320–329. doi:10.1016/j.applthermaleng.2015.12.056.

[120] M. Ohadi, K. Choo, S. Dessiatoun, E. Cetegen, Next Generation Microchannel Heat Exchangers, 2013. doi:10.1007/978-1-4614-0779-9.

[121] R. Phillips, Microchannel Reat Sinks, Lincoln Lab. J. 1 (1988) 31–48. http://scholar.google.com/scholar?hl=en&btnG=Search&q=intitle:Microchannel+Reat+Sinks#0.

[122] A. Aldossary, S. Mahmoud, R. Al-Dadah, Technical feasibility study of passive and active cooling for concentrator PV in harsh environment, Appl. Therm. Eng. 100 (2016) 490–500. doi:10.1016/j.applthermaleng.2016.02.023.

[123] K.S. Reddy, S. Lokeswaran, P. Agarwal, T.K. Mallick, Numerical Investigation of Micro-channel based Active Module Cooling for Solar CPV System, Energy Procedia. 54 (2014) 400–416. doi:10.1016/j.egypro.2014.07.283.

[124] D.B. Tuckerman, R.F.W. Pease, High-performance heat sinking for VLSI, IEEE Electron Device Lett. 2 (1981) 126–129. doi:10.1109/EDL.1981.25367.

[125] Y. Wang, G.-F. Ding, Experimental investigation of heat transfer performance for a novel microchannel heat sink, J. Micromechanics Microengineering. 18 (2008) 035021. doi:10.1088/0960-1317/18/3/035021.

[126] R.W. Knight, D.J. Hall, J.S. Goodling, R.C. Jaeger, Heat sink optimization with application to microchannels, IEEE Trans. Components, Hybrids, Manuf. Technol. 15 (1992) 832–842. doi:10.1109/33.180049.

[127] G. Mittelman, A. Dayan, K. Dado-Turjeman, A. Ullmann, Laminar free convection underneath a downward facing inclined hot fin array, Int. J. Heat Mass Transf. 50 (2007) 2582–2589. doi:10.1016/j.ijheatmasstransfer.2006.11.033.

[128] D.Y. Lee, K. Vafai, Comparative analysis of jet impingement and microchannel cooling for high heat flux applications, Int. J. Heat Mass Transf. 42 (1999) 1555–1568. doi:10.1016/S0017-9310(98)00265-8.

[129] J. Barrau, J. Rosell, D. Chemisana, L. Tadrist, M. Ibañez, Effect of a hybrid jet impingement/micro-channel cooling device on the performance of densely packed PV cells under high concentration, Sol. Energy. 85 (2011) 2655–2665. doi:10.1016/j.solener.2011.08.004.

[130] J. Barrau, M. Omri, D. Chemisana, J. Rosell, M. Ibañez, L. Tadrist, Numerical study of a hybrid jet impingement/micro-channel cooling scheme, Appl. Therm. Eng. 33–34 (2012) 237–245. doi:10.1016/j.applthermaleng.2011.10.001.

[131] J. Barrau, A. Perona, A. Dollet, J. Rosell, Outdoor test of a hybrid jet impingement/micro-channel cooling device for densely packed concentrated photovoltaic cells, Sol. Energy. 107 (2014) 113–121. doi:10.1016/j.solener.2014.05.040.

[132] M. Victoria, S. Askins, C. Domínguez, I. Antón, G. Sala, Durability of dielectric fluids for concentrating photovoltaic systems, Sol. Energy Mater. Sol. Cells. 113 (2013) 31–36. doi:10.1016/j.solmat.2013.01.039.

[133] Y.A. Abrahamyan, V.I. Serago, V.M. Aroutiounian, I.D. Anisimova, V.I. Stafeev, G.G. Karamian, G.A. Martoyan, A.A. Mouradyan, The efficiency of solar cells immersed in liquid dielectrics, Sol. Energy Mater. Sol. Cells. 73 (2002) 367–375. doi:10.1016/S0927-0248(01)00220-3.

[134] X. Han, Y. Wang, L. Zhu, The performance and long-term stability of silicon concentrator solar cells immersed in dielectric liquids, Energy Convers. Manag. 66 (2013) 189–198. doi:10.1016/j.enconman.2012.10.009.

[135] Y. Sun, Y. Wang, L. Zhu, B. Yin, H. Xiang, Q. Huang, Direct liquid-immersion cooling of concentrator silicon solar cells in a linear concentrating photovoltaic receiver, Energy. 65 (2014) 264–271. doi:10.1016/j.energy.2013.11.063.

[136] Y. Wang, Z. Fang, L. Zhu, Q. Huang, Y. Zhang, Z. Zhang, The performance of silicon solar cells operated in liquids, Appl. Energy. 86 (2009) 1037–1042. doi:10.1016/j.apenergy.2008.08.020.

[137] X. Han, Y. Wang, L. Zhu, Electrical and thermal performance of silicon concentrator solar cells immersed in dielectric liquids, Appl. Energy. 88 (2011) 4481–4489. doi:10.1016/j.apenergy.2011.05.037.

[138] L. Liu, L. Zhu, Y. Wang, Q. Huang, Y. Sun, Z. Yin, Heat dissipation performance of silicon solar cells by direct dielectric liquid immersion under intensified illuminations, Sol. Energy. 85 (2011) 922–930. doi:10.1016/j.solener.2011.02.007.

[139] L. Zhu, R.F. Boehm, Y. Wang, C. Halford, Y. Sun, Water immersion cooling of PV cells in a high concentration system, Sol. Energy Mater. Sol. Cells. 95 (2011) 538–545. doi:10.1016/j.solmat.2010.08.037.

[140] X. Wei, Y. Joshi, Stacked Microchannel Heat Sinks for Liquid Cooling of Microelectronic Components, J. Electron. Packag. 126 (2004) 60. doi:10.1115/1.1647124.

[141] K. Vafai, L. Zhu, Analysis of two-layered micro-channel heat sink concept in electronic cooling, Int. J. Heat Mass Transf. 42 (1999) 2287–2297. doi:10.1016/S0017-9310(98)00017-9.

[142] X. Wei, Y. Joshi, Optimization study of stacked micro-channel heat sinks for micro-electronic cooling, Intersoc. Conf. Therm. Thermomechanical Phenom. Electron. Syst. ITHERM. 2002–Janua (2002) 441–448. doi:10.1109/ITHERM.2002.1012490.

[143] L. Lin, M.-X. Deng, X.-X. Zhang, X.-D. Wang, Numerical analysis and parametric study of multilayered microchannel heat sinks, Adv. Mech. Eng. 7 (2015) 168781401559412. doi:10.1177/1687814015594124.

[144] C. Leng, X.D. Wang, T.H. Wang, W.M. Yan, Optimization of thermal resistance and bottom wall temperature uniformity for double-layered microchannel heat sink, Energy Convers. Manag. 93 (2015) 141–150. doi:10.1016/j.enconman.2015.01.004.

[145] C. Leng, X.D. Wang, T.H. Wang, W.M. Yan, Multi-parameter optimization of flow and heat transfer for a novel double-layered microchannel heat sink, Int. J. Heat Mass Transf. 84 (2015) 359–369.

doi:10.1016/j.ijheatmasstransfer.2015.01.040.

[146] B. Lu, W.J. Meng, F. Mei, Experimental investigation of Cu-based, double-layered, microchannel heat exchangers, J. Micromechanics Microengineering. 23 (2013). doi:10.1088/0960-1317/23/3/035017.

[147] S.L. Wang, X.Y. Li, X.D. Wang, G. Lu, Flow and heat transfer characteristics in double-layered microchannel heat sinks with porous fins, Int. Commun. Heat Mass Transf. 93 (2018) 41–47. doi:10.1016/j.icheatmasstransfer.2018.03.003.

[148] H.E. Ahmed, M.I. Ahmed, I.M.F. Seder, B.H. Salman, Experimental investigation for sequential triangular double-layered microchannel heat sink with nanofluids, Int. Commun. Heat Mass Transf. 77 (2016) 104–115. doi:10.1016/j.icheatmasstransfer.2016.06.010.

[149] L. Pang, M. Wang, W. Wang, M. Liu, J. Wang, Optimal thermal design of a stacked mini-channel heat sink cooled by a low flow rate coolant, Entropy. 15 (2013) 4716–4731. doi:10.3390/e15114716.

[150] T.C. Hung, W.M. Yan, X.D. Wang, Y.X. Huang, Optimal design of geometric parameters of double-layered microchannel heat sinks, Int. J. Heat Mass Transf. 55 (2012) 3262–3272. doi:10.1016/j.ijheatmasstransfer.2012.02.059.

[151] K.C. Chen, C.C. Wang, Performance improvement of high power liquid-cooled heat sink via non-uniform metal foam arrangement, Appl. Therm. Eng. 87 (2015) 41–46. doi:10.1016/j.applthermaleng.2015.05.005.

[152] S.H. Chong, K.T. Ooi, T.N. Wong, Optimisation of single and double layer counter flow microchannel heat sinks, Appl. Therm. Eng. 22 (2002) 1569–1585. doi:10.1016/S1359-4311(02)00083-2.

[153] K. Jeevan, I.A. Azid, K.N. Seetharamu, N. Tehal, Optimization of double layer counter flow (DLCF) micro-channel heat sink used for cooling chips directly, Electron. Packag. Technol. Conf. (2004) 553–558.

[154] L. Lin, Y.Y. Chen, X.X. Zhang, X.D. Wang, Optimization of geometry and flow rate distribution for double-layer microchannel heat sink, Int. J. Therm. Sci. 78 (2014) 158–168. doi:10.1016/j.ijthermalsci.2013.12.009.

[155] J.M. Wu, J.Y. Zhao, K.J. Tseng, Parametric study on the performance of double-layered microchannels heat sink, Energy Convers. Manag. 80 (2014) 550–560. doi:10.1016/j.enconman.2014.01.014.

[156] M.L.-J. Levac, H.M. Soliman, S.J. Ormiston, Three-dimensional analysis of fluid flow and heat transfer in single- and two-layered micro-channel heat sinks, Heat Mass Transf. 47 (2011) 1375–1383. doi:10.1007/s00231-011-0795-7.

[157] K.C. Wong, F.N.A. Muezzin, Heat transfer of a parallel flow two-layered microchannel heat sink, Int. Commun. Heat Mass Transf. 49 (2013) 136–140. doi:10.1016/j.icheatmasstransfer.2013.09.004.

[158] G. Xie, Y. Liu, B. Sunden, W. Zhang, Computational Study and Optimization of Laminar Heat Transfer and Pressure Loss of Double-Layer Microchannels for Chip Liquid Cooling, J. Therm. Sci. Eng. Appl. 5

(2013) 011004. doi:10.1115/1.4007778.

[159] H. Al-Bakhit, A. Fakheri, Numerical simulation of heat transfer in simultaneously developing flows in parallel rectangular ducts, Appl. Therm. Eng. 26 (2006) 596–603. doi:10.1016/j.applthermaleng.2005.07.002.

[160] Y.J. Cheng, Numerical simulation of stacked microchannel heat sink with mixing-enhanced passive structure, Int. Commun. Heat Mass Transf. 34 (2007) 295–303. doi:10.1016/j.icheatmasstransfer.2006.12.007.

[161] B. Shi, A. Srivastava, P. Wang, B.I. Circuits, D. Aids, Non-Uniform Micro-Channel Design for Stacked 3D-ICs ∗, Design. (2011) 658–663.

[162] T.C. Hung, W.M. Yan, Enhancement of thermal performance in double-layered microchannel heat sink with nanofluids, Int. J. Heat Mass Transf. 55 (2012) 3225–3238. doi:10.1016/j.ijheatmasstransfer.2012.02.057.

[163] A. Sakanova, S. Yin, J. Zhao, J.M. Wu, K.C. Leong, Optimization and comparison of double-layer and double-side micro-channel heat sinks with nanofluid for power electronics cooling, Appl. Therm. Eng. 65 (2014) 124–134. doi:10.1016/j.applthermaleng.2014.01.005.

[164] T.C. Hung, W.M. Yan, W.P. Li, Analysis of heat transfer characteristics of double-layered microchannel heat sink, Int. J. Heat Mass Transf. 55 (2012) 3090–3099. doi:10.1016/j.ijheatmasstransfer.2012.02.038.

[165] E.Y.K. Ng, S.T. Poh, CFD analysis of double-layer microchannel conjugate parallel liquid flows with electric double-layer effects, Numer. Heat Transf. Part A Appl. 40 (2001) 735–749. doi:10.1080/104077801753289828.

[166] P. Dixit, N. Lin, J. Miao, W.K. Wong, T.K. Choon, Silicon nanopillars based 3D stacked microchannel heat sinks concept for enhanced heat dissipation applications in MEMS packaging, Sensors Actuators, A Phys. 141 (2008) 685–694. doi:10.1016/j.sna.2007.09.006.

[167] L. Gong, J. Zhao, S. Huang, Numerical study on layout of micro-channel heat sink for thermal management of electronic devices, Appl. Therm. Eng. 88 (2015) 480–490. doi:10.1016/j.applthermaleng.2014.09.048.

[168] P. Skandakumaran, A. Ortega, T. Jamal-Eddine, R. Vaidyanathan, Multi-layered SiC microchannel heat sinks - modeling and experiment, (2004) 352–360 Vol.1. doi:10.1109/ITHERM.2004.1319196.

[169] N. Lei, A. Ortega, R. Vaidyanathan, Modeling and optimization of multilayer minichannel heat sinks in single-phase flow, ASME InterPACK Conf. (2007) 29–43. doi:10.1115/IPACK2007-33329.

[170] G. Xie, Z. Chen, B. Sunden, W. Zhang, Numerical predictions of the flow and thermal performance of water-cooled single-layer and double-layer wavy microchannel heat sinks, Numer. Heat Transf. Part A Appl. 63 (2013) 201–225. doi:10.1080/10407782.2013.730445.

[171] I. Al Al Siyabi, S. Khanna, S. Sundaram, Experimental and Numerical Thermal Analysis of Multi-Layered Microchannel Heat Sink for Concentrating Photovoltaic Application, (2019). doi:10.3390/en12010122.

[172] B. Shao, L. Wang, H. Cheng, J. Li, Optimization and numerical simulation of multi-layer microchannel heat sink, Procedia Eng. 31 (2012) 928–933. doi:10.1016/j.proeng.2012.01.1123.

[173] X. Wei, Y. Joshi, M.K. Patterson, Experimental and Numerical Study of a Stacked Microchannel Heat Sink for Liquid Cooling of Microelectronic Devices, J. Heat Transfer. 129 (2007) 1432. doi:10.1115/1.2754781.

[174] D. Ansari, K.Y. Kim, Performance analysis of double-layer microchannel heat sinks under non-uniform heating conditions with random hotspots, Micromachines. 8 (2017). doi:10.3390/mi8020054.

[175] I. Al Siyabi, K. Shanks, T. Mallick, S. Sundaram, Thermal analysis of a multi-layer microchannel heat sink for cooling concentrator photovoltaic (CPV) cells, 070001 (2017) 070001. doi:10.1063/1.5001434.

[176] A. Radwan, M. Ahmed, The influence of microchannel heat sink configurations on the performance of low concentrator photovoltaic systems, Appl. Energy. 206 (2017) 594–611. doi:10.1016/j.apenergy.2017.08.202.

[177] A. Sharma, V.V. Tyagi, C.R. Chen, D. Buddhi, Review on thermal energy storage with phase change materials and applications, Renew. Sustain. Energy Rev. 13 (2009) 318–345. doi:10.1016/j.rser.2007.10.005.

[178] a. Abhat, Low temperature latent heat thermal energy storage: Heat storage materials, Sol. Energy. 30 (1983) 313–332. doi:10.1016/0038-092X(83)90186-X.

[179] C. Liu, R.E. Murray, D. Groulx, Experimental Study of Cylindrical Latent Heat Energy Storage Systems Using Lauric Acid as the Phase Change Material, ASME 2012 Summer Heat Transf. Conf. (2012) 1–10. doi:10.1115/HT2012-58279.

[180] F. Agyenim, N. Hewitt, P. Eames, M. Smyth, A review of materials, heat transfer and phase change problem formulation for latent heat thermal energy storage systems (LHTESS), Renew. Sustain. Energy Rev. 14 (2010) 615–628. doi:10.1016/j.rser.2009.10.015.

[181] M. Esen, A. Durmuş, A. Durmuş, Geometric design of solar-aided latent heat store depending on various parameters and phase change materials, Sol. Energy. 62 (1998) 19–28. doi:10.1016/S0038-092X(97)00104-7.

[182] F. Agyenim, P. Eames, M. Smyth, A comparison of heat transfer enhancement in a medium temperature thermal energy storage heat exchanger using fins, Sol. Energy. 83 (2009) 1509–1520. doi:10.1016/j.solener.2009.04.007.

[183] Z.-X. Gong, A.S. Mujumdar, Thermodynamic optimization of the thermal process in energy storage using multiple phase change materials, Appl. Therm. Eng. 17 (1997) 1067–1083. doi:10.1016/S1359-4311(97)00012-4.

[184] Z. Gong, A. Majumdar, F. Agyenim, N. Hewitt, P. Eames, M. Smyth, M. Esen, A.A. Durmuş, A.A. Durmuş, F. Agyenim, P. Eames, M. Smyth, R. Yumrutas, O.O. Kas, I. Dincer, S. Dost, M. Esen, T. Ayhan, G. Kumaresan, R. Sridhar, R. Velraj, A review of materials, heat transfer and phase change problem formulation for latent heat thermal energy storage

systems (LHTESS), Sol. Energy. 14 (1996) 615–628. doi:10.1016/j.rser.2009.10.015.

[185] R. Velraj, R.V. Seeniraj, B. Hafner, C. Faber, K. Schwarzer, Heat Transfer Enhancement in a Latent Heat Storage System, Sol. Energy. 65 (1999) 171–180. doi:10.1016/S0038-092X(98)00128-5.

[186] J. Wang, Y. Ouyang, G. Chen, Experimental study on charging processes of a cylindrical heat storage employing multiple-phase-change materials, Int. J. Energy Res. 25 (2001) 439–447. doi:10.1002/er.695.

[187] H.A. Adine, H. El Qarnia, Numerical analysis of the thermal behaviour of a shell-and-tube heat storage unit using phase change materials, Appl. Math. Model. 33 (2009) 2132–2144. doi:10.1016/j.apm.2008.05.016.

[188] R.M. Abdel-Wahed, J.W. Ramsey, E.M. Sparrow, Photographic study of melting about an embedded horizontal heating cylinder, Int. J. Heat Mass Transf. 22 (1979) 171–173. doi:10.1016/0017-9310(79)90110-8.

[189] L.S. Yao, W. Cherney, Transient phase-change around a horizontal cylinder, Int. J. Heat Mass Transf. 24 (1981) 1971–1981. doi:10.1016/0017-9310(81)90119-8.

[190] X.-Q. Wang, A.S. Mujumdar, C. Yap, Effect of orientation for phase change material (PCM)-based heat sinks for transient thermal management of electric components, Int. Commun. Heat Mass Transf. 34 (2007) 801–808. doi:10.1016/j.icheatmasstransfer.2007.03.008.

[191] R. Baby, C. Balaji, Experimental investigations on thermal performance enhancement and effect of orientation on porous matrix filled PCM based heat sink, Int. Commun. Heat Mass Transf. 46 (2013) 27–30. doi:10.1016/j.icheatmasstransfer.2013.05.018.

[192] B.W. Webb, R. Viskanta, Natural-convection-dominated melting heat transfer in an inclined rectangular enclosure, Int. J. Heat Mass Transf. 29 (1986) 183–192. doi:10.1016/0017-9310(86)90226-7.

[193] B. Kamkari, H. Shokouhmand, F. Bruno, Experimental investigation of the effect of inclination angle on convection-driven melting of phase change material in a rectangular enclosure, Int. J. Heat Mass Transf. 72 (2014) 186–200. doi:10.1016/j.ijheatmasstransfer.2014.01.014.

[194] M. Longeon, A. Soupart, J.F. Fourmigué, A. Bruch, P. Marty, Experimental and numerical study of annular PCM storage in the presence of natural convection, Appl. Energy. 112 (2013) 175–184. doi:10.1016/j.apenergy.2013.06.007.

[195] H.M. Ettouney, I. Alatiqi, M. Al-Sahali, S.A. Al-Ali, Heat transfer enhancement by metal screens and metal spheres in phase change energy storage systems, Renew. Energy. 29 (2004) 841–860. doi:10.1016/j.renene.2003.11.003.

[196] M. a. Kibria, M.R. Anisur, M.H. Mahfuz, R. Saidur, I.H.S.C. Metselaar, Numerical and experimental investigation of phase change process in a shell and tube thermal energy storage system., Int. Commun. Heat Mass Transf. 53 (2014) 71–78. doi:10.1016/j.icheatmasstransfer.2014.02.023.

[197] M. a. Kibria, M.R. Anisur, M.H. Mahfuz, R. Saidur, I.H.S.C. Metselaar, Numerical and experimental investigation of heat transfer in a shell and tube thermal energy storage system, Int. Commun. Heat Mass Transf. 53 (2014) 71–78. doi:10.1016/j.icheatmasstransfer.2014.02.023.

[198] K. Kaygusuz, A. Sari, Thermal energy storage system using a technical grade paraffin wax as latent heat energy storage material, Energy Sources. 27 (2005) 1535–1546. doi:10.1080/009083190914015.

[199] R.E. Murray, D. Groulx, Experimental study of the phase change and energy characteristics inside a cylindrical latent heat energy storage system: Part 1 consecutive charging and discharging, Renew. Energy. 62 (2014) 571–581. doi:10.1016/j.renene.2013.08.007.

[200] R.E. Murray, D. Groulx, Experimental study of the phase change and energy characteristics inside a cylindrical latent heat energy storage system: Part 2 simultaneous charging and discharging, Renew. Energy. 63 (2014) 724–734. doi:10.1016/j.renene.2013.10.004.

[201] M. Esapour, M.J. Hosseini, A.A. Ranjbar, Y. Pahamli, R. Bahrampoury, Phase change in multi-tube heat exchangers, Renew. Energy. 85 (2016) 1017–1025. doi:10.1016/j.renene.2015.07.063.

[202] A. Caron-Soupart, J.-F. Fourmigué, P. Marty, R. Couturier, Performance analysis of thermal energy storage systems using phase change material, Appl. Therm. Eng. 98 (2016) 1286–1296. doi:10.1016/j.applthermaleng.2016.01.016.

[203] C. Liu, D. Groulx, Experimental study of the phase change heat transfer inside a horizontal cylindrical latent heat energy storage system, Int. J. Therm. Sci. 82 (2014) 100–110. doi:10.1016/j.ijthermalsci.2014.03.014.

[204] Y.B. Tao, Y.L. He, Effects of natural convection on latent heat storage performance of salt in a horizontal concentric tube, Appl. Energy. 143 (2015) 38–46. doi:10.1016/j.apenergy.2015.01.008.

[205] N.H.S. Tay, M. Belusko, F. Bruno, Experimental investigation of tubes in a phase change thermal energy storage system, Appl. Energy. 90 (2012) 288–297. doi:10.1016/j.apenergy.2011.05.026.

[206] N.H.S. Tay, F. Bruno, M. Belusko, Experimental investigation of dynamic melting in a tube-in-tank PCM system, Appl. Energy. 104 (2013) 137–148. doi:10.1016/j.apenergy.2012.11.035.

[207] N.H.S. Tay, F. Bruno, M. Belusko, Experimental validation of a CFD model for tubes in a phase change thermal energy storage system, Int. J. Heat Mass Transf. 55 (2012) 574–585. doi:10.1016/j.ijheatmasstransfer.2011.10.054.

[208] N.H.S. Tay, M. Belusko, F. Bruno, Designing a PCM storage system using the effectiveness-number of transfer units method in low energy cooling of buildings, Energy Build. 50 (2012) 234–242. doi:10.1016/j.enbuild.2012.03.041.

[209] N.H.S. Tay, M. Belusko, F. Bruno, An effectiveness-NTU technique for characterising tube-in-tank phase change thermal energy storage systems, Appl. Energy. 91 (2012) 309–319.

doi:10.1016/j.apenergy.2011.09.039.

[210] D. Mehta, X. Chaudhari, M. Rathod, J. Banerjee, effect of orientation of shell and tube latent heat storage unit on melting phenomena of phase change material, (2017).

[211] S. Seddegh, X. Wang, A.D. Henderson, A comparative study of thermal behaviour of a horizontal and vertical shell-and-tube energy storage using phase change materials, Appl. Therm. Eng. 93 (2016) 348–358. doi:10.1016/j.applthermaleng.2015.09.107.

[212] N. Kousha, M.J. Hosseini, M.R. Aligoodarz, R. Pakrouh, R. Bahrampoury, Effect of inclination angle on the performance of a shell and tube heat storage unit – An experimental study, Appl. Therm. Eng. 112 (2017) 1497–1509. doi:10.1016/j.applthermaleng.2016.10.203.

[213] D. Aydin, Z. Utlu, O. Kincay, Thermal performance analysis of a solar energy sourced latent heat storage, Renew. Sustain. Energy Rev. 50 (2015) 1213–1225. doi:10.1016/j.rser.2015.04.195.

[214] M. Lacroix, Study of the heat transfer behavior of a latent heat thermal energy storage unit with a finned tube, Int. J. Heat Mass Transf. 36 (1993) 2083–2092. doi:10.1016/S0017-9310(05)80139-5.

[215] W. Ogoh, D. Groulx, Effects of the heat transfer fluid velocity on the storage characteristics of a cylindrical latent heat energy storage system: a numerical study, Heat Mass Transf. 48 (2011) 439–449. doi:10.1007/s00231-011-0888-3.

[216] S. Lorente, A. Bejan, J.L. Niu, Constructal design of latent thermal energy storage with vertical spiral heaters, Int. J. Heat Mass Transf. 81 (2015) 283–288. doi:10.1016/j.ijheatmasstransfer.2014.09.077.

[217] M.S. Mon, U. Gross, Numerical study of fin-spacing effects in annular-finned tube heat exchangers, Int. J. Heat Mass Transf. 47 (2004) 1953–1964. doi:10.1016/j.ijheatmasstransfer.2003.09.034.

[218] D.-K. Kim, Thermal optimization of internally finned tube with variable fin thickness, Appl. Therm. Eng. 102 (2016) 1250–1261. doi:10.1016/j.applthermaleng.2016.04.060.

[219] A. Castell, M. Belusko, F. Bruno, L.F. Cabeza, Maximisation of heat transfer in a coil in tank PCM cold storage system, Appl. Energy. 88 (2011) 4120–4127. doi:10.1016/j.apenergy.2011.03.046.

[220] A. Khalifa, L. Tan, A. Date, A. Akbarzadeh, A numerical and experimental study of solidification around axially finned heat pipes for high temperature latent heat thermal energy storage units, Appl. Therm. Eng. 70 (2014) 609–619. doi:10.1016/j.applthermaleng.2014.05.080.

[221] D. Zhao, G. Tan, Numerical analysis of a shell-and-tube latent heat storage unit with fins for air-conditioning application, Appl. Energy. 138 (2015) 381–392. doi:10.1016/j.apenergy.2014.10.051.

[222] S. Mat, A.A. Al-Abidi, K. Sopian, M.Y. Sulaiman, A.T. Mohammad, Enhance heat transfer for PCM melting in triplex tube with internal-external fins, Energy Convers. Manag. 74 (2013) 223–236.

doi:10.1016/j.enconman.2013.05.003.

[223] W. Zhao, A.F. Elmozughi, A. Oztekin, S. Neti, Heat transfer analysis of encapsulated phase change material for thermal energy storage, Int. J. Heat Mass Transf. 63 (2013) 323–335. doi:10.1016/j.ijheatmasstransfer.2013.03.061.

[224] S. Bellan, J. Gonzalez-Aguilar, M. Romero, M.M. Rahman, D.Y. Goswami, E.K. Stefanakos, D. Couling, Numerical analysis of charging and discharging performance of a thermal energy storage system with encapsulated phase change material, Appl. Therm. Eng. 71 (2014) 481–500. doi:10.1016/j.applthermaleng.2014.07.009.

[225] K. Nithyanandam, R. Pitchumani, Optimization of an encapsulated phase change material thermal energy storage system, Sol. Energy. 107 (2014) 770–788. doi:10.1016/j.solener.2014.06.011.

[226] S. Kalaiselvam, M. Veerappan, A. Arul Aaron, S. Iniyan, Experimental and analytical investigation of solidification and melting characteristics of PCMs inside cylindrical encapsulation, Int. J. Therm. Sci. 47 (2008) 858–874. doi:10.1016/j.ijthermalsci.2007.07.003.

[227] J.P. Bédécarrats, J. Castaing-Lasvignottes, F. Strub, J.P. Dumas, Study of a phase change energy storage using spherical capsules. Part I: Experimental results, Energy Convers. Manag. 50 (2009) 2527–2536. doi:10.1016/j.enconman.2009.06.004.

[228] J.P. Bédécarrats, J. Castaing-Lasvignottes, F. Strub, J.P. Dumas, Study of a phase change energy storage using spherical capsules. Part II: Numerical modelling, Energy Convers. Manag. 50 (2009) 2537–2546. doi:10.1016/j.enconman.2009.06.003.

[229] N. Nallusamy, R. Velraj, Numerical and Experimental Investigation on a Combined Sensible and Latent Heat Storage Unit Integrated With Solar Water Heating System, J. Sol. Energy Eng. 131 (2009) 041002. doi:10.1115/1.3197600.

[230] M. Ezra, Y. Kozak, V. Dubovsky, G. Ziskind, Analysis and optimization of melting temperature span for a multiple-PCM latent heat thermal energy storage unit, Appl. Therm. Eng. 93 (2016) 315–329. doi:10.1016/j.applthermaleng.2015.09.040.

[231] D.M. Temperatures, Exergy analysis for the evaluation of a thermal storage system employing PCMs with dirrerent melting temperatures, (1996).

[232] T. Watanabe, H. Kikuchi, A. Kanzawa, Enhancement of charging and discharging rates in a latent heat storage system by use of PCM with different melting temperatures, Heat Recover. Syst. CHP. 13 (1993) 57–66. doi:10.1016/0890-4332(93)90025-Q.

[233] Z.X. Gong, A.S. Mujumdar, Cyclic heat transfer in a novel storage unit of multiple phase change materials, Appl. Therm. Eng. 16 (1996) 807–815. doi:10.1016/1359-4311(95)00088-7.

[234] H. Michels, R. Pitz-Paal, Cascaded latent heat storage for parabolic trough solar power plants, Sol. Energy. 81 (2007) 829–837.

doi:10.1016/j.solener.2006.09.008.

[235] R. V. Seeniraj, N. Lakshmi Narasimhan, Performance enhancement of a solar dynamic LHTS module having both fins and multiple PCMs, Sol. Energy. 82 (2008) 535–542. doi:10.1016/j.solener.2007.11.001.

[236] M. Fang, G. Chen, Effects of different multiple PCMs on the performance of a latent thermal energy storage system, Appl. Therm. Eng. 27 (2007) 994–1000. doi:10.1016/j.applthermaleng.2006.08.001.

[237] A. Bejan, Two thermodynamic optima in the design of sensible heat units for energy storage, J. Heat Transfer. 100 (1978) 708–712.

[238] R.J. Krane, A Second Law analysis of the optimum design and operation of thermal energy storage systems, Int. J. Heat Mass Transf. 30 (1987) 43–57. doi:10.1016/0017-9310(87)90059-7.

[239] R. Yumrutas, O. Kaska, Experimental investigation of thermal performance of a solar assisted heat pump system with an energy storage, Int. J. Energy Res. 28 (2004) 163–175. doi:Doi 10.1002/Er.959.

[240] G. Kumaresan, R. Sridhar, R. Velraj, Performance studies of a solar parabolic trough collector with a thermal energy storage system, Energy. 47 (2012) 395–402. doi:10.1016/j.energy.2012.09.036.

[241] B.J. Huang, T.H. Lin, W.C. Hung, F.S. Sun, Performance evaluation of solar photovoltaic/thermal systems, Sol. Energy. 70 (2001) 443–448. doi:10.1016/S0038-092X(00)00153-5.

[242] O. Ozgener, A. Hepbasli, Experimental performance analysis of a solar assisted ground-source heat pump greenhouse heating system, Energy Build. 37 (2005) 101–110. doi:10.1016/j.enbuild.2004.06.003.

[243] A. Tiwari, M.S. Sodha, Performance evaluation of solar PV/T system: An experimental validation, Sol. Energy. 80 (2006) 751–759. doi:10.1016/j.solener.2005.07.006.

[244] G. Fraisse, C. Ménézo, K. Johannes, Energy performance of water hybrid PV/T collectors applied to combisystems of Direct Solar Floor type, Sol. Energy. 81 (2007) 1426–1438. doi:10.1016/j.solener.2006.11.017.

[245] S. Dubey, G.N. Tiwari, Thermal modeling of a combined system of photovoltaic thermal (PV/T) solar water heater, Sol. Energy. 82 (2008) 602–612. doi:10.1016/j.solener.2008.02.005.

[246] K. Bakirci, B. Yuksel, Experimental thermal performance of a solar source heat-pump system for residential heating in cold climate region, Appl. Therm. Eng. 31 (2011) 1508–1518. doi:10.1016/j.applthermaleng.2011.01.039.

[247] A. Çağlar, C. Yamali, Performance analysis of a solar-assisted heat pump with an evacuated tubular collector for domestic heating, Energy Build. 54 (2012) 22–28. doi:10.1016/j.enbuild.2012.08.003.

[248] M.S. Naghavi, K.S. Ong, I.A. Badruddin, M. Mehrali, H.S.C. Metselaar, Thermal performance of a compact design heat pipe solar collector with latent heat storage in charging/discharging modes, Energy. 127 (2017) 101–115. doi:10.1016/j.energy.2017.03.097.

[249] N. Beemkumar, A. Karthikeyan, D. Yuvarajan, S. Lakshmi Sankar, Experimental Investigation on Improving the Heat Transfer of Cascaded Thermal Storage System Using Different Fins, Arab. J. Sci. Eng. 42 (2017) 2055–2065. doi:10.1007/s13369-017-2455-9.

[250] Azure Space Solar Power GMBH, Enhanced Fresnel Assembly - EFA Type: 3C42A – with 10x10mm^2 CPV TJ Solar Cell Application: Concentrating Photovoltaic (CPV) Modules, (2014) 0–4. http://www.azurspace.com/images/products/DB_3987-00-00_3C42_AzurDesign_EFA_10x10_2014-03-27.pdf.

[251] K. Shanks, H. Baig, N.P. Singh, S. Senthilarasu, K.S. Reddy, T.K. Mallick, Prototype Fabrication and Experimental Investigation of a Conjugate Refractive Reflective Homogeniser in a Cassegrain Concentrator, Sol. Energy. 142 (2017) 97–108. doi:10.1016/j.solener.2016.11.038.

[252] No Title, (n.d.). http://www.wacom-ele.co.jp.

[253] S. Sharma, L. Micheli, W. Chang, A.A. Tahir, K.S. Reddy, T.K. Mallick, Nano-enhanced Phase Change Material for thermal management of BICPV, Appl. Energy. 208 (2017) 719–733. doi:10.1016/j.apenergy.2017.09.076.

[254] G. Ferrer, C. Barreneche, A. Solé, I. Martorell, L.F. Cabeza, New proposed methodology for specific heat capacity determination of materials for thermal energy storage (TES) by DSC, J. Energy Storage. 11 (2017) 1–6. doi:10.1016/j.est.2017.02.002.

[255] R.K. Mathur, D.R. Mehrotra, S. Mittal, S.R. Dhariwal, Thermal non-uniformities in concentrator solar cells, Sol. Cells. 11 (1984) 175–188. doi:10.1016/0379-6787(84)90025-5.

[256] M. Theristis, T.S. O'Donovan, Electrical-thermal analysis of III–V triple-junction solar cells under variable spectra and ambient temperatures, Sol. Energy. 118 (2015) 533–546. doi:10.1016/j.solener.2015.06.003.

[257] G. Segev, G. Mittelman, A. Kribus, Equivalent circuit models for triple-junction concentrator solar cells, Sol. Energy Mater. Sol. Cells. 98 (2012) 57–65. doi:10.1016/j.solmat.2011.10.013.

[258] RJ. Phillips, Forced-Convection. Liquid-Cooled, Microchannel Heat Sinks, Cambridge, 1987.

[259] M. Theristis, T.S.O. Donovan, An integrated thermal electrical model for single cell photovoltaic receivers under concentration, (2014) 1–12. doi:10.13140/2.1.3601.3446.

[260] K.. Toh, X.. Chen, J.. Chai, Numerical computation of fluid flow and heat transfer in microchannels, Int. J. Heat Mass Transf. 45 (2002) 5133–5141. doi:10.1016/S0017-9310(02)00223-5.

[261] D. Ansari, K.-Y. Kim, Double-Layer Microchannel Heat Sinks With Transverse-Flow Configurations, J. Electron. Packag. 138 (2016) 031005. doi:10.1115/1.4033558.

[262] COMSOL Multiphysics Reference Guide, (2012).

[263] K. Shanks, H. Baig, S. Senthilarasu, K.S. Reddy, T.K. Mallick, Conjugate

refractive–reflective homogeniser in a 500× Cassegrain concentrator: design and limits, IET Renew. Power Gener. 10 (2016) 440–447. doi:10.1049/iet-rpg.2015.0371.

[264] K. Shanks, N. Sarmah, J.P. Ferrer-Rodriguez, S. Senthilarasu, K.S. Reddy, E.F. Fernández, T. Mallick, Theoretical investigation considering manufacturing errors of a high concentrating photovoltaic of cassegrain design and its experimental validation, Sol. Energy. 131 (2016) 235–245. doi:10.1016/j.solener.2016.02.050.

[265] K.M.A. Shanks, Identification and Development of Novel Optics for Concentrator Photovoltaic Applications, (2017).

[266] K. Shanks, S. Senthilarasu, T.K. Mallick, Optics for concentrating photovoltaics: Trends, limits and opportunities for materials and design, Renew. Sustain. Energy Rev. 60 (2016) 394–407. doi:10.1016/j.rser.2016.01.089.

[267] M. McDonald, S. Horne, G. Conley, Concentrator design to minimize LCOE, Proc. SPIE 6649, High Low Conc. Sol. Electr. Appl. II, 66490B. 6649 (2007) 66490B–66490B–11. doi:10.1117/12.735738.

[268] S. V Patankar, Numerical heat transfer and fluid flow, Ser. Comput. Phys. Process. Mech. Therm. Sci. (1980) 197.

[269] F. Agyenim, N. Hewitt, P. Eames, M. Smyth, A review of materials, heat transfer and phase change problem formulation for latent heat thermal energy storage systems (LHTESS), Renew. Sustain. Energy Rev. 14 (2010) 615–628. doi:10.1016/j.rser.2009.10.015.

[270] G. Ziskind, Modelling of heat transfer in phase change materials (PCMs) for thermal energy storage systems, Woodhead Publishing Limited, 2014. doi:10.1533/9781782420965.2.307.

[271] M. Yao, A. Chait, An alternative formulation of the apparent heat capacity method for phase–change problems, Numer. Heat Transf. Part B Fundam. 24 (1993) 279–300. doi:10.1080/10407799308955894.

[272] P.H. Biwole, P. Eclache, F. Kuznik, Phase-change materials to improve solar panel's performance, Energy Build. 62 (2013) 59–67. doi:10.1016/j.enbuild.2013.02.059.

[273] N. Özisic, Finite Difference Methods in Heat Transfer, 2nd ed., CRC Press, 1994.

[274] A.D. Brent, V.R. Voller, K.J. Reid, Enthalpy-porosity technique for modeling convection-diffusion phase change: Application to the melting of a pure metal, Numer. Heat Transf. 13 (1988) 297–318. doi:10.1080/10407788808913615.

[275] C.R. SWAMINATHAN, V.R. VOLLER, ON THE ENTHALPY METHOD, Int. J. Numer. Methods Heat Fluid Flow. 3 (2016) 233–244. doi:10.1108/EUM0000000004093.

[276] V.R. Voller, C.R. Swaminathan, General source-based method for solidification phase change, Numer. Heat Transf. Part B Fundam. 19 (1991) 175–189. doi:10.1080/10407799108944962.

[277] B. Nedjar, An enthalpy-based finite element method for nonlinear heat problems involving phase change, Comput. Struct. 80 (2002) 9–21. doi:10.1016/S0045-7949(01)00165-1.

[278] F. Session, Heat Transfer And Phase Change Simulation In COMSOL Multiphysics Session Agenda • Heat Transfer and Phase Change Simulation • Microwave Heating of Initially Frozen Sandwiches • Cooling and Phase Change of a Melt-Cast, (2015).

[279] D.A. KAMINSKI, M.K. Jensen, INTRODUCTION TO THERMAL AND FLUIDS ENGINEERING, JOHN WILEY & SONS, INC, 2005.

[280] Y.A. Cengel, Heat Transfer: A Practical Approach, Mc Graw-Hill. (2003) 785–841. http://www.ncbi.nlm.nih.gov/pmc/articles/PMC341276/pdf/nar00305-0003.pdf.

[281] Holman J.P., Heat Transfer, McGraw Hill Higher Education, 2010.

[282] S. Seddegh, X. Wang, M.M. Joybari, F. Haghighat, Investigation of the effect of geometric and operating parameters on thermal behavior of vertical shell-and-tube latent heat energy storage systems, Energy. 137 (2017) 69–82. doi:10.1016/j.energy.2017.07.014.

[283] M. Li, G.L. Li, X. Ji, F. Yin, L. Xu, The performance analysis of the Trough Concentrating Solar Photovoltaic/Thermal system, Energy Convers. Manag. 52 (2011) 2378–2383. doi:10.1016/j.enconman.2010.12.039.

Appendix A

Along with the main PhD study, the investigations of using the PCM as a passive heat sink has been investigated and published. This appendix presents the published studies which are not pointed out in any part of the thesis.

Case study 1: Multiple Phase Change Material (PCM) Configuration for PCM-Based Heat Sinks- An Experimental Study

energies

MDPI

Article

Multiple Phase Change Material (PCM) Configuration for PCM-Based Heat Sinks—An Experimental Study

Idris Al Siyabi, Sourav Khanna, Tapas Mallick * and Senthilarasu Sundaram

Environment and Sustainability Institute, University of Exeter, Penryn Campus, Cornwall TR109FE, UK; ia257@exeter.ac.uk (I.A.S.); S.Khanna@exeter.ac.uk (S.K.); S.Sundaram@exeter.ac.uk (S.S.)
* Correspondence: T.K.Mallick@exeter.ac.uk; Tel.: +44-132-625-9465

Received: 1 June 2018; Accepted: 20 June 2018; Published: 22 June 2018

check for updates

Abstract: A small-scale phase change material (PCM)-based heat sink can regulate the temperature of electronics due to high latent-heat capacity. Three different heat sinks are examined to study the effects of PCM combination, arrangement of PCMs in multiple-PCM heat sink, PCM thickness, melting temperature and intensity of heat source on the thermal behavior of heat sink. Results are obtained for the temperature distribution across the heat sink and the PCM melting profile. It is concluded that (i) PCM combination RT50–RT55 increases the thermal regulation period and also reduces the heat sink temperature at the end of the operation, (ii) the RT58–RT47 arrangement slightly reduces the maximum temperature as compared to RT47–RT58, (iii) As PCM thickness increases from 30 mm to 60 mm, the thermal-regulation-period increases by 50 min, (iv) As the PCM melting temperature increases, the thermal-regulation-period and the heat sink temperature increase and (v) The thermal-regulation-period decreases as the power rating increases from 1 to 2 W.

Keywords: phase change material; thermal regulation; heat sink

1. Introduction

Thermal management of electronics is an important issue, because the heat generated by an electronic system leads to a decrease in its efficiency or even an immediate failure [1]. The heat-related failures of electronics account for 55% of the total electronic failures as per a U.S. Air Force survey [2]. The component failure increases by 100% for a temperature increase between 10 °C and 20 °C [3] whereas the component failure reduces at a rate of approximately 4%/°C with a decrease in the temperature. This issue has become even more challenging for higher performance complex electronic systems such as smart phones and notebook computers as they are required to be light in weight and small in size [4].

Many studies have emphasized the thermal management of electronic devices and have proposed various techniques for cooling such as extended surface [5], cold plates [6], immersion cooling [7], heat pipes [8] and thermoelectric coolers [9]. Selection of the cooling technique depends on the operating temperature, heating power rate, available space and cost [10]. The limitation of these techniques is that the excessive heat must be extracted to the environment using ventilation slots. But in wet and dusty environments, the devices must be completely sealed. An integrated thermal energy storage (TES) system within the device could solve this issue.

Thermal regulation of electronics using phase change material (PCM) is considered as a promising cooling technique due to the attractive features of PCM such as high storage density, ability to withstand a large number of cycles and isothermal nature at relatively constant melting temperature [11–14]. It was first proposed for avionics thermal control in 1977 [15] and since then a lot of studies investigated the PCM-based heat sink [16–24]. The main drawback of the PCM is its low conductivity which has led

researchers to propose various enhancement techniques such as using extended surfaces of different configurations [25–28], employing multiple PCMs [29] and PCM encapsulation [30].

Many factors affect the performance of PCM-based heat sinks for electronics applications such as the container orientation [31–34], quantity of PCM [35,36], heating rate and PCM melting temperature. Kandasamy et al. [23,37] reported a numerical and experimental investigation of cooling of electronics using PCM. The studies conducted a comparison of heat sinks with and without PCM and examined the effect of heating power level of a horizontal uniform heat source ranging from 2 to 6 W. It was shown that a PCM heat sink has a major effect in improving the cooling performance compared to a non-PCM heat sink. Fok et al. [38] concluded that using a PCM in a heat sink has two advantages compared to a non-PCM heat sink such as (i) the PCM heat sink maintains the electronics at a lower temperature compared to a non-PCM heat sink and (ii) the rate of temperature rise of PCM's heat sink is lower compared to a non-PCM heat sink during the absorption of latent heat.

The selection of the melting temperature of PCM is a key factor in designing an efficient PCM heat sink. Fan et al. [26] investigated the importance of selection of the PCM melting temperature in a horizontal heat sink arrangement with a heating source ranged between 60 to 120 W. The used PCMs were eircosane and hexadecanol. The study showed that a longer thermal regulation period (the duration for which the heat sink is maintained at low temperature) is achieved when using a higher melting temperature of PCM. However, the lower PCM melting temperature performs better in terms of reducing the maximum temperature in a short period. Mahmoud et al. [39] studied the PCM-based heat sink for a heating rate ranging from 3 to 5 W for six types of paraffin wax for a horizontal heat sink. The results showed that the maximum operating temperature was reduced by 10 °C when the PCM melting temperature reduced from 42 to 29 °C. Huang et al. [40] studied the effect of PCM melting temperature in thermal regulation of PV for a constant insolation of 750 W/m^2. The results indicated that using PCM with a melting temperature of 25 °C is better than PCM with a melting temperature of 43 °C in reducing the temperature by 15 °C for 150 min. Wang et al. [41] conducted a parametric study of the PCM heat sink, examining the effect of temperature difference between the heat source and the melting point of the PCMs on the heat sink performance. The results showed that the greater the temperature difference between the heat source and the PCM's melting temperature, the higher the melting speed. On the other hand, the PCMs with lower melting temperature reduced the heat sink temperatures, as concluded by Mahmoud et al. [39].

Also, the amount of PCM used in the heat sink plays an important role in the heat sink size, weight and cost. Arshad et al. [42] experimentally studied the effect of the PCM fraction in a horizontal PCM heat sink arrangement. The results showed that the fully filled heat sink with PCM performs better than the heat sink filled with PCM volume fractions of 0.33 and 0.66. Saha et al. [43] also examined experimentally and numerically the effect of PCM fraction for a similar type of PCM heat sink with heating rate ranging between 4 and 8 W. The study found that the heat sink performance was better when using a PCM fraction of 88% compared to a full PCM heat sink. Tomizawa et al. [44] studied the effect of PCM thickness in the cooling of mobile device applications. The results show that thicker PCM results in a longer operating period.

Using two PCMs in the heat sink is considered as a thermal conductivity enhancement technique as highlighted earlier, and very few works investigated this approach for electronics heat sink applications. Emam and Ahmed [45] studied numerically the effect of using three PCMs series cavities heat sink in concentrated photovoltaics (CPV) applications of 20 concentration ratio system. The selected PCM melting temperature range is between 22.5 to 29.8 °C. The results showed that medium-low-high PCM melting temperature arrangement is the best in terms of reducing the solar cell maximum temperature (average temperature of 106 °C) for an operating time of 120 min. In a similar study of using multiple PCMs heat sink in application of thermal regulation of solar cell, Huang [29] explored numerically two types of arrangements of two PCMs of triangular cells and semi-circular cells under actual operating conditions. The PCM melting temperature is ranging between 27 to 60 °C. The author concluded that higher-lower PCM melting temperature order achieves the highest

temperature drop during the daily operation. Shaikh and Lafdi [46] studied numerically the effect of multiple PCMs in different arrangements. The study has found that using composite PCMs with different melting temperatures can significantly enhance the total energy charged compared to single PCM.

Even though several investigations have been carried out to study the performance of the PCM heat sinks for electronics thermal regulation, few studies investigated two PCMs in a heat sink. Therefore, the aim of the present work is to experimentally investigate the effect of multiple-PCM heat sink, PCM thickness, melting temperature and intensity of heat source on the thermal behavior of a heat sink.

2. Experimental Setup and Procedure

The experimental setup is designed to identify the effect of different parameters mentioned above. Hence, four heat sinks (one no-PCM heat sink and three PCM heat sinks) have been manufactured to examine the effect of PCM, PCM thickness and the 2 PCM arrangements. The no PCM heat sink consists of a heat source attached to a metal plate. The other three PCM heat sinks are denoted by A, B and C and are made up of clear acrylic to monitor the PCM melting profile with inner dimensions of $30 \times 30 \times 30$ mm, $60 \times 30 \times 30$ mm and $62 \times 30 \times 30$ mm, respectively, as shown in Figure 1. Heat sinks A and B (Figure 1a) have one cavity to be filled with one type of PCM. Heat sink C (Figure 1b) has two cavities and thus to be filled with two different types of PCMs of sizes $30 \times 30 \times 30$ mm each. The two cavities are separated using a 2 mm thick aluminum plate. An aluminum plate of 2 mm thickness has been fixed on one side of the container for heating the PCM and insulated thermally using polystyrene. The experimental setup is shown in Figure 1c.

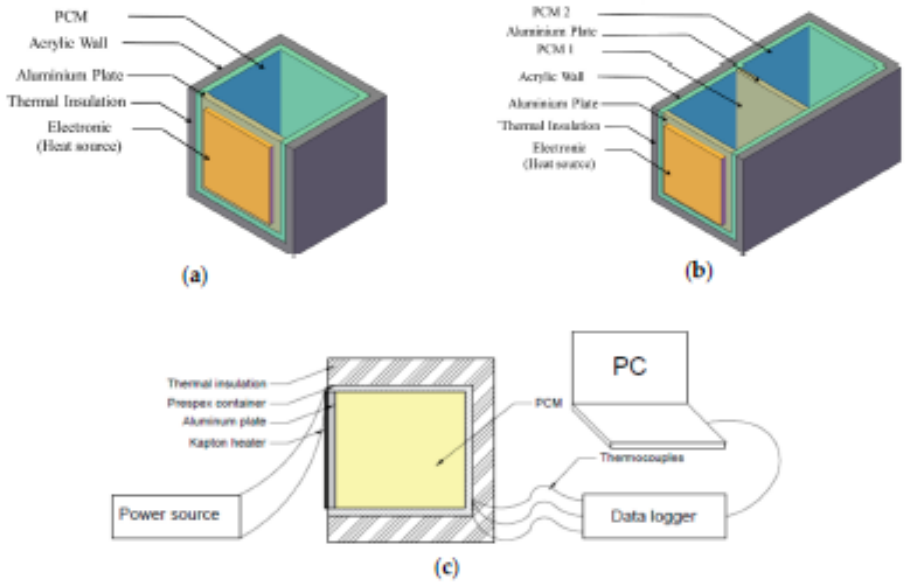

Figure 1. Schematic of the (**a**) heat sink A&B, (**b**) heat sink C and (**c**) experimental setup. PCM: phase change material.

An electrical flexible heater (Omega KHLV, OMEGA Engineering INC., Norwalk, CT, USA) has been used to simulate the generated heat by electronics. Different heating power ratings have been used through DC power supply by varying the voltage.

K type thermocouples are used for the temperature measurements. The thermocouples are fixed inside the container to measure the PCM temperature distribution across the container and also the aluminum plate temperature. The thermocouple T1 is placed on the middle of the inner surface of the aluminum plate to measure the heater temperature as shown in Figure 2. The thermocouples from

T2 to T5 are placed to measure the temperature of the PCM along the direction of the heat flow and are located 15 mm apart. A thermocouple (T6) is kept outside to measure the ambient temperature. The temperature measurements are recorded with an interval of 5 s using data acquisition system (OMEGA RDXL 12 SD, OMEGA Engineering INC., Norwalk, CT, USA). A digital camera has been used to capture images of the heat sink with a time interval of 20 min to observe the melting profile of the PCM. The thermocouples have been calibrated using the ambient temperature and the boiling water temperature (100 °C). The error in the temperature measurement is found to be less than 0.4% using a standard thermometer having a reading resolution of 0.1 °C.

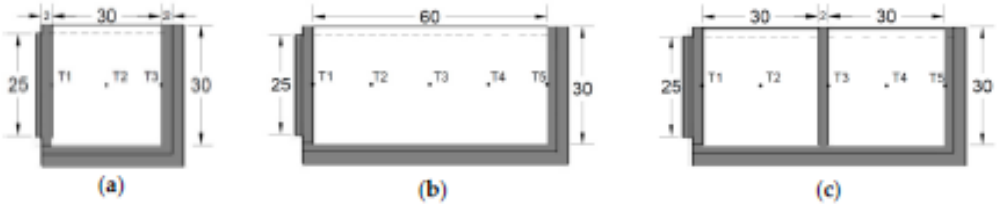

Figure 2. Thermocouple positions and dimensions of heat sinks, (**a**) A; (**b**) B and (**c**) C.

In order to analyze the effect of PCM melting temperature on the performance of heat sink, RT46, RT49, RT52, RT55 and RT58 with melting temperature of 46 °C, 49 °C, 52 °C, 55 °C and 58 °C, respectively, are used which have same latent heat capacity (170 kJ/kg), density in liquid-phase (770 kg/m^3), density in solid-phase (880 kg/m^3) and thermal conductivity (0.2 W/mK). To fill the PCM container, the PCM was melted initially. Then, the melted PCM was poured into the container. Before starting each experiment, it is made sure that the PCM is obtained at its initial temperature equal to the ambient value.

3. Results and Discussion

3.1. Comparison of Heat Sink with and without PCM

The heat sinks have been tested with and without PCM filled in the containers. The temperature measurements have been recorded until the steady state conditions were reached. It has been found that the heat sink temperature (without PCM) increased rapidly and the temperature during steady state reached 66 °C, 109 °C and 133 °C for power ratings of 1.0 W, 1.5 W and 2.0 W, respectively. This rapid increase in temperature in electronic devices is not desired and affects their performance.

Figure 3 shows a comparison between the heat sink temperature during the thermal regulation period for heat sink filled with PCM (RT47) and without PCM. The heat sink temperature is markedly decreased compared to no PCM heat sink by 10.8 °C, 50.1 °C and 69.8 °C for 1.0, 1.5 and 2.0 W power ratings, respectively. The temperature drop (achieved using PCM) increases as the power rating increases. The results also show that the duration of thermal regulation is inversely proportional to the heater power for the same amount of PCM.

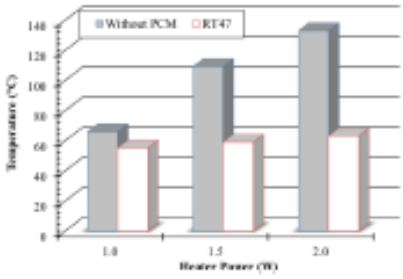

Figure 3. Comparison between PCM and no PCM heat sink temperatures for three different power ratings.

3.2. Effect of Heater Power Rating

To study the effect of power rating, heat sink A has been filled with RT47 PCM and heated up through 1.0 W, 1.5 W and 2 W power, and the surface temperature for different ratings is shown in Figure 4. The heater has been operated for 210 min in all the experiments. The PCM is not fully melted and the maximum heat sink surface temperature is 56.8 °C at 1.0 W power rating. It can be observed that during latent heat absorption, PCM keeps the heat sink temperature constant. However, the heat sink temperature in this area is much higher than the PCM melting temperature and this should be taken into consideration in designing PCM heat sinks. Also, the thermal regulation period significantly decreases as the power rating increases from 1.0 to 2.0 W. By the end of the charging period, the heat sink surface temperature becomes constant for all the power ratings.

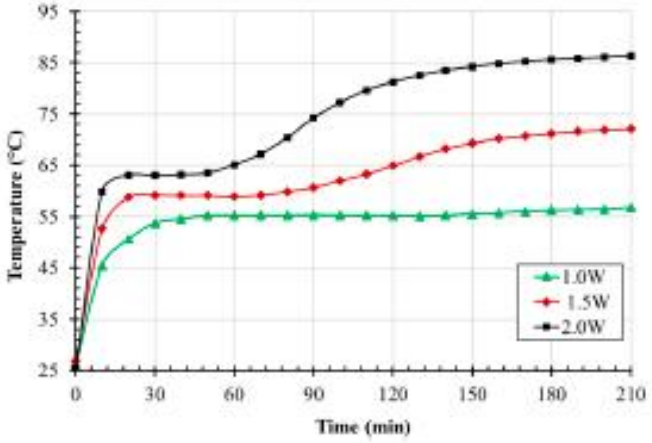

Figure 4. Heat sink surface temperature using RT47 for three different power ratings.

The PCM melting pattern (Figure 5) is defined as the shape of the two phases of the PCM during the melting process. It is considered an important measure in any thermal storage system because it indicates the heat transfer behavior of the system. Figure 5 shows the melting profile for RT47 for different power ratings at 20 min time interval. The general melting profiles of all the power ratings are the same for all PCMs. It is observed that the PCM near to the heat source melts faster and the solid PCM displaces downward and the liquid PCM is pushed upward resulting the curved PCM shape.

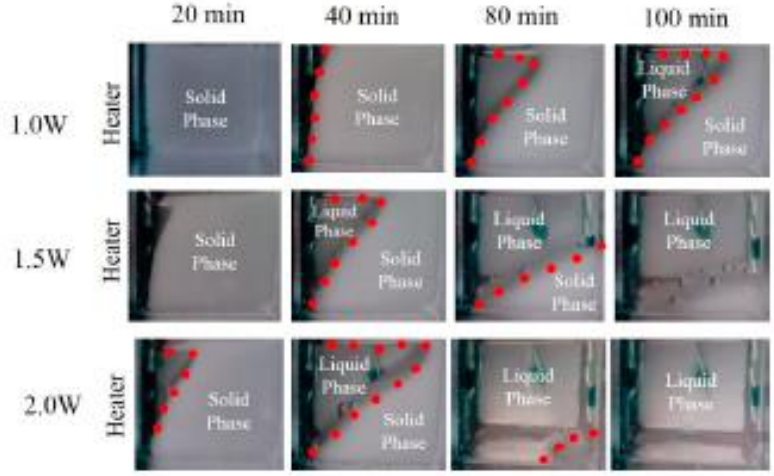

Figure 5. Images of RT47 melting profile for different power rating and time.

The effect of PCM thermal conductivity on the melting of PCM is explored by studying the temperature distribution across the heat sink as shown in Figure 6. It is noted that the heat sink temperature at front (T1) increases faster than the PCM located at the middle (T2) and the rear (T3) of the heat sink at the beginning of the operation. This is due to the low thermal conductivity of the PCM which causes a huge temperature difference between T1 and the other two temperature points and leads to delay in the melting of the PCM at rear as compared to PCM at front. It must also be noted that the high latent heat capacity also leads to delay in complete melting. As an example, the PCM with latent heat capacity of 245 kJ/kg takes three times longer for complete melting as compared to PCM with latent heat capacity of 110 kJ/kg [47].

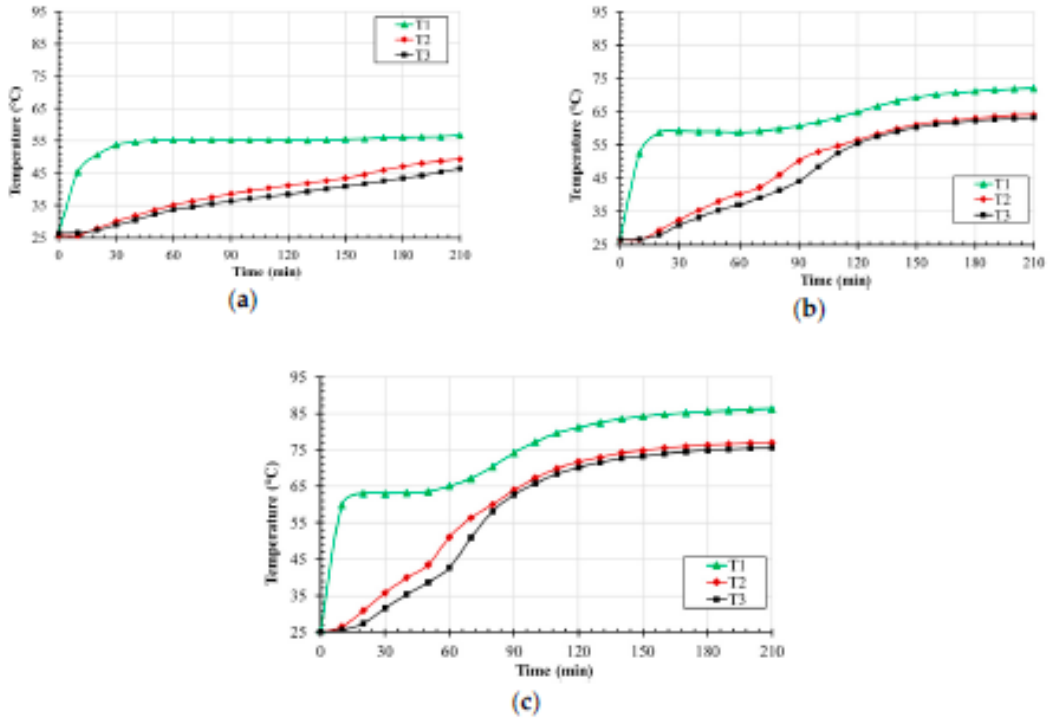

Figure 6. Temperature distribution across the heat sink A for RT47 at power rating, (**a**) 1.0 W, (**b**) 1.5 W and (**c**) 2.0 W.

3.3. *Effect of PCM Melting Temperature*

In order to study the effect of PCM melting temperature on the heat sink thermal regulation, different PCMs have been examined. Heat sink A has been used and tested for 3.5 h. The tested PCMs are RT47, RT52, and RT58 with melting temperatures of 47 °C, 52 °C and 58 °C, respectively. Figure 7 shows the heat sink surface temperature (T1) for 1.0, 1.5 W and 2.0 W power ratings for RT47, RT52 and RT58. The results show that the heat sink thermal regulation temperature of RT47 is lower than those of RT52 and RT58. This is because RT47 PCM starts melting earlier than the other two PCMs and starts absorbing heat in latent form. The thermal regulation period for RT47 is shorter compared to those of RT52 and RT58. For 2.0 W, the thermal regulation periods for RT47, RT52 and RT58 are 50, 60 and 90 min, respectively. Therefore, RT47 is suitable to reduce the heat sink maximum temperature for 2.0 W power rating if the charging time is less than 50 min. Also, RT58 is able to reduce slightly the heat sink temperature by the end of the testing period compared to RT47 and RT52 for the power ratings of 1.5 W due to incomplete melting of RT58.

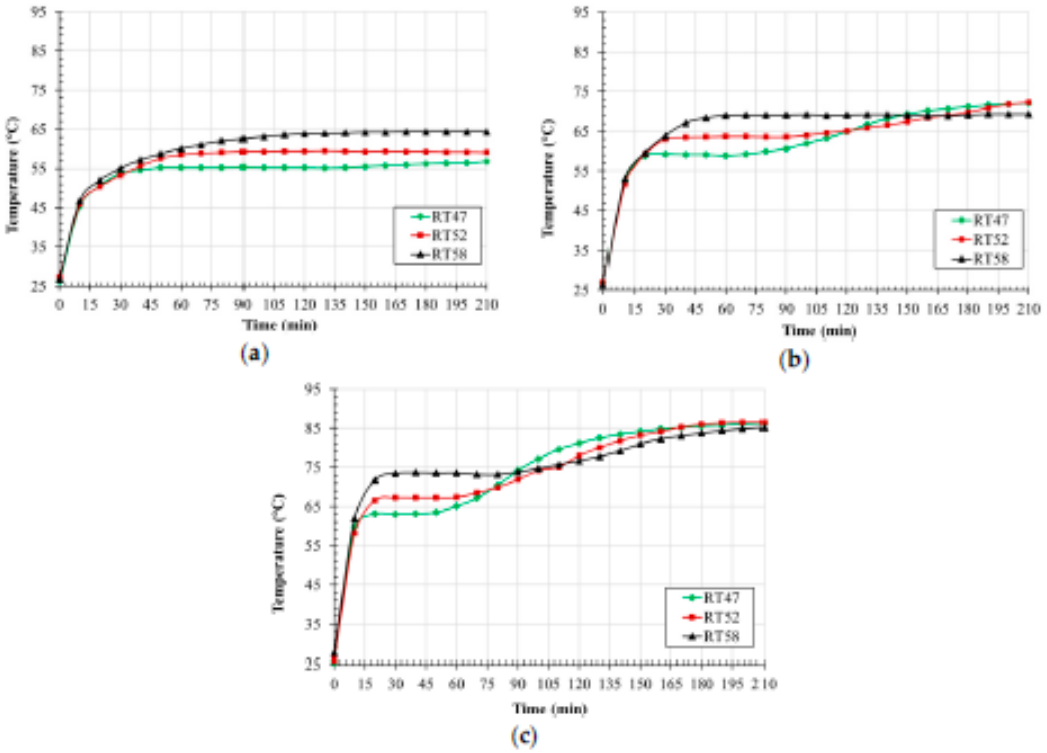

Figure 7. Surface temperature for heat sink A at power rating, (**a**) 1.0 W, (**b**) 1.5 W and (**c**) 2.0 W.

The two most important criteria to design a heat sink for cooling electronics are the thermal regulation temperature during the phase change and the heat sink temperature by the end of the charging period (maximum temperature). These temperature values are summarized in Table 1 for different PCMs and power ratings. For 1.5 W, the maximum heat sink temperature is reduced by about 5 °C by using RT58 instead of RT47. The complete melting of the PCM should be ensured by the end of the charging process for perfect utilization of the PCM.

Table 1. Heat sink temperature during heat charging.

PCM Type	Heat Sink Temperature at the Phase Change (°C)			Heat Sink Temperature at the End of Charging (210 min) °C		
	Power Rating			Power Rating		
	1.0 W	1.5 W	2.0 W	1.0 W	1.5 W	2.0 W
RT47	55.2	59.0	63.0	56.8	72.3	86.3
RT50	60.1	62.3	64.9	60.3	75.0	86.0
RT52	59.3	63.6	67.3	59.3	74.4	87.0
RT55	62.0	65.0	67.4	62.0	72.3	85.3
RT58	64.4	69.0	73.6	64.4	69.0	84.5

The melting profiles of different PCMs using 1.5 W power rating at 20 min interval are shown in Figure 8. By the end of the first 20 min, RT47 and RT52 have started melting and no melting has been noticed for RT58. By 100 min of charging, all the PCMs adjacent to the heater have melted completely and RT47 has melted faster than the other two types of PCMs.

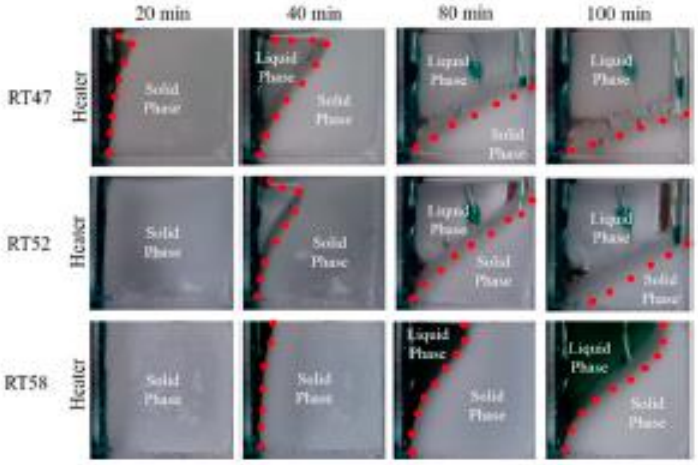

Figure 8. Melting profiles images for various PCMs at different time and 1.5 W heat input.

3.4. *Effect of PCM Thickness on Heat Sink Temperature*

The PCM thickness is an important parameter to investigate as it determines the heat sink size and its effect has been investigated using heat sink A (30 mm thick) and heat sink B (60 mm thick). Figures 9 and 10 show the effect of the PCM thickness in the heat sink temperature for RT47 and RT58, respectively. As expected, the PCM is able to maintain the heat sink at lower temperature for longer duration as the PCM thickness increased. Hence, a longer thermal regulation period is expected for the electronics for a thicker PCM. As shown in Figure 9, the PCM thickness has no effect on reducing the maximum heat sink surface temperature for 1.0 and 1.5 W whereas the maximum heat sink surface temperature has been increased by 8 °C for the 2.0 W power rating.

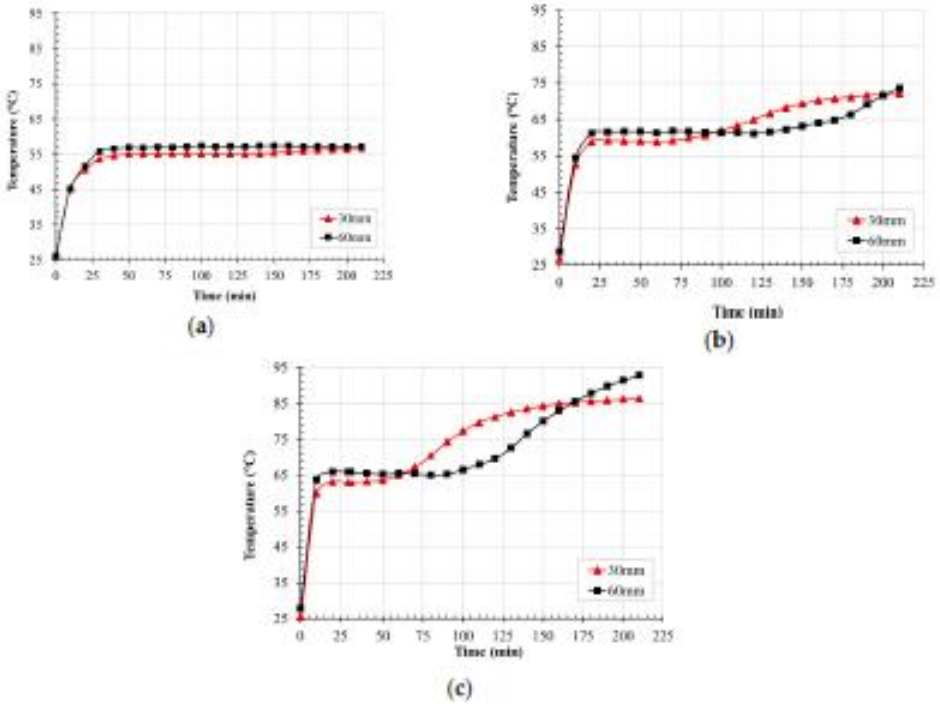

Figure 9. Heat sink surface temperature using RT47 for different thicknesses at power ratings (**a**) 1.0 W, (**b**) 1.5 W and (**c**) 2.0 W.

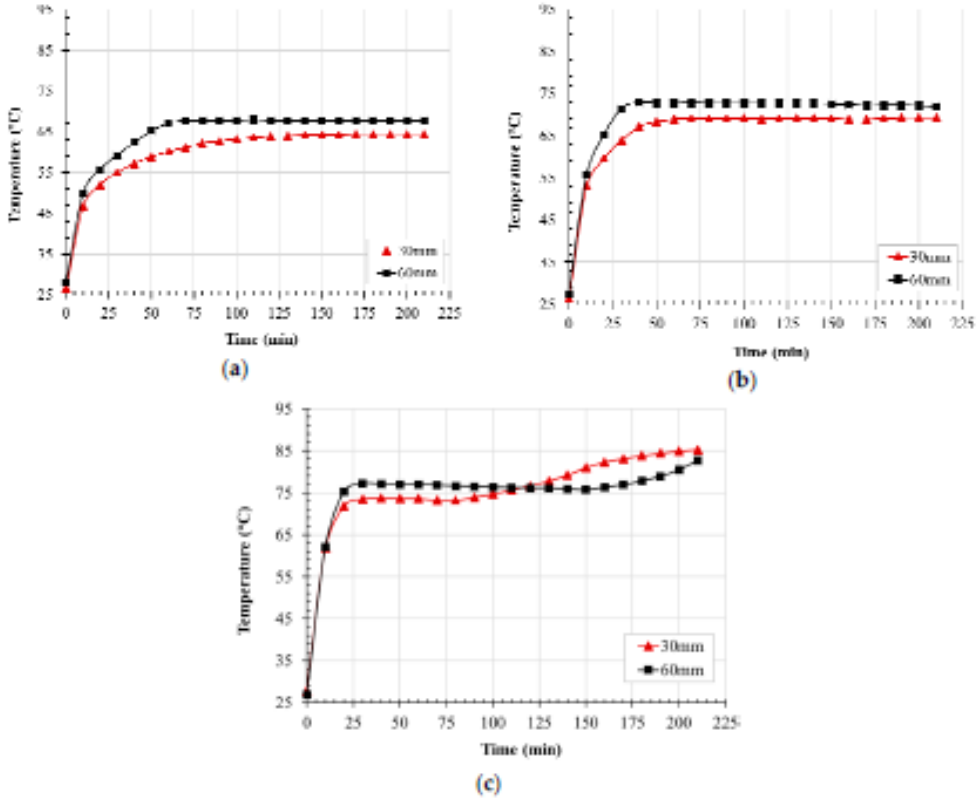

Figure 10. Heat sink surface temperature of RT58 for different thickness at power ratings (**a**) 1.0 W, (**b**) 1.5 W and (**c**) 2.0 W.

The temperature distribution across heat sink B is shown in Figure 11. It is clearly shown that the heat sink temperature at front (T1) increases rapidly as compared to the temperature at middle and rear due to the PCM low thermal conductivity which causes the heat transfer at lower rate from front to rear of the heat sink. Also, by the end of the melting process, the PCM temperatures are same for all locations as shown for 1.5 and 2.0 W. In addition, the temperature differences after the melting process between the heat sink and the PCM temperatures at the other locations are 8.2 °C and 9.4 °C for 1.5 W and 2.0 W, respectively.

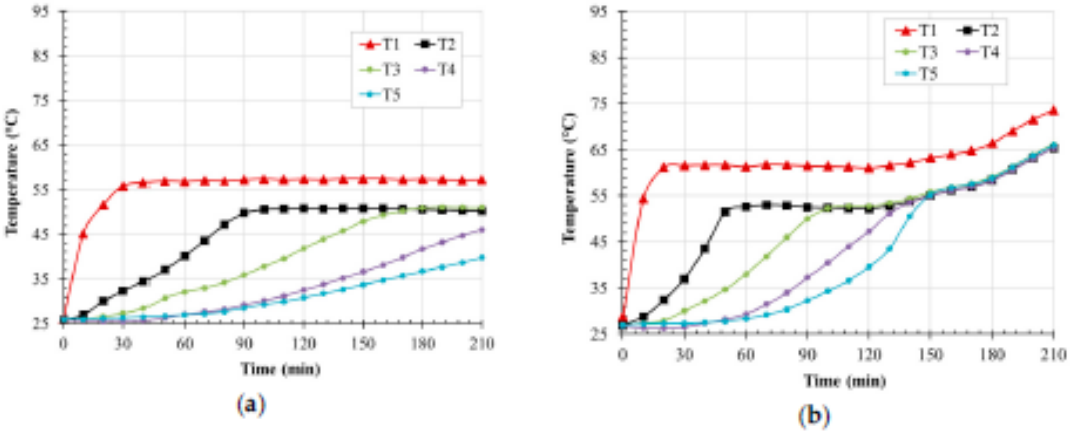

Figure 11. *Cont.*

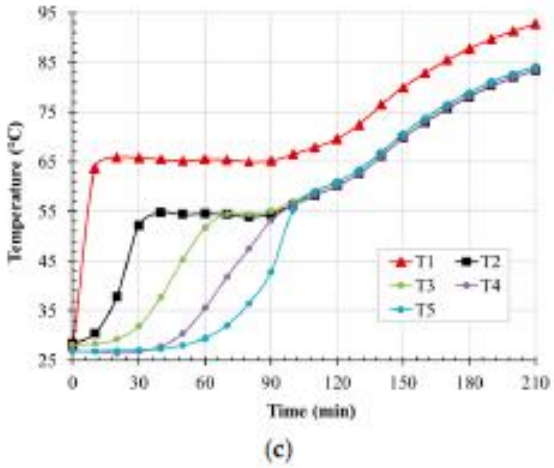

Figure 11. Temperature distribution across heat sink B for RT47 at power ratings (**a**) 1.0 W, (**b**) 1.5 W and (**c**) 2.0 W.

3.5. Effect of Using Two PCMs on Heat Sink Temperature

The effect of using two PCMs with different melting temperatures has been investigated in this section using heat sink C. The PCM with a lower melting temperature is placed in the cavity nearer to the heat source. Figure 12 shows the heat sink surface temperature versus time for two cases (a) single PCM and (b) two PCMs for the same amount of PCM for 1.0 W and 2.0 W power ratings. For the 1.0 W power rating, the heat sink temperature for RT50 and RT50–RT55 has the same thermal regulation temperature (61.4 °C) whereas the heat sink temperature is 65 °C when using RT55.

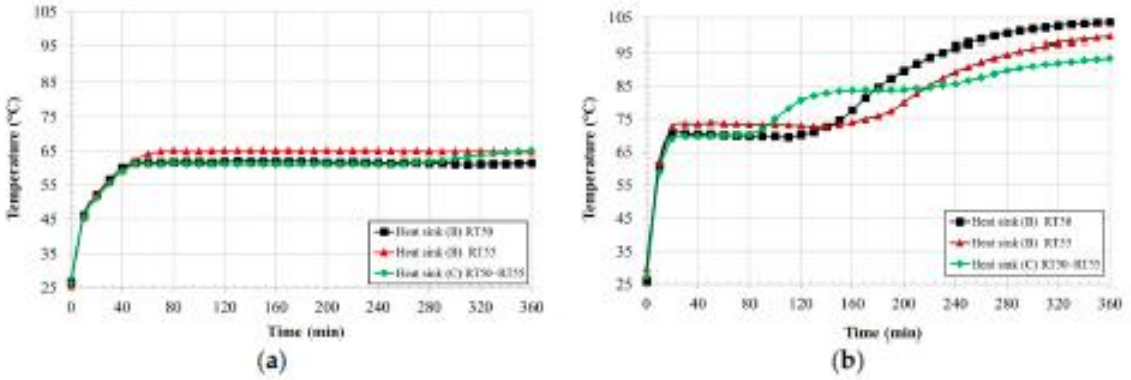

Figure 12. Surface heat sink temperature of one and two PCM heat sinks for different PCMs at power rating of, (**a**) 1.0 W and (**b**) 2.0 W.

For the 2.0 W power rating, two thermal regulation temperatures are observed at 70.1 °C and 83.0 °C in the case of RT50–RT55. The second thermal regulation period temperature is higher than the RT55 thermal regulation temperature. This can be referred to the low thermal conductivity of the PCM, and the first PCM increases the heat sink temperature after the complete melting. Also, it can be observed that during the 6 h of heat charging, the maximum heat sink temperature was reduced when using the two PCM arrangement and its maximum for RT50, RT55 and RT50–RT55 is 103.6 °C, 99.4 °C and 93.3 °C, respectively.

In order to verify the two thermal regulation periods for the two PCMs system, lower melting temperature PCMs have been selected: RT47, RT50 and RT47–RT50 as shown in Figure 13. For the 1.0 W power rating, RT47 is more effective in thermal regulation than RT50 and RT47–RT50 during the

6 h of heat charging. However, for the 2.0 W power rating, RT47–RT50 is able to slightly reduce the heat sink maximum temperature for the charging period between 160 and 320 min.

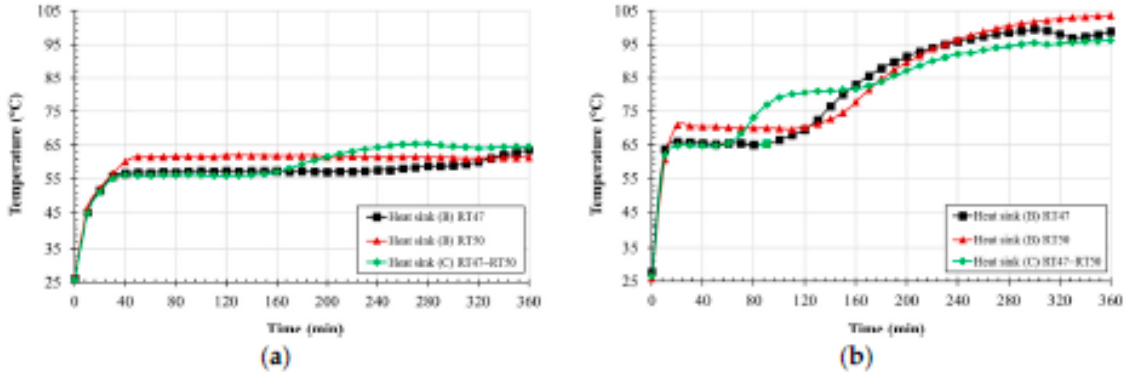

Figure 13. Heat sink surface temperature of one and two PCM heat sinks at power rating, (**a**) 1.0 W and (**b**) 2.0 W.

Exchanging the arrangement of the two PCMs to examine their effect has been investigated. Therefore, the PCM with a higher melting temperature is placed in the cavity nearer to the heat source. For the 1.5 W power rating, the heat sink temperature for RT47–RT58 is considerably lower than that of RT58–RT47 during the thermal regulation period (between 20 min and 140 min) as shown in Figure 14. After 140 min, the heat sink temperature is lower for the case of RT58–RT47. For the 2.0 W power rating, RT58–RT47 has a longer thermal regulation period in the time duration between 84 and 240 min of charging, and no change in the heat sink temperature is observed by the end of the operation.

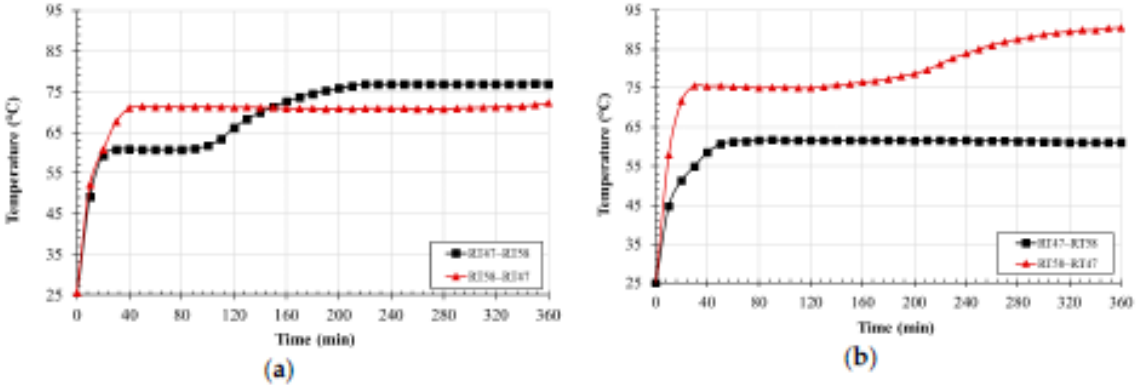

Figure 14. Heat sink surface temperature of heat sink C for different PCMs at power ratings (**a**) 1.5 W and (**b**) 2.0 W.

4. Conclusions

An experimental investigation of a PCM heat sink for electronic thermal regulation applications has been explored. The effect of the PCM heat sink has been compared to a non-PCM heat sink. Also, the variation of PCM thickness, melting temperature and the two PCM concept have been studied in this work for power ratings ranging between 1.0 W to 2.0 W. The variations in the heat sink temperature and the PCM melting profile with time have been used to analyze the system performance. The following is concluded from this work:

- Two PCM techniques with arrangement of RT50–RT55 increases the thermal regulation period by 110 min and 130 min as compared to RT50 and RT55, respectively. Using RT50–RT55, the heat sink temperature at the end of the operation is reduced by 10.3 °C and 6.1 °C as compared to RT50 and RT55, respectively, for 2.0 W.
- Two PCMs with the arrangement of RT58-RT47 reduces slightly the maximum temperature as compared to RT47–RT58.
- As PCM thickness increases from 30 to 60 mm, the thermal regulation period increases by 50 min and 35 min for 1.5 W and 2.0 W power ratings, respectively. As the PCM melting temperature increases from 47 (RT47) to 58 °C (RT58), the thermal regulation period increases from 30 to 70 min for 2.0 W. However, the heat sink temperature also increases from 63 to 74 °C.
- The thermal regulation period significantly decreases as power rating increases from 1 to 2 W. Also, the heat sink temperature increases by 29.5 °C with an increase in power rating.

Author Contributions: I.A.S. conceived, designed and performed the experiments; I.A.S. and S.K. analyzed the data; I.A.S. wrote the paper, S.K., T.M. and S.S. reviewed the paper and supervised I.A.S. research work.

Funding: Idris Al Siyabi's PhD is funded by the Ministry of Higher Education of the Sultanate of Oman as part of the national program of postgraduate scholarships.

Conflicts of Interest: The authors declare no conflict of interest.

References

1. Etemoglu, A.B. A brief survey and economical analysis of air cooling for electronic equipments. *Int. Commun. Heat Mass Transf.* **2007**, *34*, 103–113. [CrossRef]
2. Yeh, L.T. Review of heat transfer technologies in electronic equipment. *J. Electron. Packag.* **1995**, *117*, 333–339. [CrossRef]
3. Alawadhi, E.M.; Amon, C.H. PCM thermal control unit for portable electronic devices: Experimental and numerical studies. *IEEE Trans. Compon. Packag. Technol.* **2003**, *26*, 116–125. [CrossRef]
4. Faraji, M.; El Qamia, H. Passive Cooling of Protruding Electronic Components by Latent Heat of Fusion Storage. *ASME J. Electron. Packag.* **2009**, *131*, 021011. [CrossRef]
5. Jaworski, M. Thermal performance of heat spreader for electronics cooling with incorporated phase change material. *Appl. Therm. Eng.* **2012**, *35*, 212–219. [CrossRef]
6. Kandlikar, S.G.; Ii, C.N.H. Liquid Cooled Cold Plates for Industrial High- Power Electronic Devices—Thermal Design and Manufacturing Considerations Liquid Cooled Cold Plates for Industrial High-Power Electronic Devices—Thermal Design and Manufacturing Considerations. *Heat Transf. Energy* **2011**, *30*, 918–930. [CrossRef]
7. Zhu, L.; Boehm, R.F.; Wang, Y.; Halford, C.; Sun, Y. Water immersion cooling of PV cells in a high concentration system. *Sol. Energy Mater. Sol. Cells* **2011**, *95*, 538–545. [CrossRef]
8. Tardy, F.; Sami, S.M. Thermal analysis of heat pipes during thermal storage. *Appl. Therm. Eng.* **2009**, *29*, 329–333. [CrossRef]
9. Vandersande, J.W.; Fleurial, J.-P. Thermal Management of Power Electronics using Thermoelectric Coolers. In Proceedings of the Fifteenth International Conference on Thermoelectrics, Pasadena, CA, USA, 26–39 March 1996; pp. 252–255.
10. Ohadi, M.; Choo, K.; Dessiatoun, S.; Cetegen, E. *Next Generation Microchannel Heat Exchangers*; Springer: Berlin, Germany, 2013; ISBN 978-1-4614-0778-2.
11. Farid, M.M.; Khudhair, A.M.; Razack, S.A.K.; Al-Hallaj, S. A review on phase change energy storage: Materials and applications. *Energy Convers. Manag.* **2004**, *45*, 1597–1615. [CrossRef]
12. Ge, Z.; Li, Y.; Li, D.; Sun, Z.; Jin, Y.; Liu, C.; Li, C.; Leng, G.; Ding, Y. Thermal energy storage: Challenges and the role of particle technology. *Particuology* **2014**, *15*, 2–8. [CrossRef]
13. Ma, T.; Yang, H.; Zhang, Y.; Lu, L.; Wang, X. Using phase change materials in photovoltaic systems for thermal regulation and electrical efficiency improvement: A review and outlook. *Renew. Sustain. Energy Rev.* **2015**, *43*, 1273–1284. [CrossRef]

14. Sharma, A.; Tyagi, V.V.; Chen, C.R.; Buddhi, D. Review on thermal energy storage with phase change materials and applications. *Renew. Sustain. Energy Rev.* **2009**, *13*, 318–345. [CrossRef]
15. Humphries, W.; Griggs, E. *A Design Handbook for Phase Change Thermal Control and Energy Storage Devices*; NASA Technical Paper; NASA: Buffalo, NY, USA, 1977.
16. Hasan, A.; Alnoman, H.; Shah, A. Energy Efficiency Enhancement of Photovoltaics by Phase Change Materials through Thermal Energy Recovery. *Energies* **2016**, *9*, 782. [CrossRef]
17. Hasan, A.; McCormack, S.J.; Huang, M.J.; Norton, B. Energy and cost saving of a photovoltaic-phase change materials (PV-PCM) System through temperature regulation and performance enhancement of photovoltaics. *Energies* **2014**, *7*, 1318–1331. [CrossRef]
18. Krishnan, S.; Garimella, S.V. Thermal Management of Transient Power Spikes in Electronics—Phase Change Energy Storage or Copper Heat Sinks? *J. Electron. Packag.* **2004**, *126*, 308. [CrossRef]
19. Tan, F.L.; Tso, C.P. Cooling of mobile electronic devices using phase change materials. *Appl. Therm. Eng.* **2004**, *24*, 159–169. [CrossRef]
20. Hodes, M.; Weinstein, R.D.; Pence, S.J.; Piccini, J.M.; Manzione, L.; Chen, C. Transient Thermal Management of a Handset Using Phase Change Material (PCM). *J. Electron. Packag.* **2002**, *124*, 419. [CrossRef]
21. Lafdi, K.; Mesalhy, O.; Elgafy, A. Merits of Employing Foam Encapsulated Phase Change Materials for Pulsed Power Electronics Cooling Applications. *J. Electron. Packag.* **2008**, *130*, 021004. [CrossRef]
22. Saha, S.K. Cooling of Electronics with Phase Change Materials under Constant Power and Cyclic Heat Loads. *AIP Conf. Proc.* **2009**, *31*. [CrossRef]
23. Kandasamy, R.; Wang, X.-Q.; Mujumdar, A.S. Application of phase change materials in thermal management of electronics. *Appl. Therm. Eng.* **2007**, *27*, 2822–2832. [CrossRef]
24. Weinstein, R.D.; Kopec, T.C.; Fleischer, A.S.; D'Addio, E.; Bessel, C.A. The Experimental Exploration of Embedding Phase Change Materials With Graphite Nanofibers for the Thermal Management of Electronics. *J. Heat Transf.* **2008**, *130*, 042405. [CrossRef]
25. Khanna, S.; Reddy, K.S.; Mallick, T.K. Climatic behaviour of solar photovoltaic integrated with phase change material. *Energy Convers. Manag.* **2018**, *166*, 590–601. [CrossRef]
26. Fan, L.W.; Xiao, Y.Q.; Zeng, Y.; Fang, X.; Wang, X.; Xu, X.; Yu, Z.T.; Hong, R.H.; Hu, Y.C.; Cen, K.F. Effects of melting temperature and the presence of internal fins on the performance of a phase change material (PCM)-based heat sink. *Int. J. Therm. Sci.* **2013**, *70*, 114–126. [CrossRef]
27. Thapa, S.; Chukwu, S.; Khaliq, A.; Weiss, L. Fabrication and analysis of small-scale thermal energy storage with conductivity enhancement. *Energy Convers. Manag.* **2014**, *79*, 161–170. [CrossRef]
28. Baby, R.; Balaji, C. Experimental investigations on thermal performance enhancement and effect of orientation on porous matrix filled PCM based heat sink. *Int. Commun. Heat Mass Transf.* **2013**, *46*, 27–30. [CrossRef]
29. Huang, M.J. The effect of using two PCMs on the thermal regulation performance of BIPV systems. *Sol. Energy Mater. Sol. Cells* **2011**, *95*, 957–963. [CrossRef]
30. Jegadheeswaran, S.; Pohekar, S.D. Performance enhancement in latent heat thermal storage system: A review. *Renew. Sustain. Energy Rev.* **2009**, *13*, 2225–2244. [CrossRef]
31. Wang, X.Q.; Mujumdar, A.S.; Yap, C. Effect of orientation for phase change material (PCM)-based heat sinks for transient thermal management of electric components. *Int. Commun. Heat Mass Transf.* **2007**, *34*, 801–808. [CrossRef]
32. Khanna, S.; Reddy, K.S.; Mallick, T.K. Performance analysis of tilted photovoltaic system integrated with phase change material under varying operating conditions. *Energy* **2017**, *133*, 887–899. [CrossRef]
33. Avci, M.; Yazici, M.Y. An experimental study on effect of inclination angle on the performance of a PCM-based flat-type heat sink. *Appl. Therm. Eng.* **2018**, *131*, 806–814. [CrossRef]
34. Poran, S.; Ahmed, D.H. Effect of cavity shape and heat source/sink orientation on PCM melting. *J. Therm. Energy Syst.* **2018**, *3*, 1–22.
35. Khanna, S.; Reddy, K.S.; Mallick, T.K. Optimization of solar photovoltaic system integrated with phase change material. *Sol. Energy* **2018**, *163*, 591–599. [CrossRef]
36. Khanna, S.; Reddy, K.S.; Mallick, T.K. Optimization of finned solar photovoltaic phase change material (finned pv pcm) system. *Int. J. Therm. Sci.* **2018**, *130*, 313–322. [CrossRef]
37. Kandasamy, R.; Wang, X.Q.; Mujumdar, A.S. Transient cooling of electronics using phase change material (PCM)-based heat sinks. *Appl. Therm. Eng.* **2008**, *28*, 1047–1057. [CrossRef]

38. Fok, S.C.; Shen, W.; Tan, F.L. Cooling of portable hand-held electronic devices using phase change materials in finned heat sinks. *Int. J. Therm. Sci.* **2010**, *49*, 109–117. [CrossRef]
39. Mahmoud, S.; Tang, A.; Toh, C.; AL-Dadah, R.; Soo, S.L. Experimental investigation of inserts configurations and PCM type on the thermal performance of PCM based heat sinks. *Appl. Energy* **2013**, *112*, 1349–1356. [CrossRef]
40. Huang, M.J.; Eames, P.C.; Norton, B. Phase change materials for limiting temperature rise in building integrated photovoltaics. *Sol. Energy* **2006**, *80*, 1121–1130. [CrossRef]
41. Wang, X.Q.; Yap, C.; Mujumdar, A.S. A parametric study of phase change material (PCM)-based heat sinks. *Int. J. Therm. Sci.* **2008**, *47*, 1055–1068. [CrossRef]
42. Arshad, A.; Ali, H.M.; Ali, M.; Manzoor, S. Thermal performance of phase change material (PCM) based pin-finned heat sinks for electronics devices: Effect of pin thickness and PCM volume fraction. *Appl. Therm. Eng.* **2017**, *112*, 143–155. [CrossRef]
43. Saha, S.K.; Srinivasan, K.; Dutta, P. Studies on optimum distribution of fins in heat sinks filled with phase change materials. *J. Heat Transf.* **2008**, *130*, 034505. [CrossRef]
44. Tomizawa, Y.; Sasaki, K.; Kuroda, A.; Takeda, R.; Kaito, Y. Experimental and numerical study on phase change material (PCM) for thermal management of mobile devices. *Appl. Therm. Eng.* **2016**, *98*, 320–329. [CrossRef]
45. Emam, M.; Ahmed, M. Cooling concentrator photovoltaic systems using various configurations of phase-change material heat sinks. *Energy Convers. Manag.* **2018**, *158*, 298–314. [CrossRef]
46. Shaikh, S.; Lafdi, K. Effect of multiple phase change materials (PCMs) slab configurations on thermal energy storage. *Energy Convers. Manag.* **2006**, *47*, 2103–2117. [CrossRef]
47. Soares, N.; Gaspar, A.R.; Santos, P.; Costa, J.J. Experimental study of the heat transfer through a vertical stack of rectangular cavities filled with phase change materials. *Appl. Energy* **2015**, *142*, 192–205. [CrossRef]

Case study 2: Thermal regulation of building-integrated concentrating photovoltaic system using phase change material

Thermal Regulation of Building-Integrated Concentrating Photovoltaic System using Phase Change Material

Idris Al Siyabi[1, *], Shivangi Sharma[1], Tapas K. Mallick[1] and Senthilarasu Sundaram[1]

[1]*Enviroment and Sustainability Institute, University of Exeter, Penryn Campus, Cornwall TR109FE, UK*

*Corresponding author: ia257@exeter.ac.uk

Abstract. Thermal regulation of building-integrated concentrating photovoltaic (BICPV) systems have a direct influence on the photovoltaic performance. This paper investigates the thermal behavior of a BICPV and phase change material (PCM) system through numerical modeling simulations. Based on an updated mathematical model, theoretical simulation has been conducted for a BICPV-PCM system. The results show a 3% electrical efficiency improvement of the BICPV-PCM system in certain cases.

INTRODUCTION

Concentrated photovoltaic (CPV) technology has attracted a considerable amount of research focus, and is in the early stages of commercialization. The electrical generation of installed CPV systems has increased rapidly from 2MW in 2007 to around 1800 MW in 2015[1].

CPV technology concentrates solar irradiation into a small spot as shown in figure 1, which allows more radiation on the solar cell to be harvested compared to non-concentrated systems. Thus, CPV technology has the advantage of requiring less cell area and fewer materials than conventional photovoltaic.

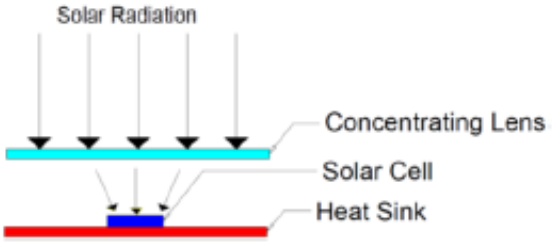

FIGURE 1. Typical CPV system arrangement.

The concentrated solar radiation that is received by the solar cell is reflected, transmitted (through the solar cell) or absorbed. The amounts of reflected and transmitted solar radiation are very small as compared to that which is absorbed. The level of absorption varies according to the band gap of the semiconductor, with only an estimated 16% of the solar energy received by the solar cell being used to generate electricity. The remaining 84% is converted into heat[2].

Integration of renewable energy resources into buildings and improving energy efficiency reduce the energy utilization within buildings and increase sustainability. Building integrated concentrated photovoltaic (BICPV) systems offer advantages over conventional building integrated photovoltaics by improving electrical conversion, reducing heat loss and requiring less space. The BICPV system consists of optical concentrators, a photovoltaic

12th International Conference on Concentrator Photovoltaic Systems (CPV-12)
AIP Conf. Proc. 1766, 090001-1–090001-8; doi: 10.1063/1.4962107
Published by AIP Publishing. 978-0-7354-1424-2/$30.00

receiver and a heat sink. A tracking mechanism is not recommended for low concentration photovoltaics (LCPV) due to high capital, operation and maintenance costs. Conventional crystalline silicon photovoltaics are more common in low concentration levels due to their low cost and reasonable performance.

As mentioned earlier, the PV is exposed to high temperatures in a CPV system due to the higher concentration of solar radiation. This excessive heat in the solar cell must be removed to avoid efficiency drop, rapid cell efficiency degradation or even permanent cell damage. There are two different approaches to cool the solar cells: passive or active. The passive approach uses natural phenomena such as conduction and convection to cool the solar cell. This is a valuable cooling technique due to its low capital , operation and maintenance costs [1]. The active approach uses mechanical means such as pumps or fans to circulate the cooled fluid (Water or Air) into the system. This is considered very efficient. The extracted heat from the CPV can be used for domestic heating. However, active cooling is complicated, more costly in terms of construction, operation and maintenance. More detail on cooling concentrated photovoltaic systems can be found in [4].

Phase change material (PCM) is a passive approach to photovoltaic thermal regulation that has been studied widely. The main characteristic of PCM is high latent heat capacity. This feature enables the materials to absorb heat during the phase change stage. In a typical PV-PCM application, the phase change materials container is attached at the back of the PV system.

In this article we have reported the effect of phase change materials on BICPV performance and its potential to regulate photovoltaic temperature. A BICPV-PCM system has been modeled and simulated using a Multiphysics engineering software package. A parametric study has been conducted for the ambient temperature effect.

NUMERICAL APPROACH

Model Case Description

The modeled BICPV-PCM system (figure 2) consists of 5 Laser Grooved Buried Contact (LGBC) crystalline silicon cells. Each solar cell is 116mm long and 6 mm wide. The solar cells are connected electrically in series with highly conductive thin strips. Sylgard 184 encapsulation has been used to fix the concentrator to the solar cell and keep the solar cell surface clean. A linear asymmetric compound parabolic concentrator (LACPC) with a concentration ratio of 3 suns.is used. An aluminum plate is placed beneath the solar cell to discharge the heat from the solar cells, Kapton tape is used for electrical insulation between the solar cells and the aluminum plate. The module geometry and properties are similar to [5].

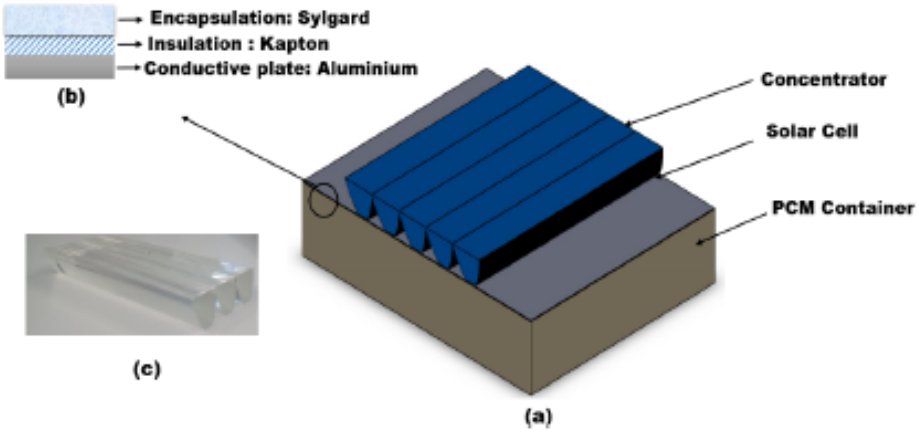

FIGURE 2. BICPV-PCM model arrangements (a) General arrangement, (b) Top cover layers, (c) Parabolic concentrator.

The above BICPV arrangement was placed in a container filled with a PCM. The container is made of thermally insulated materials (poly-methyl methacylate). RT 31 was used as the PCM in this study. The thermo-physical properties of the simulated materials are presented in tables 1 and 2.The PCM dimension is 144mm wide and 15mm

thick. The depth of the container is much larger than the thickness, so two-dimensional analysis can be applied. In addition the following boundary conditions/assumptions were applied to simplify the problem:

1. The solar cell efficiency is constant (19%).
2. The total solar radiation transmitted to the solar cell is 90% of solar irradiation collected by the concentrator.
3. PCM flow is laminar, incompressible and Newtonian.
4. The PCM is pure, homogeneous, and isotropic.
5. The melting process occurs over a range of phase transition temperature ($2\Delta T$)
6. All the PCM container sides are adiabatically insulated.
7. The ambient temperature is 22°C.
8. The top side convection heat transfer coefficient is 5.8W/m^{2}K and it is 9.5W/m^{2}K in the bottom.

TABLE 1. Thermo-physical properties of PCM used in model

Property Name	Units	Value
Heat Capacity	C_p (J/kg.K)	2000
Density(solid)	ρ_s (kg/m^3)	880
Density(Liquid)	ρ_l (kg/m^3)	760
Viscosity	μ_l (kg/m.s)	1.789×10^{-3}
Melting Temperature(main Peak)	T_m(°C)	31
Thermal Conductivity	k(W/m.K)	0.2
Latent heat of fusion	L(J/kg)	170

TABLE 2. Geometry and thermo-physical properties of BICPV components

Property Name	Solar Cell	Concentrator	Front and Back plate	Dielectric Layer	encapsulation
Material	Silicon	Acrylic	Aluminum	Kapton tape	Sylgard
ρ(kg/m^3)	2329	1162	2700	1530	1030
k(W/m.K)	149	0.1875	238	0.12	0.27
C_p (J/kg.K)	900	1465	900	1000	1030
Thickness(mm)	0.3	-	0.6	0.065	0.5

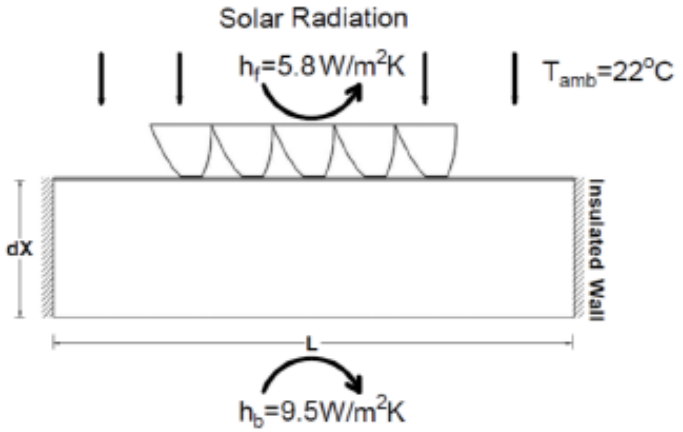

FIGURE 3. Main model boundary conditions

Mathematical Model

Modeling heat transfer

A comprehensive mathematical model for PCM heat transfer analysis has been developed by Biwole et al [8- 9]. This includes the heat transfer and fluid flow. The total heat generated by the solar cell (Q_h) is modeled as heat source and can be expressed as:

$$Q_h = (1-\eta_{elec})Q_o \tag{1}$$

Where Q_o indicates the optical power in W/m^2 at the outlet of the concentrator and η_{elec} is the electrical efficiency of the solar cell. The optical power takes into the account both the concentration ratio and the concentrator efficiency.

The heat transfer in solar cell is given by:

$$\rho C_p \frac{\partial T}{\partial t} + k\frac{\partial T}{\partial x} + h(T_{amb} - T) = Q_h \tag{2}$$

Where ρ is the density (kg/m^3), C_p is the heat capacity (J/kg K), k is the material's thermal conductivity (W/m K), h is the convective heat transfer coefficient (W/m^{2}K) and T_{amb} is the ambient temperature.

The heat transfers diffusion equation applies over the PCM and can be expressed as:

$$\rho C_p \frac{\partial T}{\partial t} + \nabla.(-k\nabla T) + \rho C_p \vec{u}.\nabla T = 0 \tag{3}$$

Where $\vec{u}$ is the velocity given by Navier-stokes equations for incompressible fluids. The changes in the PCM therm-physical properties occur during the phase transition stage and this is expressed by defining liquid fraction in the PCM domain:

$$B(T) = \begin{cases} 0, & T < (T_m - \Delta T) \\ \dfrac{T - T_m + \Delta T}{2\Delta T}, & (T_m - \Delta T) \le T < (T_m + \Delta T) \\ 1, & T > (T_m + \Delta T) \end{cases} \tag{4}$$

Where ΔT is the melting temperature range. Therefore, the PCM thermo-physical properties are as follow:

$$\rho(T) = \rho_{solid} + (\rho_{liquid} - \rho_{solid}).B(T) \tag{5}$$

$$k(T) = k_{solid} + (k_{liquid} - k_{solid}).B(T) \tag{6}$$

$$C_p(T) = C_{p\,\text{solid}} + (C_{p\,\text{liquid}} - C_{p\,\text{solid}}).B(T) + L..D(T) \tag{7}$$

Where ρ is the density, k is the thermal conductivity, C_p is the specific heat and L is the latent heat of fusion of the PCM. D(T) is a smoothed Gaussian function which is zero everywhere except in the melting interval and is expressed as:

$$D(T) = \frac{e^{(-T(T-T_m)^2)/(\Delta T^2)}}{\sqrt{\pi.\Delta T^2}} \tag{8}$$

In this model, the PCM is assumed to be in liquid phase. The mass, momentum and energy conservation equations are coupled with the heat transfer diffusion.. The momentum conversion equation is modified to model the phase change using two forces: buoyancy force (F_b) and the force to control the solid phase (F_a). These are expressed as follows:

$$\vec{F_b} = -\rho_{solid}(1-\beta(T-T_m))\vec{g} \tag{9}$$

$$\vec{F_a} = -A(T)\vec{u} \tag{10}$$

Where β is the coefficient of thermal expansion (K^{-1}) and A(T) is expressed as:

$$A(T) = \frac{-C(1-B(T))^2}{(B(T)^3 + q)} \tag{11}$$

Where C and q are constants and equal to 10^5 and 10^{-3} respectively.

RESULTS AND DISCUSSIONS

The modeling of the BICPV-PCM system presented here allows us to determine the temperature, fluid movement, PCM melting profiles and fraction at any point during the simulation time period. The BICPV-PCM system is dependent on climatic conditions such as solar radiation intensity, ambient temperature and wind speed. Therefore, geographic regions with different climate conditions will need specific designs and should be treated individually. The BICPV system without PCM is analyzed first in order to identify the solar cell and concentrator temperature requirements for the PCM type.

The Predicted BICPV Thermal Behavior for Different Solar Radiation Intensity

BICPV simulations without a PCM were undertaken for 200, 400, 600, 800 and 1000 W/m² for 3 suns. The simulations were executed using time dependent model in order to establish the time required for the system to reach the steady state condition. The predicted average PV surface temperatures and average concentrator temperature are shown in figure 4. The solar cell temperature increases as the solar radiation increases. Due to the low thermal conductivity of the concentrator materials, the difference between the solar cell temperature and the top concentrator temperature also increases. In addition, the solar cell reaches its steady state average temperature faster than the concentrator.

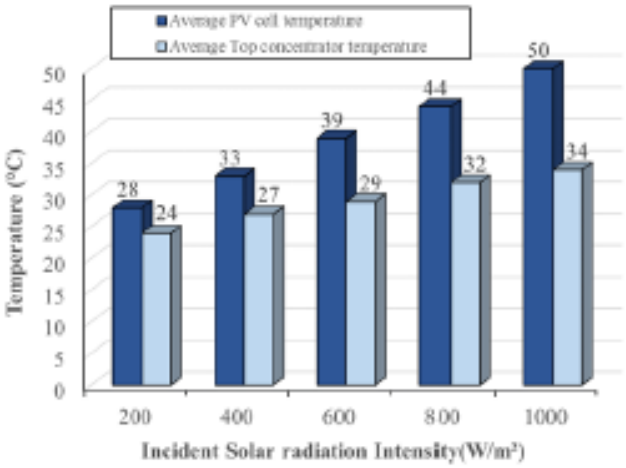

FIGURE 4. The predicted concentrator and solar cells average temperature for the BICPV system for different solar radiation intensity.

The modeled solar cell has a maximum efficiency of 19% under the standard conditions for CPV modules, which are a DNI of 1000 W/m² and 25°C. For similar solar cells, [10] has reported that the cell efficiency dropped at a rate of 0.3% per degree temperature rise. Therefore, the solar cell efficiency decreases with solar radiation intensity for 200,400,800 and 1000 W/m² at rate of 1%, 2%, 4%, 6% and 7% respectively. Thus, the BICPV system temperature for solar radiation intensity of less than 600 W/m² and a 22°C ambient temperature can be managed using a simple passive heat sink

The Predicted Thermal Behavior for the BICPV-PCM System

The simulation results obtained for the BICPV-PCM system are presented in this section. The results focused on the faces temperature (concentrator and solar cells), PCM melted fraction and the surface thermal \melting profiles.

The considered solar radiations were 600 and 800 W/m² at an ambient temperature of 22°C. This range of solar radiation is the maximum range that can be reached in the UK for long periods. Figure 5 shows the predicted front concentrator average temperature and solar cells average temperature. Initially, the solar cell temperature increases rapidly for both cases until it reaches 31°C (the PCM melting temperature). After this point, the PCM starts melting and is able to absorb the heat in latent form. The time lag between the start of PCM melting point and the solar cell stabilization temperature is due to the low thermal conductivity of the PCM and the melting occurs in a range of temperature.

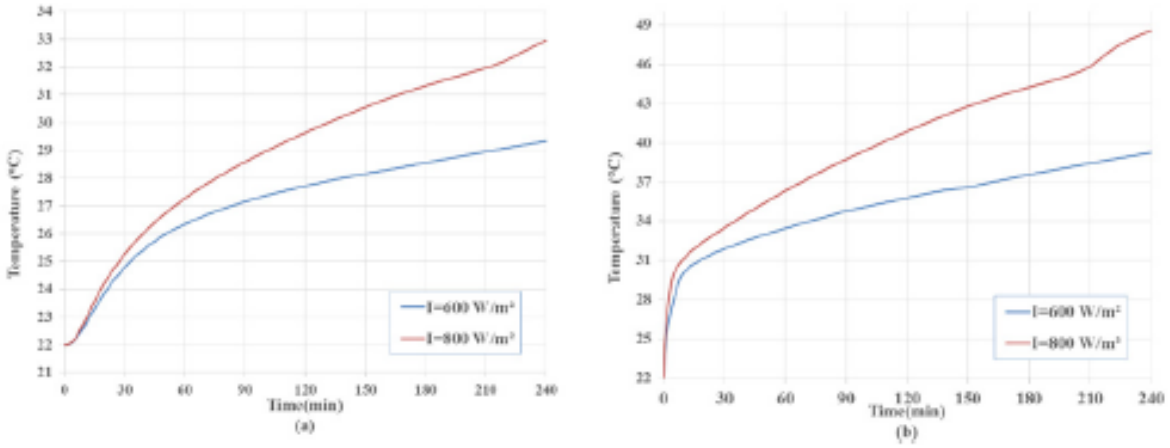

FIGURE 5. The predicted average temperature versus times, ambient temperature 22°C for different solar radiation intensity (a) Concentrator average temperature, (b) Solar cells average temperature.

The isotherms surface plots shows a straight horizontal line melting patterns. This is explained due to the low PCM thickness and thermal conductivity which allows more time for heat to spread across the PCM. The predicted PCM melting fraction is shown in figure 6. The PCM does not melt completely for 600W/m² solar radiation intensity during the simulation period. For 800W/m² solar radiation intensity, the PCM melted completely after 204 minutes. This explains the increase of temperature slope line in figure 5 for 800W/m² after this time.

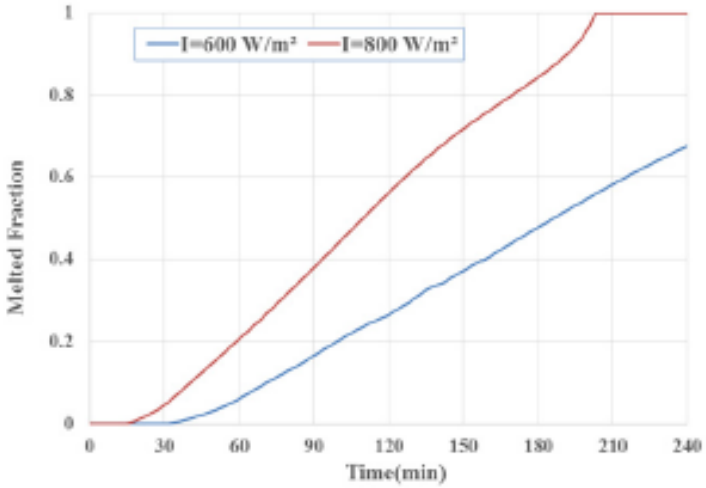

FIGURE 6. The predicted PCM melting fraction versus time, ambient temperature 22°C for different solar radiation intensity.

As stated earlier, the main objective of the PCM is to regulate the solar cell temperature. In order to find its effect in the system, the solar cells temperature difference has been calculated for BICPV and BICPV-PCM systems as shown in figure 7. The positive temperature value indicates that the solar cells experience less temperature in the system with PCM. The maximum temperature difference between the two systems occurs just before the materials

starts melting. Once melting starts, the temperature difference reduces. It can be seen that the maximum temperature difference of 800W/m² is 10°C which corresponds to 3% efficiency improvement. Also, the figure shows that solar cell temperature in BICPV-PCM system is higher than in no-PCM system for 600W/m² and 800W/m² after 220 minutes and 180 minutes respectively.

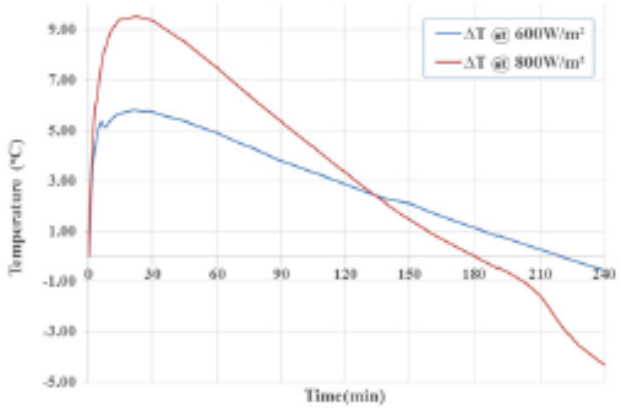

FIGURE 7. The predicted Difference of solar cells temperature BICPV with PCM and without PCM versus time, ambient temperature 22°C for different solar radiation intensity.

BICPV-PCM Thermal Behavior for Different Ambient Temperature

Natural convection plays an important role of cooling the solar cell and it directly depends on the ambient temperature. The effect of the ambient temperature on BICPV-PCM system has been studied using two different ambient temperatures: 20°C and 22°C. Figure 8 shows the predicted concentrator average temperature and solar cells average temperature at the different ambient temperatures and solar radiation intensity. As expected, the ambient temperature has an effect in reducing the system temperature. The temperature difference increases with time for both the concentrator surface temperature and solar cell temperature.

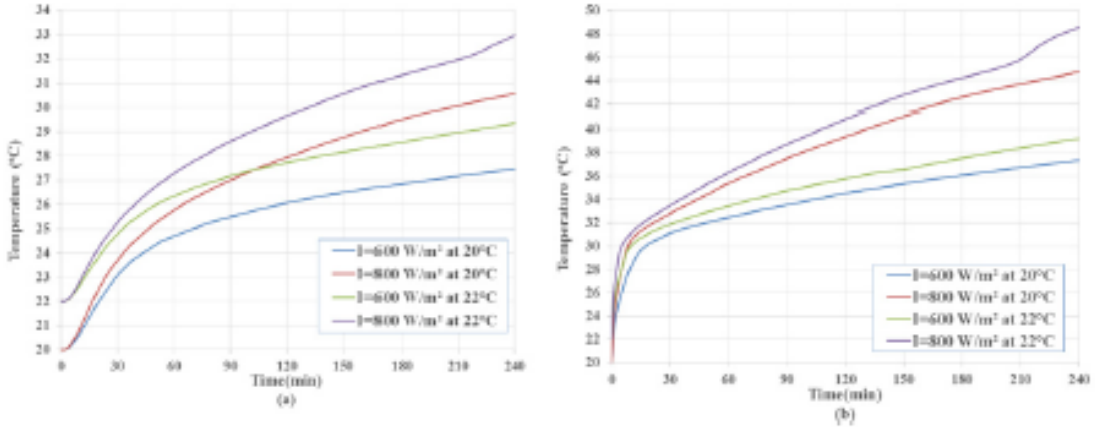

FIGURE 8. The predicted average temperature versus time for different ambient temperatures and solar radiation intensity (a) Concentrator temperature, (b) solar cell temperature.

Figure 9 shows the melting fraction for both 600W/m² and 800W/m² for different ambient temperatures. It can be noticed that the complete PCM melting in solar intensity of 800W/m² could be delayed half an hour if the ambient temperature decreases by two degrees. This result shows the importance of the climate conditions on the system and to be taken in consideration during the system design stage.

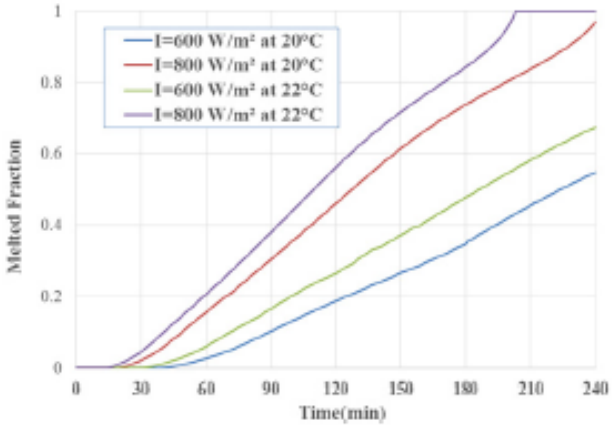

FIGURE 9. The predicted PCM melting fraction versus time for different ambient temperatures and solar radiation intensity.

CONCLUSION

The numerical model analysis of BICPV-PCM model for low CPV concentration application has been presented. The concentrator effects has been included in the model for accurate results. The heat transfer from the BICPV to the phase change material has been analyzed numerically. The results shows PCM is able to reduce/delay the solar cells temperature in certain conditions.

ACKNOWLEDGMENT

The PhD scholarship of Idris Al Siyabi is funded by the Ministry of Higher education at the Sultanate of Oman as part of the national program of postgraduate scholarships.

REFERENCES

1. O. Z. Sharaf and M. F. Orhan, "Concentrated photovoltaic thermal (CPVT) solar collector systems: Part I – Fundamentals, design considerations and current technologies," *Renew. Sustain. Energy Rev.*, vol. 50, pp. 1500–1565, 2015.
2. J. G. Ingersoll, "Simplified Calculation of Solar Cell Temperatures in Terrestrial Photovoltaic Arrays," *J. Sol. Energy Eng.*, vol. 108, no. 2, pp. 95–101, 1986.
3. B. P. Rand, J. Genoe, P. Heremans, and J. Poortmans, "Solar Cells Utilizing Small Molecular Weight Organic Semiconductors," *Prog. Photovolt Res. Appl.*, vol. 15, no. April 2012, pp. 659–676, 2007.
4. A. ROYNE, C. DEY, and D. MILLS, "Cooling of photovoltaic cells under concentrated illumination: a critical review," *Sol. Energy Mater. Sol. Cells*, vol. 86, no. 4, pp. 451–483, 2005.
5. S. Sharma, A. Tahir, K. S. Reddy, and T. K. Mallick, "Performance enhancement of a Building-Integrated Concentrating Photovoltaic system using phase change material," *Sol. Energy Mater. Sol. Cells*, vol. 149, pp. 29–39, 2016.
6. J. A. Duffie and W. A. Beckman, *Solar engineering of thermal processes*. Wiley New York etc., 1980.
7. Y. A. Cengel, S. Klein, and W. Beckman, *Heat transfer: a practical approach*. McGraw-Hill New York, 1998.
8. P. Biwole, P. Eclache, and F. Kuznik, "Improving the Performance of Solar Panels by the Use of Phase-Change Materials," *World Renew. Energy Congr.*, pp. 2953–2960, 2011.
9. P. H. Biwole, P. Eclache, and F. Kuznik, "Phase-change materials to improve solar panel's performance," *Energy Build.*, vol. 62, pp. 59–67, 2013.
10. H. Baig, N. Sarmah, K. C. Heasman, and T. K. Mallick, "Numerical modelling and experimental validation of a low concentrating photovoltaic system," *Sol. Energy Mater. Sol. Cells*, vol. 113, pp. 201–219, 2013.